

UNIVERSITY OF STRATHCLYDE
Department of Physics

Micro-pixellated AlInGaN light-emitting
diode arrays for optical communications
and time-resolved fluorescence lifetime
measurements

by

Jonathan McKendry



A thesis presented in fulfilment of the
requirements for the degree of
Doctor of Philosophy

April 2011

Declaration of Authorship

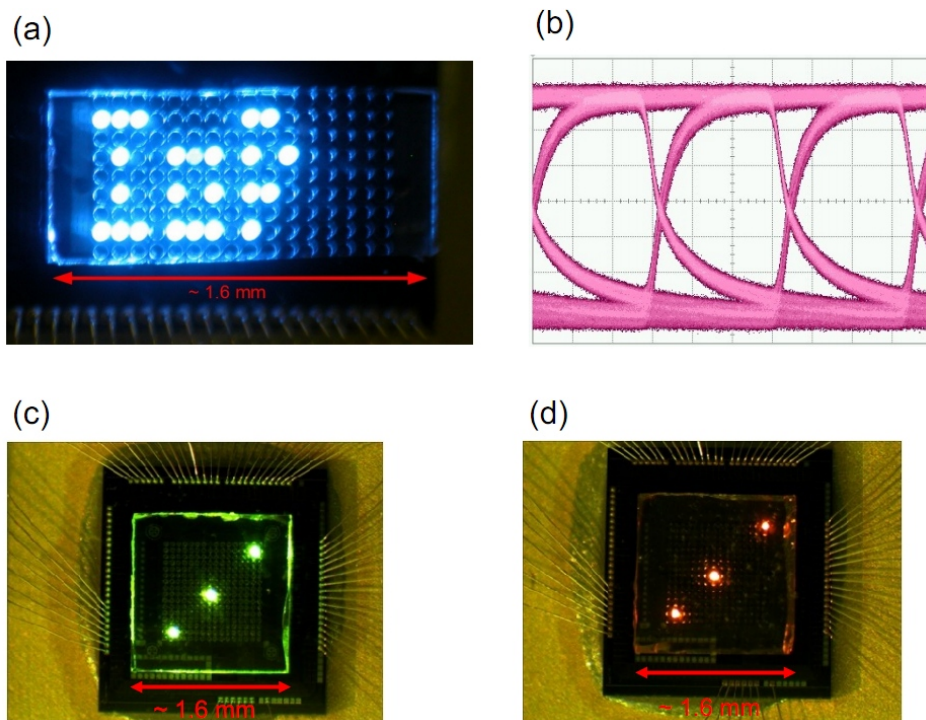
This thesis is the result of the author's original research. It has been composed by the author and has not been previously submitted for examination which has led to the award of a degree.

The copyright of this thesis belongs to the author under the terms of the United Kingdom Copyright Acts as qualified by University of Strathclyde Regulation 3.50. Due acknowledgement must always be made of the use of any material contained in, or derived from, this thesis.

Signed: _____

Date: _____

Frontispiece



(a) output pattern from a 450 nm peak emission CMOS-controlled micro-LED array, (b) eye diagram from a micro-LED pixel modulated at 155 Mbit/s, output pattern from (c) 520 nm and (d) 600 nm peak emission CMOS-controlled micro-LED arrays.

Acknowledgements

First of all I'd like to thank my supervisor, Prof. Martin Dawson, for giving me this opportunity and for his guidance and encouragement throughout the course of my studies. I have been lucky to have had support from many people, and I am grateful to everybody who has helped me. In particular I would like to thank (in no particular order!) Erdan Gu for his help and guidance, David Massoubre and Zheng Gong for fabricating such great micro-LED devices for me to work with, Tony Kelly for spending so much of his valuable time helping get the VLC measurements up and running, Robert Henderson and Bruce Rae for their work designing the CMOS control chips, Nicolas Laurand and Benoit Guilhabert for preparing samples for me, and Chris Griffin for showing me the ropes during the early stages of my studies.

I'd also like to thank all my IoP colleagues, past and present, for making it such a good place to work. I am lucky to have made some good friends during my time at the IoP.

Finally, I'd like to thank my family and my girlfriend Anne for their love and support.

This research was supported by EPSRC under the *Basic Technology: A Thousand Micro-emitters Per Square Millimetre: New Light On Organic Materials & Structures* and 'HYPIX' projects.

Contents

Declaration of Authorship	i
Acknowledgements	iii
List of Figures	vii
List of Tables	xii
Abbreviations	xiii
Abstract	xvi
1 Introduction	1
1.1 The development of light-emitting diodes	2
1.2 Summary of LED operation	6
1.2.1 Electroluminescence	8
1.2.2 The p-n diode	9
1.2.3 Quantum well structures	11
1.3 AlInGaN-based LEDs	14
1.3.1 Epitaxial growth and processing of AlInGaN alloys	15
1.3.1.1 Substrate materials	17
1.3.1.2 Contact metal deposition	19
1.3.1.3 Doping of AlInGaN materials	20
1.3.2 AlInGaN LED device structure	21
1.3.3 LED efficiency droop	22
1.4 Organic semiconductors and quantum dots	26
1.4.1 Organic semiconductors	26
1.4.2 Quantum dots	30
1.4.3 Colour-conversion, deposition and integration	32
1.5 Summary	34
2 Micro-pixelated light-emitting diode arrays	43
2.1 Introduction to micro-LED arrays	43
2.1.1 Development of micro-LED arrays	43
2.1.2 Advantages and applications of micro-LED arrays	45

2.2	Micro-LED design and fabrication	48
2.2.1	Matrix-addressable micro-LED array design	49
2.2.2	Individually-addressable flip-chip array design	51
2.2.3	‘Cluster’ flip-chip array design	53
2.3	Micro-LED array performance	54
2.3.1	I-V characteristics	54
2.3.2	DC L-I characteristics	56
2.3.3	Pulsed L-I characteristics	59
2.3.4	Emission spectra	62
2.4	Summary	65
3	CMOS-controlled micro-LED arrays	70
3.1	Complementary Metal-Oxide-Semiconductor (CMOS) technology.	71
3.1.1	Metal-Oxide-Semiconductor Field Effect Transistors (MOSFETs) .	71
3.1.2	Basic CMOS logic gates	74
3.1.3	Flip-chip bump-bonding	76
3.2	‘First-generation’ CMOS control chip	78
3.2.1	Single photon avalanche diodes (SPADS)	80
3.2.2	Device performance	82
3.2.3	Discussion	84
3.3	‘Second-generation’ CMOS control chip	85
3.4	‘Third-generation’ CMOS control chip	87
3.4.1	Voltage-controlled oscillator (VCO)	91
3.4.2	Pulse generation circuitry	93
3.4.3	Driver board and interface	93
3.4.4	Device performance	95
3.4.5	Discussion	103
3.5	Applications of CMOS-controlled micro-LED arrays	104
3.6	Summary	106
4	Micro-LEDs for time-resolved fluorescence lifetime measurements	110
4.1	Overview of fluorescence measurements	110
4.1.1	Steady-state and time-resolved measurements	110
4.1.2	Instrumentation for time-resolved fluorescence measurements . . .	113
4.2	Time-correlated single-photon counting (TCSPC)	115
4.3	TCSPC using a ‘first-generation’ CMOS-controlled micro-LED device . .	117
4.3.1	Experimental set-up	117
4.3.2	Results - quantum dot fluorescence lifetimes	120
4.4	TCSPC using a ‘third-generation’ CMOS-controlled micro-LED device . .	122
4.4.1	Lifetime measurement of organic semiconductors and colloidal quantum dots	122
4.4.2	Lifetime measurements of Rhodamine dyes using on-chip lifetime processing circuitry	127
4.5	Summary	129
5	Micro-LEDs for visible light communications	133
5.1	Visible light communication using LEDs	133
5.2	Micro-LED frequency response measurements	135

5.2.1	16 × 16 individually-addressable micro-LED frequency responses	137
5.2.2	8 × 8 individually-addressable micro-LED array frequency responses	138
5.2.3	Current dependent micro-LED frequency response	140
5.3	Data transmission using micro-LEDs	145
5.3.1	Micro-LED optical data transmission with increased modulation depth	149
5.4	Colour-conversion of micro-LED emission for white light communications	151
5.4.1	Hybrid LED/colour-converter frequency response model	152
5.4.2	Bandwidth of a hybrid micro-LED and quantum dot-based nanocomposite device	155
5.4.2.1	Experimental	155
5.4.2.2	Results and discussion	157
5.4.3	Bandwidth of hybrid micro-LED and LEP colour-converters	160
5.4.3.1	Experimental	160
5.4.3.2	Results and discussion	161
5.5	Summary	163
6	Conclusions	169
6.1	Future work	171
A	Mathcad code for extracting radiative lifetime from frequency response measurements	175
B	Publications	179

List of Figures

1.1	Applications of LEDs	2
1.2	Summary of the luminous efficacy of III-V LEDs.	4
1.3	Comparison of the efficacy of different light sources.	4
1.4	Schematic of a typical LED and a high power LED.	5
1.5	Intrinsic, n-type and p-type semiconductors.	7
1.6	Acceptor and donor energy levels in a semiconductor.	8
1.7	Band structures of direct and indirect bandgap semiconductors.	9
1.8	P-n diode under zero bias and forward bias.	11
1.9	(a)p-n and (b) p-i-n junction under forward bias.	12
1.10	One-dimensional ‘potential well’	13
1.11	Quantum well structure, illustrating that the energy of the optical transition from E_{e1} to E_{h1} exceeds the energy of the bandgap, E_g . Here, e and h refer to the electron and hole confined energy levels.	13
1.12	Room-temperature bandgap energy, E_g , and emission wavelength versus lattice constant for the AlInGaN-Nitride alloy system.	14
1.13	Schematic growth of GaN by MOCVD.	16
1.14	Schematic of an example of a typical ICP reactor.	17
1.15	(a) Sapphire crystal orientation, (b) atomic arrangement of AlN film grown on sapphire	18
1.16	Dislocation structure of an epitaxial GaN layer, grown on sapphire.	18
1.17	Proposed mechanisms for why dislocations in InGaN do not act as efficient non-radiative recombination centres.	18
1.18	Schematic illustration of (a) magnetron sputtering and (b) electron-beam evaporation techniques.	20
1.19	Schematic illustration of a typical epitaxial structure of a UV-emitting micro-LED.	21
1.20	Four common structures of AlInGaN LED die.	23
1.21	‘Efficiency droop’ in an InGaN/GaN LED.	24
1.22	Illustration of non-radiative and Auger recombination.	25
1.23	Schematic of the conduction (E_c) and valence band (E_v) energies in an InGaN-based LED heterostructure.	25
1.24	Orbital hybridisation and bonding between two carbon atoms.	27
1.25	Jablonski diagram showing the different transitions that may occur in a molecule or polymer during luminescence.	29
1.26	Absorption and photoluminescence emission (solid line) of PFO.	29
1.27	Chemical structure, absorption and emission spectra of truxene molecules.	30
1.28	‘Core-shell’ structure of a quantum dot.	31

1.29	Absorption and emission spectra of CdSe/ZnS quantum dots in toluene solution.	32
1.30	Schematic and emission spectra of a conventional phosphor-based white LED.	32
1.31	Colour-coordinates of a standard phosphor-based LED, a micro-LED/LEP hybrid and a CQD/LED hybrid.	33
1.32	Techniques for micro-patterning of nanoluminophore materials	34
2.1	Schematic and SEM image of the first reported electrically injected micro-LED devices.	44
2.2	Optical micrograph images of an individually-addressable micro-disk LED array and its output.	45
2.3	Schematic of an integrated 100 element bluegreen micro-LED array with fibre optic image projection system, and emission patterns generated at the end of the multicore image fibre.	46
2.4	Schematic of an optoelectronic tweezer device.	47
2.5	Image of micro-LED devices with different peak emission wavelengths.	49
2.6	Cross-sectional schematic of a matrix-addressable micro-LED array and a corresponding micrograph image.	50
2.7	Output power versus current of single pixels in matrix-addressable arrays.	50
2.8	Matrix-addressable micro-LED GUI and array output.	51
2.9	Process flow for fabricating individually-addressable micro-LEDs.	52
2.10	Micrograph image of section of a 16×16 and an 8×8 individually-addressable micro-LED array.	53
2.11	Optical micrograph of cluster micro-LED array.	54
2.12	Process flow for interconnected micro-LED arrays.	54
2.13	DC current versus voltage (I-V) curves for various 16×16 micro-LED devices.	55
2.14	DC current versus voltage (I-V) curves for various 8×8 micro-LED devices.	56
2.15	CW optical output power versus injected current (L-I) graph of individual $72 \mu\text{m}$ diameter pixels from 16×16 arrays, with peak emissions of 370, 405, 450 and 470 nm.	57
2.16	CW optical output power versus injected current (L-I) graph of selected pixels from 8×8 arrays with peak emissions of 370, 405, 450 and 520 nm.	58
2.17	CW optical output power versus injected current (L-I) graph of individual micro-LED pixels for different pixel sizes.	59
2.18	Schematic illustration of several forms of resonator used in OSLs.	60
2.19	Circuit diagram of a laser diode pulse driver.	61
2.20	Representative micro-LED optical output pulse.	61
2.21	Comparison of micro-LED pulsed output and reported OSL thresholds.	63
2.22	Pulsed L-I characteristics of $72 \mu\text{m}$ 405 and 450 nm peak emission micro-LED pixel.	63
2.23	Pulsed L-I characteristics of sub-arrays from a 450 nm-emitting interconnected micro-LED array.	64
2.24	Emission spectra of various micro-LED devices.	65
3.1	Schematic of n-type and p-type MOSFETs.	72
3.2	Operating regions of an NMOS transistor.	73

3.3	Current-voltage curves of an NMOS transistor.	73
3.4	NMOS and PMOS circuit diagram symbols.	74
3.5	Circuit diagram of a CMOS inverter.	75
3.6	Circuit diagram of a NAND gate.	76
3.7	Schematic illustration of the flip-chip bonding process.	77
3.8	Images of gold bump-bonds used for micro-LED flip-chip bonding.	77
3.9	Micrograph image of a ‘first-generation’ flip-chip bonded micro-LED/CMOS device.	79
3.10	SEM image of the CMOS top electrodes, showing the location of the SPADs.	79
3.11	Current-controlled micro-LED driver circuit.	80
3.12	Avalanche breakdown current within a SPAD.	81
3.13	SPAD cross-section.	82
3.14	Output of a CMOS-driven 470 nm peak emission micro-LED array.	82
3.15	L-I characteristics of CMOS-driven micro-LEDs.	84
3.16	Array output uniformity.	84
3.17	Longest and shortest output pulses obtained from a 370 nm emitting CMOS-driven micro-LED array.	85
3.18	Top-down micrograph image showing the layout of the second-generation CMOS chip.	86
3.19	Cross section of the CMOS device wafer.	87
3.20	Cross section of the third-generation CMOS chip, and micrograph image of the chip surface.	88
3.21	Optical micrograph image of the ‘third-generation’ CMOS chip.	89
3.22	Driver circuit implemented in the main 8×8 array.	90
3.23	Example of a current-starving transistor.	91
3.24	Layout of the test cell array.	92
3.25	Circuit diagram of a ring oscillator.	92
3.26	Circuit and timing diagrams of the short-pulse generator.	94
3.27	Photograph of the driver board used for testing the CMOS-controlled micro-LEDs.	94
3.28	Output pattern of a 370 nm peak emission CMOS/micro-LED device.	96
3.29	L-I characteristics of individual 72 μm diameter CMOS-controlled pixels emitting at 370, 405 and 450 nm.	97
3.30	Circuit diagram illustrating the origin of electrical crosstalk.	97
3.31	Electrical cross talk in a CMOS-controlled micro-LED array.	98
3.32	Output power uniformity of CMOS-controlled micro-LED arrays.	99
3.33	Optical pulse width versus pulse control voltage, VBMC2.	100
3.34	Optical pulse width versus <i>LED_GND</i>	101
3.35	TCSPC histogram illustrating a 300 ps optical pulse from a 370 nm-emitting micro-LED pixel.	101
3.36	Optical output pulse trains in different modes of operation.	102
3.37	Frequency response of a 450 nm-emitting CMOS-controlled micro-LED pixel.	103
3.38	Mask-free photolithography system incorporating a CMOS-controlled micro-LED array.	105
3.39	Micrograph and SEM images of exposed dots in photoresist.	105
3.40	Schematic of the CMOS-controlled micro-LED OET device.	106

3.41	Opto-electronic tweezing of cells, using a CMOS-controlled micro-LED as the light source.	107
4.1	Illustration of time-domain measurements.	113
4.2	Simplified block diagram of a TCSPC system.	116
4.3	Illustration of the basic principles of TCSPC.	116
4.4	Quantum dot absorption and emission spectra.	119
4.5	Cross-sectional schematic of the micro-LED/CMOS fluorescence excitation and detection chip.	120
4.6	Photograph of the micro-LED/CMOS TCSPC system.	120
4.7	Quantum dot absorption and emission spectra, micro-LED emission spectrum and SPAD PDP.	121
4.8	Measured fluorescence decays of quantum dot samples.	121
4.9	Cross-sectional schematic of a two chip, micro-LED/CMOS and SPAD array fluorescence excitation and detection chip.	123
4.10	Photograph of the micro-LED/CMOS and SPAD TCSPC system.	123
4.11	Absorption and emission spectra of BBEHP-PPV light-emitting polymer.	124
4.12	Measured fluorescence decay of BBEHP-PPV light-emitting polymer.	125
4.13	Measured fluorescence decay of T3 blend.	126
4.14	Measured fluorescence decay of CdSe/ZnS CQDs in toluene solution.	127
4.15	Measured fluorescence decays of R6G, RB and quantum dot samples.	128
5.1	Attenuation versus wavelength for POF.	135
5.2	Schematic of the micro-LED frequency response measurement setup.	137
5.3	Frequency response of 72 μm diameter micro-LED pixels, as a function of applied DC current.	138
5.4	Maximum modulation bandwidth of micro-LED pixels, of different diameters, for 8×8 micro-LED arrays.	139
5.5	Bandwidth versus current density for different pixel sizes from the same 450 nm-emitting 8×8 micro-LED array.	139
5.6	Radiative current versus carrier density squared for a 450 nm emitting, 44 μm diameter micro-LED pixel.	142
5.7	$B(N)$ versus N for a 450 nm emitting, 44 μm diameter micro-LED pixel.	142
5.8	I_c versus N^3 for a 450 nm emitting, 44 μm diameter micro-LED pixel.	143
5.9	$\tau(N)$ versus N for a 450 nm emitting, 44 μm diameter micro-LED pixel.	144
5.10	Illustration of the NRZ voltage input data signal to the micro-LED.	147
5.11	BERs measured from a 520 nm-emitting micro-LED at various bit rates.	148
5.12	Eye diagrams measured from a 520 nm-emitting micro-LED at various bit rate.	149
5.13	BERs measured from a 520 nm-emitting micro-LED at various bit rates and modulation depths.	150
5.14	Eye diagrams from a 520 nm-emitting micro-LED at 1.1 Gbit/s, with different modulation depths.	151
5.15	Illustration of an envisaged visible light communications network.	152
5.16	Illustration of the modulation and phase shift of a fluorescence emission, $N(t)$, relative to the excitation source, $L(t)$	153
5.17	Emission spectra of nanocomposite samples.	156

5.18	Schematic of the imaging and collection optics used to measure the response of a modulated polymer sample.	157
5.19	Photograph of the imaging and collection optics used to measure the response of a modulated nanocomposite sample.	158
5.20	Measured and fitted frequency responses of nanocomposite samples.	159
5.21	Photograph of the imaging and collection optics used to measure the response of a modulated nanocomposite sample.	159
5.22	Absorption and emission spectra of Red F and BBEHP-PPV LEPS.	161
5.23	Measured and estimated frequency response of Red F and BBEHP-PPV polymers excited by a 450 nm micro-LED.	162
6.1	Optical micrograph image of 5 pixels from a 405 nm emitting CMOS-controlled micro-LED array.	171
6.2	Frequency response of a 450 nm peak emission micro-LED driven by the new 'fourth generation' CMOS chip.	172
6.3	Optical data transmission using a CMOS-controlled micro-LED array.	173

List of Tables

1.1	Important properties of the AlInGaN alloy system [21].	15
2.1	Summary of device performance.	55
3.1	Summary of ‘third-generation’ CMOS chip.	89
4.1	Properties of the quantum dot samples investigated using this system . .	118
5.1	Fitted coefficient values for data from 450 nm emission micro-LED of various pixel diameter.	143
5.2	Average coefficient values from table 5.1 compared with literature reports	145
5.3	Nanocomposite sample composition and external conversion efficiency. . .	156

Abbreviations

AC	Alternating current
BER	Bit-error rate
BERT	Bit-error rate test system
CMOS	Complementary metal-oxide semiconductor
CQD	Colloidal quantum dot
DC	Direct current
DH	Double heterostructure
DMD	Digital micro-mirror display
EQE	External quantum efficiency
FPGA	Field-programmable gate array
FWHM	Full-width at half maximum
GUI	Graphical user interface
ICP	Inductively-coupled plasma
IQE	Internal quantum efficiency
IR	Infrared
IRF	Instrument response function
LD	Laser diode
LED	Light-emitting diode
LEP	Light-emitting polymer
LFSR	Linear feedback shift register
MOCVD	Metal-organic chemical-vapour deposition
MOSFET	Metal-oxide semiconductor field-effect transistor
MQW	Multi-quantum well
NMOS	N-type MOSFET
NRZ	Non-return to zero

OET	Opto-electronic tweezers
OSL	Organic semiconductor laser
PCB	Printed circuit board
PMOS	P-type MOSFET
PMT	Photo-multiplier tube
PRBS	Pseudo-random bit sequence
RCLED	Resonant-cavity light-emitting diode
RIE	Reactive ion etching
SEM	Scanning electron microscope
SPAD	Single-photon avalanche diode
TCSPC	Time-correlated single-photon counting
UV	Ultraviolet
VCO	Voltage-controlled oscillator
VCSEL	Vertical cavity surface-emitting laser
VLC	Visible light communication

To Mum & Dad

Abstract

Micro-pixelated light-emitting diodes ('micro-LEDs'), fabricated in the AlInGaN alloy system, are a novel format of micro-scale, spatially and temporally-controllable light source. These devices consist of arrays of LED pixels with sub-100 μm dimensions and peak emission wavelengths ranging from the ultraviolet across the visible spectrum. The emission wavelengths, high output powers of up to 5 mW per pixel, output programmability, relative compactness and simplicity of micro-LEDs make them attractive candidates as light sources for a wide range of applications ranging from micro-displays to microscopy.

This thesis will focus on investigations demonstrating the suitability of micro-LEDs for two particular applications, namely time-resolved fluorescence lifetime measurements and visible light communications. To show potential as truly practical devices for these applications, the ability to easily control the output of the micro-LED arrays is vital. As such, various designs of electronic control chips, based on Complementary Metal-Oxide-Semiconductor (CMOS) technology, are presented. The characteristics of these CMOS-controlled micro-LEDs are investigated.

Compact time-resolved fluorescence lifetime measurement systems based on CMOS-controlled micro-LEDs are shown. 'Proof-of-principle' measurements on samples of colloidal quantum dots, light-emitting polymers and organic dyes have been undertaken which allow for the fluorescence lifetime of these samples to be determined with reasonable accuracy, highlighting the potential for such measurements, typically restricted to laboratory environments due to bulky and/or expensive equipment, to be performed in a relatively simple, robust and compact system.

The potential of micro-LEDs as light sources for optical communications has also been investigated. The modulation bandwidth of various formats of micro-LED device have been measured, with bandwidths of up to 450 MHz found, amongst the highest ever reported for AlInGaN-based LEDs. Error-free transmission of optical data was demonstrated from individual micro-LED pixels at bit rates of up to 1.1 Gbit/s. These results highlight the attractiveness of micro-LEDs for visible light communication in both free-space and fibre-coupled embodiments.

Chapter 1

Introduction

This thesis focuses on the integration of micro-pixelated light-emitting diode (micro-LED) arrays with electronic control circuitry and some applications of these devices. As such, this first chapter functions as a general introduction to light-emitting diodes, with a particular focus on LEDs fabricated in the Aluminium-Indium-Gallium-Nitride (AlInGaN) alloy system, as this is the system that the micro-LEDs are fabricated from. The chapter opens with a summary of the historical development of LEDs and the future prospects for highly-efficient illumination LEDs. The subsequent section will describe the basic principles of LED operation, and the following section discusses the properties of the AlInGaN alloy system in more detail, including how these materials are grown and processed into LEDs. Finally, light-emitting polymer and quantum dot colour-converting materials are introduced. These materials will be presented later in the thesis as samples for fluorescence lifetime measurements or for colour-conversion of micro-LED emission.

Chapter 2 will follow on from the introductory chapter by describing the concept of micro-LEDs. The development and advantages of these devices will be summarised, and some novel applications of micro-LEDs will be presented. The specific design and performance of the micro-LEDs to be used throughout the thesis will then be given. To be able to easily control the output of the micro-LED arrays is vital in order to utilise their capabilities fully. Chapter 3 will discuss how micro-LEDs can be integrated with Complementary Metal-Oxide-Semiconductor (CMOS) electronic circuitry such that the LED pixels can be independently controlled. Chapter 4 will discuss one specific application of these CMOS-controlled micro-LEDs, namely as pulsed optical excitation sources for time-resolved fluorescence measurements. Specific fluorescence lifetime measurements will be presented to show the capability of these devices. Chapter 5 will discuss the potential of micro-LEDs for optical communications. The modulation bandwidths of

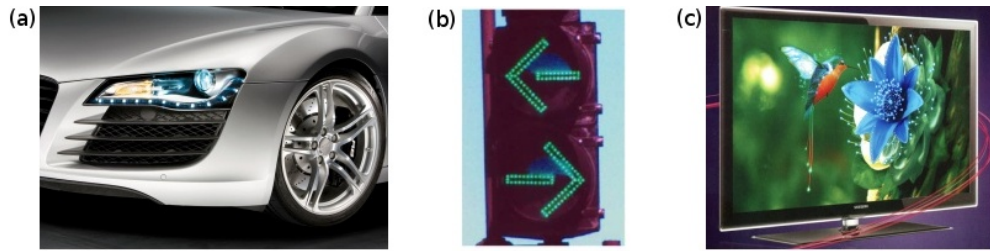


FIGURE 1.1: (a) LED headlights in the Audi A8, (b) green InGaN LEDs in traffic lights which consume less power and have longer operating lifetimes than conventional incandescent bulbs, (c) Samsung Series 8 LED television.

individual pixels will be shown to be up to ≈ 450 MHz, and a proof-of-principle optical data transmission system will be shown to be capable of transmission at up to 1.1 Gbit/s using a single micro-LED pixel. Finally, the thesis will close with some conclusions about the work presented here, along with some future work plans.

1.1 The development of light-emitting diodes

It is generally considered that the first light-emitting diode was accidentally produced in 1907 by Henry Joseph Round. It was made from Silicon Carbide (SiC) and emitted a yellowish light [1]. In the 1960s practical LEDs first began to be commercialised, with the Monsanto Corporation being the first to mass produce low-cost LEDs, beginning with red-emitting Gallium-Arsenide-Phosphide (GaAsP) LEDs in 1968. Following on from this, emission from red to green was achieved using N-doped GaAsP LEDs [2], and green-emitting N-doped GaP LEDs [3]. Early applications of these LEDs included use as indicator lamps in computers, and in displays in digital wrist watches and calculators. The output power, efficiency and wavelength coverage of LEDs has improved dramatically since those early devices and LEDs can be found in widespread applications today, including familiar everyday uses ranging from flat-panel televisions to car headlights (figure 1.1).

Although relatively efficient red to green emitting LEDs have been available since the late 1960s, it was not until the 1990s that the capability to efficiently produce light across the entire visible spectrum was made possible by advances in the fabrication of materials based on the AlInGaN alloy system. Prior to developments in AlInGaN technology in the 1980s and early 1990s, the alloy system which was believed to hold the most promise for producing efficient LEDs emitting at blue wavelengths was SiC, since this material could be grown with better crystal quality than AlInGaN. Blue-emitting SiC LEDs were sold commercially until the early 1990s, though are no longer commercially viable due to their very low efficiency ($\approx 0.005\%$). LEDs based on the AlInGaN alloy system have

since been shown to be far superior in performance. Although single-crystal GaN was first demonstrated as far back as 1969 [4], for decades the ability to fabricate LEDs from this material was held back, primarily by the inability to grow p-doped GaN due to the incorporation of oxygen and/or water vapour during growth [5]. It was not until the 1980s that breakthroughs began to be made, first by switching to growth by Metal Organic Chemical Vapour Deposition (MOCVD), a process which removes the problem of contamination. The first MOCVD-grown blue-emitting GaN LED was demonstrated in 1984 by Kawabata *et al.* [6]. Work by Amano *et al.* [7] in 1986 produced much improved crystal quality by the incorporation of an AlN buffer layer, which is now a standard process that greatly reduces the defect-density in GaN films. Further work on annealing of samples allowed low resistivity p-type GaN to be grown [8, 9], and a novel ‘two-flow’ MOCVD system was developed which allowed high quality uniform GaN films to be grown. This work has led to the development of high-power AlInGaN-based LEDs [10] and laser diodes [11] from the 1990s to the present day. The growth and processing of AlInGaN-based LEDs will be covered in more detail in section 1.3.

It is now possible to produce high-performance LEDs with light emission ranging across the entire visible spectrum, by fabricating LEDs from the phosphide, arsenide and nitride III-V materials systems. Invisible ultra-violet (UV) and infra-red (IR) light can also be generated by LEDs. The external quantum efficiency (EQE, or η_{ext}) of an LED is defined as the ratio of the number of photons emitted by the LED into free space to the number of injected charge carriers. The internal quantum efficiency (IQE), on the other hand, is the ratio of the number of photons emitted by the LED active region to the number of injected charge carriers. Figure 1.2 shows the EQE versus wavelength for LEDs made from two important III-V materials systems, along with the human eye response, $V(\lambda)$. It can be seen that the EQE is relatively poor in the green-yellow spectral region, where the human eye is most sensitive. This is referred to as the ‘green gap’ or ‘green-yellow’ gap.

This extended coverage of wavelengths has opened up many new applications for LEDs. Currently, the possibility of using AlInGaN LEDs to efficiently generate white light is attracting the most attention and is driving the advancement of this material system. AlInGaN LEDs have the potential to generate white light much more efficiently than conventional incandescent or fluorescent sources and thus to form the basis of ‘solid-state lighting’. White light can be obtained using LEDs in a number of ways, the most common of which is to combine the emission from a blue-emitting LED and a yellow-emitting phosphor, which will be discussed in more detail in section 5.4. It is anticipated that white light sources based on LEDs will eventually be up to 63% more efficient than fluorescent lamps and up to 90% more efficient than incandescent bulbs [12], with the additional advantage that LED lamps can have operating lifetimes that

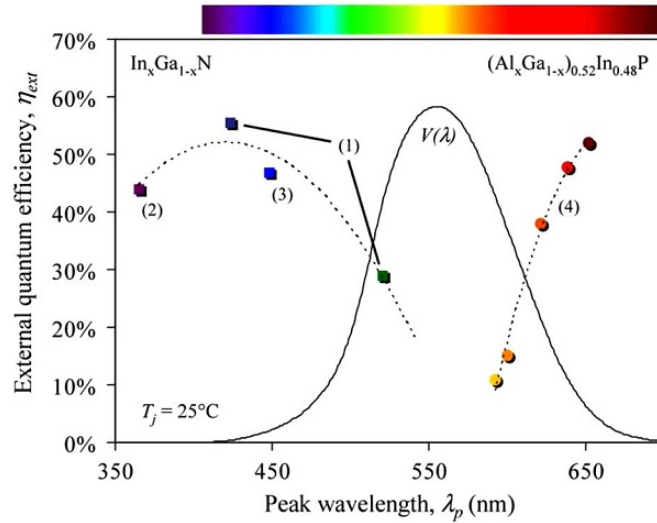


FIGURE 1.2: Summary of the luminous efficacy of III-V LEDs, from [13].

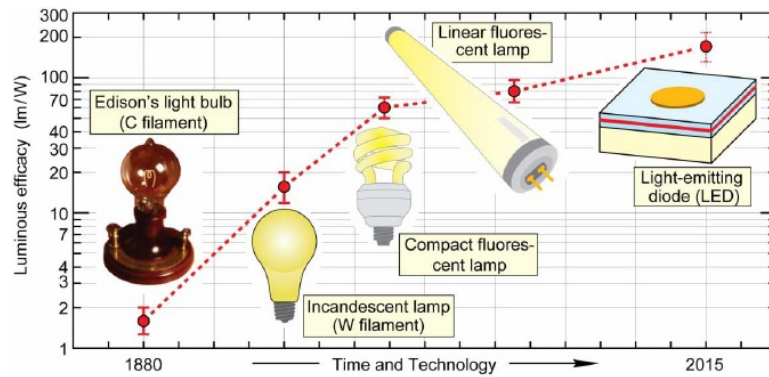


FIGURE 1.3: Comparison of the efficacy of different white light sources, from [12].

can exceed 100,000 hours, compared to 1000 hours for an incandescent bulb. There are several ‘figures of merit’ which are commonly used to quantify the performance of LEDs and other light sources. The *luminous flux* of a light source, measured in lumens (lm) is a measure of its output power as perceived by the human eye and the *luminous efficacy* of a source is defined as the ratio of the luminous flux of the source to the total output optical power, measured in lm/W. The *luminous efficiency* is defined as the ratio of the luminous flux to the total input electrical power, whereas the power efficiency (commonly referred to as the ‘wallplug efficiency’) is the ratio of the total optical output power to the total input electrical power. Figure 1.3 shows a comparison of the luminous efficacy of conventional light sources with the efficacy expected from solid-state lighting in the near future. Should such devices replace fluorescent and incandescent light sources huge economic and environmental benefits will result.

In addition to solid-state lighting, AlInGaN LEDs are also attractive light sources for other applications due to their longer operating lifetime, lower power consumption, compact form, low cost and robustness. LEDs are particularly suitable for use in portable

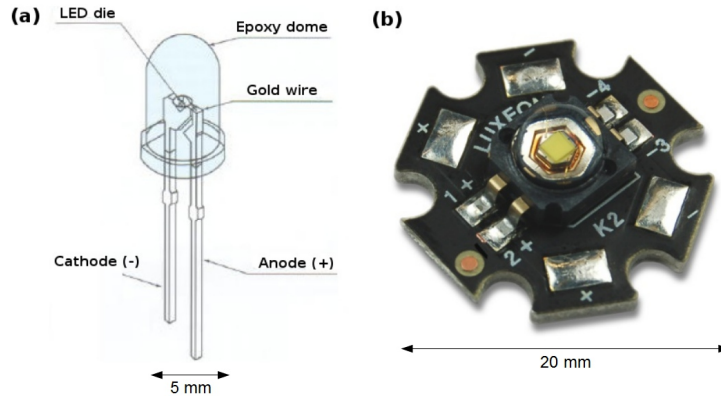


FIGURE 1.4: (a) Schematic of a typical ‘indicator’ LED and (b) a high power Luxeon Star[®] white-emitting LED.

battery-powered devices where high efficiency and robustness are vital. For example, a compact and portable water purification system which destroys harmful bacteria using UV LEDs has been demonstrated [14], offering a practical alternative to mercury vapour lamps which are undesirable for portable applications due to their high power consumption and fragility. AlInGaN LEDs have also recently been demonstrated as novel light sources for applications including the excitation of samples for fluorescence lifetime measurements [15] and airborne particle detection [16]; photo-chemical curing of photoresist for photolithography [17]; and non-line-of-sight solar-blind communications [18]. From this it can be seen that in a relatively short period of time the development of AlInGaN LEDs has facilitated a wide range of instrumentation applications, as well as holding great promise as highly efficient general illumination sources. Micro-LED pixelated arrays are a novel form of LED which themselves have been advantageously applied to a wide range of applications, and they will be discussed in greater detail in chapter 2 onwards.

The typical LED package that will be familiar to many people is shown in figure 1.4(a). The light-emitting semiconductor die typically measures around $300 \times 300 \mu\text{m}^2$. It is attached to a metal frame with leads for the anode and cathode. The primary purpose of the epoxy dome is to protect the LED from damage. The refractive index of the epoxy (≈ 1.4 - 1.6) also helps increase light extraction from the LED and the dome shape helps direct the light output. This form of LED is used mostly for low-power applications, such as indicator lights for consumer electronics. High power LEDs that are intended for general illumination require additional heat sinking to prevent the LED becoming damaged or destroyed due to excess heat during operation. These LEDs typically consist of more than one LED die within the package in order to increase the total light output. An LED package designed for high power operation is shown in figure 1.4(b). At present basic indicator-type LEDs are available from as low as a few pence per LED, with a typical high power white-emitting LED costing in the region of £5.

1.2 Summary of LED operation

Materials may be grouped into three general classes according to their ability to conduct electricity, namely *conductors*, *semiconductors* and *insulators*. Light-emitting diodes are fabricated from semiconductor materials. In general, electrons occupying the valence band are bound to atoms, and so are not able to contribute to the flow of charge when an electric field is applied to the material. By contrast, electrons in the conduction band are free to move through the material, and may contribute to a net flow of charge. The bandgap represents a range of forbidden energies between the valence and conduction bands that electrons may not occupy.

In conductors, the valence and conduction bands partially overlap, allowing some of the valence electrons to move freely through the material. In insulators, on the other hand, there are no free electrons in the conduction band, and the two bands are separated by a large bandgap (typically > 5 eV). Thus, all electrons in the material are strongly bound to atoms and cannot readily contribute to the net flow of charge. Semiconductors, as their name suggests, are a class of material with properties somewhere between that of insulators and conductors. Semiconductors have relatively small band gaps, which mean that electrons can easily be excited from the valence to conduction bands by, for example, thermal or optical excitation. Deliberate doping of the semiconductor material can also be used to engineer the conductivity of the material. Elemental semiconductors are semiconductors comprising of one element such as Si, while compound semiconductors are semiconductors comprising atoms of various elements. Common examples of binary compound semiconductors are GaAs, InP and GaN. Alloying semiconductors in this way allows the band structure of the material to be engineered.

Undoped, pure semiconductor materials are defined as ‘intrinsic’ semiconductors. In an intrinsic semiconductor, when an electron breaks free from the electrostatic attraction of its parent atom and is excited across the band gap into the conduction band, it leaves behind a vacancy, or ‘hole’, in the valence band. This hole can be filled by another electron, and it can be thought of as a positive charge which can itself also move around the semiconductor. Carriers generated in this way are known as intrinsic carriers. Since for every free negatively-charged electron a free positively charged hole is generated, intrinsic semiconductors are neutrally charged. Semiconductors can be intentionally doped in order to make them positively or negatively charged, with typical concentrations of dopant material in semiconductors ranging from 10^{15} to 10^{18} cm^{-3} or higher [19]. In order to appreciate how semiconductors are doped, consider the example of silicon. Si is in group IV in the periodic table, meaning that it has 4 valence electrons. In its crystalline state, each silicon atom shares one of its 4 valence electrons with each of its 4 neighbours. In this state, it is an intrinsic semiconductor, as all of its electrons

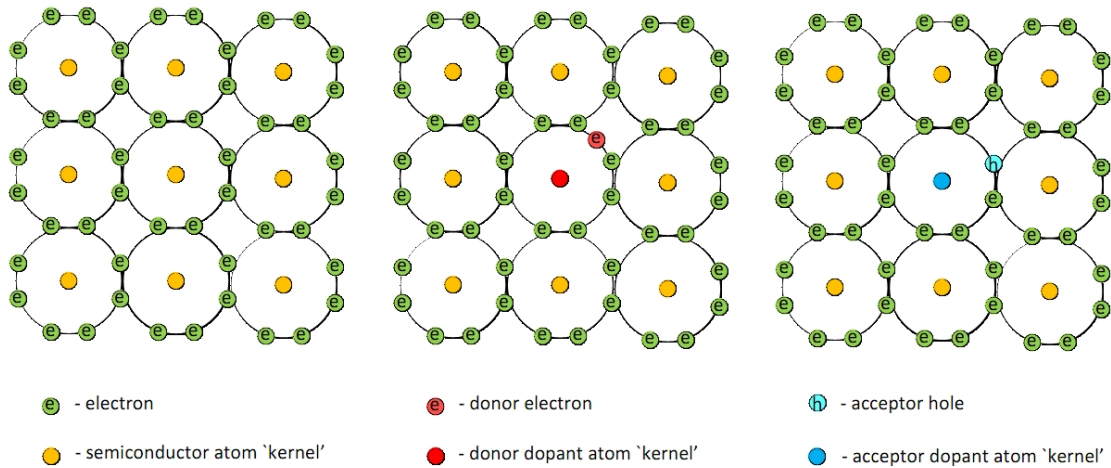


FIGURE 1.5: Illustration of (a) undoped intrinsic, (b) doped n-type and (c) doped p-type semiconductors. Here, 'kernel' describes the nucleus and inner shell valence electrons.

are in the valence band. If some of these silicon atoms are replaced with atoms of an element from group III in the periodic table, (e.g. B (boron), which has only 3 electrons in the valence band), then these dopant atoms will only have 3 electrons to share with their neighbouring 4 silicon atoms. This creates holes which contribute to the conduction process at all temperatures, making the material positively charged, or *p-type*. These dopants are known as acceptors, as they have a hole which can 'accept' electrons. Similarly, doping silicon with elements having 5 valence electrons (e.g. As) gives dopant atoms that have an extra 'free' electron which can also contribute to the conduction process, making the material negatively charged, or *n-type*. These dopants are known as donors, as they 'donate' a free electron to the crystal. Figure 1.5 illustrates how a donor or acceptor dopant atom creates a free electron or hole, respectively, in the bulk semiconductor material.

The energy levels of acceptors and donors lie within the semiconductor bandgap. The acceptor level, figure 1.6(a), lies slightly higher than the top of the valence band. Due to the small energy gap between these two levels, at room temperature electrons are thermally excited from the top of the valence band and fill the acceptor energy level, leaving behind free holes in the valence band. Similarly, electrons from the donor level, figure 1.6(b), are thermally excited into the conduction band where they are free to migrate through the crystal. The following section will show that the ability to produce p-type, n-type and intrinsic semiconductor materials is vital for fabricating LEDs.

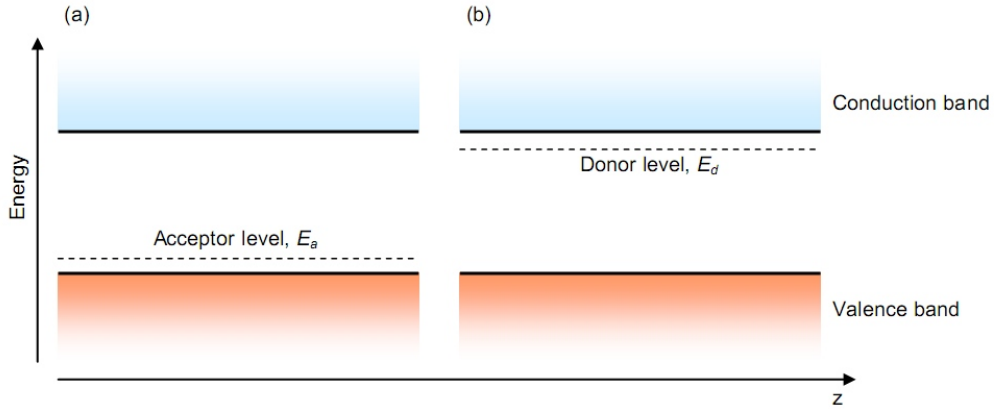


FIGURE 1.6: (a) acceptor and (b) donor energy levels in a semiconductor. As drawn, z is a spatial co-ordinate.

1.2.1 Electroluminescence

In LEDs, electrons from the conduction band recombine with holes in the valence band. The energy lost due to this transition is approximately equal to the energy of the conduction band minimum, E_c , minus the energy of the valence band maximum, E_v , or:

$$E_g = E_c - E_v \quad (1.1)$$

where E_g is the bandgap energy. This energy can be released either as heat (vibrations of the crystal lattice known as phonons) or by the emission of a photon through a process generally known as luminescence. This is the underlying process which allows LEDs to convert electrical energy into light: in LEDs, electrical carriers injected under bias recombine and emit photons via electroluminescence. By tuning the bandgap energy of the LED material it is possible to tune the wavelength of light emitted from the LED. The bandgap can be tuned in a semiconductor alloy system such as AlInGaN by altering the relative amounts of the various elements, or by using a ‘quantum well’ structure. This will be discussed in more detail later in sections 1.2.3 and 1.3 . The relationship between the bandgap energy and the wavelength of a photon emitted by electroluminescence, λ , is described by the following equation:

$$E \approx E_g \approx \frac{hc}{\lambda} \quad (1.2)$$

where E is the energy of an emitted photon, c is the speed of light in a vacuum and h is Planck’s constant. There are two general classes of semiconductor, namely direct and indirect bandgap materials. Figure 1.7 shows the simplified bandstructures for direct and indirect semiconductor materials. Here the horizontal axis represents the crystal momentum, showing the allowed momentum of electrons within the crystal structure. This is directly proportional to the electron wavenumber, k , so this is commonly referred

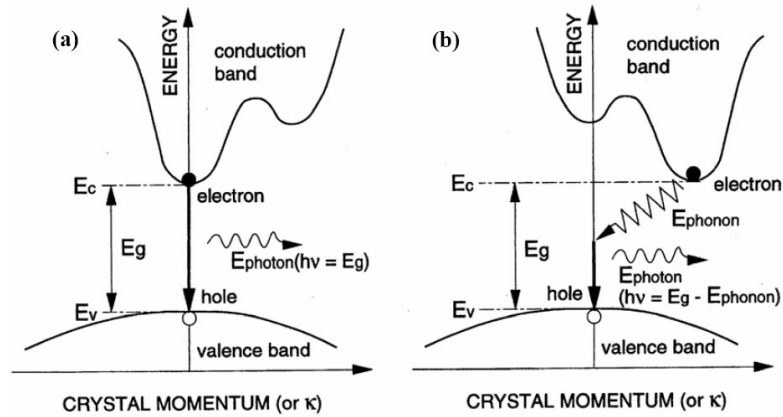


FIGURE 1.7: Band structures of (a) direct and (b) indirect bandgap semiconductors, from [20].

to as k -space representation. Holes tend to relax to the top of the valence band, and electrons to the bottom of the conduction band. In a direct bandgap semiconductor (figure 1.7(a)), the top of the valence band and the bottom of the conduction band coincide in k -space. Therefore electron transitions may occur without any change in crystal momentum. In contrast, in an indirect bandgap semiconductor (figure 1.7(b)) the top of the valence band and the bottom of the conduction band do not coincide in k -space. Therefore, electron transitions must occur with a change in momentum, which involves the assistance of a lattice vibration (phonon) in order to conserve momentum. The consequence of this is that indirect transitions are much less likely than direct transitions. Therefore the process of electroluminescence is much more efficient in direct bandgap semiconductors and most efficient LEDs are made from direct bandgap materials. The following section will describe how LEDs are designed to allow efficient injection of charge carriers and efficient radiative recombination.

1.2.2 The p-n diode

The most simple design of LED is based on a p-n diode. A p-n diode consists of adjacent layers of heavily doped p and n-type material. These layers are typically grown together by epitaxial growth (i.e. atomic layer-by-layer growth on a substrate), rather than being two separate samples joined together. A p-n diode consisting of one type of semiconductor is known as a homojunction, and one consisting of different materials is known as a heterojunction.

In the p-n diode, excess electrons from the n-type material will diffuse across the boundary between the two materials into the p-type layer, where they will recombine with excess holes. Excess holes from the p-type material will similarly diffuse into the n-type layer and recombine with excess electrons. This recombination process leaves a region

around the boundary between the two materials that is depleted of carriers, and is hence known as the ‘depletion region’. This diffusion process does not continue indefinitely. Since electrons diffuse into the p-type region, and holes also diffuse out of this region, then the p-type region will acquire a net negative charge. Similarly, the n-type region will acquire a net positive charge. This forms a potential difference across the depletion region, known as the diffusion voltage V_D , which opposes the diffusion of electrons and holes. Ultimately the diffusion of carriers will be balanced by V_D . It is the voltage V_D that free carriers must overcome in order to reach the neutral region of opposite conductivity type, in other words, the voltage that must be overcome before the diode can conduct current. V_D is given by [21]:

$$V_D = \frac{kT}{e} \ln \frac{N_A N_D}{n_i^2} \quad (1.3)$$

where k is the Boltzmann constant, T is temperature, e is the elementary charge, N_A and N_D are the acceptor and donor concentrations and n_i is the intrinsic carrier density of the semiconductor. A p-n diode under zero bias is illustrated in figure 1.8 (a). The depletion region is depicted as the blue region between the p and n-type materials

The Shockley equation describes the current-voltage (I-V) characteristics of an ideal diode, and is given as follows:

$$I = I_s (e^{eV/kT} - 1) \quad \text{where} \quad I_s = eA \left(\sqrt{\frac{D_p}{\tau_p} \frac{n_i^2}{N_D}} + \sqrt{\frac{D_n}{\tau_n} \frac{n_i^2}{N_A}} \right) \quad (1.4)$$

where $D_{n,p}$ and $\tau_{n,p}$ are the electron and hole diffusion constants and minority-carrier lifetimes, respectively, and V is the voltage applied to the diode. Diodes act as rectifiers, allowing current to pass easily in one direction, but impeding current flow in the opposite direction. Forward biasing the diode, as depicted in figure 1.8 (b), with the p and n-type materials connected to a positive and negative bias, respectively, will cause holes from the p-type region and electrons from the n-type region to flow towards the junction, screening the depletion region diffusion voltage. Under forward bias conditions, $V \gg kT/e$, and using equation 1.3, we can re-write the Shockley equation as:

$$I = eA \left(\sqrt{\frac{D_p}{\tau_p} N_A} + \sqrt{\frac{D_n}{\tau_n} N_D} \right) (e^{eV - V_D/kT}) \quad (1.5)$$

The exponential part of equation 1.5 reveals that as the applied forward voltage reaches the diffusion voltage the current will rapidly increase. The voltage at which this rapid increase begins is termed the threshold voltage, V_{th} . For an ideal diode, the threshold voltage can be approximated by the bandgap energy of the semiconductor, E_g , divided

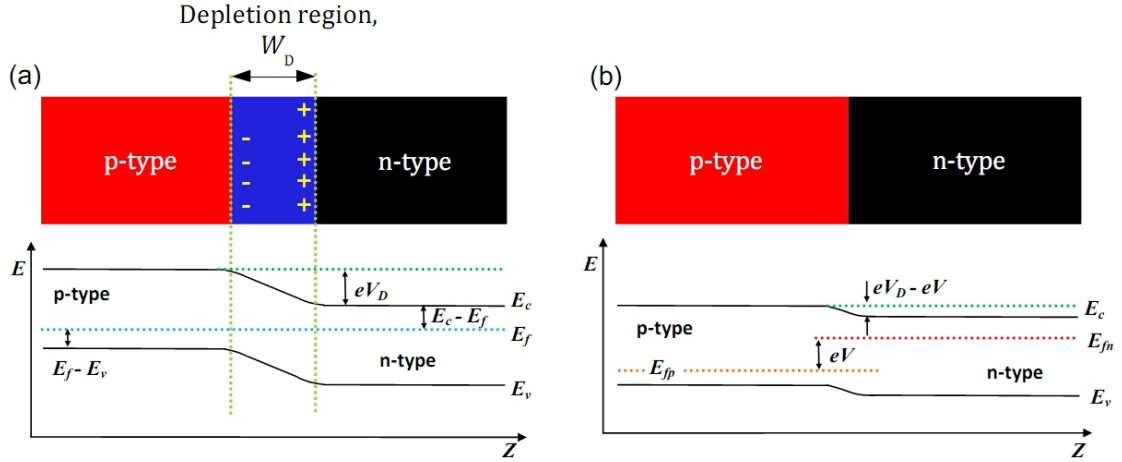


FIGURE 1.8: (a) P-n diode under zero bias, showing the depletion region, and a corresponding energy band diagram of the junction under zero bias. The diode under forward bias and the corresponding energy band diagram is shown in (b). Here, z is the spatial dimension perpendicular to the junction.

by the elementary charge:

$$V_{th} = \frac{E_g}{e} \quad (1.6)$$

Once the forward bias exceeds the built-in potential, then minority carrier injection can take place whereby electrons diffuse into the p-type layer and holes diffusing into the n-type layer. These minority carriers can recombine with a carrier of opposite type, which in an LED results in the emission of photons. Practical LEDs deviate from the ideal Shockley equation with a series resistance behaviour. This is typical of AlInGaN-based LEDs, where the parasitic series resistance may originate from properties such as electrical contact resistance or poor p-type GaN conductivity. For a forward biased LED with a parasitic series resistance, the Shockley equation can be re-written to incorporate the series resistance term, R_s , as follows:

$$I = I_s(e^{e(V-IR_s)/kT} - 1) \quad (1.7)$$

Reverse biasing the diode has the effect of increasing V_D and increasing the thickness of the depletion region, further impeding the flow of current. A very small current does flow under reverse bias, which is attributed to current which arises from the thermal generation of carriers within the diode [22]. However this current is so small that generally no current is considered to flow through an LED device under reverse bias.

1.2.3 Quantum well structures

One disadvantage of a basic p-n diode is that minority carriers diffuse over a relatively large volume, resulting in a low concentration of minority carriers (figure 1.9(a)). The

radiative recombination rate is given by the bimolecular recombination equation [21]:

$$R = Bnp \quad (1.8)$$

Here, B is the bimolecular recombination coefficient of the semiconductor and n and p are the electron and hole concentrations, respectively. Equation 1.8 clearly shows that a low carrier concentration results in a low radiative recombination rate and hence a low efficiency LED. Therefore, most efficient high-power LEDs are based on a p-i-n diode structure. In a p-i-n diode an intrinsic (undoped) layer of material with a relatively small bandgap is sandwiched between layers of heavily doped n-type and p-type material with larger bandgaps. This is known as a double heterostructure (DH). A basic p-i-n diode structure is shown in figure 1.9(b). Carriers are confined to the narrow intrinsic layer by the large potential barriers at the interfaces with the p and n-type materials, thus recombination between electrons and holes takes place in the narrow layer of intrinsic material, known as the active region. This results in large concentrations of confined carriers, which facilitates efficient radiative recombination.

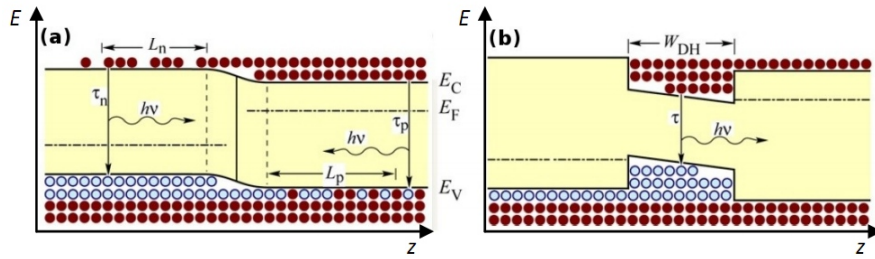


FIGURE 1.9: (a) p-n and (b) p-i-n junction under forward bias. Here, ‘DH’ refers to double heterostructure. From [21].

If the active region is made thin enough, such that it becomes comparable to the de Broglie wavelength for the thermal motion of the confined charge carriers, then quantum size effects become apparent. The de Broglie wavelength is given by:

$$\lambda = \frac{h}{p} = \frac{h}{\sqrt{2m^*kT}} \quad (1.9)$$

where m^* is the carrier effective mass and p is the carrier momentum. For electrons in GaN $\lambda \approx 10$ nm, thus for GaN active regions with thickness ≈ 10 nm we expect to observe quantum size effects. An active region in this case is referred to as a quantum well. In a quantum well the carriers are confined in one crystal direction, denoted z , so the permitted electron energy levels in this crystal direction no longer form a continuous band of energies but instead form discrete quantised energy levels. This can be explained by considering the thin active region to be a one-dimensional ‘potential well’, having potential barriers of infinite height at either side which do not permit an

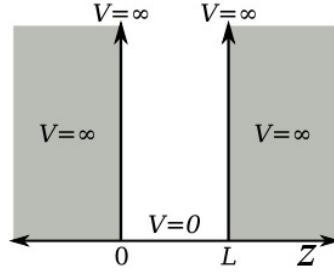


FIGURE 1.10: Theoretical one-dimensional ‘potential well’ where a region of zero electrical potential is bounded by barriers of infinite potential.

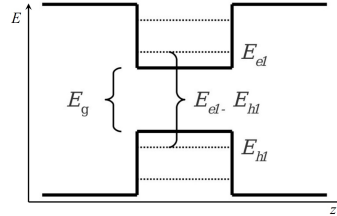


FIGURE 1.11: Quantum well structure, illustrating that the energy of the optical transition from E_{el} to E_{hl} exceeds the energy of the bandgap, E_g . Here, e and h refer to the electron and hole confined energy levels.

electron that is inside the well from escaping. This is illustrated in figure 1.10, where the region of zero potential between $W = 0$ and $W = L$ is bounded by potential barriers having infinite height (i.e. $V = \infty$). Since the particle cannot leave the potential well, it must be found within the well, so we can apply boundary conditions to the Schrödinger equation that $\psi = 0$ for $W = 0$ and $W = L$. By solving the Schrödinger equation for these conditions we find that the permitted discrete electron energy levels, denoted by the integer n , within the potential well are given by:

$$E_n = \frac{n^2 h^2}{8mL^2} \quad (1.10)$$

where m is the effective mass of the particle (electron), n is an integer and L is the width of the potential well. A consequence of Equation 1.10 is that as the potential well becomes narrower the energy level solutions, E_n , occur at higher energies and have increasing energy level separation, affecting any optical transitions that occur between levels in the well. Carefully altering the thickness of the quantum well thus allows a degree of control over the wavelength of any photons that are emitted by the well. In addition, because the energy of a particle in a potential well cannot equal zero, the optical transitions have a higher energy than the bandgap energy, E_g (figure 1.11). This means that quantum wells can be used to generate photons of shorter wavelengths from an LED. Most LEDs utilise active regions consisting of several closely-spaced quantum wells, which are referred to as multi-quantum well (MQW) regions.

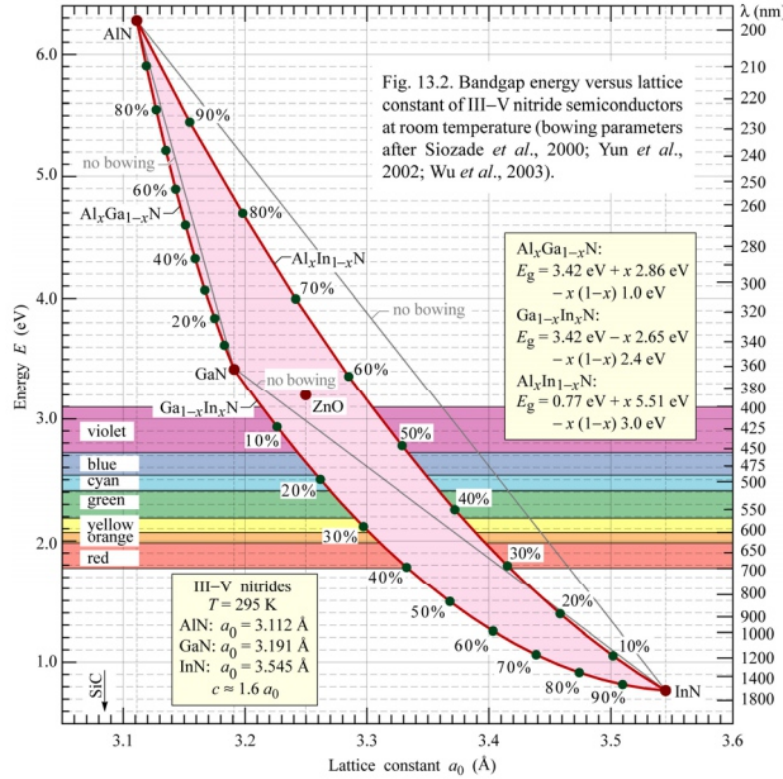


FIGURE 1.12: Room-temperature bandgap energy, E_g , and emission wavelength versus lattice constant for the AlInGaN-Nitride alloy system, from [21].

1.3 AlInGaN-based LEDs

The micro-LED arrays that are the focus of this thesis are all fabricated from commercially-obtained LED wafer material based on the AlInGaN alloy system. This section will begin by discussing the basic properties of this alloy system. The technologies used to grow the wafers and process them into (micro-)LEDs will then be covered, and this section will conclude by outlining the process flows used to fabricate micro-LED devices. The AlInGaN alloy system consists of the three basic binary alloys, Aluminium Nitride (AlN), Gallium Nitride (GaN) and Indium Nitride (InN). Generally speaking, by altering the relative amounts of the individual materials in a ternary or quaternary alloy, the bandgap energy can be ‘tuned’, which in theory allows the AlInGaN alloy system to span a very large range of wavelengths from the deep-UV to the near-infrared. This can be seen in figure 1.12, which illustrates the bandgap energy versus lattice constant and alloy composition for the AlInGaN system. Subscript notation is used to describe the relative composition of an alloy, for example $\text{In}_{0.2}\text{Ga}_{0.8}\text{N}$ describes an alloy consisting of 20% InN and 80% GaN. Currently, the shortest reported emission wavelength is 210 nm from an AlN LED [23]. Some important properties of the binary alloys are summarised in table 1.1.

TABLE 1.1: Important properties of the AlInGaN alloy system [21].

Quantity	Symbol	AlN	GaN	InN	(Unit)
Lattice Constant	$a_o =$	3.112	3.191	3.545	Å
	$c_o =$	4.982	5.185	5.703	
Bandgap energy	$E_g =$	6.28	3.425	0.77	eV
Refractive index near E_g	$n =$	2.15	2.5	2.9	-
Electron mobility	$\mu_n =$	300	1500	3200	cm^2/Vs
Hole mobility	$\mu_p =$	14	30	-	cm^2/Vs

1.3.1 Epitaxial growth and processing of AlInGaN alloys

The majority of commercial AlInGaN wafers are grown by Metal-Organic Chemical Vapour Deposition (MOCVD), also known as Metal-Organic Vapour Phase Epitaxy (MOVPE) or Organo-metallic Vapour Phase Epitaxy (OMVPE). This involves the growth of crystalline thin-film structures on a substrate by the deposition of the desired materials from a vapour phase (or a mixture of vapours). Crystal growth is by chemical reaction, rather than by the physical deposition of material. The most commonly used substrate for AlInGaN is sapphire, which will be discussed in section 1.3.1.1. The sapphire substrates used are mostly 2 inches in diameter, although there are currently efforts to try to scale this up to 4 or 6 inches. Typical growth rates are of the order of $0.5 \mu\text{m}$ per hour [24].

To grow III-nitride materials, vapours containing Gallium, Aluminium or Indium are created by combining trimethylgallium (TMG), trimethylaluminium (TMA), and trimethylindium (TMI) with complex organic gas molecules. These vapours are then flowed over the substrate heated to $\approx 1000^\circ\text{C}$. There they react with NH_3 (ammonia gas, providing the nitrogen source) as the heat breaks up the molecules, depositing the desired materials at the surface of the layer. This process takes place in a near-atmospheric-pressure reactor, typically made from stainless steel so that it can handle the temperatures involved in growth without chemically reacting with the vapours used. The structure is then built up, on an atomic layer-by-layer basis. By varying the composition of the vapour in the chamber the properties of the grown material layers can be controlled. The crystal structure of the layers will align with the substrate, thus choosing a substrate that is suitably lattice-matched is critical. Figure 1.13 shows schematically the principle of GaN growth by MOCVD.

Once the material has been grown, it must then be etched to form LEDs or other electronic devices. Since III-nitride materials are rather resistant to wet etching due to their chemically inert nature and strong atomic bonds, dry etch techniques using reactive ions are the methods of choice for etching AlInGaN materials [26]. Advantages of dry

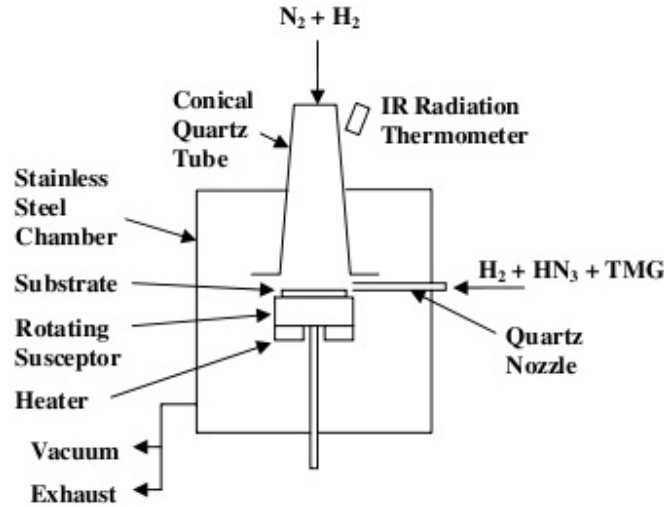


FIGURE 1.13: Schematic growth of GaN by MOCVD, from [25]

etching include high etch rates (up to $1 \mu\text{m}$ per minute), minimal damage to the wafer, and anisotropic etch profiles allowing very vertical features to be etched with smooth sidewalls. Masks are formed on top of the epitaxial material using photolithography, allowing specific areas of the wafer to be etched. Two methods of dry etching commonly used to fabricate LEDs are Reactive Ion Etching (RIE) and Inductively Coupled Plasma (ICP) etching. ICP etching is the most commonly used technique for etching AlInGaN material [26], and is used to fabricate the micro-LEDs discussed in this thesis. ICP etching is an example of a high-density plasma etch technique. The sample to be etched is placed in a high vacuum (10^{-3} Torr) within a chamber. RF power is supplied to a coil encircling the vessel, producing an alternating electric field between the coils and an alternating magnetic field in the vessel. A high density plasma is created in the chamber since the magnetic field traps electrons in the centre of the chamber. Ions are then accelerated towards the sample by a bias on the powered electrode. Representative ICP etch conditions are a $\text{Cl}_2/\text{H}_2/\text{Ar}$ plasma chemistry with flow rates of 22.5, 2.5 and 5 sccm for Cl_2 , H_2 and Ar, respectively, 150 W of RF power and an electrode DC bias of -190 ± 10 V [27]. ICP etch rates of AlInGaN up to $9800 \text{ \AA min}^{-1}$ are possible [24]. An advantage of ICP etching is that ion energy and plasma density are independently controlled parameters, allowing flexibility in optimising the etching process. For example, a high etch rate can be obtained whilst keeping the ion energy low, thereby reducing etching damage induced by high-energy ion bombardment. An illustration of an ICP machine is shown in 1.14.

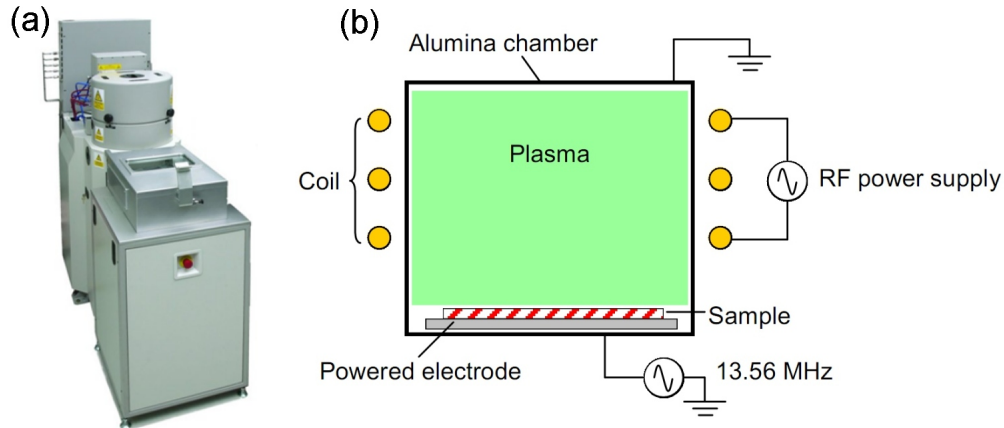


FIGURE 1.14: (a) Picture and (b) schematic of a typical ICP reactor.

1.3.1.1 Substrate materials

AllInGaN wafers are hetero-epitaxially grown, with the most commonly-used and mature substrate technology being sapphire (Al_2O_3). Other substrate materials that AllInGaN-based LEDs have been grown on include Zinc-Oxide (ZnO), SiC and Si [28, 29]. The micro-LED devices to be discussed during this thesis are all grown on sapphire substrates, so this section will focus on the implications that growing AllInGaN on sapphire has for the fabrication of LEDs. Sapphire is reasonably well lattice-matched to nitride materials, thermally stable, optically transparent and, crucially, large wafers are readily available at low cost. Although other substrate materials are available that in some respects outperform sapphire, no other substrate material presently allows high-quality AllInGaN wafers to be grown at low cost.

When growing AllInGaN wafers on sapphire, one consideration that must be taken into account is that sapphire is not electrically conductive. This means that typically both the p and n-contacts to an LED must be made on the same side of the device, i.e. the semiconductor side. This requires that part of the LED material be etched away to allow access to the n-type material. The micro-LEDs presented later in this thesis all have their electrical contacts on one side of the device, as will be discussed in detail in chapter 2. An alternative approach is to remove the sapphire substrate by, for example, laser lift-off [30]. This allows both the p and n-type materials to be accessed, allowing for novel device structures to be fabricated such as high-power thin-film [31] and vertical-injection [32] structures.

The crystal orientation of sapphire is shown in figure 1.15(a). AllInGaN grown on sapphire is conventionally grown in the c -axis crystal direction ($[0\ 0\ 0\ 1]$ orientation) of sapphire. The AllInGaN unit cell grows at a 30° angle to the sapphire c -axis, to align with the sapphire unit cell such that Al-O bonding takes place between AllInGaN and

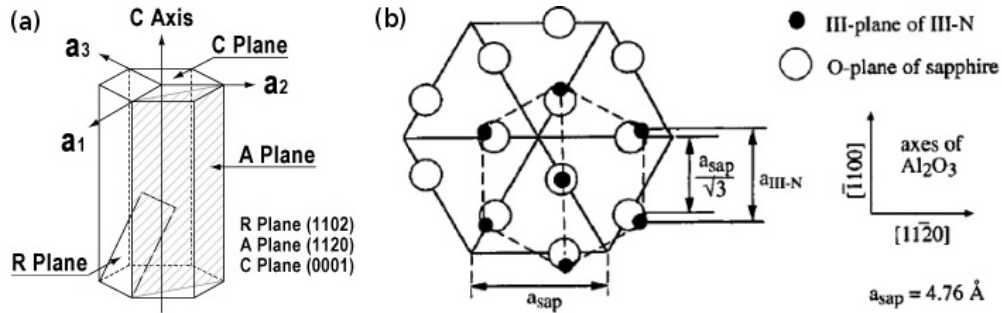


FIGURE 1.15: (a) Sapphire crystal orientation, (b) atomic arrangement of AlN film grown on sapphire, from [33].

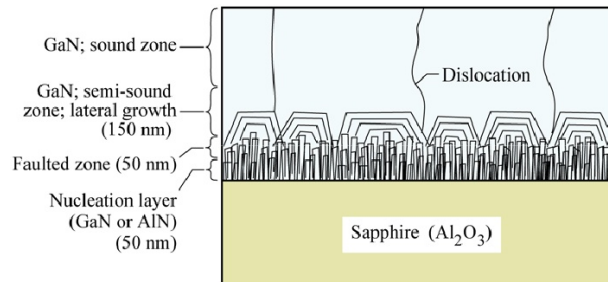


FIGURE 1.16: Dislocation structure of an epitaxial GaN layer, grown on sapphire. From [21].

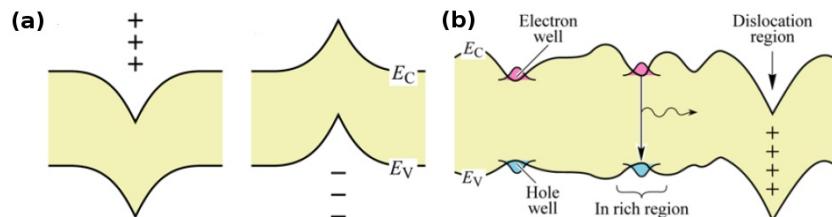


FIGURE 1.17: Proposed mechanisms for why dislocations in InGaN do not act as efficient non-radiative recombination centres (a) defects in AlInGaN that exist outside the bandgap, (b) carrier localisation due to compositional alloy fluctuations, adapted from [21].

sapphire. This is shown in figure 1.15(b), which also shows that there is approximately a 15% lattice mis-match between the two materials. As a result of this lattice mis-match, AlInGaN epitaxial films have relatively high misfit dislocation densities. The misfit dislocation density is reduced by the use of a thin ($\approx 50 \text{ nm}$) nucleation or ‘buffer’ layer to begin epitaxial growth [7]. The buffer layer reduces the dislocation density by relaxing the strain caused by the lattice mis-match between GaN and sapphire, and promoting lateral GaN growth [34]. The buffer layer is grown at relatively low temperatures ($\approx 500^\circ\text{C}$) and subsequently annealed, and transitions through a faulted zone. These contain a very high concentration of dislocations.

During annealing the dislocations undergo a process of self-annihilation, which means that subsequent layers (the ‘semi-sound’ and the ‘sound zone’) contain significantly less

dislocations. This is illustrated in figure 1.16. Although this buffer layer greatly reduces the dislocation density in GaN it still remains high, typically of the order of 10^8 to 10^9 cm^{-2} , compared to roughly 10^4 cm^{-2} for other materials such as Si. A peculiar observation is that GaN-based LEDs are still able to generate light efficiently despite these high defect densities. By contrast, the efficiency of a GaAs-based LED would be limited by a dislocation density of the order of 10^4 cm^{-2} , and at the dislocation densities associated with GaN-based LEDs it would not be expected to emit light at all [35]. This indicates that dislocations in the AlInGaN system are not efficient non-radiative recombination centres, as they are in other materials systems. Several explanations for this phenomenon have been proposed, though as yet none is generally accepted. One possible explanation is that the electronic states of the defects lie outside the bandgap [35] (figure 1.17 (a)), and hence do not lead to non-radiative recombination. Another explanation is that carriers become localised in compositional alloy fluctuations within the material. Mukai *et al.* observed that the output power of UV-emitting GaInN/GaN double-heterostructure LEDs decreased as the fraction of indium (In) incorporated in the LED active region was decreased [36]. This observation was attributed to carriers becoming localised within local potential wells caused by composition fluctuations. Figure 1.17 (b) illustrates how carriers could become trapped in localised potential minima created by In clusters within the crystal, preventing them from reaching dislocation states. LEDs with less In may have less In clustering, and would therefore not benefit as much from this carrier localisation effect. The Indium-clustering hypothesis has however been disputed, with Smeeton *et al.* suggesting that nanometre-scale In clusters observed by electron-microscope are in fact simply an artefact of the microscope measurement itself caused by electron-beam induced damage to the material [37].

1.3.1.2 Contact metal deposition

In order to fabricate a fully operational LED or micro-LED, metal contacts must be deposited onto the device. For the micro-LEDs described in this thesis, ≈ 200 nm thick layers of titanium/gold (Ti/Au) or nickel/gold (Ni/Au) alloys are used for the n and p-contacts, respectively. These layers are deposited onto the micro-LEDs by magnetron sputtering or electron-beam evaporation. Magnetron sputtering is a technique that takes place in a high vacuum, containing the sample to be coated and a ‘target’ of the material to be deposited. An inert gas, typically argon, is injected into the chamber. A high negative voltage of ≈ 300 V is applied to the target which accelerates positively charged argon ions towards it. These bombard the target and physically remove atomised material. The ejected material travels through the vacuum chamber and condenses on the surface of the semiconductor sample, thus forming a thin metal contact layer.

Electron-beam evaporation also takes place in a vacuum, and uses a beam of electrons to heat the target. The evaporated material condenses to form a thin metal layer on the semiconductor sample in a similar fashion to magnetron sputtering. Schematic representations of the magnetron sputtering and electron-beam evaporation processes are shown in figure 1.18.

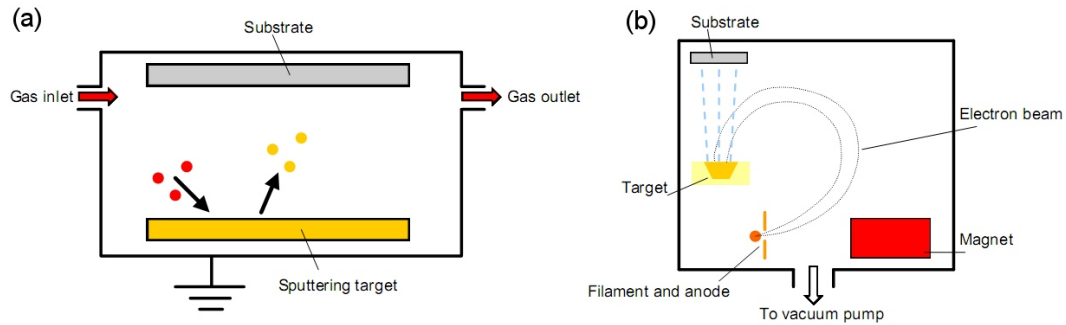


FIGURE 1.18: Schematic illustration of (a) magnetron sputtering and (b) electron-beam evaporation techniques.

1.3.1.3 Doping of AlInGaN materials

As-grown GaN is typically unintentionally an n-type material, which has been attributed to the incorporation of a dopant from an external source during growth [5]. It is relatively straightforward to intentionally create n-type GaN by doping the material with Si. P-type doping initially proved considerably more challenging; indeed for decades effective p-type doping of GaN proved to be an obstacle preventing efficient GaN-based LEDs from being fabricated. Magnesium (Mg) atoms, used for p-type doping, are chemically deactivated by bonding to hydrogen atoms during epitaxial growth. This can be overcome by high-temperature annealing of the material after growth, a process first demonstrated to produce high-efficiency blue LEDs by Nakamura *et al.* [38]. This annealing takes place in a nitrogen environment at temperatures of greater than 600°C. It is believed that during thermal annealing the relatively weak acceptor-hydrogen bonds are broken and the hydrogen is driven out of the material; since the hydrogen atoms are relatively small they can escape through the interstitial sites of the crystalline material.

Although p-type doping can thus be achieved, the doping densities are low, typically around 10^{17} to 10^{18} cm³, as opposed to densities of the order of 10^{19} cm³ for n-type doping. This can be attributed to two effects, the inherent n-type properties of the material compensating the p-type doping, and incomplete activation of the p-type dopants at room temperature [34]. As such, p-type AlInGaN materials are highly electrically resistive compared to n-type.

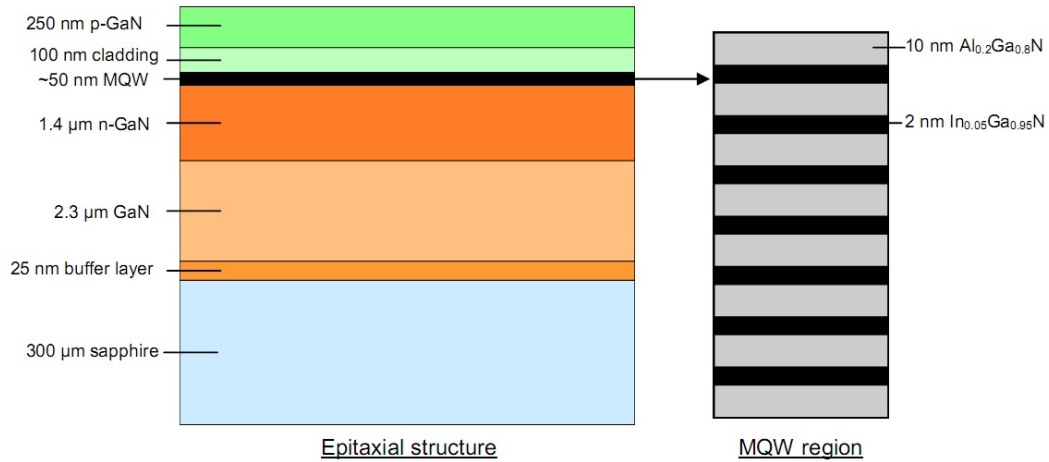


FIGURE 1.19: Schematic illustration of a typical epitaxial structure of a UV-emitting micro-LED, from [39]. The MQW region is expanded and is shown on the right. Schematic is not to scale.

1.3.2 AlInGaN LED device structure

The micro-LED devices fabricated by the Institute of Photonics are based on LED wafers with fairly standard epitaxial structures. One such epitaxial structure is shown in figure 1.19, based on a micro-LED device with a peak emission wavelength of ≈ 370 nm [39]. A 25 nm thick buffer layer of undoped GaN is grown on a *c*-plane sapphire substrate (cf. figure 1.16), followed by 2.3 μm of undoped GaN, 1.4 μm of Si-doped *n*-type GaN and then a multi-quantum well (MQW) region approximately 50 nm in thickness. The MQW is capped with a 100 nm thick Mg-doped AlGaN cladding layer, or ‘electron-blocking’ layer, which is intended to provide a potential barrier to prevent electrons overflowing and escaping the active region. The structure is finally capped with a 20 nm thick Mg-doped GaN contact layer. The MQW region consists of seven $\text{In}_{0.05}\text{Ga}_{0.95}\text{N}$ quantum wells, each of 2 nm thickness, with 10 nm thick $\text{Al}_{0.2}\text{Ga}_{0.8}\text{N}$ barriers. Thin quantum well structures are favoured for growth in *c*-plane sapphire as they minimise the spatial charge separation due to built in strain fields. This structure is fairly representative of the epitaxial structure of the micro-LEDs discussed in this thesis, and of InGaN-based LEDs in general.

Once the epitaxial wafer is complete, it must be processed into an LED structure. Four common AlInGaN-based LED structures are shown in figure 1.20. As discussed in section 1.3.1.1, most AlInGaN wafers are grown on sapphire substrates and because sapphire is not electrically conductive this influences the structure of the LED dies. Figure 1.20 (a) shows the most straightforward device structure, the ‘epitaxy-up’ structure. In this design, the *p*-type material is partially etched to expose the *n*-type material underneath and ohmic contacts are deposited onto the *p* and *n*-type layers. During operation, light is primarily extracted through the *p*-type material and the *p*-type current-spreading

layer ('p-spreader' in figure 1.20 (a)). The spreading layer, which is a thin Ni/Au bilayer, is necessary to overcome the relatively high resistivity of the p-type material and provide efficient and uniform current injection, and covers almost all of the p-type region. However, some of the light from the LED will be absorbed by this layer, reducing the output power and efficiency of the LED, a problem which is exacerbated at shorter wavelengths [40]. A further disadvantage of the epitaxy-up structure is that sapphire has a fairly poor thermal conductivity, preventing efficient heat extraction and thus limiting the performance, particularly at high injection currents. In a 'flip-chip' device, as shown in figure 1.20 (b), the device is etched in a similar fashion to the epitaxy-up design in order to have both the p and n-type materials exposed. The key difference is that the device is flipped and bonded onto another substrate, such as a silicon mount. During device operation the light is primarily extracted through the sapphire substrate. Since light no longer has to be extracted through the p-type material, the p-type spreading layer can be made thicker and may also be made reflective to act as a mirror to retro-reflect emitted light back through the sapphire substrate. The mount that the LED is bonded to may also act as a heat sink, improving the thermal management. This means that flip-chip LEDs are capable of higher output powers and higher efficiencies than otherwise identical epitaxy-up devices. The sapphire top surface of flip-chip devices also provides a flat, chemically inert and bio-compatible surface upon which additional structures and functionality can be integrated. After processing, the wafer is diced into individual LED dies, typically of the order of $300 \times 300 \mu\text{m}^2$.

Other device structures exist, including vertical-injection thin-film [32] and thin-film [31] LEDs, shown in figure 1.20 (c) and (d), respectively. These structures involve more complicated processing steps, including the removal of the sapphire substrate and patterning of the n-type surface material. They form the basis of 'power LEDs', an example of which was shown in figure 1.4(b). The micro-LED devices fabricated by the Institute of Photonics are based either on an epitaxy-up or flip-chip design and the micro-LED devices will be introduced in detail in chapter 2. Unless otherwise stated, the micro-LED devices used for the experiments in this thesis are based on a flip-chip design.

1.3.3 LED efficiency droop

LEDs fabricated in the AlInGaN alloy system are generally intended for high-power illumination applications where high operating current densities of around 100-1000 A/cm² are required. However, the internal quantum efficiency (IQE) of AlInGaN LEDs tends to peak at relatively modest current densities of around 10 A/cm² and may reduce to little over half of the peak IQE at higher current density [41], a phenomenon known

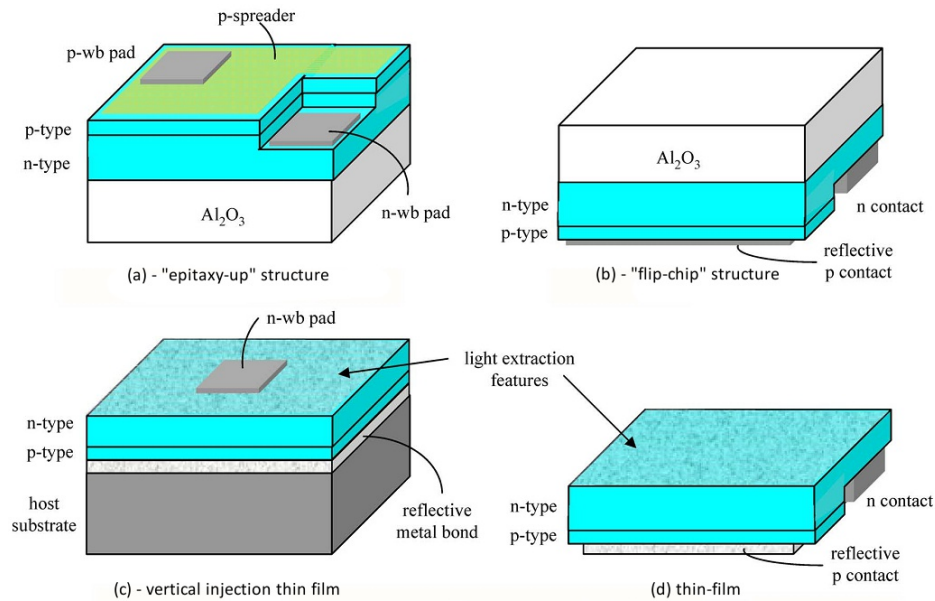


FIGURE 1.20: Four common structures of AlInGaN LED die - the micro-LEDs fabricated by the Institute of Photonics are based on the (a) ‘epitaxy-up’ and (b) flip-chip designs. From [13].

as the ‘efficiency droop’. The level of efficiency droop is enough to reduce the efficiency of LEDs below that of fluorescent light bulbs. The characteristics of efficiency droop are illustrated in figure 1.21, where the external quantum efficiency (EQE) of a blue-emitting InGaN/GaN LED, grown on *c*-plane sapphire, is shown to peak at current densities of less than 10 A/cm^2 before falling to half this peak value at around 100 A/cm^2 [42]. This drop in efficiency is observed even under pulsed conditions where device self-heating can be neglected and so cannot be explained entirely by the process of thermally-induced carrier leakage at higher temperatures. Although the underlying cause of the efficiency droop is still a topic of vigorous debate and several mechanisms have been proposed to explain the phenomenon, there are two postulated explanations which have recently gained the most credibility.

The first hypothesis is that the non-radiative recombination process known as Auger recombination begins to dominate at high current densities and thus leads to the efficiency droop. Figure 1.22 shows a band diagram within a semiconductor showing different possible recombination processes. Non-radiative recombination, also known as Shockley-Read-Hall (SRH) recombination, can occur when there is an energy state that exists within the bandgap, illustrated by E_T in figure 1.22(a). Energy states that lie within the bandgap are commonly caused by defects within the semiconductor crystal. During recombination, an excited charge carrier (electron or hole) can relax to the intermediate energy level before relaxing fully to the valence or conduction band. Typically,

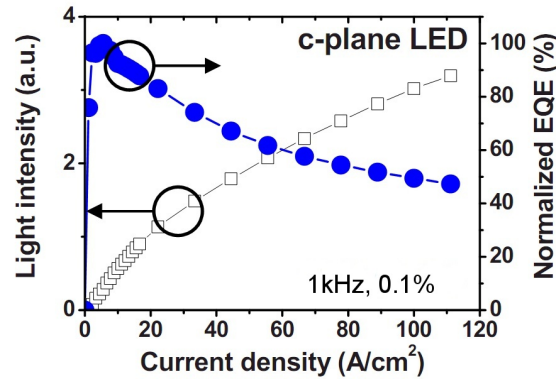


FIGURE 1.21: Total output power and normalised external quantum efficiency, showing the ‘efficiency droop’ in an InGaN/GaN LED, from [42]. These measurements were taken under pulsed conditions, with a repetition rate of 1kHz and duty cycle of 0.1%.

the energy dissipated in the two transition steps does not involve the emission of a photon. On the other hand, Auger recombination does not involve an intermediate energy state, but involves three particles - either two electrons and one hole, or two holes and one electron. In this process, during recombination between an electron and hole the energy is not released as a photon, but instead is transferred to another electron (in the conduction band) or hole (in the valence band). These extra excited particles then lose their energy thermally as they relax back to the conduction or valence band edges. Auger recombination is illustrated in figure 1.22(b). Shen *et al.* have suggested that Auger recombination may be the dominant mechanism responsible for the observed efficiency droop in AlInGaN LEDs [43]. They concluded that the Auger recombination rate (which quantifies the level of Auger recombination in a semiconductor) in InGaN was of the order of $2 \times 10^{-30} \text{ cm}^6 \text{ s}^{-1}$. This is high enough to dominate the LED performance at relatively low current densities [43], consistent with the observed efficiency droop trends. However, some argue that Auger losses would be expected to decrease with increasing bandgap due to the reduced coupling between electron and hole bands [44], and thus the Auger coefficients reported by Shen *et al.* are too high. At present, the level of Auger losses within this material system remains unclear.

A second hypothesis suggests that poor hole injection into the active region and/or electron leakage from the active region may cause a large parasitic current that leads to non-radiative recombination in the p-type material, and is the main mechanism that drives efficiency droop. Figure 1.23 illustrates the hypothesis proposed by Kim *et al.* [45] which argues that the large internal electric fields within InGaN modify the band structure, causing the triangular-shaped upward slopes observed in the conduction band in figure 1.23. These slopes impede efficient electron injection into the active region. This figure also shows that the conduction band-edge energy on the n-type side is higher than on the p-type side, which would lead to a large electron leakage current. By the

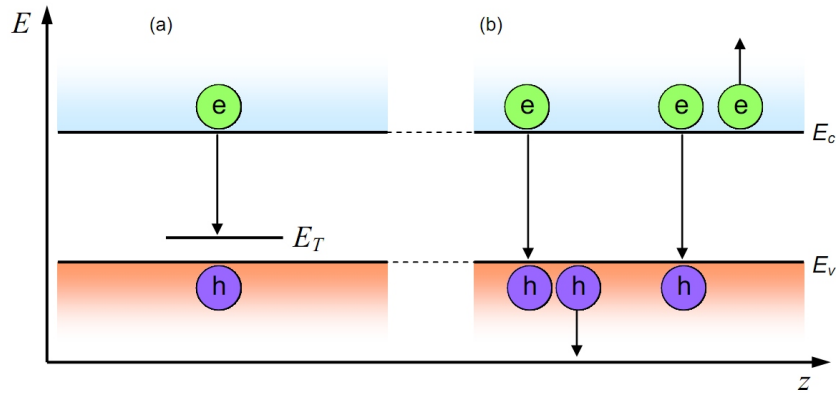


FIGURE 1.22: Illustration of (a) non-radiative and (b) Auger recombination. Electrons and holes are shown in orange and green, respectively.

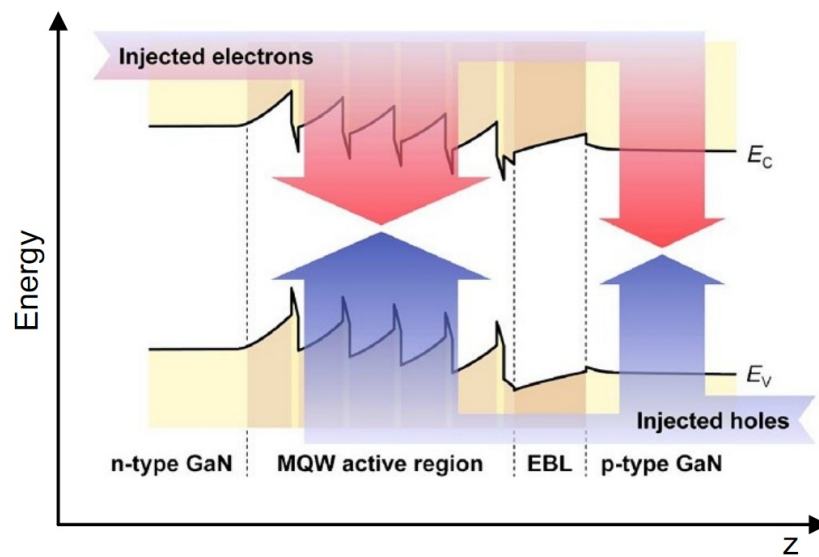


FIGURE 1.23: Schematic of the conduction (E_g) and valence band (E_v) energies in an InGaN-based LED heterostructure. Arrows indicate regions of electron and hole injection and recombination. From [48].

use of polarization-matched AlGaInN barriers the same group reported an LED with reduced efficiency droop and improved overall efficiency [46], seemingly confirming their hypothesis.

Several other explanations that have been put forward, such as density-activated defect recombination [47], but a detailed discussion of these is beyond the scope of this thesis. Analysis of the carrier recombination dynamics within AlInGaN micro-LEDs will be presented in section 5.2.3. Although this analysis uses a model of carrier lifetime, τ , versus carrier density, N , which allocates an Auger recombination term, the physical mechanism responsible for this term need not necessarily be Auger recombination, but may be another mechanism which is well fitted by the same N^3 dependence.

1.4 Organic semiconductors and quantum dots

Light-emitting polymers (LEPs) and colloidal quantum dots (CQDs) will be presented later in this thesis as fluorescent samples for demonstrations of fluorescence lifetime measurements (chapter 4) and as colour-converters for visible light communications (chapter 5). Although the exact motivations for investigating these materials will be discussed in these later chapters, the basic properties of these materials will be introduced here.

1.4.1 Organic semiconductors

Organic semiconductors are organic materials with semiconducting properties and have attracted a great deal of interest since the first report of an organic LED (OLED) by Burroughes *et al.* [49] in 1990. Conjugated semiconductor light-emitting polymers (LEPs) are a form of organic semiconductor which have beneficial properties including the ability to conveniently solution-process the materials by techniques such as ink-jet printing. The ability to process organic semiconductors in such a simple way negates the need for a set of expensive photolithographic masks, which are required to process inorganic semiconductors. They also have excellent optical properties, including high quantum efficiencies and high absorption - a thin film only 100 nm thick can absorb 90% of the light incident on it [50].

Polymers are typically long chain-like molecules with regular repeating units of atoms. The word ‘polymer’ derives from the Greek words *poly* and *mero*, meaning ‘many units’, referring to the many repeat units that make up polymer chains. Semiconducting polymers have alternating single and double covalent bonds between carbon atoms which are formed along the length of the molecule, which play an important part in determining the optical properties of LEPs. The basic electron configuration of a carbon atom is $1s^2 2s^2 2p^2$. However, when two carbon atoms are brought together their 2s and 2p orbitals can mix (hybridise) to form hybrid sp^2 orbitals. Each carbon atom then has three $2sp^2$ orbitals, spaced at 120° angles to each other, and one $2p^2$ orbital which is perpendicular to the $2sp^2$ orbitals, as shown in figure 1.24(a). One sp^2 orbital from each atom forms a σ bond between the two atoms, and the p orbitals overlap to create a π bond, as illustrated in figure 1.24(b). It is this π bond between atoms which allows electrons to become de-localised along the length of the polymer chain. In other words, instead of being localised in one orbital around one atom, the electrons are able to move along the π bonds from one carbon atom to another along the polymer chain. The number of carbon atoms along which electrons are de-localised is known as the *conjugation length*.

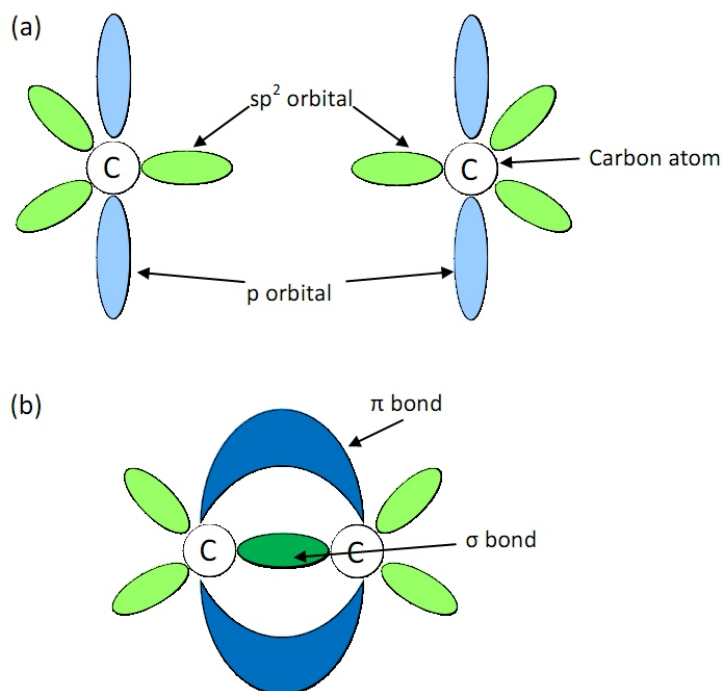


FIGURE 1.24: (a) sp^2 orbital hybridisation and (b) bonding between two carbon atoms. Electrons are able to move along the π bonds between atoms.

The π orbital is the highest occupied electronic energy state in the molecule and is fully occupied, and is thus known as the highest occupied molecular orbital (HOMO). The lowest unoccupied molecular orbital (LUMO) is an excited configuration of the π orbitals, and is thus denoted as a π^* state [51]. Thus, the HOMO and LUMO are analogous to the valence and conduction band edges in bulk semiconductors, with the energy gap between them analogous to the semiconductor bandgap. Carriers are confined along the conjugation length of the polymer, somewhat analogous to the confinement of carriers within a quantum well as described in section 1.2.3. Thus it may be determined that by altering the conjugation length of a LEP, the energy gap between the HOMO and LUMO may be tuned. This allows LEPs to be synthesised which permit emission across the visible spectrum.

The process of absorption and emission within a LEP can be shown on a Jablonski diagram, as shown in figure 1.25. The electronic energy levels (such as the HOMO and LUMO), S_0 to S_2 are depicted by the thicker black horizontal lines. The atoms in a molecule can vibrate about their bonds, which gives rise to vibrational energy levels with each electronic state [51]. The vibrational energy levels (0,1,2 etc.) are depicted by the thinner black lines. Transitions between energy levels are depicted by vertical arrows. The absorption process typically simultaneously changes both the electronic and vibrational state of the molecule, exciting an electron from the lowest energy level, S_0 , to a higher electronic and vibrational energy level, a process that occurs

on a 10^{-15} s time scale. Following absorption, the electron will rapidly relax (10^{-12} s time scale) to the lowest vibrational energy of S_1 or S_2 , in a process termed vibrational relaxation. The electron may then relax back to the ground state, emitting a photon in a process termed *fluorescence*. Fluorescence occurs on a 10^{-8} to 10^{-9} s time scale. For a sample of fluorescent molecules, the time a particular molecule spends in its excited state before subsequently emitting a photon is random, but the *average time* each molecule spends in the excited state is known as the *fluorescence lifetime*, or τ , of the fluorophore. Each molecule may leave the excited state either by a radiative process (by emitting a photon) or by a non-radiative process (without emitting a photon). Thus, the fluorescence lifetime, τ can be expressed as [52]:

$$\tau = \frac{1}{\Gamma + k_{nr}} \quad (1.11)$$

where Γ and k_{nr} are the radiative and non-radiative decay rates, respectively. The radiative decay rate of a sample is an intrinsic property of a particular fluorophore, whereas the fluorescence lifetime, τ , depends both on the properties of the fluorophore and also its environment, as will be discussed in more detail in chapter 4. The quantum yield, Q , of a sample is the fraction of fluorophores that decay radiatively and is given by:

$$Q = \frac{\Gamma}{\Gamma + k_{nr}} \quad (1.12)$$

After the emission of a photon, a subsequent vibrational relaxation from a higher vibrational energy level of S_0 usually occurs. Electrons may also relax into a triplet state, indicated as T_1) in figure 1.25. The emission of a photon from a triplet state occurs on much longer time scales (10^{-3} to 10^2 s) compared to fluorescence.

Due to the energy lost during vibrational relaxation, the transitions which involve emission of a photon occur at lower energies than transitions involved during absorption. This red-shifts the emission spectrum relative to the absorption spectrum, which is known as a Stokes shift and renders the molecule transparent to its own emission. The Stokes shift between the absorption and emission spectra of the blue-emitting polymer poly(9,9'-dioctylfluorene) (PFO) can be seen in figure 1.26. Vibronic peaks, corresponding to transitions between the lowest excited state vibrational energy and vibronic energy levels in the ground state, can also be clearly seen in the emission spectrum in figure 1.26.

As well as polymers, other classes of light-emitting organic semiconductors exist. One example is the star-shaped oligofluorene truxene (referred to as 'truxene' from now on). These star-shaped molecules consist of a truxene 'core' onto which three 'arms' consisting of conjugated fluorene units are attached, as indicated in figure 1.27(a). The number of repeat units of fluorene is indicated by $T1$, $T2...T4$, where for example, $T4$

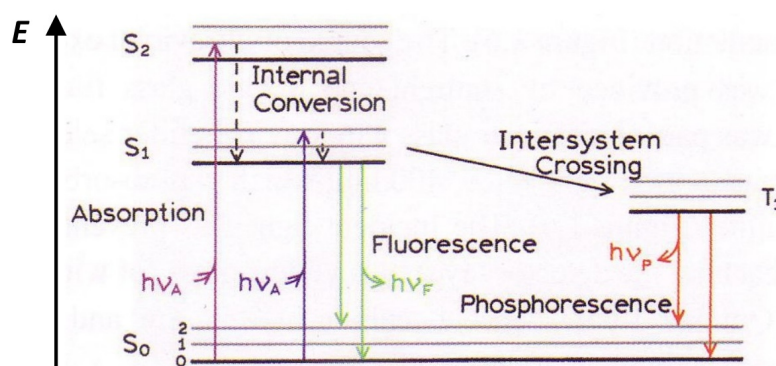


FIGURE 1.25: Jablonski diagram showing the different transitions that may occur during luminescence, from [52].

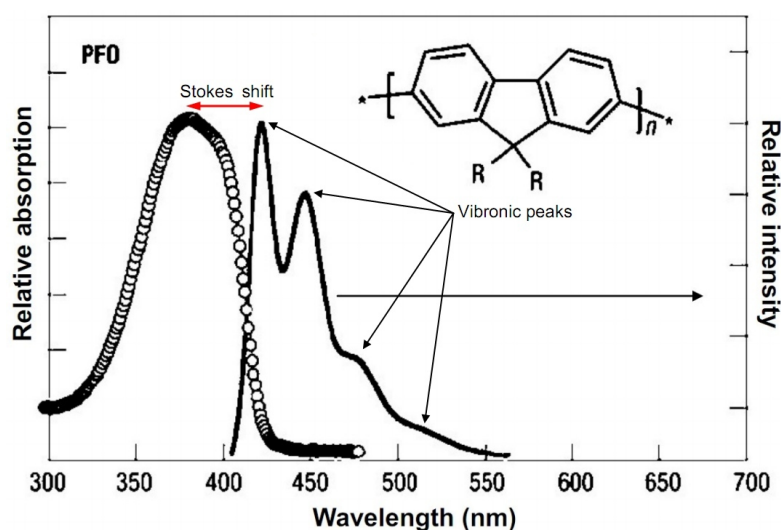


FIGURE 1.26: Absorption (circles) and photoluminescence emission (solid line) of a film of poly(9,9'-dioctylfluorene) (PFO). The chemical structure of PFO is shown inset, where where $R = C_8H_{17}$ and n being the number of repeats. From [53].

would be a truxene molecule with four repeat units. Altering the number of repeat fluorene units on the arms allows the absorption and emission spectra to be blue or red-shifted as can be seen in figures 1.27(b) and (c). Oligofluorenes such as truxene have several advantages over their conjugated polymer counterparts including a well-defined and uniform molecular structure and superior chemical purity [54].

Many of the concepts introduced here, such as the fluorescence lifetime, τ , are also applicable to organic dyes used as fluorescent 'markers' for labelling biological samples. The ability to measure τ allows useful information regarding the samples to be ascertained, which will be discussed in more detail in chapter 4.

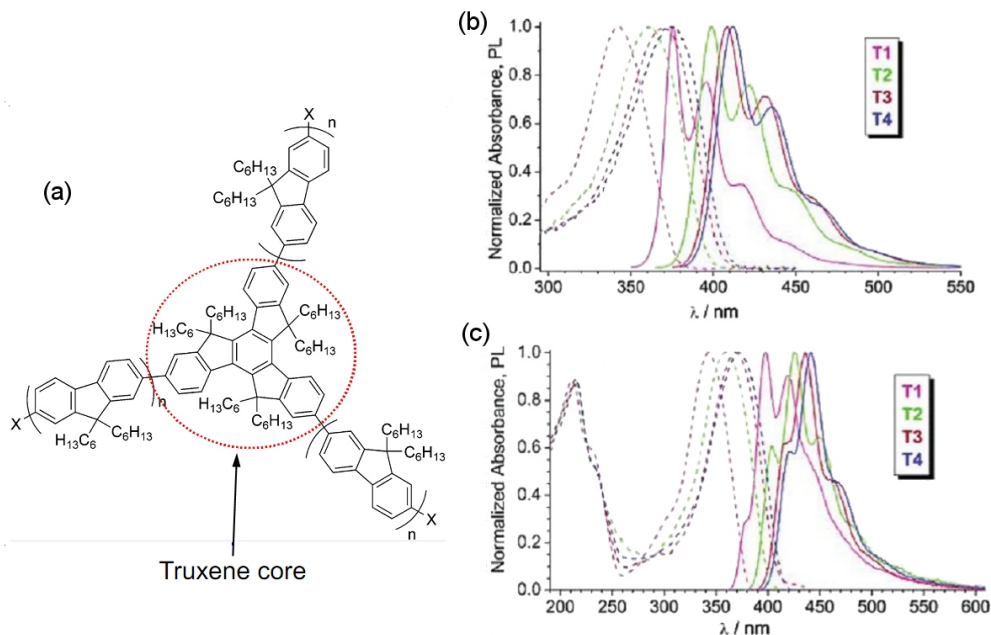


FIGURE 1.27: (a) Chemical structure of a truxene molecule, showing the truxene core at the centre of the three fluorene arms. Also shown are the absorption and emission spectra (b,c) of truxene molecules with varying numbers of repeat arm units. From [54].

1.4.2 Quantum dots

Quantum dots are nanocrystals of semiconductor material, typically with a diameter ≤ 10 nm and consisting of a few thousand atoms. Due to their geometry, they can be considered to be a ‘three-dimensional quantum well’, as they confine carriers in all three crystal directions (unlike quantum wells, which only confine the carriers in one crystal direction). Thus, they exhibit quantised electronic energy levels for all three directions of motion. We can apply the analysis of the quantum well energy levels presented in section 1.2.3 to the case of three dimensional confinement in a quantum dot. This gives an expression for the electronic energy levels in a quantum dot with dimension d in each direction as:

$$E(n_x, n_y, n_z) = \frac{h^2}{8md^2}(n_x^2 + n_y^2 + n_z^2) \quad (1.13)$$

where the quantum numbers, n_x, n_y, n_z , refer to the quantised energy levels in each direction. The energy spectrum of the quantum dot is thus discrete in all crystal directions, analogous to the spectrum of atoms. Quantum dots absorb energy when the wavelength of the excitation light exceeds the band gap between the valance and conduction bands. This promotes electrons to the higher quantised electronic energy states within the conduction band, with photon emission occurring when the carriers recombine. The lifetimes (τ) tend to be dominated by a 20-30 ns component, longer than those in organic dyes (1-5 ns) [55].

According to equation 1.13, the quantised energy levels (and thus absorption and emission spectra) in quantum dots can be tuned by tuning their size, which is illustrated in figure 1.28(a). The properties of the quantum dots also depend on the material they are made from. CdSe and ZnSe dots can emit light across the visible spectrum, whereas InP and InAs dots can emit in the near-infrared [55]. The quantum dot samples used in this thesis consist of a CdSe ‘core’ and a ZnS ‘shell’, as illustrated in figure 1.28(b). The ZnS shell passivates the CdSe core, removing surface traps and increasing the quantum efficiency of the dots [56]. It is also common for the outer shell to be coated with organic ligands, which prevent aggregation of the quantum dots, aid solubility and can also be used to add functionality to the dots, such as the ability to selectively bind to particular biological samples [57].

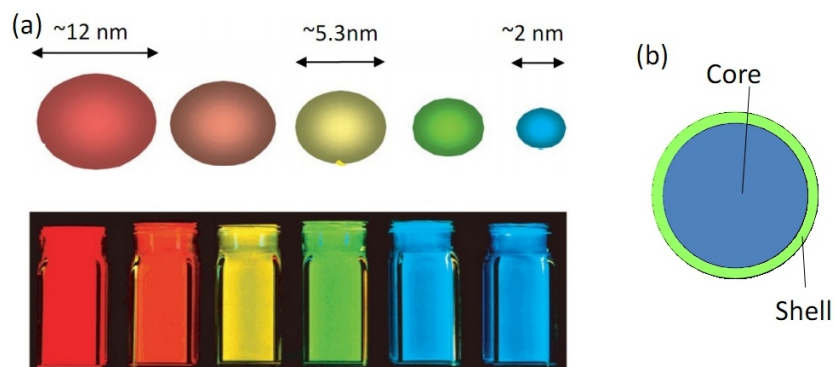


FIGURE 1.28: (a) ‘Core-shell’ structure of a CdSe/ZnS quantum dot and (b) colour photograph of quantum dots of different size, from [58].

Figure 1.29 shows absorption and emission spectra from a range of CdSe/ZnS quantum dot samples in toluene solution. The emission spectrum from a single CdSe/ZnS quantum dot can be as narrow as 13 nm at room temperature [55], with the broader emission spectra seen in figure 1.29 explained by the distribution of dot sizes within each bulk sample. Figure 1.29 also reveals that quantum dots are preferentially excited at shorter wavelengths, matching the UV-blue-green emission spectra of the AlInGaN micro-LEDs to be introduced later in this thesis. Quantum dots have high quantum yields, high stability, high resistance to photo-bleaching, broad absorption spectra and narrow, tunable emission spectra. These properties make them useful for a wide range applications including fluorescent markers for biological labelling [57], cryptography [59], single-photon sources [60], and of particular interest for this thesis, as colour converters for producing white LEDs [61]. Quantum dots are normally suspended in a solvent such as toluene, though they may also be incorporated in materials such as polymeric hosts [62] to facilitate integration with devices such as LEDs. The use of quantum dots as colour-converters, and their integration with micro-LEDs, will be discussed in the following section.

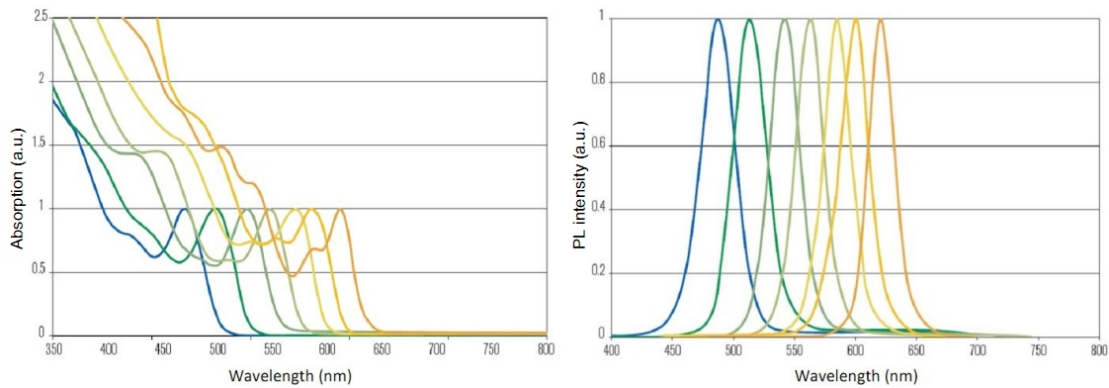


FIGURE 1.29: (l) Absorption and (r) emission spectra of CdSe/ZnS quantum dots in toluene solution, (after Evident Technologies, Inc).

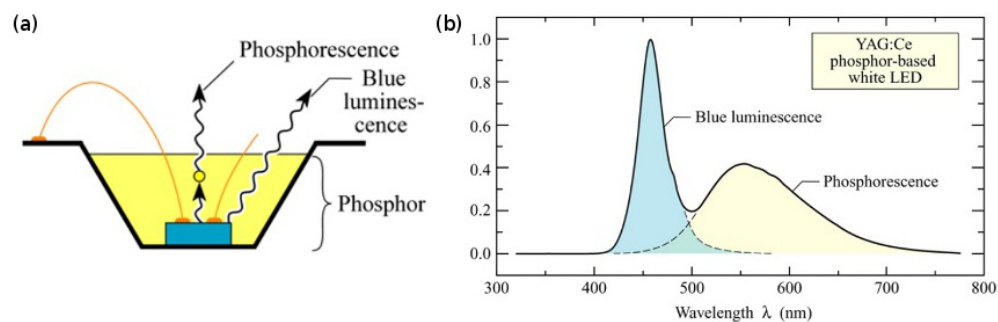


FIGURE 1.30: Conventional white LED (a) schematic and (b) emission spectra [21]. In such a device, emission from a blue LED is combined with a yellow phosphor to produce an overall white light emission.

1.4.3 Colour-conversion, deposition and integration

Both LEPs and CQDs are interesting materials for ‘colour-conversion’ of LED light. This refers to the use of an intermediate material to convert the emission from an LED from one colour to another. This approach is commonly used in white solid-state lighting, where most conventional white LEDs use a blue LED and a yellow-emitting phosphor to produce white light. The phosphor most commonly used is a YAG:Ce phosphor powder that is suspended within the epoxy resin dome of the LED, as shown in figure 1.30(a). Some of the blue light from the LED is absorbed by the phosphor and converted to yellow light. Figure 1.30(b) shows the resulting emission spectrum from such an LED. The human eye then perceives this mixture of colours as white light.

A potential benefit of using LEPs or CQDs instead of the phosphor-based approach discussed above is that these materials are capable of producing white light with a higher colour rendering index (CRI) than a standard phosphor-based white LED. Standard phosphor-based white LEDs typically have a CRI of less than 80, and a colour temperature of below 4000 K, whereas indoor lighting requires a CRI greater than 80 and a target colour temperature of around 3200 K to produce a ‘warm’ white light [13]. Figure 1.31

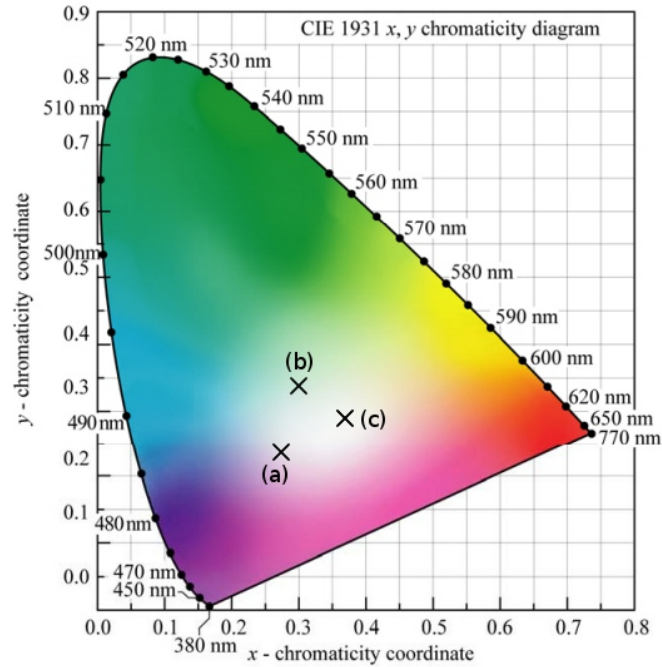


FIGURE 1.31: Colour-coordinates of (a) a standard phosphor-based LED, (b) a micro-LED/LEP hybrid [63] and (c) a CQD/LED hybrid [61].

shows a Commission internationale de l'éclairage (CIE) chromaticity diagram showing the colour-coordinates of (a) a standard phosphor-based LED, (b) a micro-LED/LEP hybrid [63] and (c) a CQD/LED hybrid [61]. Both the LEP and CQD-based approaches provide white light which is closer to the zero saturation white ($x = 0.33, y = 0.33$) than the standard phosphor-based approach. The colour from these LEP and CQD blends can also be tuned by, for example, adjusting the relative composition of the LEP blends [63], or by controlling the inter-spacing between individual CQD layers [64]. Another interesting property of the LEPs and CQDs is that their carrier lifetimes are much shorter than those of phosphor materials. This has important implications when considering the optical modulation bandwidth of the colour-converted light if these materials are to be used within optical communications systems. This will be discussed in more detail in chapter 5.

An attractive feature of both materials is that they are solution-processable, making them easy to integrate onto LED devices by simple and inexpensive techniques such as spray-coating and ink-jet printing. Furthermore, these materials are capable of being micro-patterned in such a way that a pattern of colour-converters can be integrated onto a micro-LED array, allowing the emission across a micro-LED array to be selectively colour-converted whilst retaining the advantage of the micro-pixelated nature of the micro-LED arrays. It should be noted that this is not readily possible using standard phosphors due to the large phosphor grain sizes. Figure 1.32 shows examples of patterned colour-converters which have been deposited onto micro-LED devices by our

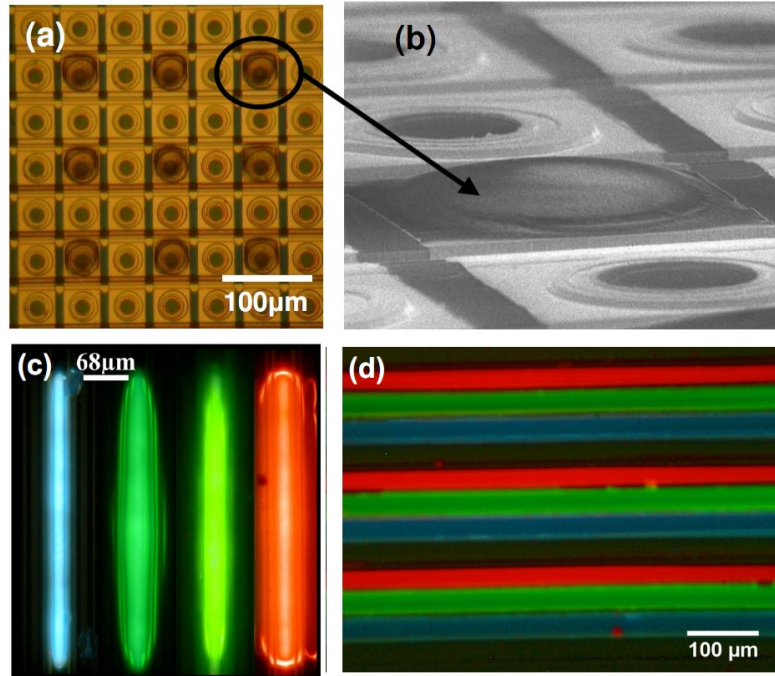


FIGURE 1.32: Micro-patterning of nanoluminophore materials by (a) & (b) ink-jet printing [67], (c) laser writing onto a micro-LED stripe array [66] and (d) integration with a micro-LED stripe array by a self-aligned writing process [62].

group using ink-jet printing [65], laser writing [66] and direct deposition by a novel ‘self-aligned writing’ process [62]. For some of these light-emitting materials, the material is mixed with a transparent polymeric ‘host’ material. The purpose of the host material is to facilitate the deposition and patterning of the light-emitting materials, and also to protect the material from the environment. The host material may affect the optical properties of the light-emitting material, for example, slightly lengthening the fluorescence lifetime, however in general the optical properties of the emitter-host blend are comparable to that of the emitter material in solution.

1.5 Summary

In this chapter the basics of light-emitting diodes were introduced. The historical development of LEDs was discussed, in particular the relatively recent development of LEDs based on the AlInGaN alloy system, as the micro-LEDs to be discussed in the rest of the thesis are all based on AlInGaN materials. It was seen that AlInGaN LEDs are currently a topic of great interest, and in particular that such devices hold great promise for use as highly efficient white-emitting general illumination light sources.

The principles of operation of LEDs were covered in section 1.2. LEDs are fabricated from semiconductor materials, the electrical properties of which can be tailored by alloying and intentional doping. The most basic form of LED, the p-n junction diode, was introduced in order to describe the basic mechanisms by which electrical charge carriers (holes and electrons) are injected into the semiconductor before recombining through the process of electroluminescence, allowing an LED to emit light. Virtually all AlInGaN LED structures now use quantum wells to improve their efficiency and to tailor their output wavelength, so the basic principles of the operation of quantum wells was given in section 1.2.3.

Subsequently, the focus of discussion turned to more specific details about LEDs fabricated from the AlInGaN alloy system, including how these devices are grown and processed into working LED devices. Details about typical epitaxial LED structures and die configurations was provided. A brief summary of the phenomenon of ‘efficiency droop’ was given, in order to introduce the reader to one of the most hotly debated areas of present AlInGaN LED research. Some work later in this thesis, in section 5.2.3 will touch upon some of the issues raised here, in particular the degree of non-radiative Auger recombination within AlInGaN LEDs. Finally, some of the colour-converting materials which will be used for experiments in chapters 4 and 5 were introduced. The mechanisms by which these materials absorb and emit light was discussed. More specific details about the motivation for using them will be discussed in the relevant chapters.

References

- [1] H.J. Round. A note on carborundum. *Electrical World*, 19(309), 1907.
- [2] W.O. Groves, A.H. Herzog, and M.G. Craford. The effect of nitrogen doping on $GaAs_{1-x}P_x$ electroluminescent diodes. *Applied Physics Letters*, 19(6):184–186, 1971.
- [3] R. A. Logan, H. G. White, and W. Wiegmann. Efficient green electroluminescence in nitrogen-doped GaP p-n junctions. *Applied Physics Letters*, 13(4):139–141, 1968.
- [4] H. P. Maruska and J. J. Tietjen. The preparation and properties of vapor-deposited single-crystalline GaN. *Applied Physics Letters*, 15(10):327–329, 1969.
- [5] Rakesh B. Jain and Herbert Paul Maruska. How it really happened: The history of p-type doping of gallium nitride. *Physica Status Solidi (a)*, 204(6):1970–1976, 2007.
- [6] Toshiharu Kawabata, Toshio Matsuda, and Susumu Koike. GaN blue light emitting diodes prepared by metalorganic chemical vapor deposition. *Journal of Applied Physics*, 56(8):2367–2368, 1984.
- [7] H. Amano, N. Sawaki, I. Akasaki, and Y. Toyoda. Metalorganic vapor phase epitaxial growth of a high quality GaN film using an AlN buffer layer. *Applied Physics Letters*, 48(5):353–355, 1986.
- [8] Hiroshi Amano, Masahiro Kito, Kazumasa Hiramatsu, and Isamu Akasaki. P-type conduction in Mg-doped GaN treated with Low-Energy Electron Beam Irradiation (LEEBI). *Japanese Journal of Applied Physics*, 28(Part 2, No. 12):L2112–L2114, 1989.
- [9] Shuji Nakamura, Masayuki Senoh, and Takashi Mukai. Highly P-Typed Mg-Doped GaN Films Grown with GaN Buffer Layers. *Japanese Journal of Applied Physics*, 30(Part 2, No. 10A):L1708–L1711, 1991.
- [10] Shuji Nakamura, Takashi Mukai, and Masayuki Senoh. Candela-class high-brightness InGaN/AlGaIn double-heterostructure blue-light-emitting diodes. *Applied Physics Letters*, 64(13):1687–1689, 1994.
- [11] Shuji Nakamura, Masayuki Senoh, Shin ichi Nagahama, Naruhito Iwasa, Takao Yamada, Toshio Matsushita, Hiroyuki Kiyoku, and Yasunobu Sugimoto. InGaIn-based multi-quantum-well-structure laser diodes. *Japanese Journal of Applied Physics*, 35 (Part 2, No. 1B):L74–L76, 1996.

- [12] J. K. Kim and E. F. Schubert. Transcending the replacement paradigm of solid-state lighting. *Optics Express*, 16:21835–21842, 2008.
- [13] M.R. Krames, O.B. Shchekin, R. Mueller-Mach, G.O. Mueller, Ling Zhou, G. Harbers, and M.G. Craford. Status and future of high-power light-emitting diodes for solid-state lighting. *Display Technology, Journal of*, 3(2):160–175, June 2007. ISSN 1551-319X. doi: 10.1109/JDT.2007.895339.
- [14] Sari Vilhunen, Heikki Särkkä, and Mika Sillanpää. Ultraviolet light-emitting diodes in water disinfection. *Environmental Science and Pollution Research*, 16(4):439–442, JUN 2009. ISSN 0944-1344.
- [15] Tsutomu Araki and Hiroaki Misawa. Light emitting diode-based nanosecond ultraviolet light source for fluorescence lifetime measurements. *Review of Scientific Instruments*, 66(12):5469–5472, 1995. doi: 10.1063/1.1146519.
- [16] Kristina Davitt, Yoon-Kyu Song, William Patterson III, Arto Nurmikko, Maria Gherasimova, Jung Han, Yong-Le Pan, and Richard Chang. 290 and 340 nm UV LED arrays for fluorescence detection from single airborne particles. *Optics Express*, 13(23):9548–9555, 2005.
- [17] Rosanne M. Guijt and Michael C. Breadmore. Maskless photolithography using UV LEDs. *Lab On A Chip*, 8(8):1402–1404, Aug 2008. ISSN 1473-0197.
- [18] Gang Chen, Feras Abou-Galala, Zhengyuan Xu, and Brian M. Sadler. Experimental evaluation of LED-based solar blind NLOS communication links. *Optics Express*, 16(19):15059–15068, 2008.
- [19] M. Ali Omar. *Elementary solid state physics*. Pearson Education Inc., 1999.
- [20] M. Fukuda. *Optical Semiconductor Devices*. John Wiley & Sons, New York, 1999.
- [21] E.F. Schubert. *Light Emitting Diodes*. Cambridge University Press, 2nd edition, 2006.
- [22] T. Misawa. Saturation current and large-signal operation of a read diode. *Solid-State Electronics*, 13(10):1363 – 1368, 1970.
- [23] Y Taniyasu, M Kasu, and T Makimoto. An aluminium nitride light-emitting diode with a wavelength of 210 nanometres. *Nature*, 441(7091):325–328, MAY 18 2006. ISSN 0028-0836. doi: {10.1038/nature04760}.
- [24] O Ambacher. Growth and applications of group III-nitrides. *Journal of Physics D: Applied Physics*, 31(20):2653, 1998.

- [25] Shuji Nakamura, Yasuhiro Harada, and Masayuki Seno. Novel metalorganic chemical vapor deposition system for GaN growth. *Applied Physics Letters*, 58(18):2021–2023, May 1991.
- [26] Hyun Cho Jewon Lee, D.C. Hays, C.R. Abernathy, S.J. Pearton, R.J. Shul, G.A. Vawter, and J. Han. Dry etching of GaN and related materials: Comparison of techniques. *IEEE Journal of Selected Topics in Quantum Electronics*, 4(3):557–563, May/June 1998.
- [27] R. J. Shul, G. B. McClellan, S. A. Casalnuovo, D. J. Rieger, S. J. Pearton, C. Constantine, C. Barratt, Jr. R. F. Karlicek, C. Tran, and M. Schurman. Inductively coupled plasma etching of GaN. *Applied Physics Letters*, 69(8):1119–1121, 1996.
- [28] F. Hamdani, A. Botchkarev, W. Kim, H. Morkoç, M. Yeadon, J. M. Gibson, S.-C. Y. Tsen, David J. Smith, D. C. Reynolds, D. C. Look, K. Evans, C. W. Litton, W. C. Mitchel, and P. Hemenger. Optical properties of GaN grown on ZnO by reactive molecular beam epitaxy. *Applied Physics Letters*, 70(4):467–469, 1997.
- [29] D. G. Zhao, S. J. Xu, M. H. Xie, S. Y. Tong, and Hui Yang. Stress and its effect on optical properties of GaN epilayers grown on Si(111), 6H-SiC(0001), and c-plane sapphire. *Applied Physics Letters*, 83(4):677–679, 2003.
- [30] M. K. Kelly, O. Ambacher, R. Dimitrov, R. Handschuh, and M. Stutzmann. Optical process for lift-off of Group III-nitride films. *Physica Status Solidi (a)*, 159:R3, 1997.
- [31] O. B. Shchekin, J. E. Epler, T. A. Trottier, T. Margalith, D. A. Steigerwald, M. O. Holcomb, P. S. Martin, and M. R. Krames. High performance thin-film flip-chip InGaN–GaN light-emitting diodes. *Applied Physics Letters*, 89(7):071109, 2006.
- [32] L. Zhou, J. E. Epler, M. R. Krames, W. Goetz, M. Gherasimova, Z. Ren, J. Han, M. Kneissl, and N. M. Johnson. Vertical injection thin-film AlGaIn/AlGaIn multiple-quantum-well deep ultraviolet light-emitting diodes. *Applied Physics Letters*, 89(24):241113, 2006.
- [33] S. C. Jain, M. Willander, J. Narayan, and R. Van Overstraeten. III-nitrides: Growth, characterization, and properties. *Journal of Applied Physics*, 87(3):965–1006, 2000.
- [34] S.P. Denbaars. Gallium-Nitride-Based Materials for Blue to Ultraviolet Optoelectronics Devices. *Proceedings of the IEEE*, 85(11):1740–1749, 1997.
- [35] S. D. Lester, F. A. Ponce, M. G. Craford, and D. A. Steigerwald. High dislocation densities in high efficiency GaN-based light-emitting diodes. *Applied Physics Letters*, 66(10):1249–1251, 1995.

- [36] Takashi Mukai, Daisuke Morita, and Shuji Nakamura. High-power UV InGaN/Al-GaN double-heterostructure LEDs. *Journal of Crystal Growth*, 189-190:778 – 781, 1998. ISSN 0022-0248.
- [37] T. M. Smeeton, M. J. Kappers, J. S. Barnard, M. E. Vickers, and C. J. Humphreys. Electron-beam-induced strain within InGaN quantum wells: False indium “cluster” detection in the transmission electron microscope. *Applied Physics Letters*, 83(26): 5419–5421, 2003.
- [38] Shuji Nakamura, Masayuki Senoh, and Takashi Mukai. P-GaN/N-InGaN/N-GaN double-heterostructure blue-light-emitting diodes. *Japanese Journal of Applied Physics*, 32(Part 2, No. 1A/B):L8–L11, 1993. doi: 10.1143/JJAP.32.L8.
- [39] Chan-Wook Jeon, Hoi Wai Choi, E. Gu, and M.D. Dawson. High-density matrix-addressable AlInGaN;-based 368-nm microarray light-emitting diodes. *IEEE Photonics Technology Letters*, 16(11):2421 – 2423, 2004.
- [40] H. X. Zhang, D. Massoubre, J. McKendry, Z. Gong, B. Guilhabert, C. Griffin, E. Gu, P. E. Jessop, J. M. Girkin, and M. D. Dawson. Individually-addressable flip-chip AlInGaN micropixelated light emitting diode arrays with high continuous and nanosecond output power. *Optics Express*, 16(13):9918–9926, 2008.
- [41] N. F. Gardner, G. O. Muller, Y. C. Shen, G. Chen, S. Watanabe, W. Gotz, and M. R. Krames. Blue-emitting InGaN-GaN double-heterostructure light-emitting diodes reaching maximum quantum efficiency above 200 A/cm². *Applied Physics Letters*, 91(24):243506, 2007.
- [42] Shih-Chun Ling, Tien-Chang Lu, Shih-Pang Chang, Jun-Rong Chen, Hao-Chung Kuo, and Shing-Chung Wang. Low efficiency droop in blue-green m-plane InGaN/-GaN light emitting diodes. *Applied Physics Letters*, 96:231101, 2010.
- [43] Y. C. Shen, G. O. Mueller, S. Watanabe, N. F. Gardner, A. Munkholm, and M. R. Krames. Auger recombination in InGaN measured by photoluminescence. *Applied Physics Letters*, 91(14):141101, 2007.
- [44] J. Hader, J. V. Moloney, B. Pasenow, S. W. Koch, M. Sabathil, N. Linder, and S. Lutgen. On the importance of radiative and Auger losses in GaN-based quantum wells. *Applied Physics Letters*, 92(26):261103, 2008.
- [45] Min-Ho Kim, Martin F. Schubert, Qi Dai, Jong Kyu Kim, E. Fred Schubert, Joachim Piprek, and Yongjo Park. Origin of efficiency droop in GaN-based light-emitting diodes. *Applied Physics Letters*, 91(18):183507, 2007.

- [46] Martin F. Schubert, Jiuru Xu, Jong Kyu Kim, E. Fred Schubert, Min Ho Kim, Sukho Yoon, Soo Min Lee, Cheolsoo Sone, Tan Sakong, and Yongjo Park. Polarization-matched GaInN/AlGaInN multi-quantum-well light-emitting diodes with reduced efficiency droop. *Applied Physics Letters*, 93(4):041102, 2008.
- [47] J. Hader, J. V. Moloney, and S. W. Koch. Density-activated defect recombination as a possible explanation for the efficiency droop in GaN-based diodes. *Applied Physics Letters*, 96(22):221106, 2010.
- [48] M.H. Crawford. LEDs for solid-state lighting: Performance challenges and recent advances. *Selected Topics in Quantum Electronics, IEEE Journal of*, 15(4):1028–1040, 2009. ISSN 1077-260X.
- [49] J. H. Burroughes, D. D. C. Bradley, A. R. Brown, R. N. Marks, K. Mackay, R. H. Friend, P. L. Burns, and A. B. Holmes. Light-emitting diodes based on conjugated polymers. *Nature*, 347(6293):539–541, 1990.
- [50] Ifor D. W. Samuel and Graham A Turnbull. Organic semiconductor lasers. *Chemical Reviews*, 107:1272–1295, 2007.
- [51] Mark Fox. *Optical Properties of Solids*. Oxford University Press, 2001.
- [52] Joseph R. Lakowicz. *Principles of Fluorescence Spectroscopy*. Springer, 3rd edition, 2006.
- [53] John Chappell, David G. Lidzey, Paul C. Jukes, Anthony M. Higgins, Richard L. Thompson, Stephen O’Connor, Ilaria Grizzi, Robert Fletcher, Jim O’Brien, Mark Geoghegan, and Richard A. L. Jones. Correlating structure with fluorescence emission in phase-separated conjugated-polymer blends. *Nature Materials*, 2:616–621, 2003.
- [54] Alexander L. Kanibolotsky, Rory Berridge, Peter J. Skabara, Igor F. Perepichka, Donal D. C. Bradley, and Mattijs Koeberg. Synthesis and Properties of Monodisperse Oligofluorene-Functionalized Truxenes: Highly Fluorescent Star-Shaped Architectures. *Journal of the American Chemical Society*, 126(42):13695–13702, 2004.
- [55] Warren C. W. Chan, Dustin J. Maxwell, Xiaohu Gao, Robert E. Bailey, Mingyong Han, and Shuming Nie. Luminescent quantum dots for multiplexed biological detection and imaging. *Current Opinion in Biotechnology*, 13(1):40 – 46, 2002. ISSN 0958-1669.
- [56] Margaret A. Hines and Philippe Guyot-Sionnest. Synthesis and characterization of strongly luminescing ZnS-capped CdSe nanocrystals. *The Journal of Physical Chemistry*, 100(2):468–471, 1996.

- [57] Wolfgang J Parak, Teresa Pellegrino, and Christian Plank. Labelling of cells with quantum dots. *Nanotechnology*, 16:R9–R25, 2005.
- [58] Andy Watson, Xingyong Wu, and Marcel Bruchez. Lighting up cells with quantum dots. *Biotechniques*, 34(2):296–303, 2003.
- [59] Ming Zhou, Shoude Chang, and Chander Grover. Cryptography based on the absorption/emission features of multicolor semiconductor nanocrystal quantum dots. *Optics*, 12(13):2925–2931, 2004.
- [60] Julien Claudon, Jol Bleuse, Nitin Singh Malik, Maela Bazin, Prine Jaffrennou, Niels Gregersen, Christophe Sauvan, Philippe Lalanne, and Jean-Michel Gerard. A highly efficient single-photon source based on a quantum dot in a photonic nanowire. *Nature Photonics*, 4:174–177, 2009.
- [61] Sedat Nizamoglu, Gulis Zengin, and Hilmi Volkan Demir. Color-converting combinations of nanocrystal emitters for warm-white light generation with high color rendering index. *Applied Physics Letters*, 92(3):031102, 2008.
- [62] B. Guilhabert, D. Elfström, and D. Massoubre A.J.C. Kuehne, H.X. Zhang, S.R. Jin, A.R. Mackintosh, E. Gu, R.A. Pethrick, and M. D. Dawson. Integration by self-aligned writing of nanocrystal/epoxy composites on InGaN micro-pixelated light-emitting diodes. *Optics Express*, 16(23):18933–18941, 2008.
- [63] C R Belton, G Itskos, G Heliotis, P N Stavrinou, P G Lagoudakis, J Lupton, S Pereira, E Gu, C Griffin, B Guilhabert, I M Watson, A R Mackintosh, R A Pethrick, J Feldmann, R Murray, M D Dawson, and D D C Bradley. New light from hybrid inorganic-organic emitters. *Journal of Physics D: Applied Physics*, 41(9):094006 (12pp), 2008.
- [64] Neslihan Cicek, Sedat Nizamoglu, Tuncay Ozel, Evren Mutlugun, Durmus Ugur Karatay, Vladimir Lesnyak, Tobias Otto, Nikolai Gaponik, Alexander Eychemüller, and Hilmi Volkan Demir. Structural tuning of color chromaticity through nonradiative energy transfer by interspacing CdTe nanocrystal monolayers. *Applied Physics Letters*, 94(6):061105, 2009.
- [65] M. Wu, E. Gu, A. Zarowna, A. L. Kanibolotsky, A. J. C. Kuehne, A. R. Mackintosh, P. R. Edwards, O. J. Rolinski, I. F. Perepichka, P. J. Skabara, R. W. Martin, R. A. Pethrick, D. J. S. Birch, and M. D. Dawson. Star-shaped oligofluorene nanostructured blend materials: controlled micro-patterning and physical characteristics. *Applied Physics A - Materials Science & Processing*, 97(1):119–123, OCT 2009. ISSN 0947-8396. doi: {10.1007/s00339-009-5308-x}.

-
- [66] D Elfström. *Novel photo-patterning technology for direct writing in resist based systems*. PhD thesis, University of Strathclyde, Institute of Photonics, 2010.
- [67] M. Wu, Z. Gong, A. J. Kuehne, A. L. Kanibolotsky, Y. J. Chen, I. F. Perepichka, A. R. Mackintosh, E. Gu, P. J. Skabara, R. A. Pethrick, and M. D. Dawson. Hybrid GaN/organic microstructured light-emitting devices via ink-jet printing. *Optics Express*, 17(19):16436–16443, 2009.

Chapter 2

Micro-pixellated light-emitting diode arrays

In this chapter the concept of micro-pixellated light-emitting diode arrays ('micro-LED arrays', or 'micro-LEDs') fabricated in the AlInGaN alloy system will be introduced. A summary of the development of micro-LED arrays by various research groups, including the Institute of Photonics, will be given. Then the advantages of the micro-structured nature of these devices will be discussed in relation to some applications that have been demonstrated. The various formats of GaN-based micro-LEDs to be used later will be described, and the process flow used to fabricate these devices will be detailed. Finally, the basic electrical and optical performance of these devices will be summarised in terms of such properties as the maximum output power per pixel and the emission spectra of the devices.

2.1 Introduction to micro-LED arrays

2.1.1 Development of micro-LED arrays

An overview of conventional 'broad area' LEDs has been presented in chapter 1 and now an overview of micro-pixellated LED arrays ('micro-LEDs') will be given. In simple terms, micro-LEDs are LEDs which have been patterned by photolithography such that they consist of an array of separate emitter pixels, each having dimensions of 100 μm or less. This contrasts with the large die used in a conventional 'broad area' LED, which typically has a single emission area ranging from approximately $300 \times 300 \mu\text{m}^2$ to 1mm^2 . High power illumination LEDs commonly use several of these large die. Therefore, a micro-LED array can have hundreds, or even thousands, of individual emitters in the

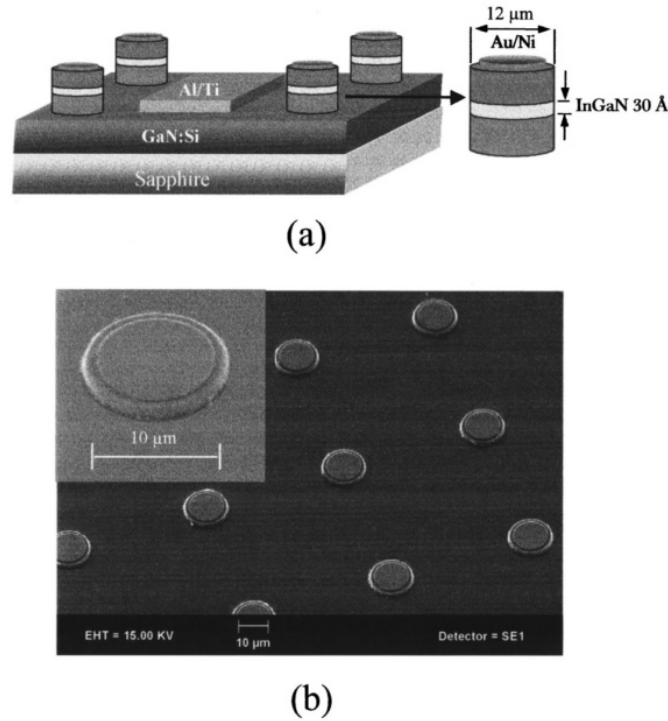


FIGURE 2.1: (a) Schematic and (b) oblique SEM image of the first reported electrically injected AlInGaN micro-LED devices, from [1].

same area as a single broad area LED. The first electrically-injected AlInGaN micro-LED device was demonstrated in 2000 by H.X. Jiang's group, then at Kansas State University [1]. Individually-addressable micro-LED discs of 12 μm diameter with peak emission at 408 nm wavelength were fabricated from an InGaN/GaN quantum well LED wafer by photolithography and ICP etching, as shown in figure 2.1. Since no electrical bonding scheme had at the time been developed, each pixel could only be addressed using a probe station. Each pixel demonstrated modest continuous wave (CW) output powers of up to 20 μW and had a high turn-on voltage of around 7-8 V. However, this was an important first step in the development of micro-LED devices. Indeed, in 2001, the same group reported a 10 × 10 array of blue-emitting micro-LEDs (figure 2.2), each element of which could be addressed via separate p and n contacts for each pixel [2]. This addressing scheme is shown in figure 2.2, where the individual contacts for pixel can be seen at the edge of the array. Such an addressing scheme would be impractical for a large array of elements. A method of simplifying this arrangement is to implement a matrix-addressing scheme, whereby row and column addressing is used to control the elements in the micro-LED array. The first matrix-addressable micro-LED array was demonstrated by Ozden *et al.* in 2001 [3]. The advantage of this approach is that for an array of $m \times n$ elements, only $m + n$ contacts are needed to address the array rather than $\geq m \times n$ contacts using an individually-addressable scheme. For example, a 64 × 64 micro-LED array would need 128 contacts with a matrix-addressing scheme, or

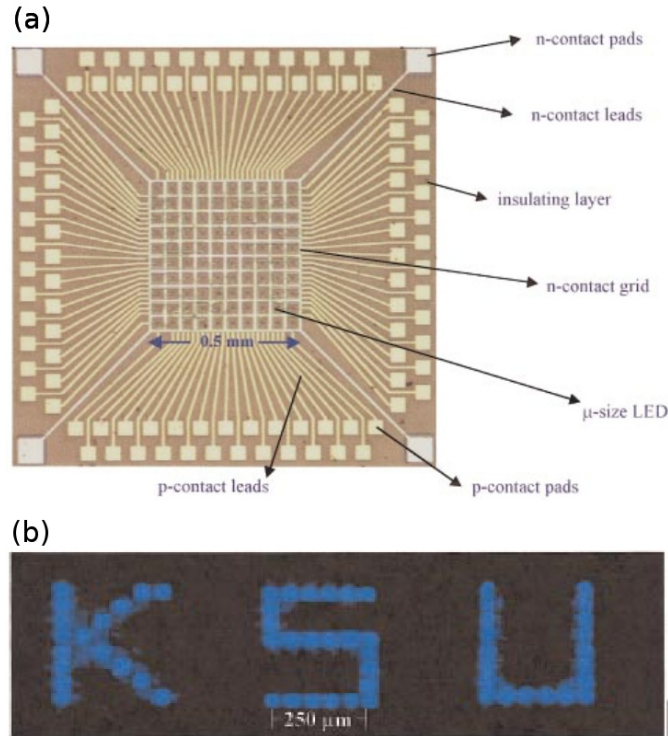


FIGURE 2.2: Optical micrograph image of (a) an individually-addressable micro-disk LED array and (b) output from the array, from [2].

>4000 if each pixel was to be individually addressed. Matrix-addressable micro-LED arrays fabricated by the Institute of Photonics, the first of which was reported in 2002, will be discussed in detail in section 2.2.1. It should be noted that to produce an image on a matrix-addressed micro-LED array the array must be raster-scanned, that is to say that the rows must be addressed one at a time. Assuming that this raster-scan is done quickly enough, then to the human eye there appears to be one continuous image. This approach has the disadvantage that since each row is only active for a fraction of the time then the average output power of each pixel, and of the overall array, is greatly reduced. For certain applications it is desirable to be able to individually address each pixel, removing the need to raster-scan the array and therefore maximising the average output power of each element. For such applications, individually-addressable micro-LEDs suitable for integration with an array of CMOS drivers have been designed within the Institute of Photonics. These devices will be introduced in section 2.2.2 and the relevant CMOS driver arrays will be introduced in chapter 3.

2.1.2 Advantages and applications of micro-LED arrays

Micro-LEDs offer several advantages over conventional ‘broad area’ LEDs. Perhaps the most obvious advantage is that a micro-LED array provides a simple method of generating a micro-scale spatiotemporal light pattern which may then be imaged into

a light-sensitive sample of interest. One such example is shown in figure 2.3, where the emission of micro-LED arrays with pixels of $50 \mu\text{m}$ diameter were imaged into a multi-core optical fibre and projected into biological samples for photo-excitation [4]. Another advantage of micro-LEDs is that the optical output power density is higher compared to a broad area LED with an identical epitaxial structure. For example, Jin *et al.* demonstrated that an array of ≈ 100 interconnected micro-LED pixels emitted light with more than 60% more efficiency than a comparable standard LED having the same effective active area [5]. Micro-LEDs have also been demonstrated to have shorter optical turn-off times than broad area LEDs [6], making them particularly useful for applications that require short optical pulses or high modulation bandwidths. As such, time-resolved fluorescence measurements using micro-LEDs will be discussed in chapter 4 and the modulation bandwidth of micro-LEDs will be investigated in chapter 5.

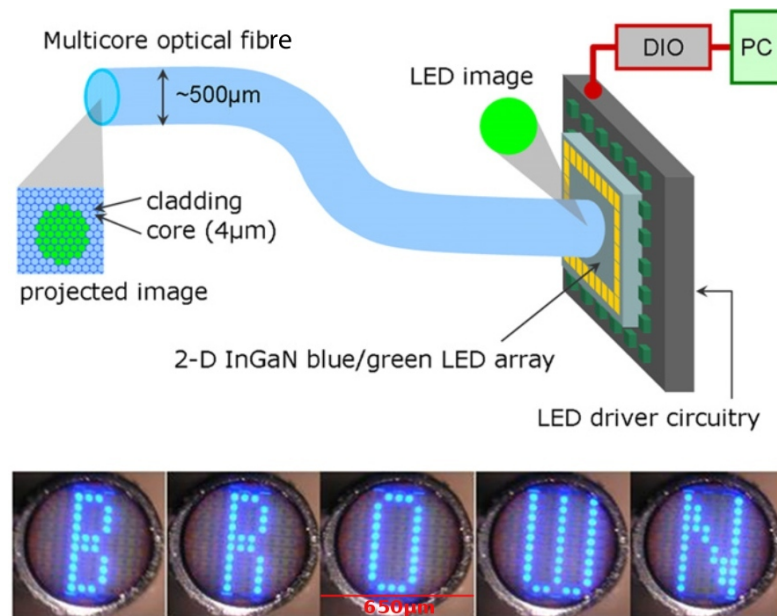


FIGURE 2.3: (Above) Schematic of an integrated 100 element bluegreen micro-LED array with fibre optic image projection system. (Below) emission patterns generated at the end of the multicore image fibre, from [4].

As well as having advantages over conventional broad area LEDs, micro-LEDs also have some advantages over other formats of micro-display technologies. Micro-displays which modulate a blanket illumination source using either a liquid crystal display (LCD) or a digital micromirror display (DMD, also known as a Digital Light Processor, DLP), are a relatively mature technology commonly found in commercial television or data projectors. These systems have also been used for scientific instrumentation, for example, figure 2.4 shows the schematic of an optoelectronic tweezer (OET) device [7], which uses a DMD to project a modulated image from a single LED source into a photoconductive layer of amorphous silicon. Wherever the light illuminates the photoconductive layer, a localised non-uniform electric field is created, which will either attract or repel cells.

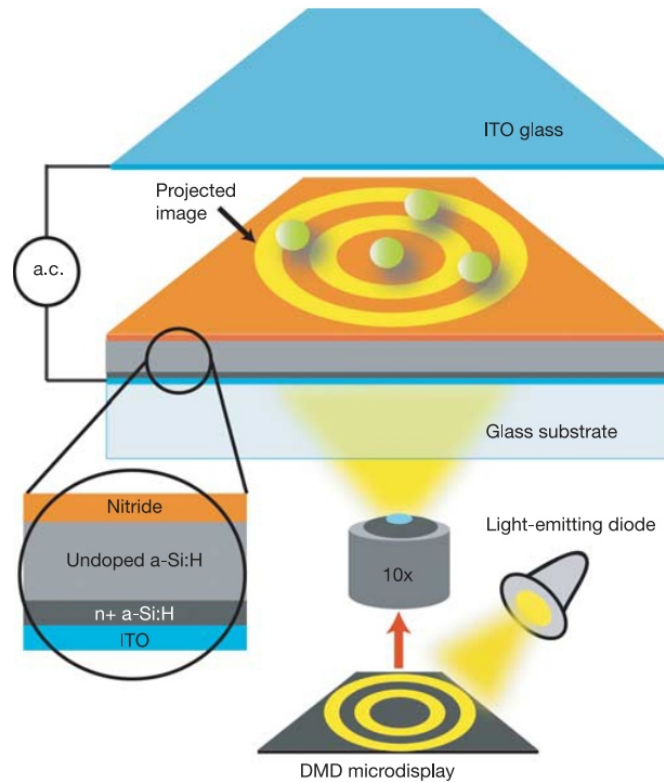


FIGURE 2.4: Schematic of an optoelectronic tweezer device, used for parallel cell manipulation, from [7].

By changing the modulated output from the DMD, cells can be moved and manipulated. Another example is that of a DMD-based microfabrication system for constructing three-dimensional polymer scaffolds for cell tissue engineering [8]. In both cases, replacing the relatively bulky DMD-based light pattern projection system with a LED with a micro-LED array, these devices could be made considerably more compact. Indeed, a miniaturised OET device that utilises CMOS-controlled individually-addressable micro-LEDs has recently been demonstrated and will be described in Chapter 3 [9]. Another example of micro-LEDs being used to reduce the complexity of a system is for mask-free photolithography [10], which removes the need for hard photo-masks by instead using a varying micro-LED output and translation of the photoresist sample to write features into photoresist. This system will be discussed in more detail in chapter 3, section 3.5. An array of individually-addressable stripe micro-LEDs has also been demonstrated to be capable of replacing a mechanical moving grating for the application of optical sectioning microscopy, providing improved reliability [11].

As well as compactness, micro-LED arrays also offer other advantages over modulated micro-displays, including higher efficiency, higher contrast between array elements and increased brightness. This potentially makes micro-LEDs better suited to applications

such as Head-Up Displays (HUDs), where the higher brightness and contrast of a micro-LED could make for a higher clarity HUD than one based on a modulated micro-display, particularly when the display has to be clearly read under direct sunlight conditions. Another format of micro-displays are those based on organic light-emitting diodes (OLEDs). Unlike the modulated micro-displays discussed above, OLED displays are similar to micro-LED arrays in the sense that they are emissive displays consisting of arrays of individual LEDs, with the key difference being that the material that emits light in an OLED display is an organic semiconductor light-emitting molecule or polymer. A key advantage of organic semiconductor technology is that the light-emitting materials can be processed in a considerably more straightforward manner than for inorganic materials [12]. However, the main disadvantage of organic semiconductors is their comparatively low light output power density compared to inorganic LEDs. There are also issues with the operating lifetime and robustness of OLEDs - while OLEDs have been reported with operating lifetimes of the order of 7000 hours [13], inorganic LEDs may operate for as many as 100,000 hours [14], and inorganic LEDs are also able to withstand far more harsh operating environments. Inorganic LEDs are also several times more efficient [14], which is an important concern in a battery-powered portable device.

2.2 Micro-LED design and fabrication

In this section the design and fabrication of some types of micro-LED arrays will be presented. These devices are based on LED wafers grown on c-plane sapphire substrates, which are subsequently processed into micro-LED wafers using the processing techniques that were outlined in section 1.3.1. A wide variety of micro-LED devices, with different peak emission wavelengths, array layouts, addressing schemes etc., have been fabricated in house since 2001. The peak emission wavelengths at which micro-LEDs have been fabricated range from the near-UV (370 nm), violet (405 nm), blue (450 and 470 nm) to green (520 nm); more recently yellow (560 nm) and red-emitting (600 nm) micro-LED devices have also been fabricated. Images of micro-LED devices with peak emission wavelengths ranging from 370 to 600 nm are shown in figure 2.5. It would not be practical to exhaustively detail every variation of micro-LED that has been produced by our group, therefore this section will focus primarily on describing the basic design and fabrication of some of our most commonly-used micro-LED devices. Section 2.3 will then focus in more detail on the performance characteristics of the specific variations of micro-LED devices which were used in the experimental work to be presented in chapters 3 to 5.

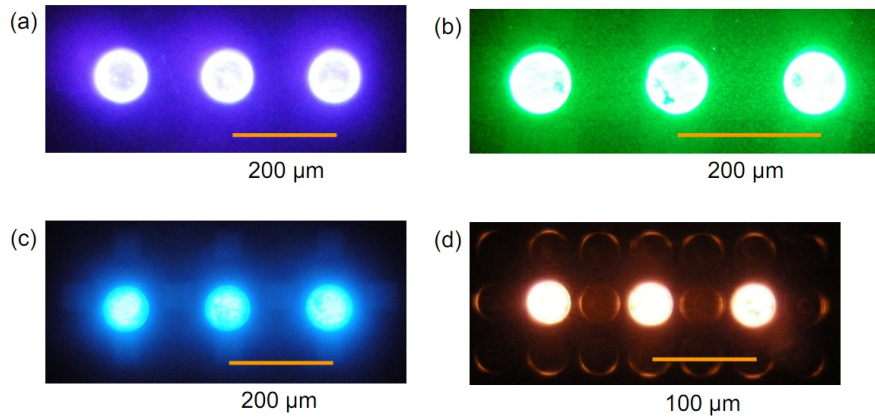


FIGURE 2.5: Image of micro-LED devices with peak emission wavelengths of (a) 405 (b) 520 (c) 450 and (d) 600 nm.

2.2.1 Matrix-addressable micro-LED array design

As discussed previously, matrix-addressable micro-LED arrays are a particularly interesting format of device, as they allow large arrays to be addressed with relatively few electrical contacts. Each row of pixels in a matrix-addressable micro-LED array shares a common n-contact, while each column shares a common p-contact. Therefore, any individual element in the array can be driven by electrically addressing the appropriate row and column. Figure 2.6(a) shows a cross-sectional schematic of a matrix-addressable micro-LED array. This device consists of a 64×64 array of $16 \mu\text{m}$ diameter elements with a $50 \mu\text{m}$ centre-to-centre pitch. The process for fabricating such a device is as follows [15]. First of all, the individual rows are defined by ICP etching down to the sapphire substrate. Then, individual pixel mesas are defined on each of these rows by a second ICP etch step. Early micro-LED devices used an anisotropic etch to define mesas having nearly vertical sidewalls, [2, 3, 16], however it is extremely difficult to deposit the necessary continuous contact metal tracks on structures with sharp vertical trenches. To overcome this, planarisation techniques were initially used [16], which use a sacrificial metal layer and either chemical-mechanical polishing or dry etching to define a flat surface upon which contact metal can easily be deposited. Unfortunately, this approach tends to cause damage to LED p-GaN surface, which degrades device performance. Therefore, an isotropic etch technique was developed by our group [17] which forms mesas with side walls sloped at $20\text{-}45^\circ$ allowing lines of contact metal to be deposited along and across the mesa slopes. Since no planarisation process is needed, such devices showed improved electrical and optical performance. In addition, micro-LED devices with sloped mesa sidewalls have also been demonstrated to increase the light extraction efficiency, which was attributed to light scattering from the mesa sidewalls that would otherwise be trapped in the LED die by total internal reflection [18]. The next step involves the thermal evaporation of a current spreading layer on top of each

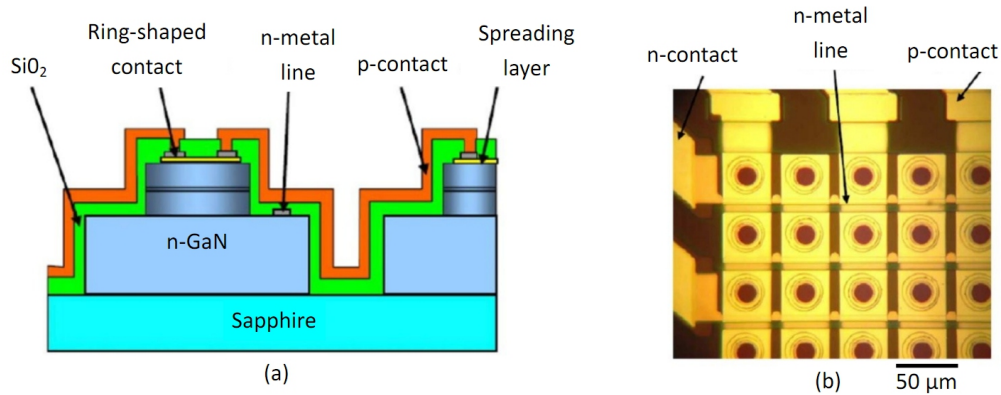


FIGURE 2.6: (a) Cross-sectional schematic of a 64×64 element matrix-addressable micro-LED array and (b) a corresponding micrograph image, from [15]. Pixels are $16 \mu\text{m}$ in diameter with a $50 \mu\text{m}$ centre-to-centre pitch between pixels.

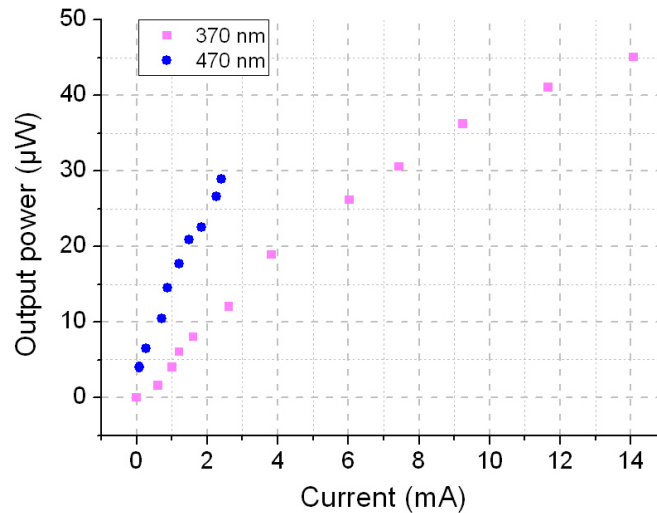


FIGURE 2.7: Output power versus current of single $16 \mu\text{m}$ diameter pixels from ‘epitaxy-up’ matrix-addressable arrays with peak emission wavelengths of 370 and 470 nm, respectively. From [15].

pixel, and the deposition of n-contact metal lines and pixel ring-contacts by sputtering. A SiO_2 layer is deposited to act as an isolation layer, before this layer is selectively etched to expose the n-contact pads (i.e. the row contacts) and the ring contacts on top of each pixel. Finally, p-contact metal lines to address each column are deposited by a sputtering process. An optical micrograph image of a finished device is shown in figure 2.6(b), clearly showing pixels from the array and the p and n-contacts. Representative output power versus current (L-I) curves from single pixels from ‘epitaxy-up’ 64×64 matrix-addressable arrays, with peak emission wavelengths of 370 and 470 nm, respectively, are shown in figure 2.7. Further detail on the characteristics of these devices has been published elsewhere [15].

These matrix-addressable devices are controlled via a computer interface and a driver board. A PIC (Programmable Interface Controller) microcontroller interfaces between

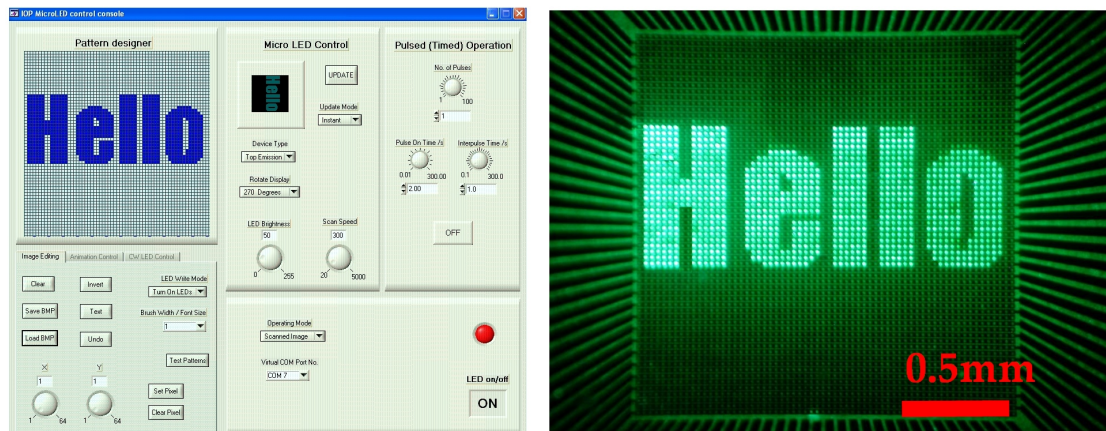


FIGURE 2.8: (l) Matrix-addressable micro-LED GUI and (r) optical micrograph image of the array output.

a computer and the driver circuitry, which allows the appropriate row and column addressing information to be passed to the driver circuitry depending on the desired output image set by the user. The circuitry, developed by V. Poher at Imperial College London based on a design by Dr. Gareth Valentine of the Institute of Photonics, is able to raster-scan the entire array, at a rate of up to 600 MHz, in order to build up an image that appears continuous and flicker-free to the human eye. Each p-contact column is addressed by a MIC5891 programmable voltage source, which provides the positive forward bias required to turn-on the micro-LED pixels. In order to compensate for the non-uniformity in performance across the array, each row is driven by MAX6971 constant-current sink drivers which ensure that the same current flows through each row even if each row has different turn-on voltage and series resistance characteristics. Thus, this constant-current driving scheme improves the emission uniformity across the array. The brightness of the array can be adjusted either by adjusting the micro-LED drive current or by use of a pulse-width modulation (PWM) scheme. User-friendly graphical user interfaces (GUIs) have been developed which allow the user to easily control the output parameters of the matrix array such as array brightness, output pattern, raster-scan speed, etc. The GUI and an optical micrograph image of the corresponding micro-LED array output is shown in figure 2.8.

2.2.2 Individually-addressable flip-chip array design

Figure 2.9 illustrates schematically how an individually-addressable, flip-chip, micro-LED array is fabricated [19]. The unprocessed LED wafer is patterned using standard photolithographic techniques (figure 2.9(a)) and individual mesa structures are defined by an ICP etch down to the n-GaN layer (figure 2.9(b)). Once the micro-LED mesas have been defined, Ni-Au spreading contacts are evaporated onto the top of each pixel and

subsequently alloyed by a rapid thermal anneal. These define the individual electrical p-contacts (figure 2.9(c)). Ti-Au is then deposited in the spaces between the pixels to act as an n-contact common to each pixel. Finally, a SiO_2 layer is deposited and patterned (figure 2.9(d)), this layer acts to electrically isolate each micro-LED pixel and protect the array from its environment.

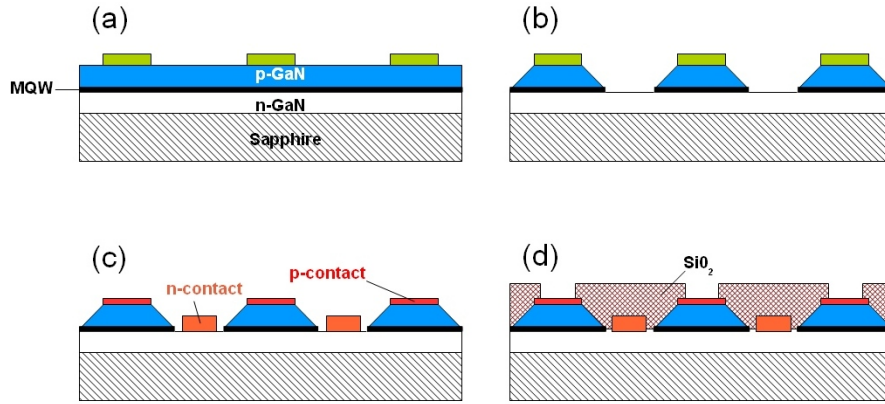


FIGURE 2.9: Process flow for fabricating individually-addressable micro-LEDs - (a) unprocessed wafer (b) individual mesa structures are formed by etching down to the n-GaN (c) p and n-contacts are deposited and (d) SiO_2 is deposited.

Various designs of individually-addressable micro-LEDs were used throughout the course of this thesis. The ‘standard’ design are 16×16 arrays of $72 \mu\text{m}$ diameter pixels on a $100 \mu\text{m}$ pitch. Micro-LED devices of this design will be referred to as 16×16 arrays during the subsequent work. Figure 2.10(a) shows a plan view of part of a 16×16 array, clearly showing the layout and dimensions of the array. A 32×32 array of $30 \mu\text{m}$ pixels on a $60 \mu\text{m}$ pitch have also been fabricated within our group but, for brevity, will not be discussed in detail here. Further detail on the 32×32 devices has, however, been reported elsewhere [19].

An alternative design of individually-addressable micro-LED array consists of an 8×8 array of micro-LED pixels, on a $200 \mu\text{m}$ pitch, which was designed specifically to be bonded onto the 8×8 array of CMOS drivers to be discussed in detail in chapter 3. Each pixel on this array has an adjacent p-contact pad allowing electrical contacts to be deposited away from the pixels themselves. The diameter of the pixels in each row ranges from $14 \mu\text{m}$ to $84 \mu\text{m}$, in $10 \mu\text{m}$ increments. The advantages of this design are improved uniformity of light output from each pixel, and that smaller micro-LED pixels can be bonded more easily. An example of such an array is shown in figure 2.10(b). The output power, emission spectra and current-voltage (IV) characteristics of the 16×16 and 8×8 devices will be given in the following sections.

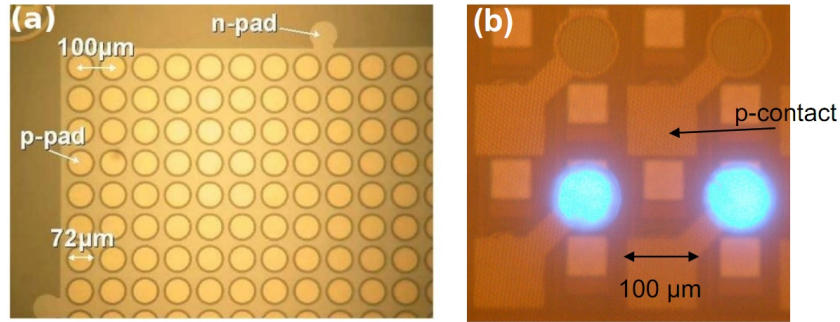


FIGURE 2.10: Micrograph image of section of (a) a 16×16 individually-addressable micro-LED array, and (b) an 8×8 array as viewed vertically down through the sapphire substrate.

2.2.3 ‘Cluster’ flip-chip array design

‘Cluster’ or ‘inter-connected’ arrays were fabricated consisting of $30 \mu\text{m}$ diameter pixels on a $35 \mu\text{m}$ pitch, defined in a similar fashion to the individual pixels of the 16×16 device discussed previously. However, here each pixel is deliberately not individually-addressable, but rather they share common p and n-contacts with a group of adjacent pixels. This allows a group of micro-LED pixels covering a relatively large area to be conveniently driven simultaneously by addressing only 2 contacts. The purpose of this design was to enable an array of micro-LEDs to be pulsed simultaneously to function as an optical pump source for a light-emitting polymer laser structure (see chapter 1). The proposed advantage of using many micro-LED pixels, rather than a single LED die of similar area, is that the micro-LED format allows for higher overall output power densities due to improved thermal management [19, 20]. In other words, a micro-LED array can provide a higher output power than a single large LED die with an identical active area. In addition, the smaller capacitance of the micro-LED pixels also helps to facilitate the short optical pulses ($\approx 1 - 10 \text{ ns}$) required for successful optical pumping of a polymer laser.

As shown in figure 2.11, there are several sub-sections in each cluster array, each containing a different arrangement of micro-LED pixels. The area of the largest square array is $520 \times 520 \mu\text{m}^2$. The process flow used to fabricate these arrays is shown in figure 2.12, and is described as follows: clusters of separate pixels are defined in a similar fashion as the individually-addressable devices described earlier, using photolithography and ICP etching (figure 2.12(a)), before p and n-contact metals are deposited (figure 2.12(b)). A SiO_2 isolation layer is then deposited (figure 2.12(c)) which crucially leaves an open aperture above each pixel. Finally, an interconnecting metal layer is deposited to electrically connect each pixel within each cluster (figure 2.12(d)).

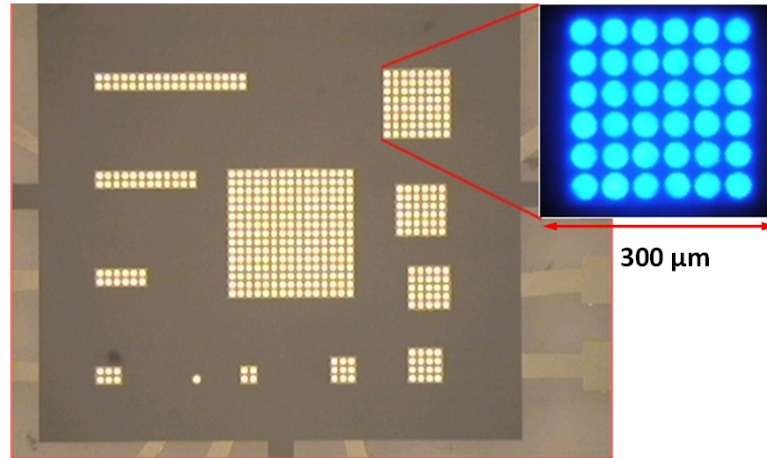


FIGURE 2.11: Optical micrograph of cluster micro-LED array, (inset) section of the array in operation. Courtesy of Dr. Z Gong.

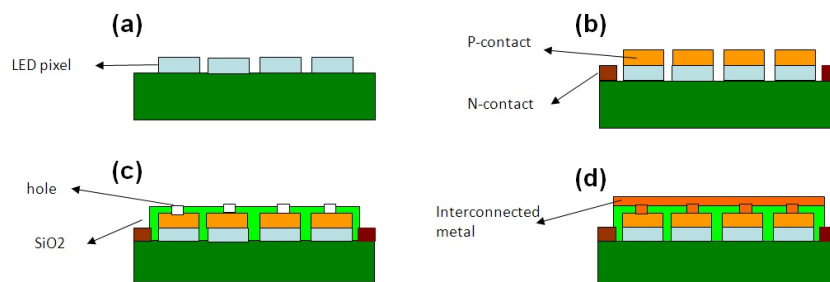


FIGURE 2.12: Process flow for interconnected micro-LED arrays, (a) individual pixels are defined by ICP etching, (b) n and p-contacts are deposited, (c) SiO_2 passivation and opening, (d) inter-connecting metal layer is deposited. Courtesy of Dr. Z Gong.

2.3 Micro-LED array performance

A summary of the characteristics of micro-LEDs which form a key part of this work is given in table 2.1. A more detailed description about these characteristics will be presented in the following sections.

2.3.1 I-V characteristics

The relationship between the current through an LED, I , and the applied bias voltage, V is known as the I-V characteristic of the device. The fundamental principles that define the I-V characteristic of an LED were described in 1.2.2. Practical devices show I-V characteristics that vary according to the properties of each particular design of LED, such as its epitaxial structure and geometry. For research-grade devices, such as the micro-LEDs presented in this thesis, some unintentional variation in device-to-device performance is to be expected due to variations in device fabrication. The I-V characteristics of micro-LED devices are measured using a probe station and parametric

TABLE 2.1: Summary of device performance.

Nominal peak emission (nm)	Array format	Pixel diameter (μm)	Turn-on voltage (V)	Max. DC output (mW) per pixel	Series resistance (Ω)
370	16×16	72	4.37	0.315	112.7
405	16×16	72	4.02	1.4	29.7
450	16×16	72	3.66	5.2	7.16
370	8×8	14, 24...84	5.86, 6.00...4.59	1.1*	127.2, 79.6...46.9
405	8×8	14, 24...84	6.79, 5.78...4.64	3.26*	124.2, 90.0...46.2
450	8×8	14, 24...84	5.94, 5.51...4.09	4.94*	50.3, 26.5...19.3
520	8×8	14, 24...84	7.31, 6.97...5.75	0.43*	103.9, 84.4...48.0

* - $84\mu\text{m}$ diameter pixel

analyser (HP4155B parametric analyzer). Figure 2.15 shows the I-V characteristics from three different individually-addressable micro-LED pixels, each with a pixel diameter of $72\ \mu\text{m}$, but having different peak wavelengths of 370, 405 and 450 nm, respectively. As explained in the previous chapter in section 1.2.2, the threshold voltage of an LED is expected to increase with increasing bandgap energy. As such, in figure 2.13 the threshold voltage is seen to increase as the bandgap energy is increased. The series resistance, R_s , which can be determined by taking the slope of the linear part of the I-V plot, also increases for the shorter wavelength devices. The relatively poorer crystalline quality of the epitaxial materials and the increased Al concentration also contribute to the higher threshold voltages and series resistances for the shorter wavelength-emitting devices [19].

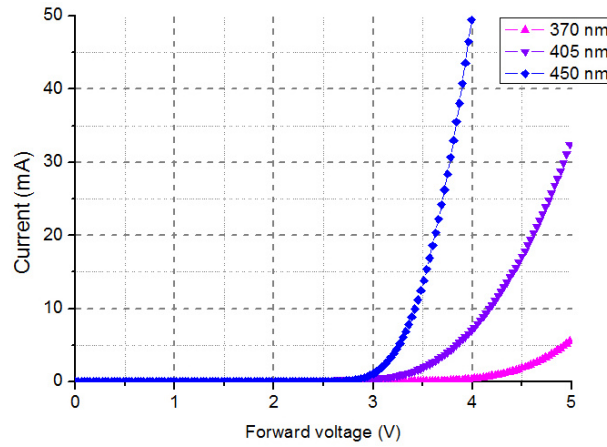


FIGURE 2.13: DC current versus voltage (I-V) curves for individually-addressable $72\ \mu\text{m}$ diameter pixels from 16×16 micro-LED arrays with peak emission of 370, 405, 450 and 520 nm.

Figure 2.14 provides the I-V characteristics from selected pixel sizes from 4 different 8×8 micro-LED devices, with peak wavelengths of 370, 405, 450 and 520 nm. Here it can

be seen that for pixels with identical epitaxial structure, V_{th} and R_s both increase as the pixel size decreases. This has been attributed to an increase in the series resistance for pixels with smaller surface areas [20].

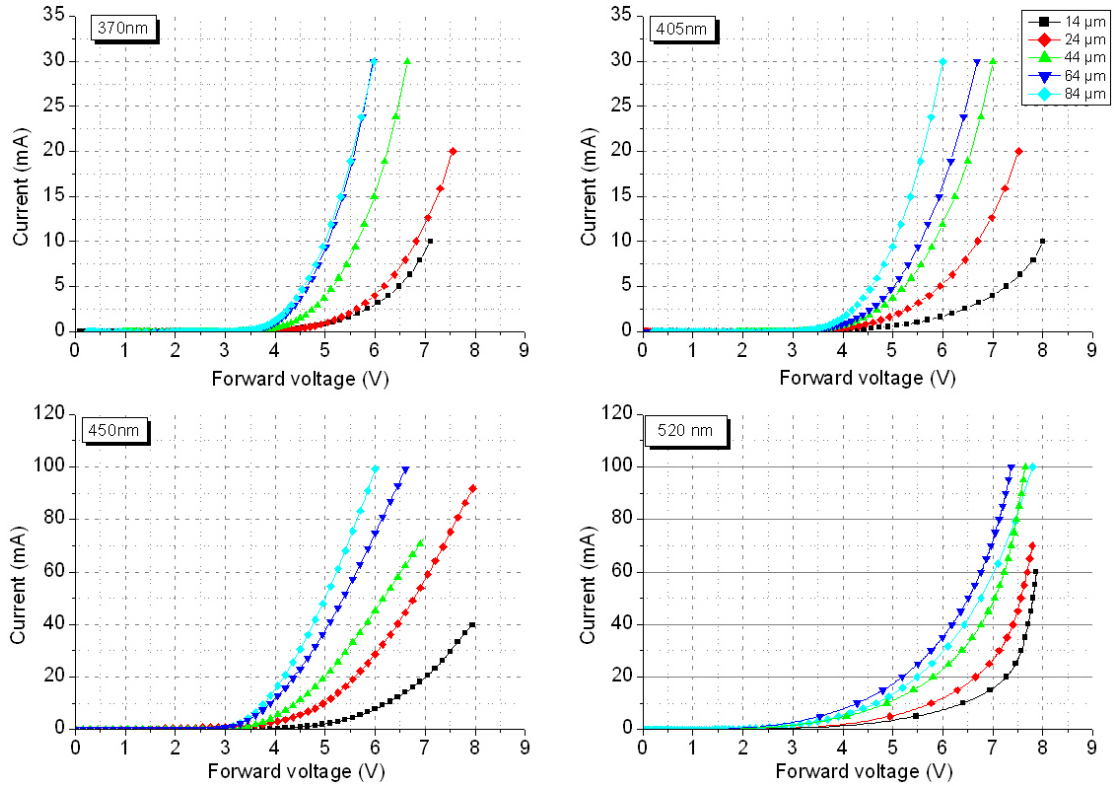


FIGURE 2.14: DC current versus voltage (I-V) curves for pixels of varying diameter in 8×8 micro-LED arrays with peak emission of 370, 405, 450 and 520 nm.

2.3.2 DC L-I characteristics

The optical output power versus injected current (L-I) performance is a fundamental characteristic of an LED, which depends on several factors including the LED die size, epitaxial structure and packaging. In order to ascertain the basic fundamental L-I characteristics of a specific design of micro-LED, the output power is measured by a calibrated photodiode (Hamamatsu, S1227-33BQ) which is placed in close proximity to the micro-LED surface. The corresponding injected current is measured by placing an ammeter in series with the micro-LED pixel under test. Figure 2.15 shows the L-I characteristics of four 16×16 micro-LED arrays, with peak emissions of 370, 405, 450 and 470 nm, respectively. These arrays are held by a printed circuit board (PCB) holder, and electrical contacts were made to individual pixels by wirebonds. As such, figure 2.15 shows the L-I characteristics of these devices with no intentional heat-sinking. With appropriate heat-sinking, the maximum output powers attainable from these devices would be anticipated to increase, as will be demonstrated in chapter 3.

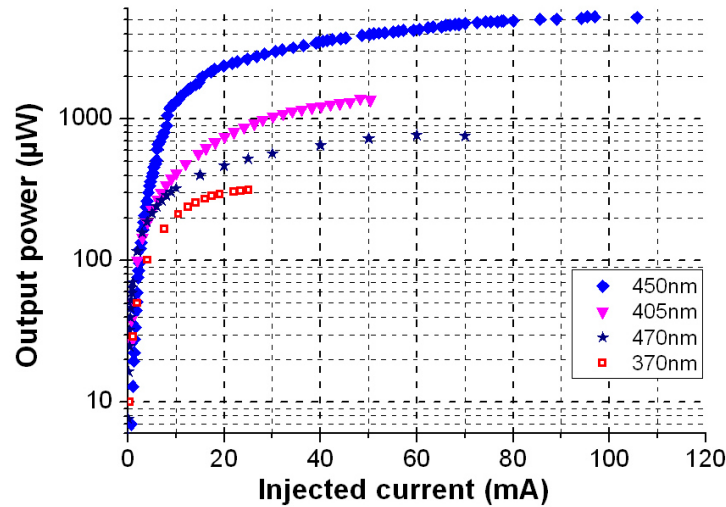


FIGURE 2.15: CW output power versus injected current (L-I) graph of individual $72\ \mu\text{m}$ diameter pixels from 16×16 arrays, with peak emissions of 370, 405, 450 and 470 nm, respectively.

It can be seen from figure 2.15 that the maximum continuous (CW) output power from a single pixel in a 16×16 array is approximately 5 mW, in the case of the 450 nm-emitting device. At 20 mA, the standard ‘calibration current’ for conventional broad area LEDs, the output power is ≈ 2.35 mW. The L-I characteristics of the pixels are also shown to vary considerably depending on the emission wavelength (and hence epitaxial structure) of the particular micro-LED array; notably the output power is reduced as the peak emission wavelength is shortened. Near-UV emitting LEDs are more sensitive to lattice defects than their longer-wavelength counterparts which have a higher indium content [21]. One explanation for this observation is that as the indium content of the epitaxial wafer is reduced as the peak emission wavelength is shortened, then there are less indium-rich clusters within the wafer to confine the carriers and prevent them from diffusing towards defects [22]. Therefore, micro-LED devices emitting at shorter wavelengths will suffer from more non-radiative recombination, making them less efficient and less powerful than their longer-wavelength emitting counterparts.

Figure 2.16 shows L-Is from selected pixels from 8×8 arrays with peak emissions of 370, 405, 450 and 520 nm, respectively. These arrays were driven by the ‘third generation’ CMOS driver chip, to be discussed in chapter 3. It clearly shows that, as may be expected, that the larger micro-LED pixels show the highest total output powers. However, if we examine the output power density (the optical power output from the pixel, divided by its active area), rather than the absolute output power from each pixel, we observe that the output power density of the smaller pixels is higher than their larger counterparts. Figure 2.17 shows L-I characteristics from 5 pixels from a single 450 nm peak-emission 8×8 device, with the pixels having a diameter varying from 14 to $84\ \mu\text{m}$. We can observe that above approximately $2\ \text{kA}/\text{cm}^2$ the output power density of

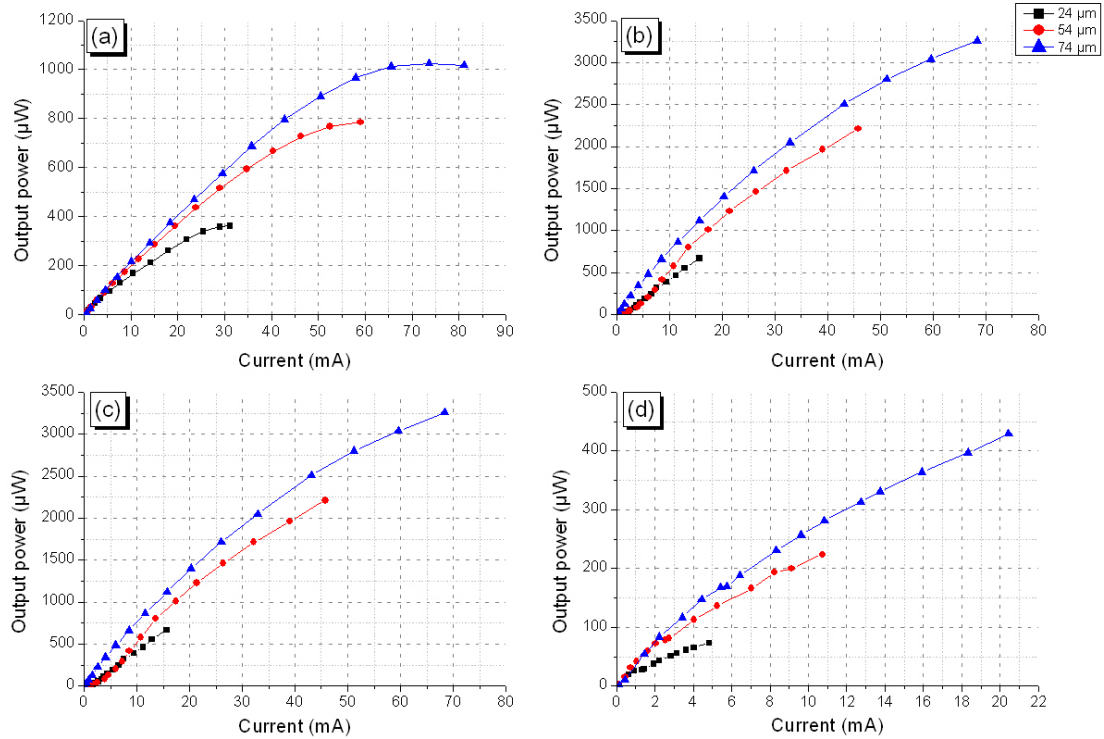


FIGURE 2.16: CW optical output power versus injected current (L-I) graph of selected pixels from 8×8 arrays with peak emissions of (a) 370, (b) 405, (c) 450 and (d) 520 nm, respectively. These arrays were driven by the ‘third generation’ CMOS driver chip, to be discussed in chapter 3.

the largest ($84 \mu\text{m}$) pixel begins to saturate and roll-over, whereas the output power densities of the smaller pixels continue to increase. A clear trend emerges, showing that the smaller the micro-LED pixel the higher its maximum output power density, and the higher the current density that can be sustained before device failure. It is worth noting that conventional broad-area LEDs for high-power illumination operate at current densities of $0.1\text{-}1 \text{ kA}/\text{cm}^2$, whilst the micro-LEDs can operate at current densities of up to $17.5 \text{ kA}/\text{cm}^2$. An explanation for this observation is that smaller pixels dissipate heat more effectively due to the increased ratio between their surface area and volume, resulting in less device self-heating at a given current density for smaller micro-LED pixel diameters [20]. Increased device operating temperatures reduce the radiative efficiency of an LED, because negative effects such as carrier leakage from active regions and non-radiative recombination are temperature-dependent [23]. It has been estimated that the maximum junction temperature for a $40 \mu\text{m}$ diameter micro-LED pixel is approximately 80 K lower than an otherwise identical pixel of $300 \mu\text{m}$ in diameter [24]. This reduced dependence of device operating temperature with injected current allows for a more efficient device that is also able to operate at higher input current densities.

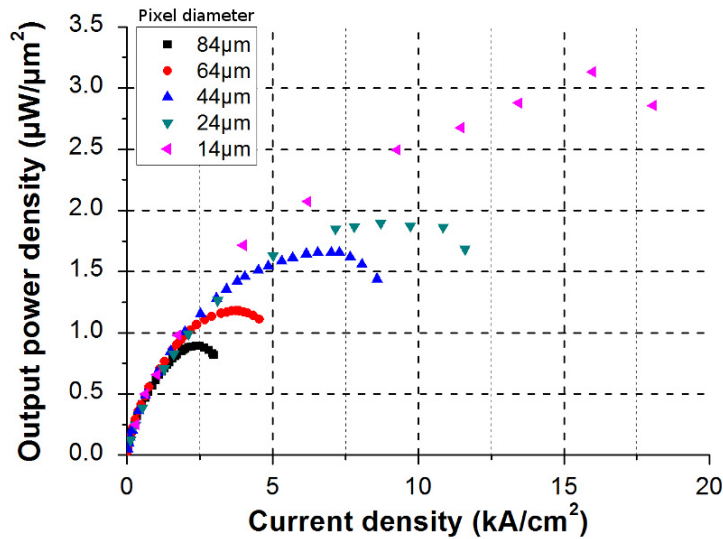


FIGURE 2.17: CW optical output power versus injected current (L-I) graph of individual micro-LED pixels for different pixel sizes, from a 8×8 device emitting at 450 nm.

2.3.3 Pulsed L-I characteristics

The ability to produce high-intensity nanosecond optical pulses from micro-LEDs is of particular interest, for example because micro-LEDs could potentially be used to pump organic semiconductor lasers (OSLs). OSLs are a type of laser, which use organic light-emitting semiconductor materials, such as the conjugated polymers introduced in chapter 1, as an optical gain medium. The resonator in an OSL can take many forms, simplified schematics of which are given in figure 2.18. The organic light-emitter can be integrated with these resonators by simple processes such as spin-coating.

There are several attractive features of OSLs. They are inexpensive and simple to process, may be readily integrated with other devices and have broadly tuneable emission throughout the visible spectrum. This makes OSLs particularly relevant to applications such as spectroscopy, sensing, data communications and displays. At present, virtually all reported OSLs are optically pumped by external laser sources, such as frequency-doubled titanium-sapphire or Nd:YAG lasers. Because of the complexity, high cost and bulk of these external sources, this pumping configuration has so far limited the practical usefulness of OSLs. Direct electrical pumping of an OSL would be extremely desirable, as this would enable compact, battery-powered OSLs to be available. However, a definitively electrically-pumped OSL has proved elusive. There are several reasons why electrically pumped OSLs are difficult to achieve, including the low carrier mobilities in organic materials, losses due to the formation of electrical contacts, and absorption losses due to the high density of injected charge carriers [12]. Electrically pumped OSLs would

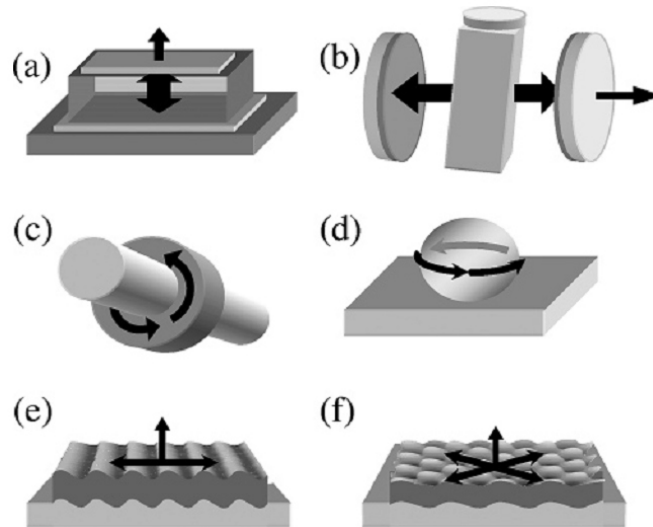


FIGURE 2.18: Schematic illustration of several forms of resonator used in OSLs. The arrows indicate the direction of the propagation of the resonant laser field: (a) planar micro-cavity, (b) Fabry-Perot laser dye cavity, (c) micro-ring resonator surrounding an optical fibre, (d) spherical micro-cavity, (e) distributed feedback (DFB) resonator and (f) 2D DFB resonator. From [12].

therefore be expected to have lasing thresholds many times higher than comparable optically pumped OSLs.

Given the difficulties in producing electrically pumped OSLs, and the desire for a compact OSL device, so-called ‘indirect electrical pumping’ offers an alternative. Indirect electrical pumping uses an electrically-driven LED to optically pump an OSL. In 2008 Yang *et al.* demonstrated the first hybrid indirectly electrically pumped hybrid polymer laser, consisting of an optically pumped OSL integrated with a nanosecond pulsed broad area LED [25]. Micro-LEDs are interesting candidates for optical pumping of OSLs as they show higher output power densities than broad area LEDs [5, 19]. The array nature of micro-LEDs could also be exploited by, for example, spatially and temporally sweeping the gain across an OSL structure by sequentially pulsing adjacent micro-LEDs along the OSL.

In order to assess whether micro-LEDs might be capable of optically pumping an OSL, commercially-available laser diode drivers were initially used to pulse micro-LED pixels at high intensities. These drivers typically operate using a high-voltage DC external supply (up to 150 V or higher) to charge a bank of capacitors. When the driver is triggered by an internal or external clock signal, then these capacitors are discharged through the micro-LED. A schematic of one of the laser diode drivers used (Directed Energy Inc., PCO-7110-40-4 Laser Diode Driver Module) is shown in figure 2.19 [26]. The circuit operates as follows: when the switch, S_1 , is open the pulse-forming capacitor C_{pfn} is charged by the input voltage $HVIN$ via the resistor R_{pfn} and the clamping

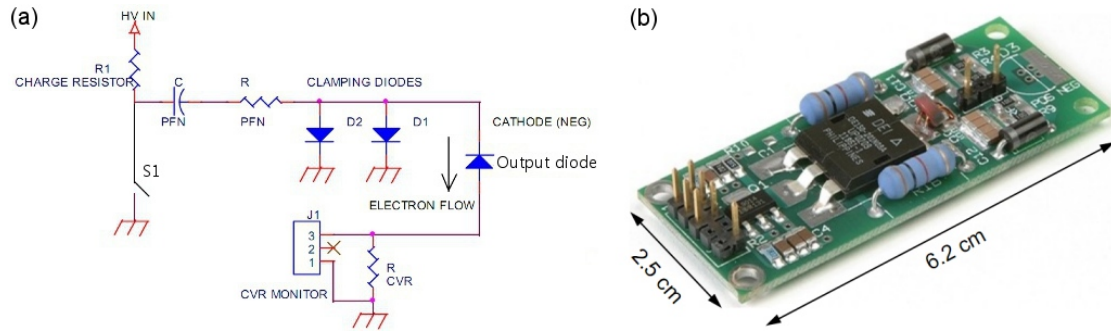


FIGURE 2.19: (a) circuit diagram and (b) a photograph of a laser diode pulse driver used to pulse micro-LEDs [26].

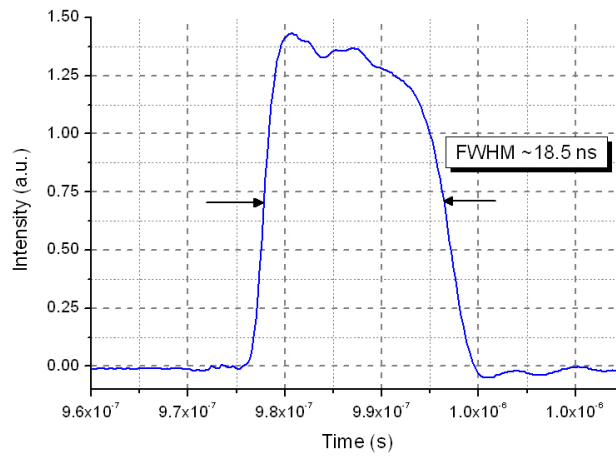


FIGURE 2.20: Representative optical output pulse from a 450 nm-emitting $72 \mu\text{m}$ diameter micro-LED pixel, as driven by the PCO-7110-40-4 laser diode driver. Repetition rate 2.5 kHz, optical pulse energy approximately 220 pJ.

diodes $D1$ and $D2$. The output diode (e.g. a laser diode or a micro-LED pixel) is reverse biased in this configuration, hence no current flows through the output device. When $S1$ is closed the diodes $D1$, $D2$ and the output diode are effectively connected in parallel with C_{pfn} . $D1$ and $D2$ are reverse biased in this case, and the output diode is forward biased. Hence, C_{pfn} rapidly discharges through the output diode, resulting in a short input current pulse through the output diode. The charge accumulated by C_{pfn} , and hence the input current pulse to the output diode, are directly proportional to the input voltage $HVIN$, allowing the intensity of the optical output pulse to be controlled. The input current to the micro-LEDs was measured using AC current probe (Tektronix CT-1). The optical output pulses were measured using a photomultiplier tube (PMT, Hamamatsu H5783P). A signal generator was used to trigger the output pulses from the micro-LED with typical repetition rates ranging from 2.5 to 10 kHz. Optical output pulses of the order of 10-35 ns FWHM were found, giving output duty cycles of approximately 0.0005 to 0.02%. A representative optical pulse 18.5 ns FWHM optical pulse is shown in figure 2.20. In order to measure the average energy per optical

pulse, and the average optical peak intensity of the pulses, the average output power of the micro-LEDs was measured using a calibrated Si photodiode. The average energy per pulse, E , and the average peak intensity, I_{peak} , were then calculated according to equations 2.1 and 2.2 respectively.

$$E = \frac{L}{f} \quad (2.1)$$

$$I_{peak} = \frac{E}{t * A} \quad (2.2)$$

where L is the average output power from the pulsed micro-LED, f is the pulse repetition rate, t is the optical pulse FWHM and A is the active area of the pixel under test. Micro-LED devices with peak emission at 405 and 450 nm were primarily investigated, as these wavelengths are a good match for the absorption spectra of several LEPs under consideration for use in producing OSLs [27]. The energy density and energy per pulse versus injected pulse current density for individual 72 μm diameter micro-LED pixels from a 16×16 arrays are shown in figures 2.22(a) and (b) for pixels with peak emission of 405 and 450 nm, respectively. The highest average peak intensities observed were 3.56 $\mu\text{W}/\mu\text{m}^2$ for 450 nm, and 2.19 $\mu\text{W}/\mu\text{m}^2$ for 405 nm. The maximum energy densities were approximately 12000 and 5900 $\mu\text{J}/\text{cm}^2$ for the 450 and 405 nm peak emission devices, respectively, corresponding to maximum pulse energies of 500 and 240 pJ. Figure 2.21 shows a comparison between the pulsed output of our micro-LED devices and reported OSL thresholds. Considering that typical state of the art thresholds for OSL range from 1-100 $\mu\text{J}/\text{cm}^2$ [28], with reported thresholds as low as 36nJ/cm² [29], then these measurements indicate that micro-LEDs are potentially suitable candidates for indirect optical pumping of OSLs. The pulsed L-I performance from various sub-arrays from a cluster micro-LED device with a peak emission at 450 nm is also given in figure 2.23, indicating that inter-connected groups of micro-LEDs allows the pulsed performance of the micro-LEDs to be scaled up to larger emission areas, with output pulse energies of greater than 2 nJ for a pulse width of ≈ 25 ns being measured. At present there is ongoing work towards demonstration of optical pumping of an OSL using a micro-LED device. This work focuses on such areas as further improving the micro-LED pulsed output powers (by, for example, improved heat-sinking), further reducing the OSL thresholds and improved integration between the micro-LEDs and the OSLs.

2.3.4 Emission spectra

The emission spectrum of an LED is determined by the product density of states, which is proportional to $\sqrt{(E - E_g)}$ for bulk semiconductor material, and the Boltzmann distribution of carriers, $\propto \exp(-E/kT)$. The intensity, I , versus energy, E can be defined

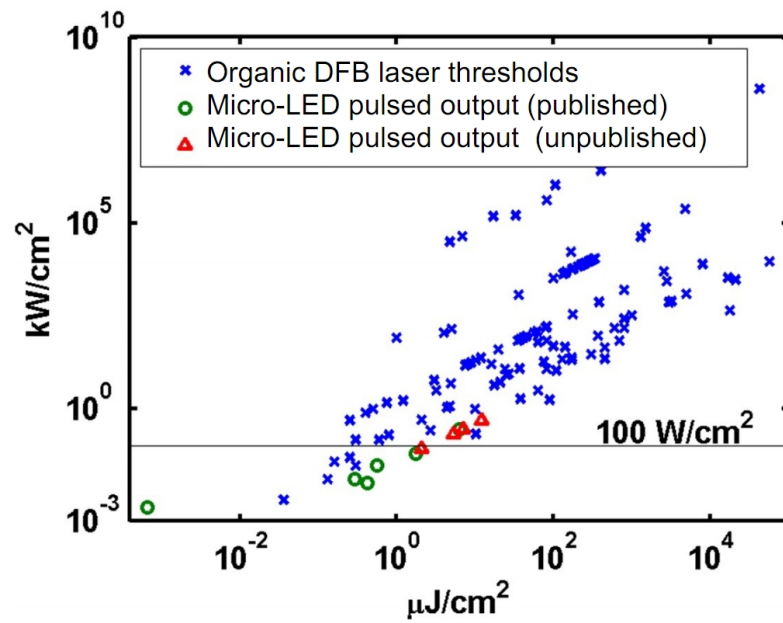


FIGURE 2.21: Comparison of micro-LED pulsed outputs and reported OSL thresholds, indicating that optical pumping of OSLs using micro-LED pixels is feasible. Figure courtesy of Mr. Johannes Herrnsdorf.

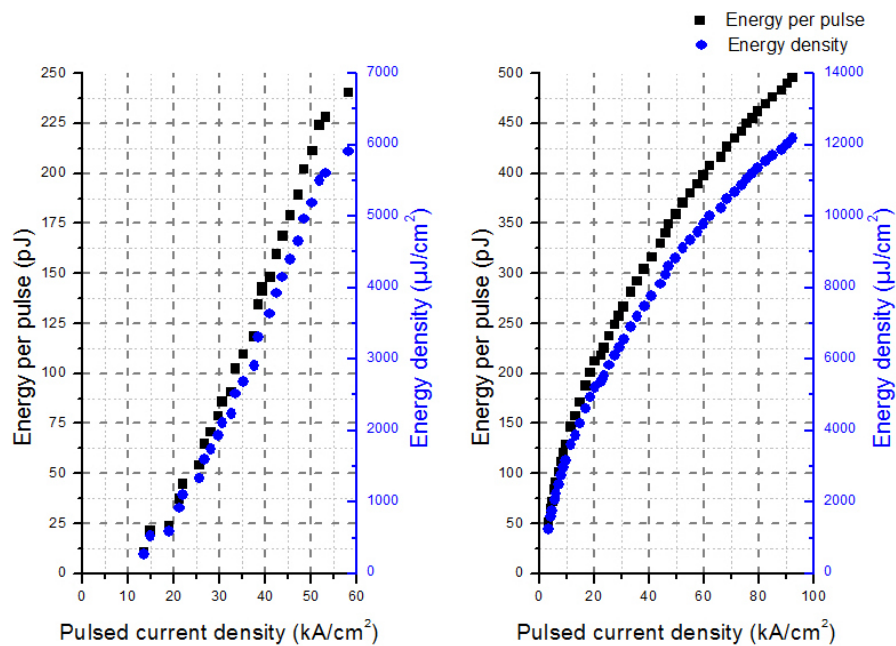


FIGURE 2.22: Pulsed L-I characteristics of $72 \mu\text{m}$ (a) 405 nm and (b) 450 nm peak emission micro-LED pixel.

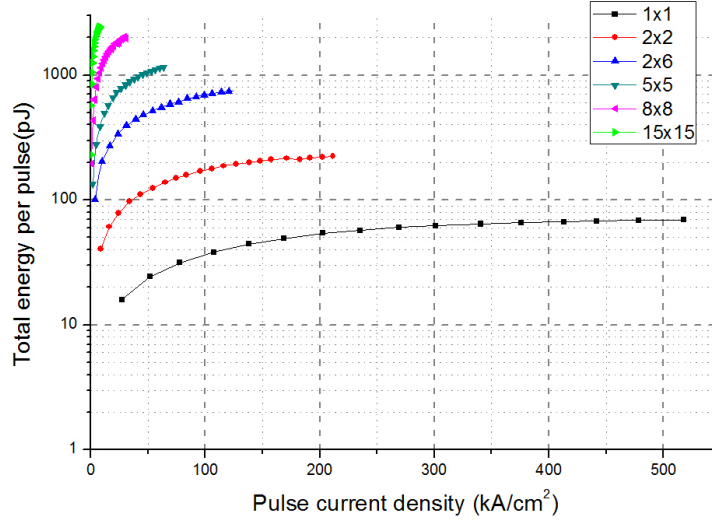


FIGURE 2.23: Pulsed L-I characteristics of sub-arrays from a 450 nm-emitting interconnected micro-LED array.

as [23]:

$$I(E) \propto \sqrt{E - E_g} e^{-E/kT} \quad (2.3)$$

where E_g is the bandgap energy in eV. Because carriers have an average kinetic energy equal to kT , the maximum energy intensity occurs at an energy above the bandgap energy, according to:

$$E = E_g + \frac{1}{2}kT \quad (2.4)$$

and the full width at half-maximum (FWHM) of the emission spectra, ΔE , is given by:

$$\Delta E = 1.8kT \quad (2.5)$$

Equations 2.3 to 2.5 show that the emission spectrum of an LED is primarily determined by the semiconductor bandgap energy, E_g and the device operating temperature. The emission spectra of micro-LED devices with different peak emission are shown in figure 2.24. These spectra were measured using an Ocean Optics USB4000 Miniature Fibre Optic Spectrometer, with a spectral resolution of ≈ 0.3 nm. Each spectrum is measured from $84 \mu\text{m}$ diameter pixels, operating at a DC current of 20 mA.

The evenly spaced peaks that are observed in the main electroluminescence peaks may be attributed to, for example, interference fringes caused by whispering gallery modes trapped within the micro-LED pixel [18]. For clarity, the emission from each device is described by the nominal peak emission wavelength as specified from the manufacturer, i.e 370, 405, 450 or 520 nm. However, as the table inset in figure 2.24 shows, the true peak emission does vary. One reason is that the tolerance of the peak emission wavelength specified by the manufacturer is typically $\pm 10\%$. The peak emission will

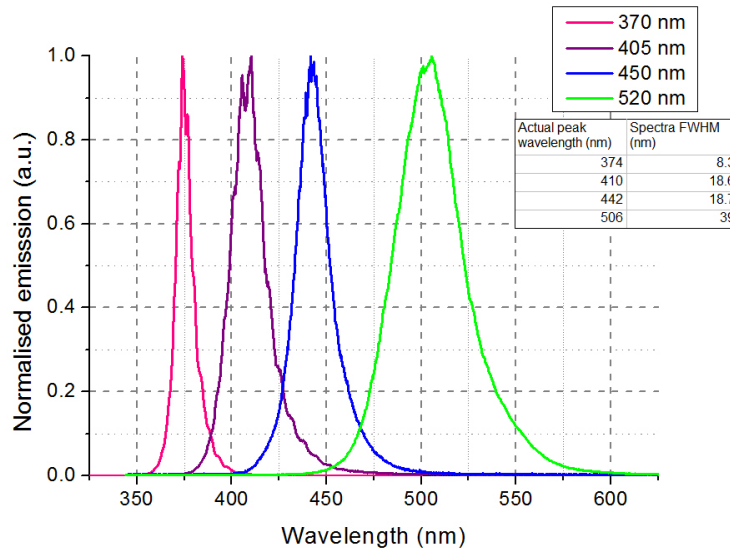


FIGURE 2.24: Emission spectra of various micro-LED pixels. Each pixel was $84 \mu\text{m}$ in diameter and was operated with a DC current of 20 mA.

also vary with operating current. A high current density a red-shift is observed which is attributed to a reduction in the bandgap energy at higher operating temperatures [24]. Two mechanisms which contribute to a blue-shift in the emission spectra at lower current densities are the band-filling effect and the screening of the quantum-confined Stark effect. The band-filling effect refers to the processes whereby the lowest levels of the conduction band and the highest levels of the valence band are first to be fully occupied by carriers. As more carriers are injected they are forced to occupy states that lie higher/lower in the conduction/valence bands. This increases the average separation in terms of energy between the electrons and holes, increasing the average energy of the photons that are subsequently emitted during recombination. Strong polarisation fields cause the electron and hole wave functions to be spatially-separated, a phenomenon known as the quantum-confined Stark effect (QCSE). This also decreases the separation in energy between electrons and holes. As more carriers are injected into the active region the strong polarisation fields are screened, counteracting the QCSE and thus blue-shifting the emission spectrum. Finally, as the strain and composition varies across an AlInGa_N wafer, devices fabricated from different sections of the wafer may show variation in peak emission.

2.4 Summary

This chapter began by introducing the concept of micro-LED arrays. These devices are fabricated by photolithography from standard LED semiconductor wafers, and consist

of arrays individual micro-emitters with sub-100 μm dimensions, compared with standard ‘broad area’ LEDs which consist of single die typically around $300 \times 300 \mu\text{m}^2$ in area. The historical development of micro-LEDs, starting with the first demonstration of 408 nm peak emission micro-LEDs reported in 2000 by H.X. Jiang’s group at Kansas State University [1], was covered in outline before the motivation for fabricating micro-LEDs was discussed. Micro-LEDs offer spatial and temporal control over a micro-scale light output pattern using simple computer control. This allows micro-scale light patterns to be imaged into a wide range of samples of interest for a wide range of applications, ranging from biophotonics [4] to mask-free photolithography [10] and optical sectioning microscopy [11]. A range of other light sources which offer similar light output capabilities were introduced, including digital micro-displays and organic LEDs. Micro-LEDs however offer several advantages over these technologies, including higher contrast, higher power densities, improved robustness against harsh operating environments and low fabrication cost.

The specific design of the micro-LEDs fabricated in our group was then presented, showing the examples of the process flows used for fabricating the devices and the layout and dimensions of the arrays. The key performance metrics of some representative arrays were presented, including the current-voltage (I-V) and output power versus current (L-I) characteristics, the nanosecond pulsed performance and emission spectra. There are a wide range of different micro-LED arrays with different device layouts, formats and peak emission wavelengths. For clarity, the performance of the devices that will be discussed later in this thesis were summarised in table 2.1.

References

- [1] S. X. Jin, J. Li, J. Z. Li, J. Y. Lin, and H. X. Jiang. GaN microdisk light emitting diodes. *Applied Physics Letters*, 76(5):631, 2000.
- [2] H. X. Jiang, S. X. Jin, J. Li, J. Shakya, and J. Y. Lin. III-nitride blue microdisplays. *Applied Physics Letters*, 78(9):1303, 2001.
- [3] I. Ozden, M. Diagne, Arto Nurmikko, J. Han, and T. Takeuchi. A Matrix Addressable 1024 Element Blue Light Emitting InGaN QW Diode Array. *Physica Status Solidi (a)*, 188(1):139–142, 2001.
- [4] H Xu, J Zhang, K M Davitt, Y-K Song, and A V Nurmikko. Application of blue/green and ultraviolet micro-LEDs to biological imaging and detection. *Journal of Physics D: Applied Physics*, 41(9):094013, 2008.
- [5] S. X. Jin, J. Li, J. Y. Lin, and H. X. Jiang. InGaN/GaN quantum well interconnected microdisk light emitting diodes. *Applied Physics Letters*, 77(20):3236, 2000.
- [6] S. X. Jin, J. Shakya, J. Y. Lin, and H. X. Jiang. Size dependence of III-nitride microdisk light-emitting diode characteristics. *Applied Physics Letters*, 78(22):3532, 2001.
- [7] P. Y. Chiou, A. T. Ohta, and M. C. Wu. Massively parallel manipulation of single cells and microparticles using optical images. *Nature*, 436:370–372, 2005.
- [8] Yi Lu, Gazell Mapili, Gerry Suhali, Shaochen Chen, and Krishnendu Roy. A digital micro-mirror device-based system for the microfabrication of complex, spatially patterned tissue engineering scaffolds. *Journal of Biomedical Materials Research Part A*, 77A(2):369–405, 2006.
- [9] A. Zarowna-Dabrowska, S.L. Neale, D. Massoubre, J. McKendry, B.R. Rae, R.K. Henderson, M.J. Rose, H. Yin, J.M. Cooper, E. Gu, and M.D. Dawson. Miniaturized optoelectronic tweezers controlled by GaN micro-pixel light emitting diode arrays. *Optics Express*, 19(3):2720–2728, 2011.
- [10] D. Elfström, B. Guilhabert, J. McKendry, S. Poland, Z. Gong, D. Massoubre, E. Richardson, B. R. Rae, G. Valentine, G. Blanco-Gomez, E. Gu, J. M. Cooper, R. K. Henderson, and M. D. Dawson. Mask-less ultraviolet photolithography based on CMOS-driven micro-pixel light emitting diodes. *Optics Express*, 17(26):23522–23529, 2009.

- [11] V. Poher, H. X. Zhang, G. T. Kennedy, C. Griffin, S. Oddos, E. Gu, D. S. Elson, M. Girkin, P. M. W. French, M. D. Dawson, and M. A. Neil. Optical sectioning microscopes with no moving parts using a micro-stripe array light emitting diode. *Optics Express*, 15(18):11196–11206, 2007.
- [12] Ifor D. W. Samuel and Graham A Turnbull. Organic semiconductor lasers. *Chemical Reviews*, 107:1272–1295, 2007.
- [13] O. Prache. Active matrix molecular OLED microdisplays. *Displays*, 22(2):49 – 56, 2001.
- [14] Z Y Fan, J Y Lin, and H. X. Jiang. III-nitride micro-emitter arrays: development and applications. *Journal of Physics D: Applied Physics*, 41(9):094001, 2008.
- [15] Z. Gong, H.X. Zhang, E. Gu, C. Griffin, M.D. Dawson, V. Poher, G. Kennedy, P.M.W. French, and M.A.A. Neil. Matrix-Addressable Micropixelated InGaN Light-Emitting Diodes With Uniform Emission and Increased Light Output. *IEEE Transactions on Electron Devices*, 54(10):2650–2658, Oct. 2007. ISSN 0018-9383.
- [16] C.-W. Jeon, K.-S. Kim, and M. D. Dawson. Fabrication of Two-Dimensional InGaN-Based Micro-LED Arrays. *Physica Status Solidi (a)*, 192(2):325–328, 2002.
- [17] H.W. Choi, C.W. Jeon, and M. D. Dawson. Fabrication of matrix-addressable micro-LED arrays based on a novel etch technique. *Journal of Crystal Growth*, 268(3-4):527–530, 2004.
- [18] H. W. Choi, C. W. Jeon, M. D. Dawson, P. R. Edwards, R. W. Martin, and S. Tripathy. Mechanism of enhanced light output efficiency in InGaN-based microlight emitting diodes. *Journal of Applied Physics*, 93(10):5978, 2003.
- [19] H. X. Zhang, D. Massoubre, J. McKendry, Z. Gong, B. Guilhabert, C. Griffin, E. Gu, P. E. Jessop, J. M. Girkin, and M. D. Dawson. Individually-addressable flip-chip AlInGaN micropixelated light emitting diode arrays with high continuous and nanosecond output power. *Optics Express*, 16(13):9918–9926, 2008.
- [20] V Adivarahan, S Wu, WH Sun, V Mandavilli, MS Shatalov, G Simin, JW Yang, HP Maruska, and MA Khan. High-power deep ultraviolet light-emitting diodes based on a micro-pixel design. *Applied Physics Letters*, 85:1838–1840, 2004.
- [21] Asif Khan, Krishnan Balakrishnan, and Tom Katona. Ultraviolet light-emitting diodes based on group three nitrides. *Nature Photonics*, 2:77–84, 2008.
- [22] Takashi Mukai, Daisuke Morita, and Shuji Nakamura. High-power UV InGaN/Al-GaN double-heterostructure LEDs. *Journal of Crystal Growth*, 189-190:778 – 781, 1998. ISSN 0022-0248.

-
- [23] E.F. Schubert. *Light Emitting Diodes*. Cambridge University Press, 2nd edition, 2006.
- [24] Zheng Gong, Shirong Jin, Yujie Chen, Jonathan McKendry, David Massoubre, Ian. M. Watson, Erdan Gu, and Martin D. Dawson. Size-dependent light output, spectral shift, and self-heating of 400 nm InGaN light-emitting diodes. *Journal of Applied Physics*, 107(1):013103, 2010.
- [25] Y Yang, G. A. Turnbull, and I. D. W. Samuel. Hybrid optoelectronics: A polymer laser pumped by a nitride light-emitting diode. *Applied Physics Letters*, 92:163306, 2008.
- [26] *PCO-7110 Laser Diode Driver Module : Installation and Operation Notes*. Directed Energy Inc., 2000. Doc 9100-0214 Rev 4.
- [27] Boon Yar Kap, Ruidong Xia, Mariano Campoy-Quiles, Paul N. Stavrinou, and Donal D. C. Bradley. Simultaneous optimization of charge-carrier mobility and optical gain in semiconducting polymer films. *Nature Materials*, 7:376–380, May 2008.
- [28] Ifor D. W. Samuel, Ebinazar B. Namdas, and Graham A. Turnbull. How to recognize lasing. *Nature Photonics*, 3:546–549, 2009.
- [29] C. Karnutsch, C. Pflumm, G. Heliotis, J. C. de Mello, D. D. C. Bradley, J. Wang, T. Weimann, V. Haug, C. Gärtner, and U. Lemmer. Improved organic semiconductor lasers based on a mixed-order distributed feedback resonator design. *Applied Physics Letters*, 90:131104, 2007.

Chapter 3

CMOS-controlled micro-LED arrays

Individually-addressable and matrix-controlled micro-LED arrays have both been presented in the previous chapter. Whilst matrix-addressing schemes are considerably easier to implement, from a physical layout and electrical-addressing point of view, they have the drawback of requiring raster-scanned operation of the array. This means that individual pixels may not be operated in true DC mode. Individually-addressable arrays however allow for complete *independent* control of each element in a micro-LED array, yielding a much more flexible device. However, independently addressing individual pixels in an array consisting of several hundred or thousand micro-LEDs is not straightforward. In this section, the design of several iterations of electronic driver chips based on Complementary Metal-Oxide Semiconductor (CMOS) technology will be presented. These represent progress towards large-scale, high-density arrays of individually-addressable micro-LEDs. All CMOS design presented in this chapter was undertaken by collaborators from Dr. Robert Henderson's group in the Institute for Integrated Micro and Nano Systems, The School of Engineering, University of Edinburgh. The design parameters, chip layout and compatibility with the micro-LED devices were, however, determined in full collaboration with our group. These chips are flip-chip bonded to the micro-LEDs using gold bump-bonds, such that individual pixels in a micro-LED array are bonded directly to their own dedicated individually-controllable CMOS driver. CMOS-controlled micro-LED arrays will be shown containing up to 64 individually-controllable micro-LED elements. The performance of each generation of chip will be discussed; DC output powers of up to 4 mW per pixel and sub-nanosecond optical pulses as short as 300 ps FWHM are shown, indicating the potential of such devices for a wide variety of applications. The limitations of each chip generation are identified and solutions implemented to overcome these limitations in subsequent designs are discussed.

Finally, the chapter closes with a summary of some possible applications of these CMOS-controlled micro-LED arrays and progress that has been made to date in demonstrating them.

3.1 Complementary Metal-Oxide-Semiconductor (CMOS) technology.

3.1.1 Metal-Oxide-Semiconductor Field Effect Transistors (MOSFETs)

Over the last 25-30 years, Complementary Metal-Oxide-Semiconductor (CMOS) has become the dominant technology used in the fabrication of electronic integrated circuits (ICs) on silicon (Si) wafers. Compared to other technologies, such as transistor-transistor logic (TTL), CMOS has the advantages of being reliable, cheap, scalable, manufacturable, more compact, requiring fewer processing steps and having lower power consumption. The term ‘CMOS’ is used interchangeably to refer both to the particular design of the circuitry involved and the related family of processes used to fabricate the devices. The nomenclature applied to the CMOS process used to fabricate a particular device refers to the smallest transistor dimensions that the process can produce and the voltage supply to the transistors. For example, a ‘5 Volt 0.35 μm CMOS process’ can fabricate transistors with minimum feature sizes of 0.35 μm , with a voltage supply of 5 V.

The basic building block of CMOS technology is the Metal-Oxide-Semiconductor Field-Effect Transistor (MOSFET). Both n and p-type MOSFETs, also known as NMOS and PMOS, respectively, are used together to implement digital logic circuitry. Simplified cross-sectional diagrams of NMOS and PMOS transistors are shown in figure 3.1. First the NMOS transistor will be considered. The NMOS transistor consists of four terminals, termed the Body (B), Source (S), Gate (G) and Drain (D). Since the body and source are typically connected together, and virtually no current flows through the body terminal, the body is generally neglected and the device can be thought of as a three terminal device. The main substrate consists of p-type Si and the source and drain wells consist of n-type Si. The source and drain regions are formed by doping them using ion implantation [1]. The gate is insulated from this substrate by a layer of SiO_2 , typically 0.05 to 0.1 μm thick [2], so negligible current can flow through the gate. By controlling the voltage between the gate and source, V_{GS} , the flow of current into the drain, i_D can be controlled. Depending on the magnitude of voltage applied between the drain and source, V_{DS} , and the gate voltage, V_{GS} , the transistor can be said to be operating in one of three regions. The first region is known as the ‘cutoff region’. An NMOS transistor

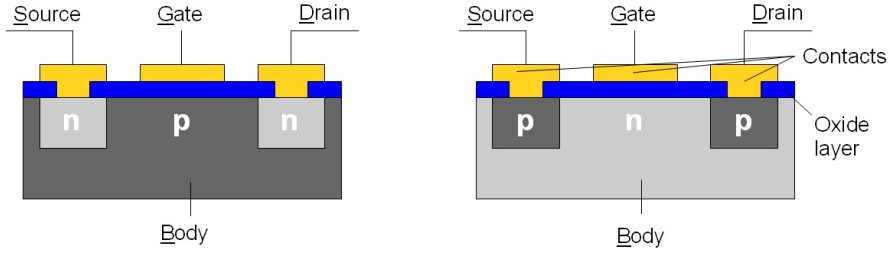


FIGURE 3.1: Cross-sectional schematics of an NMOS (l) and PMOS (r) transistor, showing the source, gate, drain and body terminals.

operating in the cutoff region is illustrated in figure 3.2(a). Consider that a positive voltage, V_{DS} is applied to the drain relative to the source, and that the gate voltage, $V_{GS} = 0$ V. In this case, virtually no current can flow into the drain terminal because the drain/body junction is reverse-biased by V_{DS} , i.e. $i_D = 0$ A. As long as V_{GS} remains below a certain threshold voltage, V_{to} then i_D will remain zero. This is the cutoff region of operation, where no current can flow into the drain terminal:

$$i_D = 0 \quad \text{when} \quad V_{GS} \leq V_{to} \quad (3.1)$$

When $V_{DS} < V_{GS} - V_{to}$ and $V_{GS} \geq V_{to}$ the transistor is operating in the ‘triode region’. When a large enough positive voltage is applied to the gate then an electric field between the gate and the main p-type body exists which repels holes from, and attracts electrons to, the layer of p-type material directly underneath the gate terminal. This layer can then be said to be inverted, i.e. it is no longer p-type, but is now n-type. This creates an ‘inversion channel’ of n-type material between the source and drain, as highlighted in figure 3.2(b). Thus, a positive bias across V_{DS} will cause a current, i_D , to flow from the source to the drain via the inversion channel. For small values of V_{DS} the current i_D is proportional to both V_{DS} and the excess gate voltage, $V_{GS} - V_{to}$. It can be seen that the NMOS transistor can be thought of as a ‘switch’, which allows current to flow between the source and drain only when the gate voltage is above a certain threshold. As the voltage V_{DS} continues to be increased, the channel charge is attracted to the drain thus depleting the inversion channel as it approaches the drain. This results in a tapering of the inversion channel, as shown in figure 3.2(c), which causes the resistance of the channel to become larger with increasing V_{DS} . The current i_D is no longer proportional to V_{DS} in this case. When V_{DS} reaches a certain level, the inversion channel becomes completely depleted at the drain. Above this value of V_{DS} , the current i_D will no longer increase at all, this region of operation is referred to as the ‘saturation region’. Characteristic current-voltage (I-V) curves of an NMOS transistor are shown in figure 3.3, showing the cutoff, triode and saturation regions of operation of the transistor. The relationship between the drain current, i_D , the gate voltage V_{GS} and the drain-source voltage V_{DS} are also clearly shown.

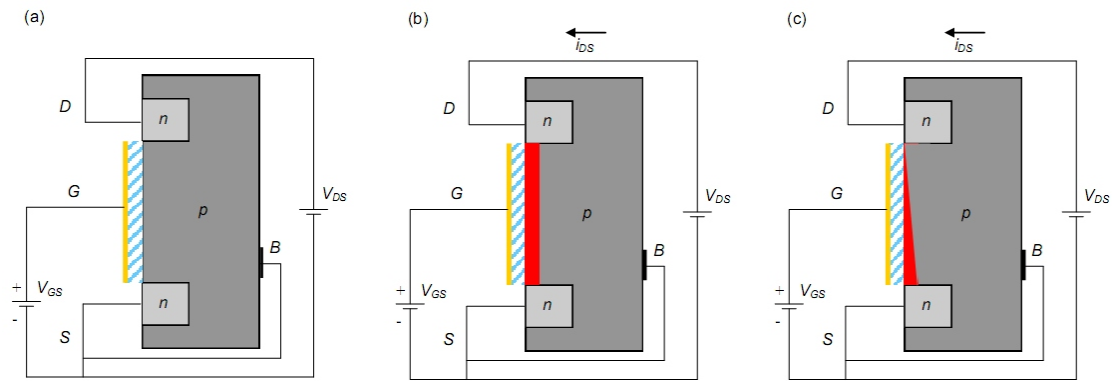


FIGURE 3.2: Schematic illustration of an NMOS transistor operating in the (a) cutoff (b) triode and (c) saturation regions. Note the tapering of the channel in (c).

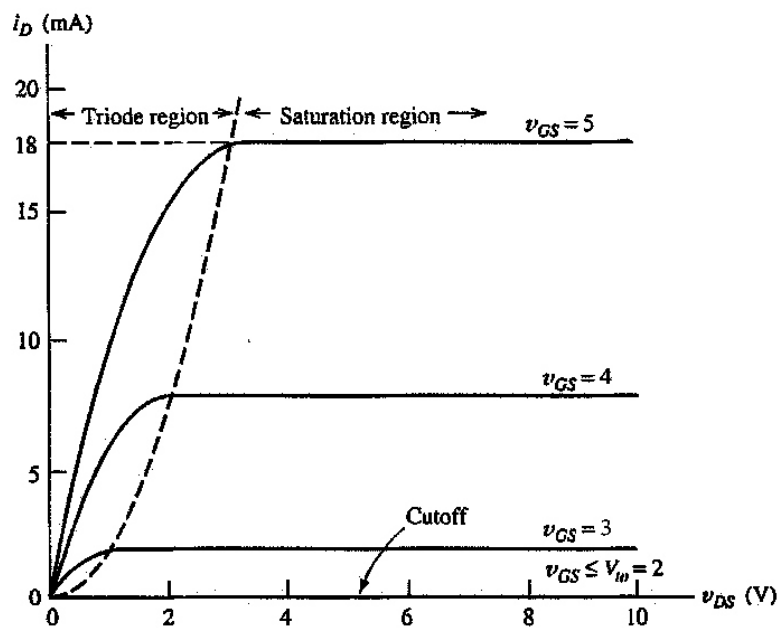


FIGURE 3.3: Characteristic current-voltage curves from an NMOS transistor. From [2].

PMOS transistors are analogous to NMOS transistors, except that the p and n-type regions are reversed in comparison to NMOS, as shown in figure 3.1. The characteristics of the two devices are very similar, but the voltage polarities are reversed. Whereas an NMOS transistor allows current to flow between the source and drain because a positive gate voltage attracts electrons to the gate to form an n-type inversion layer, the PMOS transistor instead attracts holes to the gate in order to form p-type inversion layer. In other words, an NMOS transistor conducts between the source and drain when the gate-source voltage, $V_{GS} \geq V_{to}$, and a PMOS transistor conducts when $V_{GS} \leq V_{tp}$. Thus, PMOS and NMOS transistors can be considered ‘mirror images’ of each other. The circuit diagram symbols used to depict NMOS and PMOS transistors are shown in figure 3.4. The ‘complementary’ part of the term CMOS refers to the fact that in

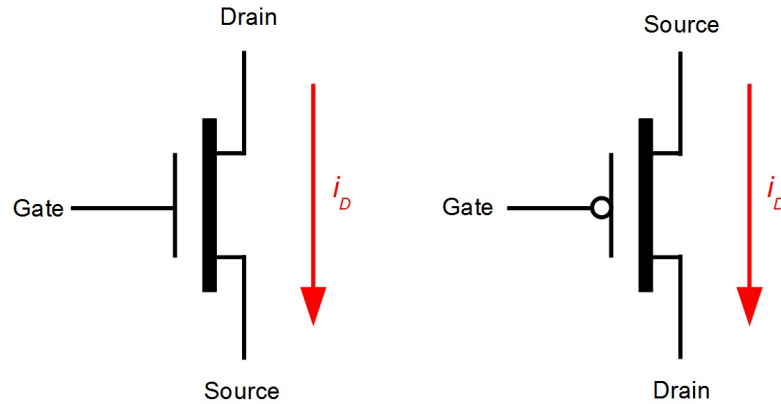


FIGURE 3.4: (l) NMOS and (r) PMOS circuit diagram symbols. The red arrow depicts the flow of the drain current, i_D .

CMOS design the symmetry and complementary functionality of the NMOS and PMOS transistors is used to design digital logic, as will be shown in the following section.

3.1.2 Basic CMOS logic gates

All of the functionality provided by the micro-LED CMOS control chips to be discussed in this chapter are controlled by digital logic gates, including element addressing, clock frequency, pulse duration, etc. We shall thus briefly discuss how some simple logic gates can be constructed in CMOS technology using a combination of NMOS and PMOS transistors.

The most simple logic gate, an inverter or NOT gate, can be constructed using one n-type MOSFET (NMOS) and one p-type MOSFET (PMOS). The inverter is a vital ‘building block’ used to build digital logic circuits. A circuit diagram of a CMOS inverter is shown in figure 3.5. V_{dd} is the positive voltage supply rail, V_{ss} is ground, A is the logic input and Q is the logic output. Logic 1 is defined as being a voltage above the threshold required to turn on/off an NMOS/PMOS transistor. Similarly, logic 0 is defined as being a voltage below the threshold required to turn off/on an NMOS/PMOS transistor. In the case where $A = 0$, the upper PMOS transistor is on, and the lower NMOS transistor is off. Therefore, there is a path from V_{dd} to Q , thus $Q = 1$. In the case where $A = 1$, the upper PMOS transistor is off, and the lower NMOS transistor is on. Therefore, there is a conductive path from V_{ss} to Q , thus $Q = 0$. From this it is clear that $Q = \bar{A}$, in other words Q is the logical inverse of A . It can also be appreciated how the PMOS and NMOS can be considered ‘complementary’, the PMOS is connected between the output and V_{dd} , the NMOS between the output and V_{ss} . The PMOS controls whether the output is connected to logic 1, the NMOS controls whether the output is connected to logic 0. Each transistor complements the functionality of the other.

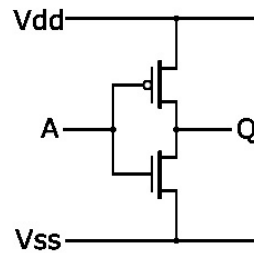


FIGURE 3.5: Circuit diagram of a CMOS inverter (NOT gate) showing the logic input A and the logic output Q .

There are several features of the CMOS NOT gate that have allowed CMOS to become the dominant technology for the fabrication of ICs. First, is the low power consumption of CMOS. CMOS inverters do not consume any static power, so CMOS inverters only consume power during output logic transitions. During a logic transition on the input of a CMOS NOT gate there will be a brief point when the voltage lies somewhere between the logic 0 and 1 levels, in which case the NMOS and PMOS transistor inputs can be said to be ‘floating’. In this state, both transistors may conduct, allowing current to briefly flow between Vdd and Vss . However, this dynamic power consumption is relatively low when compared to other technologies that must consume power continuously in order to maintain the output logic level. The second advantage of CMOS is that allows for a higher density of logic functions on a chip compared to other technologies.

PMOS and NMOS transistors can be used to implement other digital logic gates. NAND gates are a very important type of logic gate since they can be used to construct any other type of logic gate. The most basic NAND gate consists of two inputs, A and B , and one output Q . Q is equal to 1, except when when A and B are both 1, i.e. $Q = \overline{A + B}$. A NAND gate circuit diagram and corresponding truth table are provided in figure 3.6. From the circuit diagram it can be seen that the PMOS transistors are connected in parallel, while the NMOS transistors are connected in series. Only in the case when A and B both equal logic 1 will the current path from Q to Vss be made. The path from Q to Vdd is blocked by the PMOS transistors and $Q = 0$. In all other cases the path to Vss will be broken by one or both of the NMOS transistors being in the off state, and a current path from Q to Vdd will be created through one or both of the PMOS transistors. To increase the NAND gate to more than two input terminals, extra pairs of PMOS and NMOS transistors can simply be inserted into the circuit.

NAND gates and NOT gates are two of the most basic gates used in the fabrication of the various logic circuits within the CMOS control chips used to drive micro-LED arrays. The specific functionality of the circuits will be discussed in more detail later in this chapter.

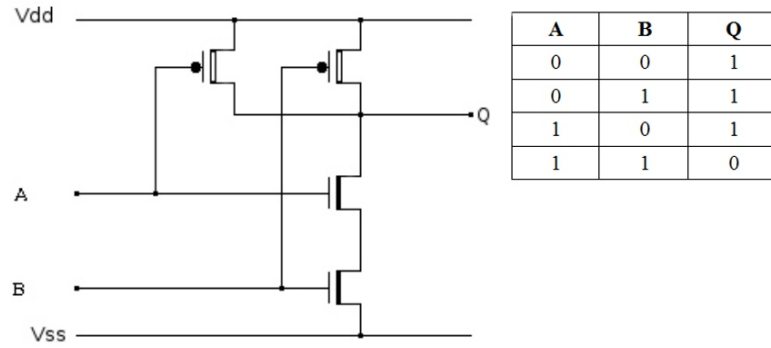


FIGURE 3.6: Circuit diagram of a NAND gate and corresponding truth table.

3.1.3 Flip-chip bump-bonding

Clearly, being able to mechanically and electrically bond micro-LED and CMOS devices together is of critical importance. There exist several chip inter-connect technologies which are potentially suitable for bonding micro-LED and CMOS devices. These have primarily been developed by the semiconductor industry, which has been looking to chip-stacking as an alternative to the shrinking of transistor dimensions as a means of maintaining Moore's Law. The methods include through-silicon vias [3], copper electroplating [4] and dielectric glue layers [5]. The method that was chosen here for integrating micro-LEDs and CMOS was flip-chip bump-bonding. This method uses gold bump bonds to provide interconnects between two chips.

The procedure of flip-chip bonding a micro-LED array to a CMOS control chip consists of two stages. The first stage involves depositing gold bump bonds onto one of the chips. Typically, the bumps were deposited onto the CMOS chip as our empirical observations revealed that the gold bumps adhered to the CMOS devices more readily than to the micro-LED. The CMOS devices were mounted into an automatic wire-bonder machine (Palomar Technologies Inc., Palomar 8000). A bonding tip was fed gold wire with a diameter of 20 μm via a capillary. As the tip came into contact with a target bonding site on the CMOS chip, a combination of thermal, electrical and ultrasonic energy was applied at the end of the bonding tip to melt the gold wire and form a gold ball with an approximate diameter of 70 μm , which attached to the CMOS chip. The machine was programmed to automatically visit each element in the CMOS array until each bond pad was populated with a gold bump bond. This procedure is illustrated schematically in figures 3.7(a) and (b). An oblique side-profile scanning electron microscope (SEM) image of a representative gold bump bond is shown in figure 3.8(a), revealing that the bumps have an 'up-turned mushroom' shape. Figure 3.8(b) is a micrograph image showing a top-down view of several bump bonds that have been deposited onto a CMOS chip.

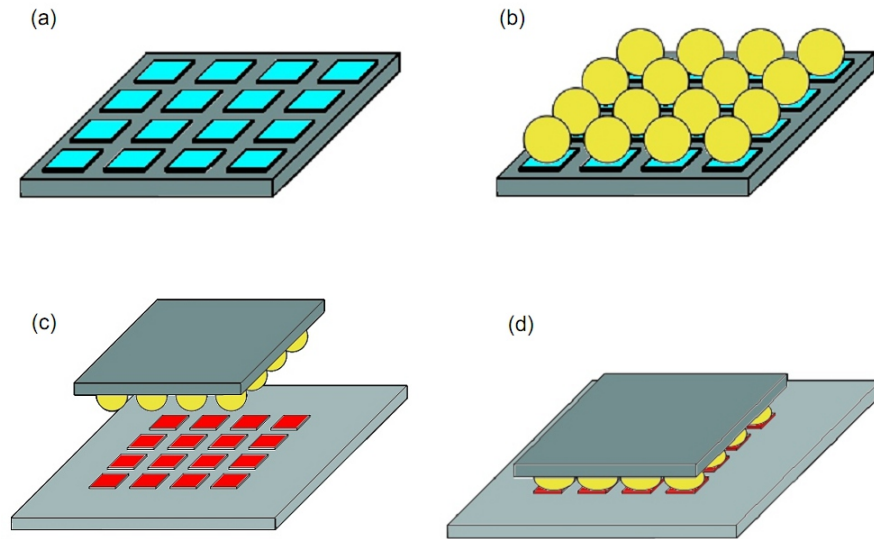


FIGURE 3.7: Schematic illustration of the flip-chip bonding process. Gold bumps are deposited onto the first substrate (a,b). This substrate is flipped and aligned above the second substrate (c) before the two substrates are held together and the gold bumps are melted by thermo-sonic bonding to create the electrical connections (d).

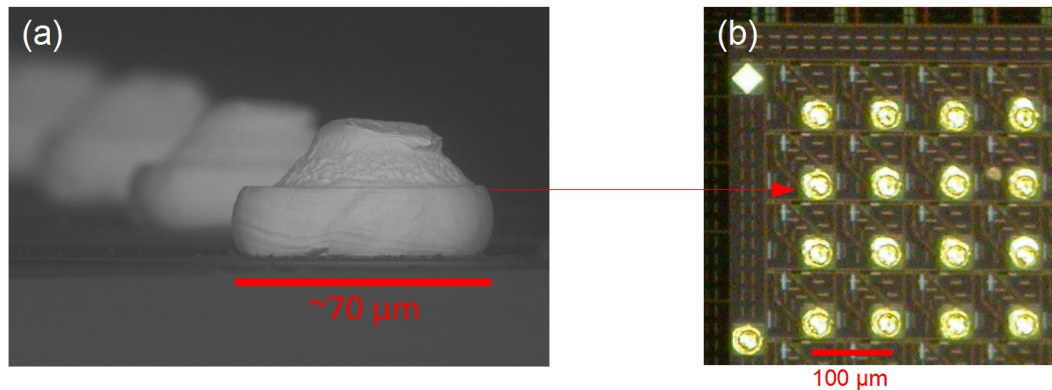


FIGURE 3.8: (a) SEM image showing gold bump bonds that have been deposited onto a CMOS control chip and (b) top-down micrograph image showing the gold bumps deposited on the CMOS chip.

Once the CMOS chip was populated with gold bump bonds it was then transferred to another machine, a flip-chip bonder (Finetech Fineplacer; Finetech, GmbH and Co. KG). The CMOS device was held flat on a heated vacuum plate and the micro-LED array to be bonded to the CMOS device was held on a mechanical arm by means of a vacuum head, such that the micro-LED metal contacts faced down. The micro-LED device was carefully aligned above the CMOS array, as shown in figure 3.7(c), before the two chips were mechanically pressed together. Ultrasonic energy (1500 mW for 800 ms) and thermal energy (80 °C rising to 200°C over 50 seconds) was then applied, melting the gold bumps situated between the two arrays and creating the bonds, as shown in figure 3.7(d). After this step, bonding is complete, although an additional optional step which flows an underfill material between the two chips may be used to provide greater

mechanical stability.

3.2 ‘First-generation’ CMOS control chip

This chapter will describe several designs of CMOS driver arrays. For clarity, the first CMOS driver chip to be used for driving micro-LEDs will be named the ‘first-generation’ device, and subsequent designs will be named ‘second-generation’, ‘third-generation’, etc. This section will detail the design and performance of micro-LED arrays bonded to the first-generation CMOS device. A micrograph image of one of these devices which has been flip-chip bonded onto a micro-LED array is shown in figure 3.9. The micro-LED array can be seen on the bottom right quadrant of the rectangular CMOS device. This CMOS device was not custom designed for driving micro-LEDs, instead it was originally intended for electrowetting, i.e. for the purpose of manipulating nano or micro-litre droplets of biological samples by means of controlling the applied voltage across an array of electrodes [6]. However, the ready availability and suitability in terms of its electrode layout and electrical drive capabilities meant that this design of chip was adopted for the first demonstration of a CMOS-controlled micro-LED array.

The CMOS device was fabricated in a $0.35\ \mu\text{m}$ high voltage CMOS process from the Austria Microsystems foundry, and consisted of a 16×4 array of electrodes, each with dimensions of $200 \times 100\ \mu\text{m}$, and each containing a single photon avalanche diode (SPAD). The operation of the SPADs will be discussed in section 3.2.1. Four metal layers were available from the CMOS process provided by the foundry, the first (i.e. bottom) two layers were used for routing signals around the chip, the third layer acted as a ‘shield’ to protect the underlying layers from the high-voltage signals above, and the fourth (uppermost) layer was patterned into an array of electrodes. The layout of the CMOS electrode array fortuitously matched the layout of the individually-addressable micro-LED arrays in the design fabricated at that time, which have a diameter of $72\ \mu\text{m}$ and a pixel centre-to-centre pitch of $100\ \mu\text{m}$, such that a 16×4 array of CMOS-bonded micro-LEDs could be fabricated, albeit that every second column of micro-LEDs had to remain unbonded because of the $200\ \mu\text{m}$ dimensions of the CMOS electrodes in that direction. The micro-LEDs to be bonded to this CMOS device had to be diced to approximately $1 \times 1.6\ \text{mm}$ in order to fit into the appropriate area on the CMOS chip. A scanning electron microscope (SEM) image of three adjacent CMOS electrodes is shown in figure 3.10, which shows the location of SPADs within the electrode area.

The driver circuit contained within each element in the CMOS array is shown in figure 3.11. It consists of three main elements. The first is an addressing element, which controls the state of the driver output, i.e. whether the output is on or off. The desired

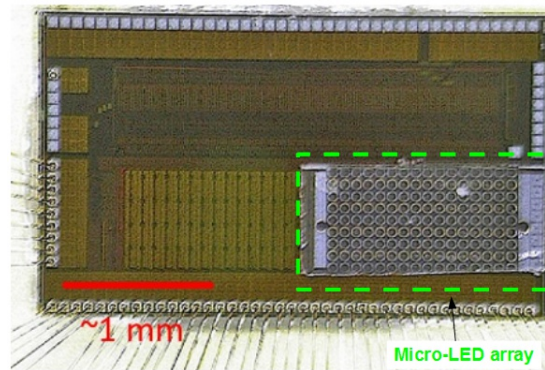


FIGURE 3.9: Micrograph image of a ‘first-generation’ flip-chip bonded micro-LED/CMOS device.

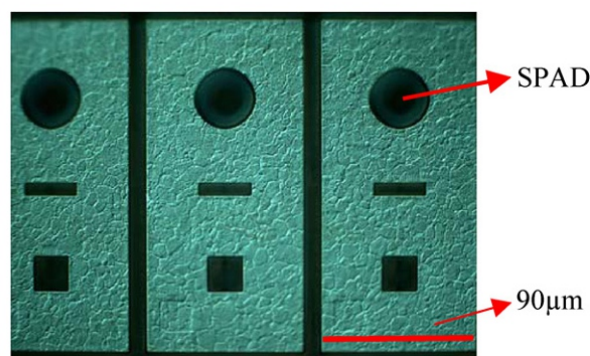


FIGURE 3.10: SEM image of three adjacent CMOS top electrodes, showing the location of the SPADs.

state of the driver is set by the user by setting the signal *Input* to be either high or low (on or off). When a particular element is addressed (when both *Row* and *Column* are high) then on the next rising clock edge the output of the D-type flip-flop, and thus the output of the driver, will match the value of *Input*. The clock is generated away from the main array of drivers, and is common to every element in the array. The D-type flip-flop allows the state of the driver circuit to be held at the desired value even when the element is no longer directly addressed.

The second part of the circuit is a timing element. Two signals, *SQIN* and *SQIND* are generated on the CMOS chip, but away from the main 16×4 array of drivers, and are broadcast to each element. *SQIN* and *SQIND* are essentially the same pulsed signal, but with a small propagation delay between the two. This propagation delay is controlled by a delay line consisting of 120 pairs of inverters. Each pair has a propagation delay of 408 ps, so by selecting via software control how many pairs of inverters is placed in the path between *SQIN* and *SQIND* the propagation delay between the two signals can be varied from 408 ps to ≈ 49 ns, in increments of 408 ps. The delay between the two signals is fed to the NOR gate in each driver to generate a short electrical output pulse, the pulse being equal to the propagation delay between *SQIN* and *SQIND*. The inputs

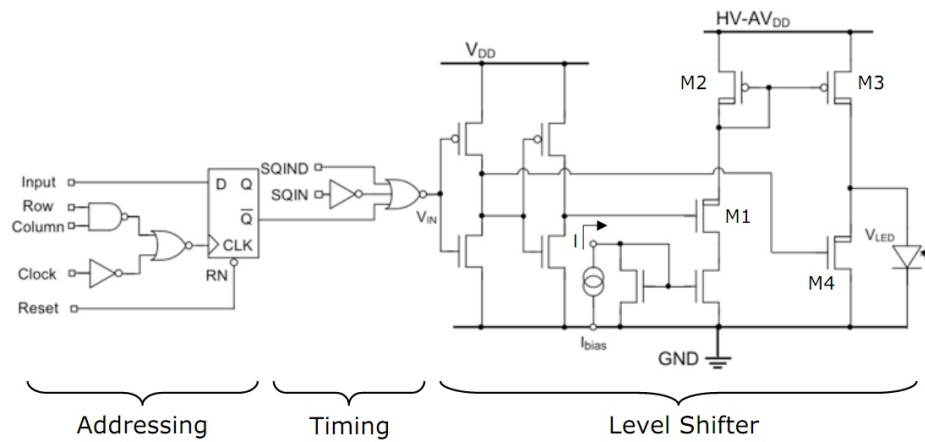


FIGURE 3.11: Current-controlled micro-LED driver circuit. Each electrode in the 16×4 CMOS array contains the same driver circuit. From [7].

$SQIN$ and $SQIND$ can be disabled, allowing the drivers to be operated using DC or square-wave signals.

The third element is a level shifter, which allows the 3.3 V output of the control logic contained in the first two sections to be capable of driving voltages of up to 50 V on the output electrode. The maximum voltage to the electrodes is set via the user-definable voltage HV_AV_{DD} , the current drawn by a micro-LED for a given value of HV_AV_{DD} depends on the individual I-V characteristic of each micro-LED. In addition, the current supply, I_{bias} , can be used to control the maximum current the driver element will supply, and is controlled globally by the transistor M_1 . I_{bias} is then ‘mirrored’ to each micro-LED pixel via the current mirror transistors M_2 and M_3 . The current drawn by each micro-LED pixel will be limited *either* by I_{bias} or by HV_AV_{DD} . In summary, the pixel addressing, pulse duration and mode of operation are controlled via a software interface, whereas the current and voltage bias to the micro-LED pixels are controlled via variable resistors on board the device motherboard or by an external DC power supply.

3.2.1 Single photon avalanche diodes (SPADS)

As already mentioned, each electrode in the 16×4 array contains a single photon avalanche diode (SPAD). As shown in figure 3.10, the SPAD in each electrode is contained within the circular gap in the electrode metal. SPADs are essentially p-n avalanche photodiodes which are reverse biased above their breakdown voltage, a mode of operation commonly referred to as the Geiger mode. In Geiger mode, prior to breakdown the diode remains in a zero current state for a relatively long time, of the order of milliseconds [8]. During this time, a very high electric field exists in the p-n junction, forming an avalanche multiplication region. An electron-hole pair, generated within the avalanche

multiplication region by an incoming photon, will be greatly accelerated by the high electric field and generate secondary carriers by impact ionisation. These secondary carriers can generate even more carriers by the same process, thus a large current pulse can be generated very rapidly by the SPAD in response to the incoming photon. Thus, the output of a SPAD is a train of short pulses which indicate the arrival times of photons at the SPAD. The avalanche breakdown process is illustrated in figure 3.12.

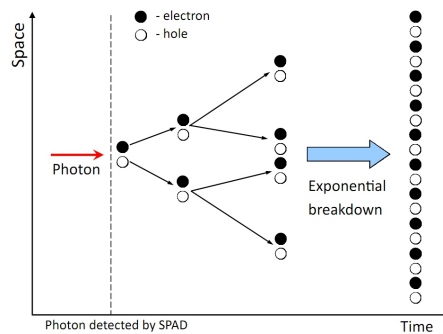


FIGURE 3.12: Illustration of the generation of an avalanche breakdown current within a SPAD by the process of impact ionisation.

A schematic of the SPAD design implemented in this CMOS driver chip is shown in figure 3.13. The p+/deep n-tub junction provides the avalanche multiplication region, which is surrounded by a relatively lightly-doped p-type ‘guard ring’. The guard ring acts to reduce electric field gradients at the periphery of the SPAD, helping to ensure that multiplication occurs across the whole SPAD planar region rather than at the edges of the SPAD and reducing the likelihood of premature avalanche breakdown [9]. Guard rings also help to reduce electrical crosstalk caused by adjacent circuits injecting current into one another [10]. The active region of each SPAD is approximately $10\ \mu\text{m}$ in diameter. After an avalanche breakdown occurs, an electronic quenching circuit reduces the voltage at the diode below the threshold voltage for a short time, in order to halt the avalanche breakdown. The SPAD is subsequently recharged, after which it is ready to detect another photon. The time between breakdown and being ready to detect another photon is known as the SPAD ‘dead time’, and is 40 ns for the SPADs implemented in this CMOS device. Timing jitter is defined as the statistical fluctuation in the time delay between the arrival of a photon and the subsequent output pulse, and is given as 100 ps for these SPADs [11]. It is important to note that avalanche breakdowns are not always triggered by incoming photons. Thermally-generated electron-hole pairs within the junction can also trigger avalanches and are indistinguishable from avalanches generated by photons. The dark count rate (DCR) defines the temperature-dependent rate at which these thermal avalanches occur and is specified as 10 Hz at room temperature for these SPADs [9].

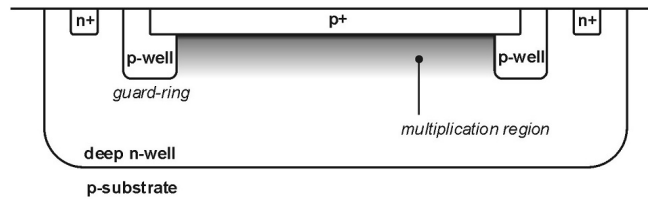


FIGURE 3.13: SPAD cross-section, from [9].

SPADs have been implemented onto this CMOS control chip as they are able to provide optical feedback. During operation, all SPADs within the 16×4 array are operational, however the output from only one SPAD is observed at any given time. As will be demonstrated in section 4.3, one application of this optical feedback involves using the SPADs to detect fluorescence from a sample that has been optically excited by the micro-LED array driven by the same CMOS device. SPADs are particularly useful for such time-correlated applications, as they provide extremely accurate information about the arrival time of detected photons. SPADs are also much more compact than other single-photon detectors such as photo-multiplier tubes (PMTs), allowing miniaturised systems to be devised.

3.2.2 Device performance

Two types of 16×16 micro-LED arrays, having peak emission wavelengths of 370 and 470 nm, respectively, were flip-chip bonded to the ‘first-generation’ CMOS device using the bonding process introduced in section 3.1.3. The pixels were all of $72 \mu\text{m}$ diameter. This section will summarise the performance of these devices and discuss some of the performance limitations that were observed. A 470 nm-emitting device can be seen being operated in DC mode in figure 3.14, displaying an ‘IoP’ pattern, thereby confirming that this CMOS driver array allows the output pattern of an individually-addressable micro-LED array to be controlled.

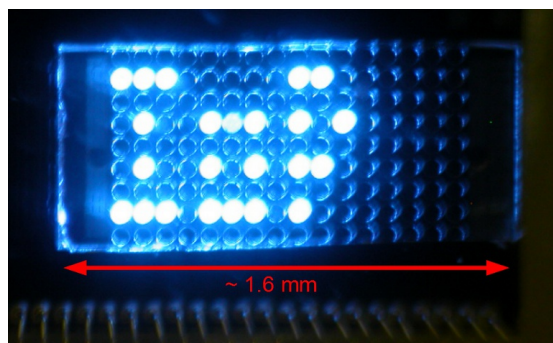


FIGURE 3.14: A CMOS-driven 470 nm peak emission wavelength micro-LED array displaying an ‘IoP’ output pattern.

The L-I characteristics from a selected pixel from each array are shown in figure 3.15. This reveals that the highest DC optical output powers achieved from a single $72\ \mu\text{m}$ diameter micro-LED pixel are 10 and $180\ \mu\text{W}$ for the 370 and 470 nm-emitting arrays, respectively. The electrode voltage, HV_{AVDD} , was set to a maximum of 15 and 25 V for the 370 and 470 nm devices, respectively. This figure also reveals that the maximum current that could be supplied to the micro-LEDs was approximately 4.5 mA. At higher currents, the element would fail and no longer emit light. Recalling the L-I characteristics of the ‘bare’ micro-LED pixels presented in section 2.3.2, figure 2.15, these pixels should be able to be driven with up to 25 mA for the 370 nm device, and 70 mA for the 470 nm device. Therefore, this failure was attributed to failure of the CMOS drive circuitry rather than the micro-LEDs. Figure 3.16 shows the maximum power obtained from a selection of pixels across each array, when each pixel is provided with the same maximum current (2 and 2.5 mA, for the 370 and 470 nm devices, respectively) and voltage (15 and 25 V for the 370 and 470 nm devices, respectively) inputs. It reveals clearly that there were some issues with array uniformity. Some micro-LED elements did not emit any light at all, their failure to do so being attributed to partial failure of the flip-chip bonding process. The variation in performance between operational pixels was attributed to variation in the effective series resistance of the micro-LEDs, a variation which itself was tentatively attributed to variations in the quality of the bump-bond electrical contacts from pixel to pixel, because the unbonded micro-LED arrays were highly uniform as verified using a probe station. A slightly different series resistance from micro-LED pixel-to-pixel would place different source resistances onto the current mirrors in each CMOS driver circuit in the array, resulting in each micro-LED sourcing different bias currents despite each being driven by the same driver circuit design and input parameters.

For many potential applications, such as time-resolved fluorescence lifetime measurements [12] or optical pumping of organic light-emitting polymer structures [13], the ability to produce very short optical pulses of the order of a few nanoseconds or less is vital. As mentioned previously, the drivers in this CMOS array can provide electrical pulses which range from 408 ps to 48 ns, in steps of 408 ps. However, due to the fact that this CMOS array was not designed for the purpose of driving micro-LEDs and was not optimised for driving the relatively large load capacitance of the micro-LEDs (which was measured to be $\approx 3\ \text{pF}$ for a $72\ \mu\text{m}$ diameter pixel), optical pulses as short as 408 ps were not obtained from any micro-LEDs driven with this CMOS device. Figure 3.17 illustrates the shortest and longest optical pulses obtained from the 370 nm-emitting micro-LED device. These pulses were measured using the time-correlated single-photon counting (TCSPC) technique, to be discussed in detail in section 4.2. The shortest pulse was $1.1 \pm 0.18\ \text{ns}$, with the longest pulse being $47.9 \pm 0.18\ \text{ns}$. The uncertainty in the

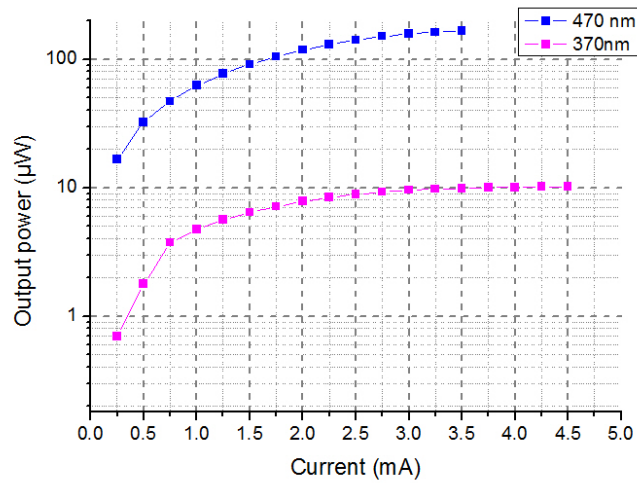


FIGURE 3.15: L-I characteristics of CMOS-driven micro-LEDs emitting at 370 and 470 nm. Micro-LED pixel diameter is $72 \mu\text{m}$.

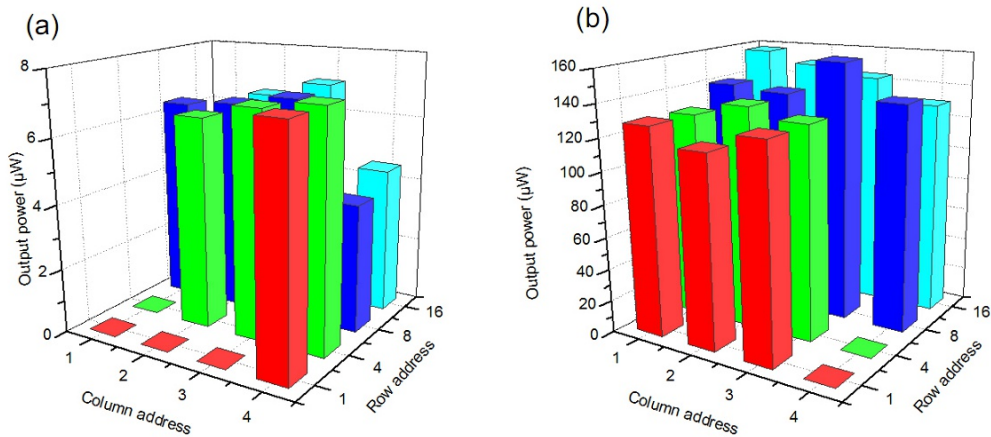


FIGURE 3.16: Output power uniformity for selected elements across 16×4 arrays emitting at (a) 370 and (b) 470 nm.

pulse duration arises from the transit time spread of 180 ps from the PMT used in the measurements (Becker & Hickl, GmbH, PMH-100). These results were reported in [11].

3.2.3 Discussion

Micro-LED arrays have been presented where a 16×4 array of pixels can be individually addressed by local CMOS drivers. The micro-LED arrays and CMOS devices were bonded together successfully using a flip-chip bonding process utilising gold bump-bonds. To our knowledge, this was the first demonstration of an electronically-controlled individually-addressable micro-LED array and indeed the first AlInGaN LED of any type to be driven by CMOS.

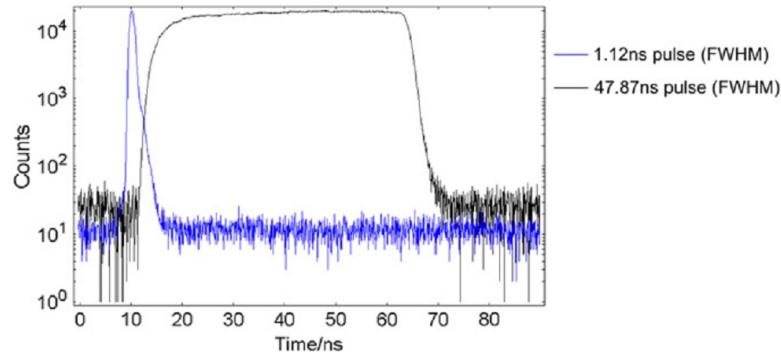


FIGURE 3.17: Longest and shortest output pulses obtained from a 370 nm emitting CMOS-driven micro-LED array. Pulse widths are 47.9 and 1.1 ± 0.18 ns, respectively.

It was found that the maximum output power from the micro-LED pixels was limited by the performance of the CMOS driver. Sub-nanosecond optical output pulses could not be obtained due to the large load capacitance of the micro-LEDs. However, bearing in mind that this CMOS device was not designed for the purpose of driving micro-LED arrays, then some limitation in performance was to be expected. Furthermore, despite the limited performance of these devices they are still suitable for certain applications, including a proof-of-principle demonstration of a single-chip time-resolved fluorescence lifetime measurement system, as will be presented in section 4.3.

Following on from the analysis of these ‘first-generation’ CMOS/micro-LED devices, a new custom-designed 16×16 array of CMOS drivers was produced specifically for the purpose of driving the individually-addressable micro-LED arrays and will be discussed in the following section.

3.3 ‘Second-generation’ CMOS control chip

Following the success of the first-generation CMOS/micro-LED devices, a new custom-designed ‘second-generation’ CMOS control chip was fabricated. For reasons to be discussed shortly, the second-generation CMOS devices all failed after flip-chip bonding to micro-LED arrays, despite the CMOS chips fully functioning electrically prior to bonding. A re-designed ‘third-generation’ chip was then fabricated to overcome the issue of device failure and since it maintained virtually the same circuitry as the second-generation chip, the circuitry design will be covered in the subsequent section. This section will therefore summarise the physical layout of the second-generation chip, discuss the mechanisms behind the device failure and the modifications made to subsequent chip designs to avoid these problems recurring.

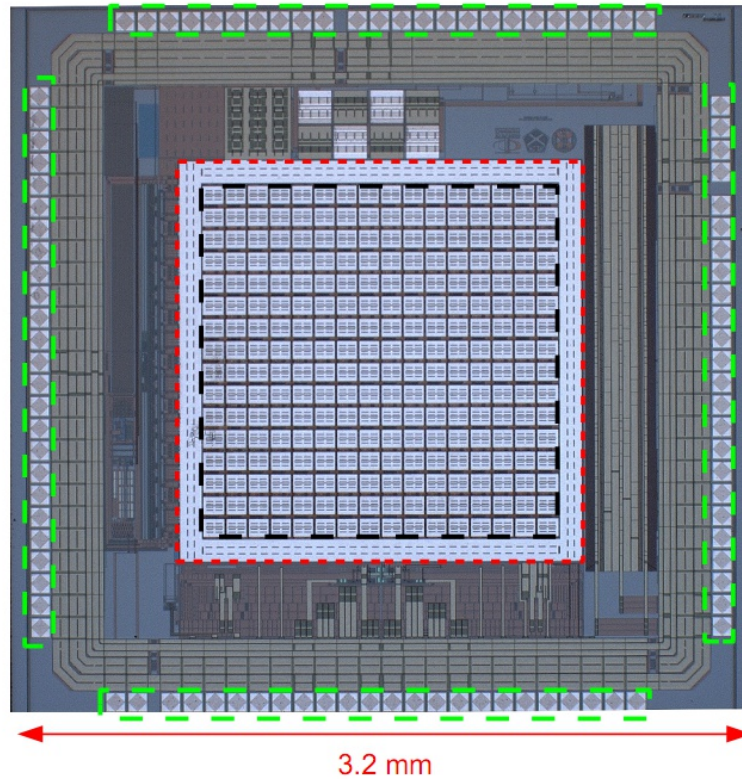


FIGURE 3.18: Top-down micrograph image showing the layout of the second-generation CMOS chip. The main 16×16 array is circled in black, the ground ring in red, and the wire-bond pads in green.

The second-generation CMOS design was implemented in a standard $0.35 \mu\text{m}$ CMOS technology from Austria Microsystems, rather than a high voltage process as with the previous design. The device consisted of four metal layers, the bottom three being used for driver logic and signal routing, and the top layer being patterned into an array of electrodes for connecting to the micro-LED array. The main electrode array consisted of a 16×16 array of $100 \times 100 \mu\text{m}^2$ electrodes, specifically chosen to exactly match the layout of the 16×16 micro-LED arrays. In principle this provided every micro-LED element in the array with its own driver, allowing for full control of all 256 micro-LEDs in the array. A top-down micrograph image of a second-generation CMOS control chip is shown in figure 3.18. In the centre of the chip, indicated by black dashes, is the main 16×16 array. It is surrounded by a ground ring, shown with red dashes in figure 3.18, for connecting with the micro-LED n-contacts. Bonding pads, to allow the chip to be bonded out to a chip carrier, are situated at the edge of the array and are highlighted in green.

Early electrical tests indicated that the second-generation chips were operating fully as expected. These tests were conducted prior to any flip-chip bonding process. However, after subsequently bonding the CMOS devices to micro-LEDs a short circuit between the global input voltage and global ground signals was observed for all arrays, causing

the devices to fail. These signals are physically located on metal layers 3 and 4 (Metal 3 and Metal 4) on the CMOS chip. Figure 3.19 is a cross-sectional diagram of the second-generation CMOS chip, showing the different metal layers and inter-metal dielectric (IMD) insulating layers between them. A short circuit between Metal 3 and Metal 4 would indicate that IMD 3 was damaged during the bump-bonding process, causing Metal 3 and Metal 4 to come into contact. Because the signals on Metal 3 and Metal 4 are common to the whole array, one single short circuit caused by the bump-bonding process would render the entire device inoperable, not just one driver element. One possible explanation for why this chip failed during bonding, but the first-generation chip did not, is that the top-most metal layer on this chip is only 925 nm thick, compared to 2800 nm on the first-generation chip. This extra thickness of top metal may have provided extra mechanical strength. From this experience, it was concluded that placing circuitry underneath bonding sites was a rather naive approach. Although placing circuitry under bonding sites is possible [14], a more cautious approach was favoured for the re-designed chip. As such, the third-generation CMOS chip provided dedicated stacks of metal with no underlying circuitry and bonding sites. This approach proved successful and the re-designed chip will be discussed in detail in the following section.

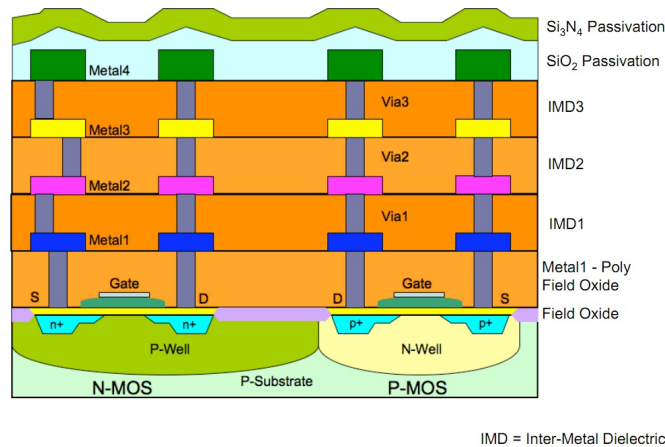


FIGURE 3.19: Schematic cross section of the ‘second generation’ CMOS device wafer. Shorting between Metal 3 and Metal 4 was observed, indicating damage to inter-metal dielectric 3 during the flip-chip bonding process. From [7].

3.4 ‘Third-generation’ CMOS control chip

After the experience of chip failure with the second-generation CMOS devices, a re-designed chip was fabricated. It was fabricated in a $0.35\ \mu\text{m}$ 5 V CMOS technology from Austria Microsystems. The driver circuitry on the ‘third-generation’ chip was virtually identical to that of the previous design. The key difference was that instead of bonding onto the top metal layer of a multi metal layer stack, dedicated bond pads were

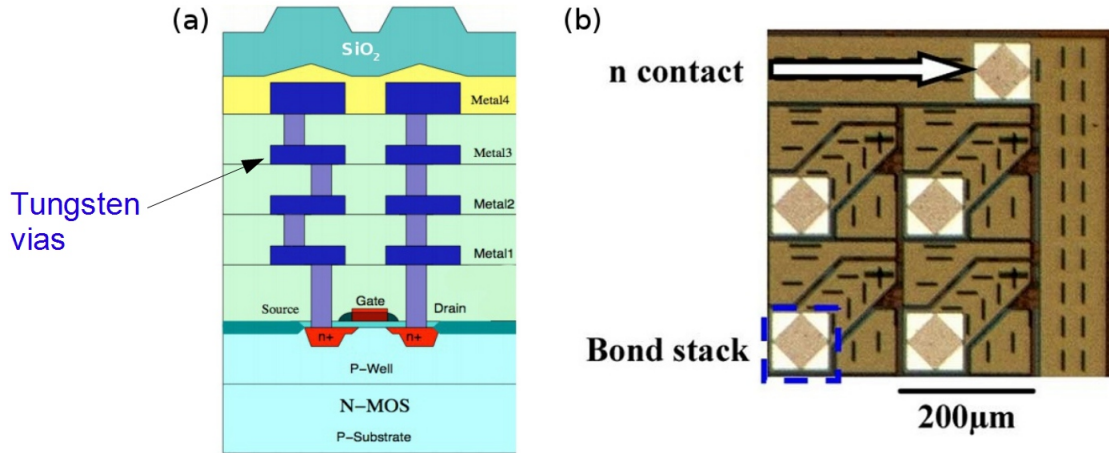


FIGURE 3.20: (a) Schematic cross-section of ‘third-generation’ CMOS chip, showing tungsten bond vias, and (b) micrograph image of a part of the actual CMOS chip showing the dedicated bonding sites at the surface of the chip.

used instead. These dedicated bond pads consisted of tungsten vias, which propagated vertically through the entire chip. Figure 3.20(a) shows a cross-sectional schematic of the third-generation device, showing that the tungsten vias form a solid column of metal through the chip. Bump bonds are placed on the top surface of the tungsten vias. Figure 3.20(b) shows part of the surface of the chip, highlighting the $100 \times 100 \mu\text{m}^2$ area of the dedicated bonding sites. The advantage of these dedicated bonding columns is that they provide excellent mechanical stability. However, since these bond pads each have a footprint of $100 \times 100 \mu\text{m}^2$, and no circuitry can be routed through them or underneath them, this leaves less room for the actual driver circuitry. As a consequence, the third-generation CMOS device consisted of an 8×8 array of drivers, each with an overall area of $200 \times 200 \mu\text{m}$. This contrasts with the previous chip, which had a 16×16 array of drivers, each with an overall area of $100 \times 100 \mu\text{m}$. The layout of the third-generation chip was chosen to match the layout of the 16×16 micro-LED arrays, however only every second row and column of micro-LEDs could be connected to a CMOS driver, i.e. $3/4$ of the micro-LED array area is not used.

A top-down micrograph image of one of the third-generation CMOS chips is shown in figure 3.21. The main 8×8 array is shown with black dashes, with the surrounding ground ring shown in red. Wire-bond pads are shown in green and are located at the edges of the chip. The same flip-chip bonding procedure as the previous designs was used for this third-generation chip. Table 3.1 summarises the physical and electrical specifications of the CMOS chip.

The driver circuit implemented in the main 8×8 array is shown in figure 3.22. The addressing circuitry is implemented using 3.3 V logic and is shown on the left. The elements of the array are addressed in an identical manner to that described for the

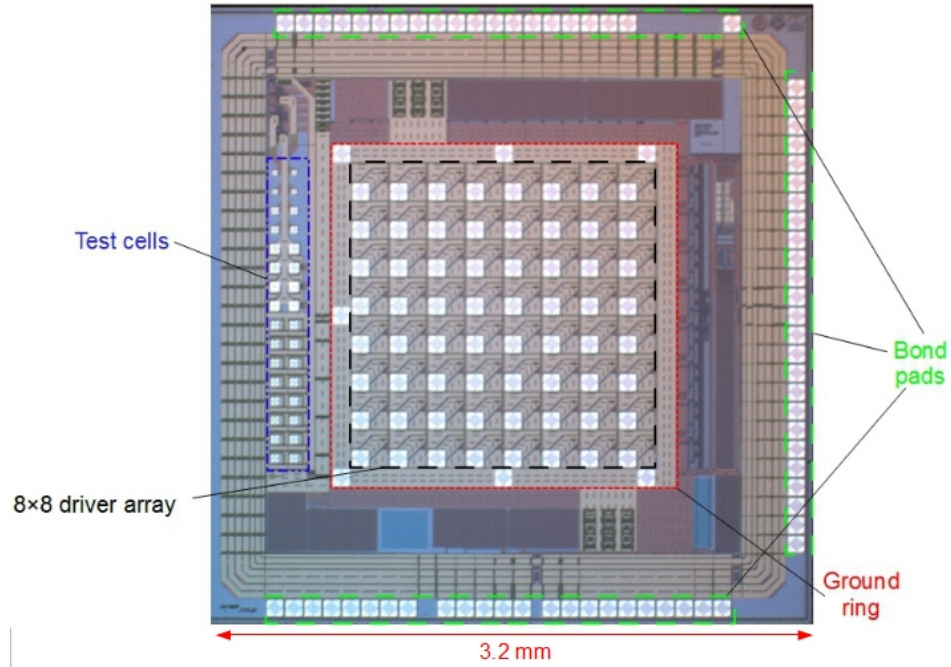


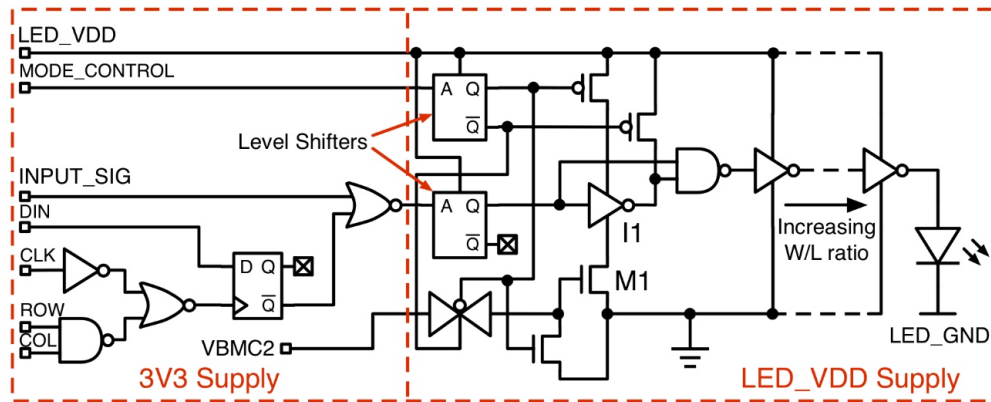
FIGURE 3.21: Optical micrograph image of the ‘third-generation’ CMOS chip.

TABLE 3.1: Summary of ‘third-generation’ CMOS chip.

Chip dimensions	$3.2 \times 3.2 \text{ mm}^2$
Array size	8×8
Driver pitch	$200 \mu\text{m}$
Maximum current (per driver)	236 mA
Maximum voltage	5 V
Electrical pulse duration	0.3 to 48 ns
Internal clock range	7 to 800 MHz

first-generation device in section 3.2. All the driver input signals were based on 3.3 V logic. The output of each driver is then subsequently level-shifted to the user-definable LED_VDD , which can be up to 5 V. The signal $Mode_Control$ controls the output mode of the driver. When $Mode_Control$ is high, the driver will follow $Input_Sig$. $Input_Sig$ can be a DC signal from the chip itself, an on-chip voltage-controlled oscillator (VCO), or an external signal fed from off-chip. When $Mode_Control$ is low the driver operates in pulsed mode, and will generate a short electrical output pulse. The operation of the VCO and the short pulse generation circuitry will be discussed in separate sections.

One key feature of the chip design is that the ground terminal of the micro-LED, LED_GND , is physically separate from the ground of the main CMOS device, GND . This means that by connecting the positive terminal of an external DC power supply to GND , and the negative terminal to LED_GND , LED_GND can be shifted to be negative with respect to GND . This effectively allows forward voltages of greater than the 5 V

FIGURE 3.22: Driver circuit implemented in the main 8×8 array.

maximum that can be supplied by LED_VDD to be applied to the CMOS-controlled micro-LEDs. For example, if $LED_VDD = 5\text{ V}$ and LED_GND is biased with -2 V with respect to GND , then the total forward bias across the micro-LED will be $5 - (-2) = 7\text{ V}$. This is an important feature, given the relatively high turn-on voltages of GaN-based LEDs (cf. chapter 2).

The CMOS chip also contains a voltage-controlled oscillator (VCO), capable of supplying a clock signal to the other circuitry. The principle of operation the VCO will be discussed in further detail in section 3.4.1. As well as being directly driven by the VCO, each of the 8 columns in the main array was capable of using the output from an on-chip linear feedback shift register (LFSR) as their input. The LFSRs provide pseudo-random bit patterns, mimicking data, a feature intended for testing the optical data transmission capabilities of the arrays. A final on-chip circuit which could be used to provide inputs to the CMOS drivers was a short pulse generation circuit. The operation of this circuit is somewhat different to that of the first-generation chip and will be discussed in section 3.4.2.

A key feature of several of the CMOS driver sub-circuits to be discussed is the ability to control the transition time of a logic gate, i.e. the time it takes for the gate to change output logic levels. NMOS and PMOS transistors have depletion capacitances between their source and drain wells and the main body of the substrate, and the time taken for these capacitances to charge/discharge essentially defines the transition time of the transistors. By controlling how much current can flow through the source and drain, we may control the time these depletion capacitances take to charge or discharge, and hence we may control the transition time of logic gates. Controlling the transition times of logic gates in this manner is achieved in the third-generation CMOS chip by use of a ‘current-starving’ transistor. An example of a current-starving transistor being used to control the flow of current through an inverter is shown in figure 3.23. Recalling from section 3.1.1 that the current that can flow through the source-drain path of a

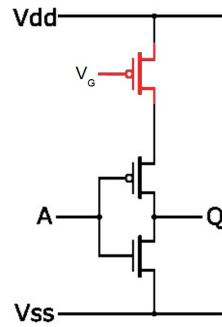


FIGURE 3.23: Example of a current-starving transistor (red) used to control the flow of current through an inverter.

transistor is dependent on the gate voltage, then by varying the voltage V_G in figure 3.23 the current that can flow between the source-drain terminals of each transistor can also be controlled. In this manner, the transition time of the inverter can be controlled by controlling the voltage, V_G .

As shown within blue dashes in figure 3.21, to one side of the main array is a 2×8 array of ‘test cells’. A schematic layout of the test cells is shown in figure 3.24. The test cells were on a $100 \mu\text{m}$ pitch, allowing them to be bonded to section of an existing 16×16 micro-LED array. The cells consisted of different designs of drivers than the main array, having bond pads of 25, 35 and $50 \mu\text{m}$ in diameter, respectively. The purpose of the test cells was to investigate whether bond pads with smaller area could be used in future designs. Smaller bond pads would allow the pitch of the drivers to be reduced and/or allow additional circuitry to be added to each driver. A micro-LED array was successfully bump-bonded to all of the CMOS drivers in the test cell array, indicating that bonding micro-LEDs to smaller CMOS bond pads was feasible. As a result, for the subsequent fourth-generation CMOS design, the bonding pads for each CMOS driver were shrunk from $100 \times 100 \mu\text{m}^2$ to $50 \times 50 \mu\text{m}^2$. The reduction in area required for bond pads allowed the fourth-generation array to be scaled up to a 16×16 array on a $100 \mu\text{m}$ pitch, as compared to the third-generation CMOS 8×8 array on a $200 \mu\text{m}$ pitch.

3.4.1 Voltage-controlled oscillator (VCO)

A voltage-controlled oscillator was included to provide an on-chip clock, capable of supplying a clock signal to the other circuitry. The advantages of generating a clock signal on-chip include removing the need for e.g. an off-chip crystal oscillator, potentially reducing system complexity and cost. Due to the capacitance associated with device packaging and bonding wires, it is also not trivial to generate high frequency clock

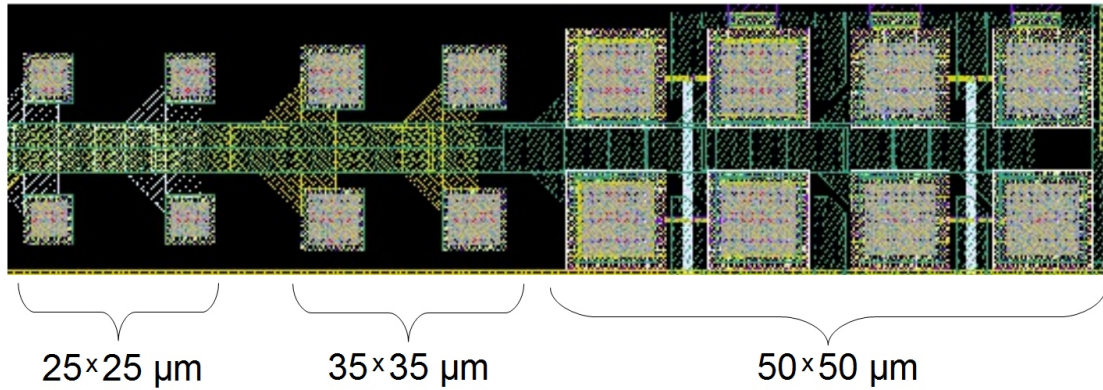


FIGURE 3.24: Layout of the test cell array.

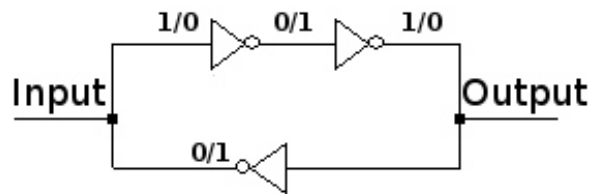


FIGURE 3.25: Circuit diagram of a ring oscillator.

signals off-chip and supply them to the device, making on-chip generation of high-speed clock frequencies preferable.

The VCO used in this case is known as a ‘ring oscillator’, a simple example of which is shown in figure 3.25. It can be seen that the output of each of the three inverters is connected to the input of the next inverter in the loop. If the output of the first inverter is 0, the output of the next will be 1, and the output of the third will be 0 which will force the first inverter to 1 causing the cycle to repeat indefinitely. Assuming that the inverters are identical, then the output of the ring oscillator will be a square wave with a 50% duty cycle. The frequency of the ring oscillator output will be determined by the propagation delay through each inverter, in other words by the length of time it takes for the output logic level transitions of the inverters.

The frequency of the VCO operation is given by the equation [10]:

$$f_{osc} = \frac{1}{n * (t_{lh} + t_{hl})} \quad (3.2)$$

where t_{lh} and t_{hl} are the low to high and high to low logic level transition times, and n is the number of transistors in the ring oscillator.

The ring oscillator on board the third-generation CMOS chip is voltage-controlled (making it a VCO) by the implementation of current-starving transistors. A voltage, denoted

VCO_VBIAS , is controlled off-chip. VCO_VBIAS is the gate voltage to the current starving transistors within the ring-oscillator. By adjusting the gate voltage of these current starving transistors the transition times of the inverters, and hence the VCO output frequency, could be controlled. The output frequency of the VCO could optionally be divided by 0, 4, 16 or 64 times using a digital divider circuit. The core frequency of the VCO could be varied from approximately 450 to 800 MHz, with 7 MHz being the lowest frequency obtainable by use of the 64 times digital divider. An SMA port on the driver board was available, which allowed the VCO output to be monitored for triggering and synchronisation purposes.

3.4.2 Pulse generation circuitry

As with the previous designs, each driver was capable of generating sub-nanosecond output pulses. A simplified circuit diagram and timing diagram is shown in figure 3.26 [15]. The input signal, $Input_Sig$, is a digital input that triggers the optical pulses. The source of this input can be an external trigger, or it may be the internal VCO clock output. In the example in figure 3.26, $Input_Sig$ is a digital square wave with a 50% duty cycle. $Input_Sig$ is fed directly to one of the input terminals of a two-input NAND gate. $Input_Sig$ is also fed into an inverter, whose output Inv_Input_Sig is fed to the other terminal of the NAND gate. Because of the finite propagation delay through the inverter, Inv_Input_Sig is delayed with respect to Inv_Input , as indicated by the red lines in figure 3.26. Due to this delay there is a short period, equal to the propagation delay through the inverter, where both Inv_Input and Inv_Input_Sig are equal to logic 1. Recalling the NAND gate truth table from figure 3.6, it is evident that short electrical output pulses from the NAND gate will occur with the same frequency as the input trigger, $Input_Sig$, with a pulse width that is determined by the propagation delay through the inverter. The pulsed NAND gate output is used to provide the pulsed electrical input to the micro-LED pixels.

The inverter shown in figure 3.26 also has a current-starving transistor, labelled M1 in the circuit diagram shown in figure 3.22, which allows the propagation delay through this inverter to be controlled by an off-chip bias voltage. By adjusting the gate voltage to this current-starving transistor between approximately 0.9 to 3.2 V, the electrical pulses can be adjusted between approximately 250 ps to 40 ns.

3.4.3 Driver board and interface

In order to drive this generation of CMOS-controlled micro-LED array, a test board was developed. This board is shown in figure 3.27. On the main motherboard are a bank

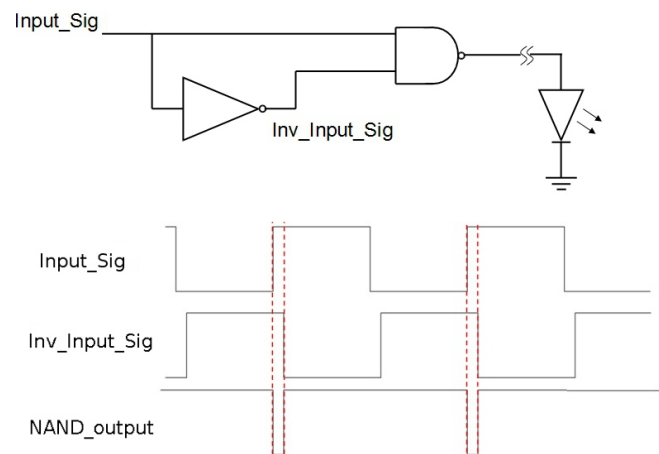


FIGURE 3.26: Circuit and timing diagrams of the sub-nanosecond electrical pulse generator.

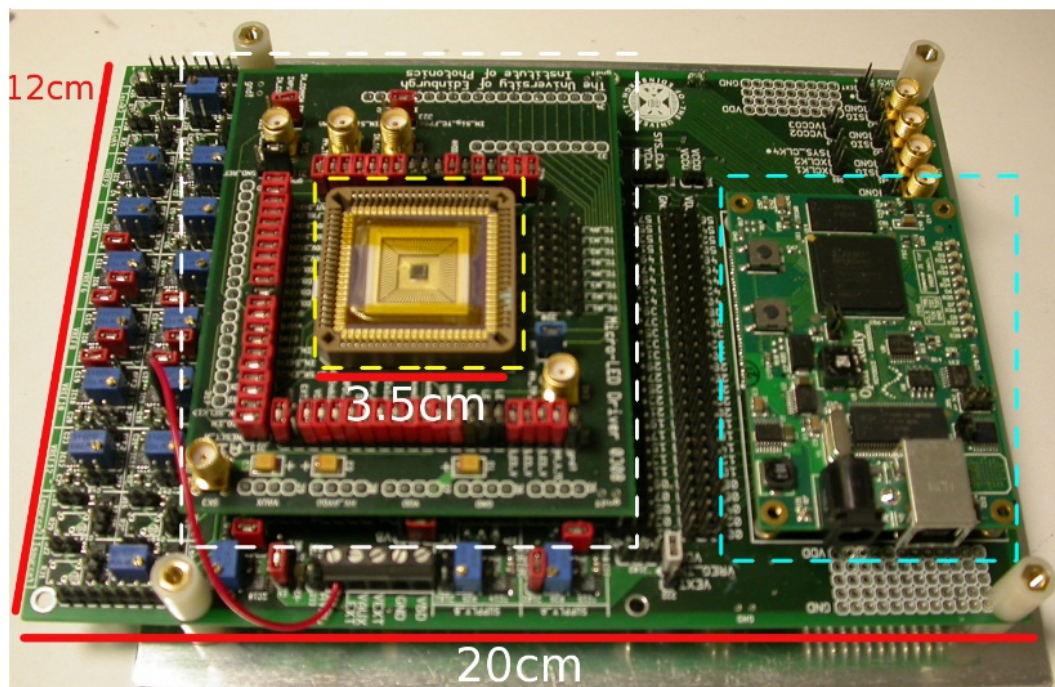


FIGURE 3.27: Photograph of the driver board used for testing the CMOS-controlled micro-LEDs. Attached to the motherboard is the FPGA board (cyan dashes), the daughter card (white dashes) and the CMOS/micro-LED chip itself (yellow dashes).

of variable resistors, which can be seen on the left side of the board in figure 3.27. The variable resistors can be adjusted by the user in order to determine the main control voltages applied to the CMOS chip which are used to define the micro-LED forward bias, the VCO clock frequency and the optical pulse duration. A field-programmable gate array (FPGA) module (Opal Kelly, XEM3010-1500P) is attached to the motherboard (cyan dashes in figure 3.27). The FPGA module interfaces with a computer via a universal serial bus (USB) interface in order to receive instructions from the operating software. The software interface allows the user to control which elements are addressed and the operating mode of the array (DC, pulsed, etc.). The FPGA board also powers the CMOS-controlled micro-LED array using the power supplied from the computer USB port, meaning that no external power supply is needed to power the device. The daughter card, shown by white dashes in figure 3.27, maps the input signals from the main board to the appropriate pins on the CMOS chip, and also provides several input/output SMA ports which can be used for purposes such as trigger inputs/outputs to/from the CMOS device. For subsequent designs of CMOS chip the same motherboard/FPGA board is used, and only a re-designed daughter card is required to take into account the different pin layout.

3.4.4 Device performance

Micro-LED devices of various peak emission wavelengths, of both 16×16 and 8×8 format, were successfully bonded to the third-generation CMOS device. All devices were observed to work both electrically and optically, indicating that the chosen approach of providing dedicated bonding pads for flip-chip bonding the CMOS and micro-LED devices was successful. A micrograph image of a simple output pattern from a 370 nm-emitting CMOS/micro-LED device is shown in figure 3.28, along with a screenshot of the graphical user interface (GUI) used to control the settings of the device.

One major limitation of the first-generation CMOS device was the low current (< 5 mA DC) that could be supplied to each micro-LED, which in turn severely limited the optical output powers that could be achieved per pixel. The current delivering capabilities of the third-generation device was designed to be much greater. The DC L-I characteristics from pixels from three CMOS/micro-LED devices are given in figure 3.29. Each pixel is $72 \mu\text{m}$ in diameter, from 16×16 micro-LED arrays with peak emission at 370, 405 or 450 nm, respectively. It can be seen that the third-generation CMOS drivers can provide > 100 mA of DC current to a single micro-LED pixel. For these devices, maximum DC output powers of 0.75, 0.58 and 4 mW were obtained for the 370, 405 and 450 nm devices, respectively. At 20 mA, the respective values were 0.44, 0.31 and 1.31 mW. The L-I characteristic the 450 nm-emitting device is similar to that of an identical

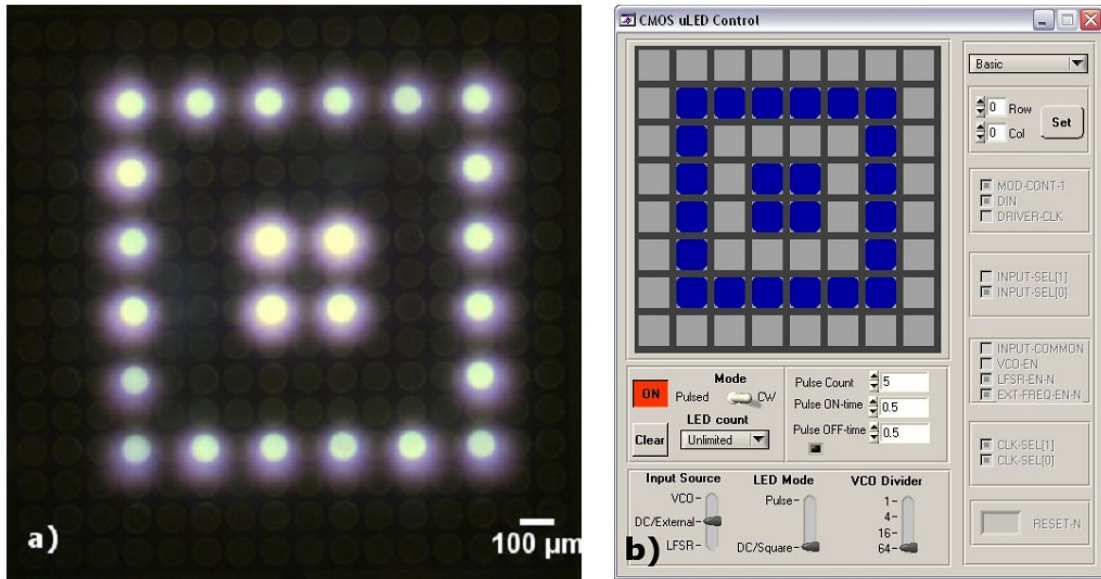


FIGURE 3.28: (a) Output pattern from a 370 nm peak emission 16×16 micro-LED array bonded to a third-generation CMOS control chip and (b) the GUI used to control the device.

‘bare’ micro-LED, as presented in section 2.3.2. However, the maximum output of the 405 nm device is $\approx 45\%$ less than for a similar bare micro-LED pixel. This has been attributed to damage to the micro-LED pixel caused during the bump-bonding process. Conversely, the 370 nm-emitting pixel bonded onto CMOS is seen to deliver more than double the output power from the CMOS-controlled pixel compared to an identical bare pixel. In addition, the CMOS-bonded pixel was able to withstand up to 90 mA of DC current before failure, compared to ≈ 30 mA for an identical bare pixel. This enhanced performance is tentatively attributed to improved thermal management due to the gold bump-bond and CMOS substrate acting as a heat-sink for the micro-LEDs.

One of the possible limitations on the output power from each CMOS-controlled micro-LED pixel is the maximum forward bias voltage that can be applied to the micro-LEDs. There exists a limitation on how far LED_GND can be shifted w.r.t. GND due to electrical crosstalk within the chip. The origin of the crosstalk issue can be understood by examining the micro-LED driver circuit shown in figure 3.30. The signal LED_GND is common to every micro-LED pixel within the array, and the ‘top rail’ (p-contact) of each *unaddressed* micro-LED pixel is 0 V. If LED_GND is shifted sufficiently below GND , then all micro-LEDs in the array can effectively be forward biased above their threshold voltage, whether or not they have been addressed. In order to prevent this unwanted scenario, LED_GND must not exceed -2 to -3 V. Figure 3.30 shows that it is possible for a parasitic current path to flow through the NMOS transistor when LED_GND is sufficiently negative. Figure 3.31 shows the effect the issue of crosstalk has on the operation of an actual device. Moving from left to right, each image shows

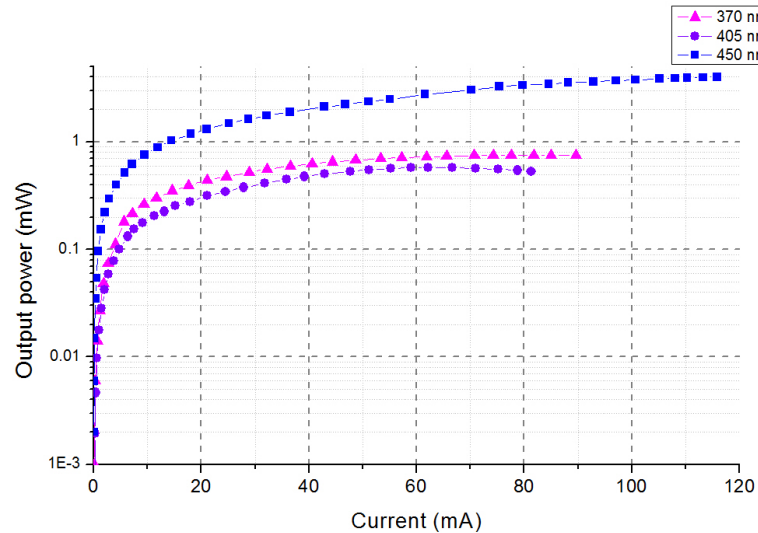


FIGURE 3.29: L-I characteristics of individual $72 \mu\text{m}$ diameter CMOS-controlled pixels emitting at 370, 405 and 450 nm, respectively.

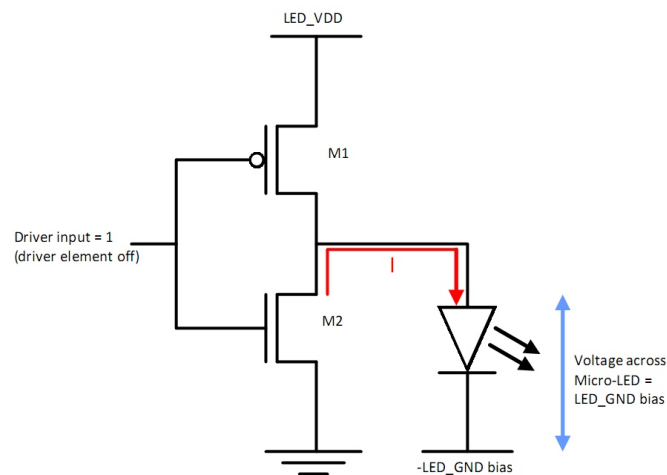


FIGURE 3.30: Circuit diagram illustrating the origin of electrical crosstalk. Current is able to flow through the NMOS transistor and unaddressed micro-LEDs along the parasitic path from GND to LED_GND when the effective forward bias on the micro-LEDs exceeds the turn-on voltage.

the effect of LED_GND being progressively shifted from 0 V to -4 V. When $LED_GND = 0$ V, only one addressed pixel emits light. However, the remaining *unaddressed* pixels progressively emit more light as LED_GND is shifted to -4 V w.r.t. to GND . This issue can be remedied by blocking the parasitic path for array elements which have not been addressed.

It is important to note that the L-I's shown in figure 3.29 represent the 'best', or brightest pixel from each particular array. Because the third-generation CMOS chip drives the micro-LEDs using voltage, rather than by controlling current as with the first-generation device, relatively small changes in micro-LED series resistance can result in fairly large

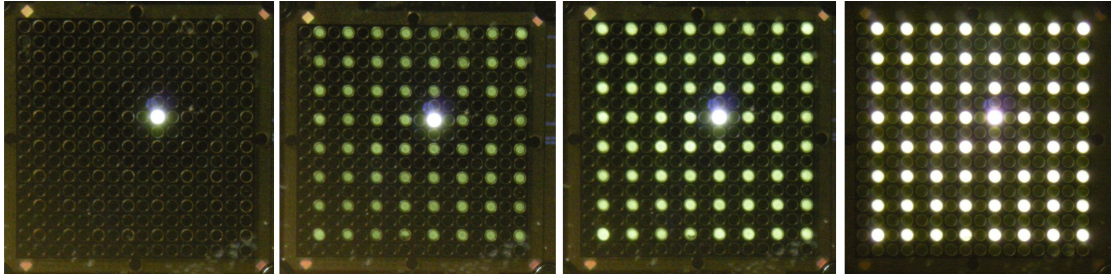


FIGURE 3.31: Optical micrograph image showing the electrical cross talk in a CMOS-controlled micro-LED array. From left to right LED_GND is being progressively shifted from 0 V to -4 V in 1 V increments, causing unaddressed micro-LED pixels to emit light.

differences in current for a given forward bias voltage. The output power uniformity of each array, which shows the output power from each micro-LED in the array for a fixed forward bias voltage, is shown in figure 3.32. It reveals that the devices are not particularly uniform - some pixels can be almost three times brighter than their neighbours. This non-uniformity has been attributed to variations in the flip-chip bonding process from pixel-to-pixel, and could be improved in future by optimising the bonding process and/or the bonding areas on the micro-LEDs or possibly by bonding the micro-LED and CMOS devices using a different bonding technique. Despite these non-uniformities, the vast majority of bonded micro-LEDs were observed to work and the devices are still suitable for applications where high uniformity across the array is not of critical importance.

Section 3.4.2 discussed the design of the CMOS short-pulse generation circuitry. Each driver in the CMOS array is capable of producing electrical pulses ranging from ≈ 250 ps to 40 ns. The current starving NMOS transistor, labelled M1 in figure 3.22, is controlled by a voltage named VBMC2. By tuning VBMC2 off-chip, the user is able to tune the electrical input pulse width to the CMOS driver array. The relationship between VBMC2 and the optical pulse width for a $72 \mu\text{m}$ diameter, 370 nm-emitting CMOS/micro-LED pixel is shown in figure 3.33. The optical pulses were measured using the time-correlated single-photon counting (TCSPC) technique, to be discussed in detail in section 4.2. In this instance, $LED_VDD = 4.88$ V, and $LED_GND = 0$ V. This graph shows that the optical pulse width can be tuned from 40 ns to ≈ 0.46 ns, ± 0.18 ns. The measurement error is based on the transit time spread of 180 ps from the PMT used in the measurements (Becker & Hickl, GmbH, PMH-100). Shorter pulses are achieved by increasing the gate voltage on the NMOS starving transistor that controls the optical pulses widths, allowing more current to flow through the inverter shown in figure 3.26 and thus increasing its transition speed. Eventually, increasing VBMC2 does not result in an increase in current flow as the current starving transistor is saturated, i.e. it cannot allow any more current to flow. This means that for VBMC2 voltages greater than ≈ 2

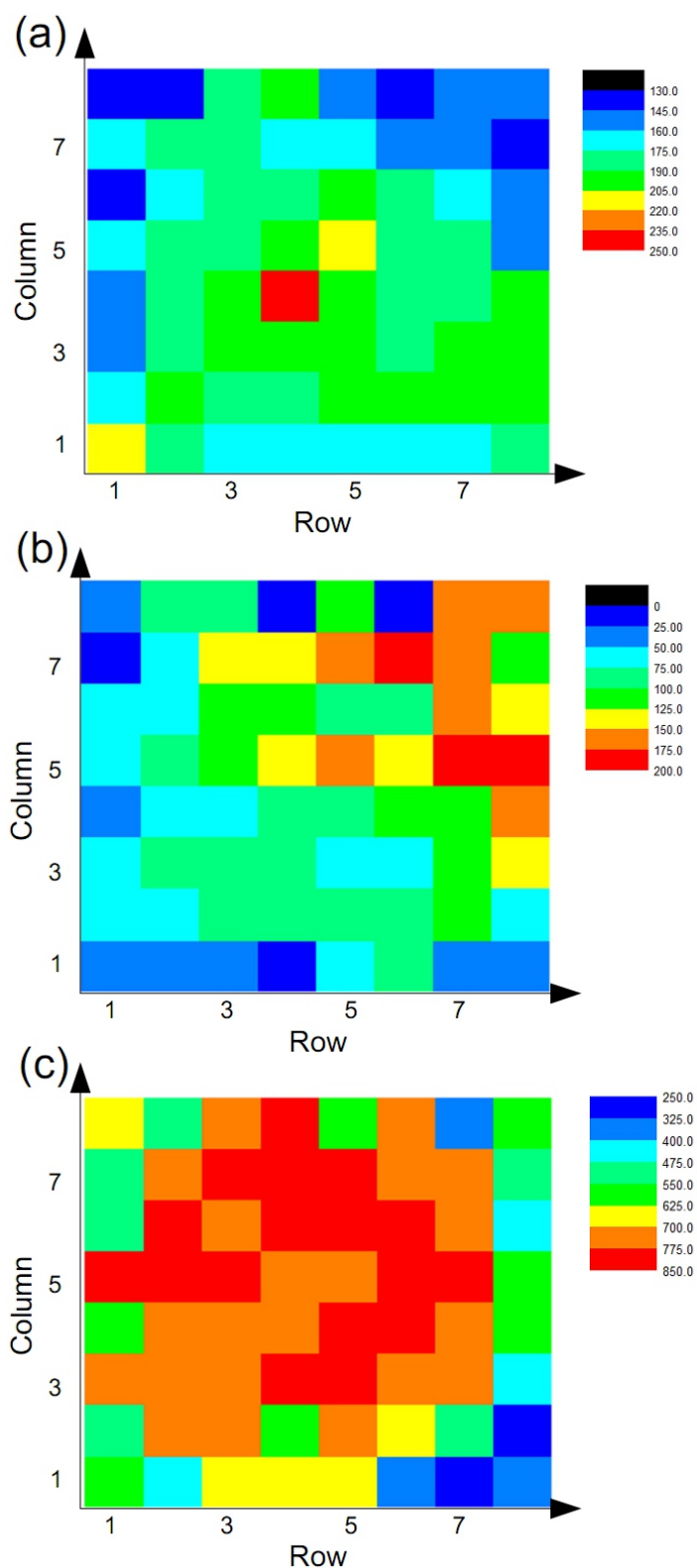


FIGURE 3.32: Output power uniformity of CMOS-controlled micro-LED arrays emitting at (a) 370 (b) 405 and (c) 450 nm. The colour scale represents intensity in arbitrary units, with red being high. Each pixel in each array is driven with the same forward bias voltage and in DC operation.

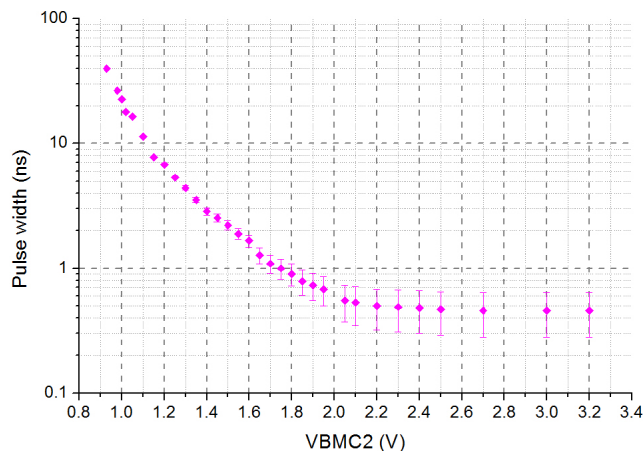


FIGURE 3.33: Optical pulse width versus pulse control voltage, VBMC2. Micro-LED pixel peak emission is 370 nm, diameter 72 μm . $LED_VDD = 4.88$ V, $LED_GND = 0$ V. Estimated 180 ps timing error due to transit time spread of PMT.

V, the optical output pulse of from the micro-LED does not decrease, as can be seen in figure 3.33.

The fall time of the micro-LED optical pulses are generally determined by the spontaneous minority carrier recombination lifetime within the micro-LED quantum wells. However, reverse-biasing the micro-LED in the off-state can reduce the fall time of the optical pulse. When the device is reverse-biased, free carriers within the quantum wells can be ‘swept out’ of the active region by the applied electric field in a time that is shorter than the minority carrier recombination lifetime. This means that the fall time of the micro-LED can be determined by the carrier sweep-out time, rather than the comparatively slower minority carrier recombination time, resulting in shorter optical pulses. Since LED_GND is separate from GND , the third-generation CMOS device allows the principle of carrier sweep-out to be used to reduce the fall-time and FWHM of the micro-LED optical pulses. Figure 3.34 shows the effect of changing LED_GND on the optical pulse duration from a single 72 μm diameter 450 nm-emitting micro-LED pixel. Reverse-biasing the micro-LED in the off-state ($LED_GND = +1$ V) reduces the pulse width to 0.92 ns, compared to 1.5 ns when the micro-LED is forward-biased in the off-state ($LED_GND = -1$ V). The shortest optical pulses from micro-LEDs driven by the third-generation CMOS device were obtained using the carrier sweep-out technique. The shortest pulses obtained from 72 μm diameter micro-LED pixels were 300, 640 and 820 ± 180 ps FWHM, for 370, 405 and 450 nm-emitting micro-LEDs, respectively. The shortest optical pulse obtained, from the 370 nm-emitting device, is presented in figure 3.35. With sub-nanosecond optical pulses being obtained, the pulsed performance of the third-generation device represents a significant improvement on the performance of the first-generation device.

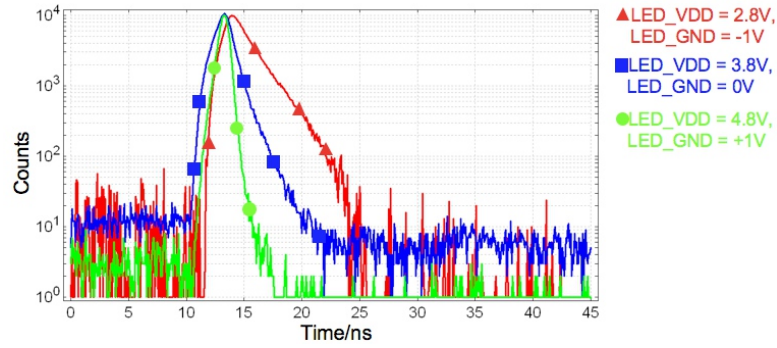


FIGURE 3.34: Optical pulse width versus *LED_GND*. It can be seen that although the same forward bias is applied to the micro-LED in each case, reverse biasing the micro-LED after the initial electrical input reduces the optical turn-off time by sweeping carriers out of the active region.

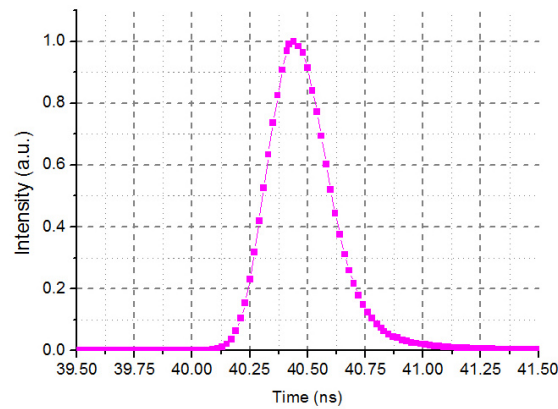


FIGURE 3.35: TCSPC histogram illustrating a 300 ± 180 ps optical pulse from a 370 nm-emitting micro-LED pixel.

As mentioned previously, an on-chip VCO can be used to provide a square-wave input signal for driving the micro-LEDs, and the VCO output can also be used as a clock for triggering the short-pulse and LFSR circuits. Figure 3.36 shows the optical output from a single $72 \mu\text{m}$ diameter pixel from a CMOS-controlled micro-LED array as measured by a PMT (Hamamatsu H5783P), with the CMOS driver in four different modes of operation. Figure 3.36(a) shows the square wave output when the CMOS driver is triggered by the VCO output. Figure 3.36(b) shows the pseudo-random optical output when the VCO output is used to drive the on-chip LFSR, which in turn is used as the input signal to the CMOS drivers. Figures 3.36(c) and (d) show the pulsed VCO-driven and pulsed-LFSR modes of operation, respectively. The VCO clock frequency for each case is 10 MHz.

For some potential applications of the CMOS-controlled micro-LED devices, such as time-resolved fluorescence measurements or optical communications, the maximum modulation frequency or pulse repetition rate that the devices can achieve can be important. The on-chip VCO has a maximum frequency of approximately 800 MHz. However, the

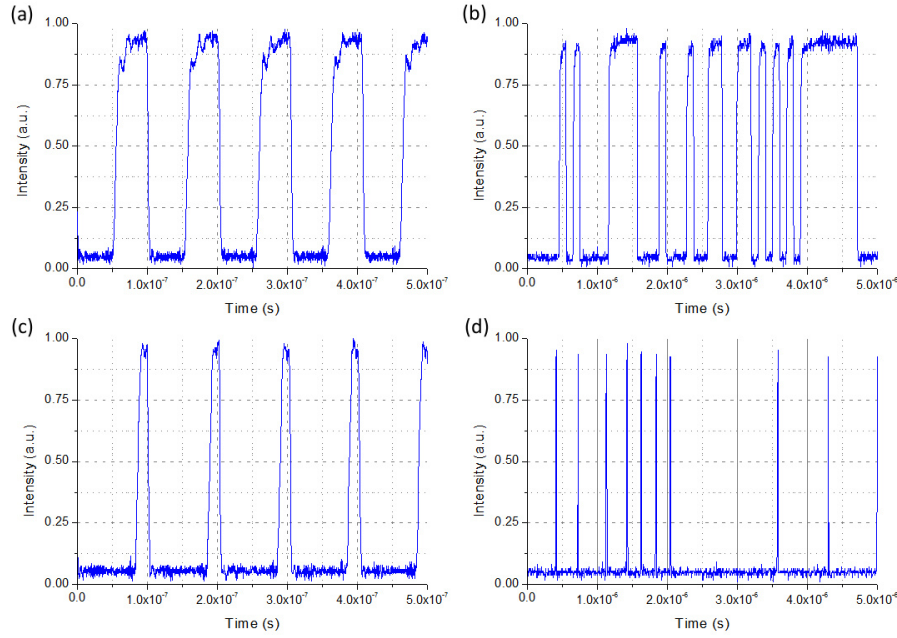


FIGURE 3.36: Optical output pulse trains, as measured using a PMT, of a 405 nm, 72 μm CMOS-controlled micro-LED with drive signals provided by (a) on-chip VCO, (b) on-chip LFSR, (c) VCO under pulsed mode and (d) LFSR under pulsed mode. VCO frequency for all figures is 10 MHz.

output of the on-chip VCO is loaded with all 64 CMOS driver elements in the array. This large load capacitance means that the signals that the VCO can deliver to the CMOS drivers are lower in bandwidth than the core VCO clock frequency. The optical modulation bandwidth of CMOS-controlled micro-LEDs was analysed by measuring the amplitude of the optical square-wave output from a single pixel, when driven by the VCO input signal, as a function of VCO frequency. The amplitude versus frequency measurement from a CMOS-controlled 450 nm-emitting pixel, of 44 μm diameter is shown in figure 3.37. For this measurement, $LED_VDD = 3.3$ V, and $LED_GND = -4$ V. The amplitude was measured using a fast amplified photodiode (Newport 818-BB21A) and a sampling oscilloscope. The VCO frequency was measured by observing the VCO electrical output directly from an output SMA socket. An estimated systematic error of 10% in measuring the output amplitude is assumed, due to difficulties in manually measuring the irregular square-wave pulse shapes. The frequency response (amplitude versus frequency) of the pixel, $P(\omega)$, and the bandwidth, f_{3dB} , of the pixel are defined as follows [16]:

$$P(\omega) = \frac{1}{\sqrt{1 + (\omega\tau)^2}} = \frac{1}{2} \quad (3.3)$$

$$f_{3dB} = \frac{\sqrt{3}}{2\pi\tau} \quad (3.4)$$

The above equation for $P(\omega)$ was used for a non-linear least squares fit to the measured

data. The corresponding modulation bandwidth of the pixel was found to be 113 MHz. As will be discussed in section 5.2, the frequency response of a similar ‘bare’ micro-LED is in excess of 400 MHz, thus it is reasonable to conclude that the modulation bandwidth observed in this case is limited by the design of the CMOS device rather than the micro-LEDs. An external signal could be used to drive the micro-LEDs instead of the VCO, however this method would encounter similar problems in routing high-frequency signals to the driver array. A more careful design utilising a VCO output ‘clock tree’ may allow higher modulation bandwidths to be obtained.

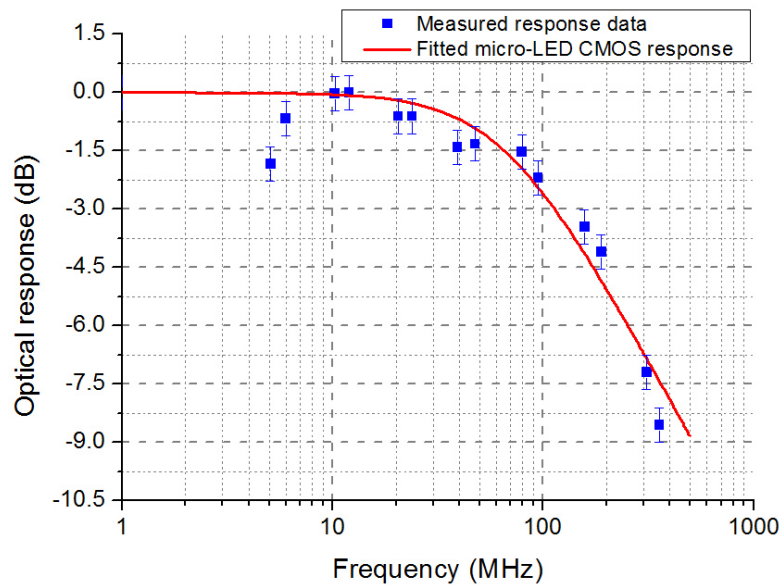


FIGURE 3.37: Frequency response of a 450 nm-emitting CMOS-controlled micro-LED pixel. Measured data shown in black, fitted curve shown in red. Estimated 10% systematic error. $LED_VDD = 3.3$ V, and $LED_GND = -4$ V. Estimated bandwidth is 113 MHz.

3.4.5 Discussion

The performance of the third-generation CMOS device was a significant improvement on that of the previous two devices. Providing dedicated bonding pads on the CMOS chip solved the chip failure problems that were seen with the second-generation device. Considerably shorter, sub-nanosecond optical pulses were obtained and much higher optical output powers were achieved using the third-generation device, indicating that the driver design represented a significant improvement on the performance of the first-generation drivers. These shorter, more intense optical pulses make the third-generation devices better suited to time-resolved fluorescence lifetime measurements. A fluorescence lifetime measurement system implementing a third-generation CMOS-controlled micro-LED device will be presented in section 4.4.

Several issues were identified with the third-generation device which were taken into consideration when a new ‘fourth-generation’ chip was designed. Although a detailed discussion about the design and performance of the fourth-generation device is beyond the scope of this thesis, it has been shown to be a further improvement on the third-generation device shown here. Smaller bond pads, of $50 \times 50 \mu\text{m}$ have been used with the fourth-generation device, allowing the driver array to be scaled up to a 16×16 array on a $100 \mu\text{m}$ pitch. The electrical crosstalk issue has been solved by the addition of an extra PMOS transistor to each driver, preventing unaddressed micro-LEDs from being forward-biased. Finally, a ‘clock-tree’ allows for high-speed signals to be routed to all the drivers in the array, such that the frequency response of the micro-LEDs is no longer limited by the CMOS drivers themselves. Results taken recently with this CMOS chip are described in the Conclusions, chapter 6.

3.5 Applications of CMOS-controlled micro-LED arrays

The independent computer control of individual pixels in the CMOS/micro-LED devices presented in this chapter make these devices particularly useful for a number of applications. Chapters 4 and 5 describe full investigations in the areas of time-resolved fluorescence measurements and optical communications, respectively. Here, we briefly discuss some other applications. One such application is for mask-free photolithography. A mask-free photolithography system utilising the third-generation driver chip is shown in figure 3.38 [17]. The CMOS-controlled micro-LED array used in the mask-free photolithography system has a peak emission wavelength of 370 nm, designed to emit light close to the *i*-line emission (365 nm) from mercury lamps typically used in conventional photolithography. Microscope objectives were used to collect the emission from the micro-LED array and subsequently image it onto the photoresist sample, giving spot sizes of as small as $8 \mu\text{m}$ in diameter at the sample surface. The micro-LED pixels were $72 \mu\text{m}$ in diameter, but by 10:1 de-magnification of the pixel output smaller spot sizes could be imaged on to the photoresist surface. Changing the output pattern from the micro-LED array and/or moving the photoresist sample by use of a piezoelectric positioning stage allowed patterns to be exposed into the photoresist without the need for an expensive hard lithography mask. Using this system, features were written into photoresist with dimensions of $\approx 10 \mu\text{m}$, as shown in figure 3.39. As can be seen in figure 3.39, very well-defined and uniform features can be exposed into photoresist. Typical exposure rates of $100 \mu\text{m/s}$ were required to write channels into photoresist, or $\approx 40 \text{ s}$ to expose the features seen in figure 3.39. More recently, using smaller micro-LED pixels, features down to 500 nm in diameter have been achieved using this system. Full details of this work has been published [17].

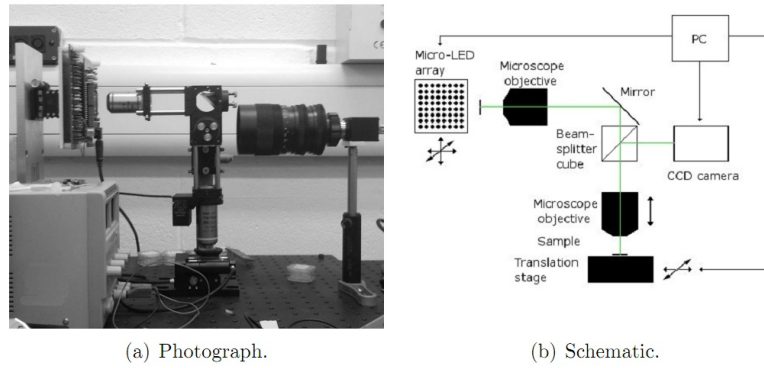


FIGURE 3.38: Mask-free photolithography system incorporating a 370 nm-emitting CMOS-controlled micro-LED array. From [17].

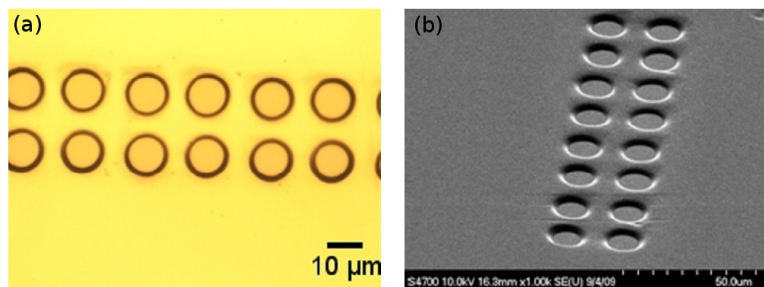


FIGURE 3.39: (a) Micrograph image showing an array of exposed dots in photoresist, each with a diameter of $\approx 9 \mu\text{m}$. (b) Oblique SEM image of the same array, showing well defined sidewalls and good dot-to-dot uniformity. From [17].

This system could in principle operate with a matrix-addressable device, however, the raster-scanned nature of the matrix-addressed device output means that each pixel in the array may only be operational for a fraction of the time, resulting in longer exposure times being required. The use of the CMOS-controlled individually addressable array overcomes this issue. Furthermore, if the CMOS device is operated in pulsed mode it allows the photoresist exposure dose to be very finely controlled by virtue of the control the user has over the optical output pulses.

Another demonstrated application of the CMOS-controlled micro-LED devices is for opto-electronic tweezing (OET). This is a technique that uses a light patterned photoconductor to provide real time control over the positioning of electric fields for the micro-manipulation of cells and other particles. The ability to manipulate micro-objects in is essential for numerous cell biology experiments, such as cell sorting. A schematic of an typical OET system is shown in figure 3.40. The system consists of a liquid layer, containing the particles to be trapped, in between two ITO electrodes. One electrode is coated with a photoconductive layer of amorphous silicon (a-Si). An AC signal is applied between both electrodes. In the dark state, the a-Si layer is highly resistive, so most of the AC voltage is dropped across this layer. However, if the a-Si is illuminated, its resistance can drop dramatically. In this case, the voltage is then dropped across the liquid

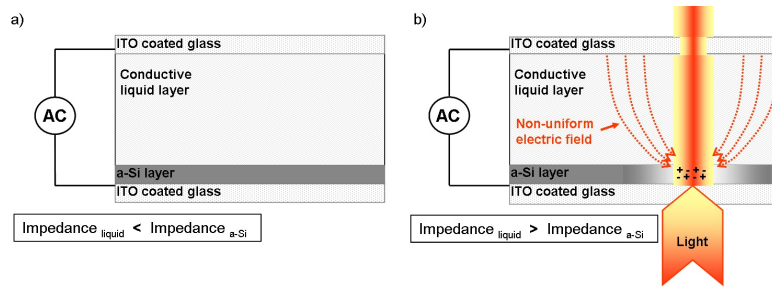


FIGURE 3.40: Schematic of the OET device: a) in the dark state no voltage is dropped between ITO electrodes; b) under localised illumination, the impedance of the photoconductive layer, a-Si, reduces dramatically and the voltage is then dropped across the liquid layer in the proximity of the illumination. This generates a non-uniform electric field for tweezing.

layer. An electric field will exist in the liquid layer in proximity to the illuminated a-Si, thus by creating a non-uniform illumination of the a-Si layer, a non-uniform electric field can be generated in the liquid layer for trapping particles. Reported OET systems use digital micro-display (DMD)[18] or liquid crystal displays (LCDs)[19] to create the light patterns, which are bulky and relatively expensive. The alternative approach of using a micro-LED array provides a much more compact pattern-programmable light source for OET. An integrated micro-LED/OET system has great potential as a portable and low-cost micromanipulation device.

In the micro-LED/OET system we demonstrated, a 520 nm peak emission wavelength CMOS-controlled micro-LED array was used as the pattern programmable light source. Micro-LED CW output powers of up to 300 μW were used during tweezing. A low-cost lens was placed between the micro-LED device and the 300 nm thick a-Si layer to image (1:1) the micro-LED emission. Successful tweezing of both 10 μm polystyrene beads (in low-concentration KCl solution) and Chinese Hamster Ovary (CHO) cells (in an isotonic sugar solution) have been achieved. Figure 3.41 shows the CHO cells that have been selectively trapped in the area illuminated by several micro-LED pixels [20]. Particles in solution could be attracted towards the illuminated spots from hundreds of microns away, at velocities of up to 4 $\mu\text{m s}^{-1}$. Once again, the ability to operate an array of micro-LED pixels in true DC output is an advantage of the CMOS-controlled micro-LEDs over their matrix-addressable counterparts. Further details on this work have recently been reported [20].

3.6 Summary

In this chapter, the performance of various iterations of CMOS-driven, individually-addressable micro-LED arrays has been presented. In section 3.2 a ‘first-generation’ 16

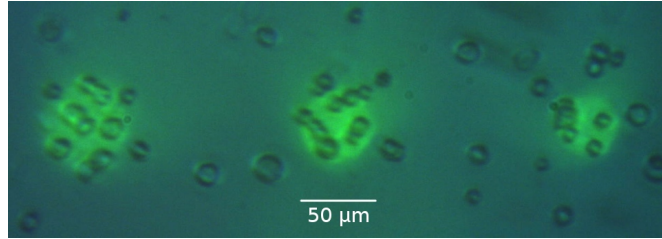


FIGURE 3.41: Opto-electronic tweezing of cells, using pixels from a third-generation 520 nm-emitting CMOS-controlled micro-LED as the light source.

$\times 4$ array of CMOS drivers, with integrated SPADs, was shown to be capable of driving micro-LED pixels. Although there were limitations in the optical output power and the minimum optical pulse duration, this device is still suitable for practical applications. A proof-of-concept single-chip time-resolved fluorescence measurement system will be shown in section 4.3 which uses the first-generation CMOS/micro-LED device.

A custom-designed ‘second-generation’ CMOS device was introduced in section 3.3. Although this device was found to work electrically, after flip-chip bonding to micro-LED arrays these devices were found to have failed. The cause of failure was identified as two CMOS metal layers being damaged and shorting together during the bonding process. A re-designed ‘third-generation’ chip was thus developed, which used the same driver circuitry as the second-generation chip, but used dedicated bonding pads to prevent damage to the chip during bonding. This approach proved to be successful. The third-generation chip was shown to be capable of producing sub-nanosecond optical pulses, which could be shortened by reverse-biasing the micro-LEDs in their off-state. Optical output powers from the micro-LEDs were found to be up to 4 mW from a single $72 \mu\text{m}$ diameter pixel, though a potential limit to the output power per pixel was identified as coming from electrical crosstalk when LED_GND was biased too far below GND . The modulation bandwidth of the CMOS-controlled micro-LEDs was found to be approximately 113 MHz when driven using the on-chip VCO. This bandwidth is below that of the fundamental micro-LED bandwidth indicating that this response is limited by the CMOS drivers rather than the micro-LEDs. The limitations of the third-generation chip were identified and corrected for a subsequent ‘fourth-generation’ design, which was briefly introduced. The fourth-generation chip, whilst not covered in detail in this thesis, has been shown to solve the electrical crosstalk issue, to have a higher modulation bandwidth and to have scaled up the main driver array from 8×8 on a $200 \mu\text{m}$ pitch to a 16×16 array with a $100 \mu\text{m}$ pitch.

References

- [1] Wan-Kai Chen, editor. *The Electrical Engineering Handbook*. Elsevier Academic Press, 2004.
- [2] Allan R. Hambley. *Electrical Engineering Principles and Applications*. Prentice Hall, 2nd edition, 2002.
- [3] S. Spiesshoefer and L. Schaper. IC stacking technology using fine pitch, nanoscale through silicon vias. *Proceeding of the 53rd Electronic Components and Technology Conference*, pages 631–633, 2003.
- [4] Pradeep Dixit, Chee Wee Tan, Luhua Xu, Nay Lin, Jianmin Miao, John H L Pang, Petra Backus, and Robert Preisser. Fabrication and characterization of fine pitch on-chip copper interconnects for advanced wafer level packaging by a high aspect ratio through AZ9260 resist electroplating. *Journal of Micromechanics and Microengineering*, 17(5):1078, 2007.
- [5] R.J. Gutmann, J.Q. Lu, Y. Kwon, J.F. McDonald, and T.S. Cale. Three-dimensional (3D) ICs: a technology platform for integrated systems and opportunities for new polymeric adhesives. *First International IEEE Conference on Polymers and Adhesives in Microelectronics and Photonics*, pages 173 –180, 2001.
- [6] Y. Li, W. Parkes, L.I. Haworth, A.A. Stokes, K.R. Muir, P. Li, A.J. Collin, N.G. Hutcheon, R. Henderson, B. Rae, and A.J. Walton. Anodic Ta_2O_5 for CMOS compatible low voltage electrowetting-on-dielectric device fabrication. *Solid-State Electronics*, 52(9):1382 – 1387, 2008. ISSN 0038-1101. Papers Selected from the 37th European Solid-State Device Research Conference - ESSDERC'07.
- [7] Bruce R. Rae. *Micro-Systems for Time-Resolved Fluorescence Analysis Using CMOS Single-Photon Avalanche Diodes and Micro-LEDs*. PhD thesis, The University of Edinburgh, August 2009.
- [8] C. Niclass, A. Rochas, P.-A. Besse, R.S. Popovic, and E. Charbon. CMOS imager based on single photon avalanche diodes. *The 13th International Conference on Solid-State Sensors, Actuators and Microsystems*, 1:1030 – 1034, 2005.
- [9] Cristiano Niclass, Maximilian Sergio, and Edoardo Charbon. A single photon avalanche diode array fabricated in deep-submicron CMOS technology. *Proceedings of the conference on Design, automation and test in Europe*, pages 81–86, 2006.
- [10] R. Jacob Baker. *CMOS: Circuit design, layout and simulation*. John Wiley & Sons, 2008.

-
- [11] B R Rae, C Griffin, J McKendry, J M Girkin, H X Zhang, E Gu, D Renshaw, E Charbon, M D Dawson, and R K Henderson. CMOS driven micro-pixel LEDs integrated with single photon avalanche diodes for time resolved fluorescence measurements. *Journal of Physics D: Applied Physics*, 41(9):094011, 2008.
- [12] Joseph R. Lakowicz. *Principles of Fluorescence Spectroscopy*. Springer, 3rd edition, 2006.
- [13] Y Yang, G. A. Turnbull, and I. D. W. Samuel. Hybrid optoelectronics: A polymer laser pumped by a nitride light-emitting diode. *Applied Physics Letters*, 92:163306, 2008.
- [14] Kuo-Yu Chou, Ming-Jer Chen, and Chi-Wen Liu. Active devices under CMOS I/O pads. *IEEE Transactions on Electron Devices*, 49(12):2279 – 2287, 2002.
- [15] J. McKendry, B. R. Rae, Z. Gong, B. Guilhabert, D. Massoubre, E. Gu, D. Renshaw, R.K. Henderson, and M.D. Dawson. Individually-addressable III-nitride micro-LED arrays for integrated CMOS control, Paper TuN2. In *22nd Annual Meeting of the IEEE Photonics Society, Belek-Antalya, Turkey*. IEEE, October 2009.
- [16] E.F. Schubert. *Light Emitting Diodes*. Cambridge University Press, 2nd edition, 2006.
- [17] D. Elfström, B. Guilhabert, J. McKendry, S. Poland, Z. Gong, D. Massoubre, E. Richardson, B. R. Rae, G. Valentine, G. Blanco-Gomez, E. Gu, J. M. Cooper, R. K. Henderson, and M. D. Dawson. Mask-less ultraviolet photolithography based on CMOS-driven micro-pixel light emitting diodes. *Optics Express*, 17(26):23522–23529, 2009.
- [18] P. Y. Chiou, A. T. Ohta, and M. C. Wu. Massively parallel manipulation of single cells and microparticles using optical images. *Nature*, 436:370–372, 2005.
- [19] Hyundoo Hwang, Yong-Je Choi, Wonjae Choi, Se-Hwan Kim, Jin Jang, and Je-Kyun Park. Interactive manipulation of blood cells using a lens-integrated liquid crystal display based optoelectronic tweezers system. *Electrophoresis*, 29(6):1203–1212, 2008.
- [20] A. Zarowna-Dabrowska, S.L. Neale, D. Massoubre, J. McKendry, B.R. Rae, R.K. Henderson, M.J. Rose, H. Yin, J.M. Cooper, E. Gu, and M.D. Dawson. Miniaturized optoelectronic tweezers controlled by GaN micro-pixel light emitting diode arrays. *Optics Express*, 19(3):2720–2728, 2011.

Chapter 4

Micro-LEDs for time-resolved fluorescence lifetime measurements

In this chapter, the application of micro-LED arrays to time-resolved fluorescence lifetime measurements is presented. The first section summarises the principles of fluorescence, why fluorescence measurements are of interest and which equipment is commonly used for fluorescence excitation and detection. The motivations for implementing micro-LEDs as fluorescence excitation sources is also discussed.

The following section briefly introduces the principle of time-correlated single-photon counting (TCSPC), which is the most commonly used time-domain fluorescence lifetime measurement technique. The final two sections describe two different TCSPC systems based on CMOS-controlled micro-LEDs, which are demonstrated to allow the fluorescence lifetimes of some quantum dot and light-emitting polymer samples to be accurately determined. These demonstrations represent proof-of-principle demonstrations showing the capability and potential of micro-LED arrays for use in fluorescence lifetime measurements.

4.1 Overview of fluorescence measurements

4.1.1 Steady-state and time-resolved measurements

Fluorescence measurements involve analysing a luminescent sample, or a sample that has been stained with a luminescent dye, under optical excitation from an external

source. Information from the sample can be ascertained by examining the properties of the fluorescence emission. There are thousands of known fluorescent probes, so it is impractical to list all of them here. The fluorescent probes may, however, be divided into two basic categories, intrinsic and extrinsic fluorophores. Intrinsic fluorophores occur naturally within the sample of interest, for example aromatic amino acids within proteins and chlorophyll in plants. Broadly speaking, intrinsic fluorophores generally have absorption maxima in the UV or near UV. Extrinsic fluorophores on the other hand are probes which are added to a sample of interest when no intrinsic fluorescence exists, or when the spectral properties of the sample must be altered. Examples of commonly used extrinsic fluorophores are fluorescein and rhodamine dyes. Over the last 12 years, colloidal quantum dots have also been increasingly utilised as novel fluorophores for labelling biological cells [1]. The excitation wavelengths of extrinsic fluorophores can range from the UV to the IR. From this, it can be seen that the emission wavelengths of AlInGaN LEDs are suitable for excitation of the majority of common fluorescent samples.

Fluorescence measurements can be grouped into two categories, namely steady-state and time-resolved measurements. Steady-state measurements are the most common and are relatively straightforward. The sample is continuously illuminated and the property of interest such as the emission spectrum or fluorescence intensity is also measured continuously. Time-resolved measurements are also fairly common. These measurements involve analysing the fluorescence lifetime, τ , of the sample. The concept of the fluorescence lifetime, τ , and the processes involved in absorption and emission of light was discussed in relation to organic semiconductors in chapter 1, section 1.4.1, and applies more generally to fluorophores used in time-resolved measurements of e.g. biological samples. Because τ typically ranges from 10^{-8} to 10^{-9} s time scales, time-resolved measurements require considerably more complicated equipment and techniques than the relatively simple steady-state measurements. However, these more complicated measurements have several advantages over their steady-state counterparts. The steady-state fluorescence intensity, for example, is highly sensitive to the sample quantity, sample concentration, sample distribution, the instrumental setup and scattered light, making quantitative measurements difficult. On the other hand, because the fluorescence lifetime is independent of sample volume and concentration, time-resolved measurements are much more robust and are capable of measuring subtle changes in the sample. Time-resolved measurements can distinguish a mixture of two samples with overlapping emission spectra but different fluorescence lifetimes, something which would be impossible using steady-state techniques. Furthermore, the fluorescence lifetime of a fluorophore is dependent on its local environment, so measuring τ can provide insight into many of the properties of

the sample such as its local pH [2], the local viscosity [3] and the structural conformation of macromolecules such as proteins [4].

Time-resolved measurements can be further sub-divided into two general groups, time-domain and frequency-domain measurements, both of which are in widespread use. Figure 4.1 illustrates the principle behind time-domain measurements. In time-domain measurements, the sample to be analysed is excited by a pulse of light, which (in the ideal case) has a pulse duration that is much shorter than the fluorescence lifetime of the sample itself, such that the excitation pulse can be considered a delta function. The fluorescent sample will emit light in response to this excitation pulse. The time-dependent intensity of the fluorescence emission at time t , for a simple mono-exponential decay is given by:

$$I(t) = I_0 \exp(-t/\tau) \quad (4.1)$$

where I_0 is the intensity at $t = 0$ (the intensity of the delta-function excitation pulse). Time-resolved measurements aim to capture $I(t)$ in order that a value for τ can be extracted. In practical measurements, the excitation pulse is too wide to be considered a delta function, so the measured curve is a convolution of the excitation pulse and the emission from the sample. De-convolution allows $I(t)$ to be obtained. The non-linear least squares (NLLS) [5] method is most commonly used to test whether a particular mathematical model provides an accurate representation of the measured data and to determine the fitted parameter values (including τ) which provide the best fit to the data. NLLS fitting software aims to achieve this by finding a ‘best fit’ to the data by finding parameters which minimise the goodness-of-fit parameter, χ^2 . In an ideal case χ^2 should equal unity and a plot of the standard deviation residuals can highlight any problems with the fit. The most commonly used form of time-domain measurement, time-correlated single-photon counting (TCSPC), will be covered in more detail in section 4.2.

Frequency-domain measurements use an intensity modulated light source to optically excite the sample. The frequency of the modulation of the excitation light is typically around 100 MHz. Because of the time lag between the absorption and emission processes, there will be a phase shift, ϕ , and an intensity de-modulation, m , of the fluorescence emission relative to the excitation source, which will be a function of frequency, ω , and of the fluorescence lifetime of the sample. Frequency-domain measurements will not be covered in detail in this chapter, although the theory will be covered in more detail in section 5.4.1. It is reasonable to say that frequency-domain measurements use a simpler technique and simpler measurement instrumentation, so if time-domain measurements can be demonstrated using micro-LEDs, then frequency-domain measurements should be feasible using the same, or similar, equipment.

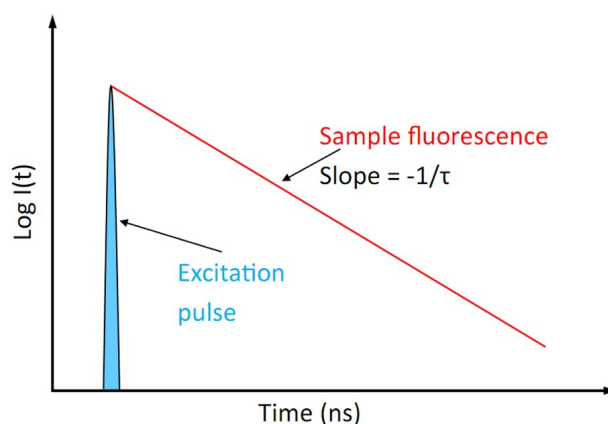


FIGURE 4.1: Illustration of time-domain measurements.

4.1.2 Instrumentation for time-resolved fluorescence measurements

Broadly speaking, time-resolved fluorescence measurements have three major sub-systems: a pulsed or modulated light source to optically excite the sample, a detector to measure the resulting fluorescence, and some electronics to record and analyse the fluorescence lifetime data. Time-domain measurements require a pulsed light source, with a pulse duration which is as short as possible, ideally much shorter than the fluorescence decay time, τ , of the sample. Early time-domain measurements in the 1970s commonly used coaxial flashlamps. However, these lamps have some drawbacks, most significant of which is the low pulse repetition rate which is typically 20 kHz [6]. This means that a decay curve with 500,000 counts could take up to 40 minutes to accumulate. As such, laser sources are presently the light source of choice for performing time-domain measurements. Titanium sapphire (Ti:sapphire) lasers can provide femtosecond regime pulse widths with multi-Watt average output power [7] and, via nonlinear frequency conversion, can be tuned from the UV to the infra-red. This performance and flexibility makes Ti:sapphire lasers excellent sources for time-resolved fluorescence measurements, however they have the disadvantages of being very expensive, bulky and complex. As such, the development over the last decade of relatively cheap and simple to operate pulsed laser diodes (LDs) and LEDs, emitting at wavelengths which are suitable for exciting commonly-used intrinsic and extrinsic fluorophores, has allowed time-domain measurements to be available to many more researchers than before. Blue-violet-emitting LDs have been reported with optical pulses of as short as 3 ps [8] and LEDs with pulses as short as several hundred ps [9]; both sources are commercially available with high repetition rates of up to 80 MHz. The emission spectra from such devices can be chosen to be centred from the UV through the visible spectrum, and recent the push towards UV LED emission has allowed pulsed LEDs to be capable even of exciting intrinsic protein fluorescence for ‘label free’ detection of biological material [9]. There have been

many reports of LDs and LEDs being used in fluorescence lifetime systems in both time-domain [10] and frequency-domain [2] lifetime measurements. The compact, robust and efficient nature of LEDs makes them particularly suitable for portable devices, allowing fluorescence lifetime-based detection of, for example, single airborne particles [11] of potentially dangerous pathogenic materials. For these reasons it is anticipated that these devices will become the most commonly used light sources for standard time-domain measurements.

Although previous work has shown that using LEDs for fluorescence lifetime measurements can reduce the price, complexity and size of time-domain measurement systems, they are still largely confined to specialist research laboratories. Arguably, the main reason is the photon detectors that these systems commonly use, such as photo-multiplier tubes (PMTs), avalanche photodiodes (APDs) or streak cameras. These detectors are generally bulky, fragile and not suitable for low cost miniaturisation, mass production or for use in portable compact instrumentation. However single photon avalanche diodes (SPADs), as described in chapter 3, section 3.2.1, offer an interesting alternative, which in principle can be mass-produced at a low cost. SPADs have previously been demonstrated as suitable detectors for fluorescence lifetime measurements [12], including direct integration with microfluidics [13]. As described in section 3.2, they can also be directly integrated with a CMOS control chip used to drive a micro-LED array, in principle allowing fluorescence excitation and detection to be performed using a single monolithically integrated device. Such a system will be presented in section 4.3. Micro-LED arrays themselves are a novel alternative light source for fluorescence lifetime measurements for a number of reasons. First of all, micro-LEDs have been demonstrated to have shorter optical turn-off times than their broad-area counterparts [14], making them more suitable for time-domain measurements. The array nature of the micro-LEDs could also be exploited to excite multiple samples in parallel on a single chip. Micro-LEDs and SPADs would provide miniaturised, mass-producible and cheap alternatives to fluorescence excitation and detection devices commonly used today. Furthermore, recent advancements in CMOS-based real-time on-chip fluorescence lifetime computation [15, 16] also allow the possibility of removing the need for the expensive and specialised timing electronics required for performing fluorescence lifetime measurements. A system that uses a CMOS-controlled micro-LED chip and a SPAD array chip with integrated fluorescence lifetime computation circuitry is presented in section 4.4. This system moves towards a truly compact fluorescence lifetime measurement system.

4.2 Time-correlated single-photon counting (TCSPC)

Time-correlated single photon counting (TCSPC) is the most commonly used technique for time-domain fluorescence lifetime measurements. Time-resolved fluorescence measurement systems based on micro-LEDs will be discussed in subsequent sections, so first the basic principles of TCSPC will be introduced. A simplified schematic of a TCSPC system is given in figure 4.2 and may be described as follows. An electronic ‘start’ signal simultaneously triggers an optical excitation pulse and triggers the time-to-amplitude converter (TAC). The TAC creates an analog voltage signal which linearly increases in amplitude with time, so the TAC effectively acts as a timer in this system. The optical excitation pulse excites the fluorescent sample, which subsequently emits light. Some of the light emitted by the sample will pass through an optical filter, used to block light from the excitation source, and impinge on the detector. If and when the detector measures a single photon of fluorescence from the sample, then an electronic ‘stop’ signal is sent to the TAC to stop the timer. The analogue value of the TAC is then converted to a digital value, and sent to the multi-channel analyser (MCA). The MCA is a form of memory, where the memory addresses (or ‘time bins’) are proportional to the time measured from the TAC. Every time a photon is detected, the ‘count’ value of the time bin corresponding to this arrival time is incremented by one. This process is repeated many thousands of times, until a histogram of the photon detection probability is stored in the MCA. Once a photon has been counted, the system is idle until the next excitation pulse, so at most only one photon is counted in any given period.

Figure 4.3 illustrates the basic measurement process of TCSPC. The sample is repeatedly excited by optical pulses from a light source, and the time delay between an excitation pulse and the subsequent arrival time of an individual fluorescence photon is recorded and used to re-construct the intensity decay of the fluorescent sample. A key feature of TCSPC is that the probability of detecting an individual photon is very low; typically for every 100 excitation pulses, only one emitted photon from the sample is counted. Figure 4.3(a) illustrates how in most inter-pulse periods, no fluorescence photons are detected. At such a low probability of detection, the measured signal represents the probability distribution of the emitted photons, in other words, the probability of detecting a fluorescence photon at a given time delay, t . The probability of detecting a photon is highest at the time when the fluorescence intensity of the sample is highest, so the probability distribution in effect represents the intensity decay versus time of the sample. Figure 4.3(b) shows that a histogram of the photon detection probability (shown in cyan) is used to represent the intensity decay versus time of the fluorescence sample (shown in green).

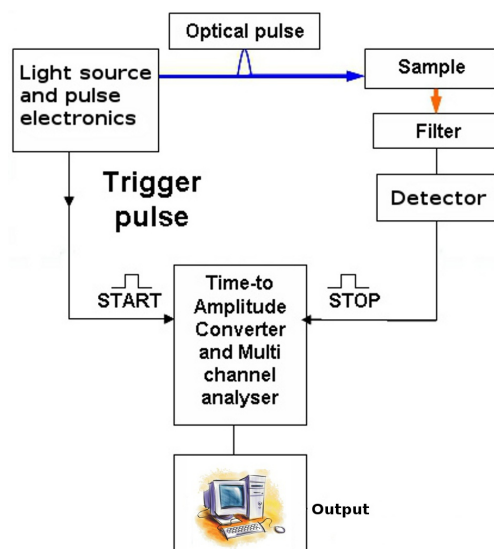


FIGURE 4.2: Simplified block diagram of a TCSPC system.

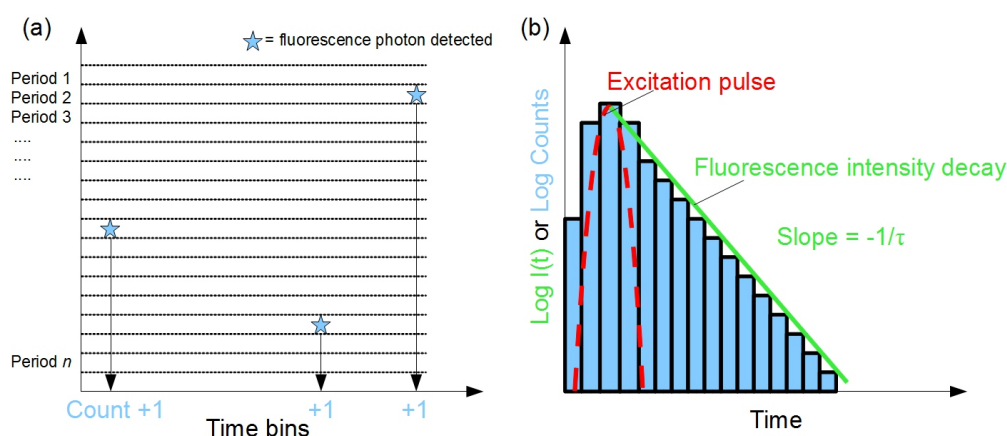


FIGURE 4.3: Illustration of the basic measurement process of TCSPC.

It is important to note that there are variations on this basic description of TCSPC. One variation, which will be mentioned in subsequent sections, is the ‘reverse mode’, or ‘reversed start-stop’. This is very similar to the method discussed above, except the start signal is given by the detection of a photon, and the stop signal is given by the next excitation pulse. The advantage of this method is that the TAC is only used when a photon is detected. This means that the TAC does not need to be reset after periods where no photon is detected. Resetting the TAC can take 10-20 ns, which is long enough to become problematic at high excitation-pulse repetition rates.

The main advantage of TCSPC is its excellent time resolution. For analog signal recording techniques, the time resolution is determined by the bandwidth of the detector. In TCSPC, the time resolution is determined by how accurately the arrival time of photons can be determined. This accuracy is set by the transit time spread (TTS) of the detector. The TTS of a given detector is typically an order of magnitude lower than

its bandwidth [17], thus TCSPC allows for measurements with higher time resolution. TCSPC is also highly precise and highly sensitive, allowing low light levels to be measured. In addition, TCSPC is able to record photons at a rate of up to about 5×10^6 photons per second, meaning that reasonable fluorescence lifetime measurements can be achieved on millisecond time scales [17]. In the subsequent sections, novel and compact TCSPC systems will be presented which utilise micro-LEDs as excitation sources.

4.3 TCSPC using a ‘first-generation’ CMOS-controlled micro-LED device

4.3.1 Experimental set-up

In this section, a monolithically integrated, single-chip excitation and detection system will be presented which uses the TCSPC technique to measure the fluorescence lifetime of colloidal quantum dot (CQD) samples. The excitation source is a UV (370 nm peak wavelength) micro-LED array, and the detector is an array of single photon avalanche diodes (SPADs). The micro-LED array is bump-bonded to, and controlled by, the ‘first-generation’ CMOS control chip which was introduced in chapter 3, section 3.2. The SPAD array is integrated within the CMOS chip itself, as detailed in chapter 3, section 3.2.1. The fabrication and performance of this device is covered in detail in section 3.2; this section will concentrate on the application of the device to TCSPC.

The TCSPC system was configured such that it operated in reverse mode. Examining the sub-system blocks in figure 4.2, the light source and pulse electronics is provided by the CMOS-controlled micro-LED array, the detector is the SPAD array on the CMOS chip, and the TAC, MCA and other timing electronics are provided by an external TCSPC module (Becker & Hickl, SPC-730). The excitation pulses from the micro-LED array are synchronised to the rising edge of the system clock, which is also used to synchronise the TCSPC module. Each micro-LED pixel was biased to draw 4 mA of current and the clock frequency was set to ≈ 3.7 MHz. The optical pulse width output from the micro-LEDs is controlled electrically via a graphical user interface (GUI), as described in section 3.2. For the subsequent measurements, the optical pulse width from the micro-LEDs was set to 8 ± 0.12 ns, with a rise and fall time of 2.15 and 3.31 ns, respectively. Although optical pulse durations as short as ≈ 1.1 ns were possible with this setup, at such short pulse durations the pulse intensity decreases. This subsequently reduces the intensity of the resulting fluorescence emission from the sample, decreasing the signal-to-noise ratio in this initial, non-optimised system. The voltage pulse output from the SPAD array was used as the start signal to trigger the TAC timing. The

voltage pulses had a duration of approximately 30 ns FWHM, with 100 ps of timing jitter. The SPAD dark count rate is given as 10 Hz at room temperature. Assuming that external light is completely blocked, then the dark count rate effectively determines the background count rate, i.e. the rate of SPAD counts that are not due to micro-LED or fluorescence emission. Measurements were performed with minimal background room light, and with a blackout cloth covering the system to protect it from external light.

The samples measured were CdSe/ZnS colloidal ‘core-shell’ quantum dots (CQDs) in a toluene solution (supplier, Evident Technologies Inc.). The basic characteristics of such CQDs were discussed in chapter 1. Quantum dots were chosen for this initial ‘proof of principle’ demonstration as they have a relatively long fluorescence lifetime of 15-20 ns. Additionally, they have a high quantum yield and their absorption spectra are suited for excitation by the UV-emitting micro-LED array. Quantum dots are also used as fluorescent probes for labelling biological cells [1, 18], so demonstrating the capability to measure the fluorescence lifetimes of quantum dots has merit beyond simple proof of principle demonstrations.

Figure 4.4 shows the absorption and emission spectra, in toluene, of the three quantum dot samples used, named ‘Adirondak Green’, ‘Catskills Green’ and ‘Hops Yellow’ by the supplier, and table 4.1 provides some properties of the samples. The samples were sealed in a $24 \times 24\text{mm}^2$ coverslip in order to prevent evaporation. The coverslip was then positioned on top of the sapphire substrate of the micro-LED array, as illustrated schematically in figure 4.5. A photograph of the system in operation is shown in figure 4.6. Excitation light from the pulsed micro-LED array caused the quantum dots to emit light and the subsequent emission from the quantum dots was measured by the SPAD array situated on the CMOS driver chip underneath the micro-LED array. Thus, a single chip performed the dual function of fluorescence excitation and detection. The pulsed output from the SPAD was passed to the external TCSPC timing module to record the fluorescence decay histogram.

TABLE 4.1: Properties of the quantum dot samples investigated using this system

Sample	Peak absorption (nm)	Peak emission (nm)	Emission FWHM (nm)	Concentration (nmol ml^{-1})
Adirondak Green	< 400	542.5	24.8	77
Catskills Green	< 400	563	25.25	69
Hops Yellow	< 400	571	42.6	57

One disadvantage of the single chip fluorescence excitation and detection approach is that it was not practical, at least in this first demonstration, to place an optical filter between the micro-LED and SPAD arrays due to their close proximity. In an ideal TCSPC system, the excitation source should be isolated from the detector using spectral

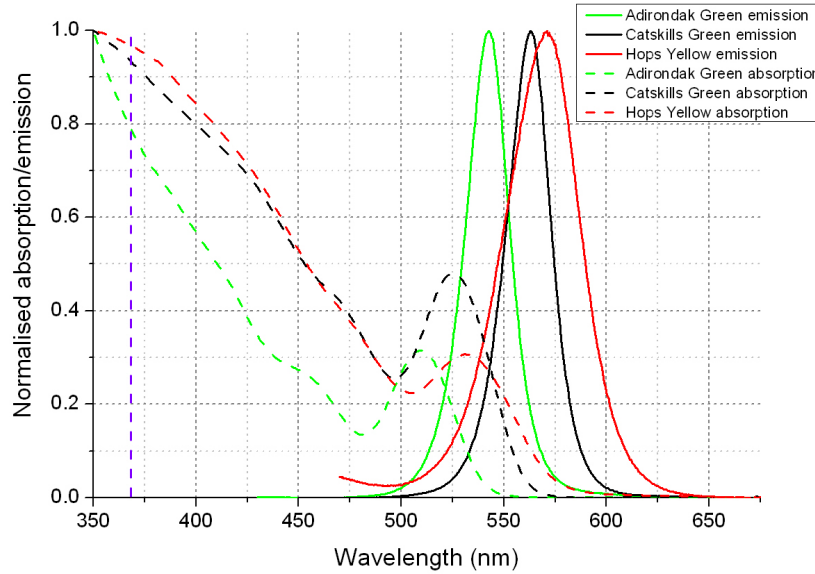


FIGURE 4.4: Quantum dot absorption and emission spectra for the samples in toluene. The 370 nm peak emission of the micro-LED is indicated by the purple dashed line.

filters in order to prevent unabsorbed excitation light being measured during photon counting. If present in the output histogram, excitation light could obscure some features from the fluorescence decay curve. However, even though spectral filters could not be implemented, an alternative approach was used to minimise the level of micro-LED excitation light that was detected from by the SPAD array. First of all, ‘spatial filtering’ was used, in other words a single micro-LED pixel was used to excite the sample and a single SPAD was used to measure the output and by ensuring that the micro-LED pixel and SPAD were as far apart as possible on the chip then the level of micro-LED light detected by the SPAD could be kept to a minimum. The spacing in this case was $800 \mu\text{m}$, corresponding to a separation of 8 rows of the CMOS driver chip. The SPAD photon detection probability (PDP) is a measure of the probability that a photon that impinges on the SPAD active area will trigger an avalanche breakdown, in other words a measure of the probability of whether a particular photon will be measured by the SPAD. The PDP is strongly wavelength dependent. As figure 4.7 illustrates, the SPAD PDP is relatively low at wavelengths corresponding to the emission of the UV micro-LED (10-15%), and higher at wavelengths corresponding to the emission from the quantum dots ($\approx 25\%$). Thus, the SPADs are more sensitive to the fluorescence emission than the micro-LED emission, helping to discriminate between fluorescence emission and micro-LED emission.

It should be noted that significant micro-LED emission was still detected by the SPAD when measuring the quantum dot samples. However, as the duration of the micro-LED excitation pulse was significantly shorter than the fluorescence lifetime of the quantum

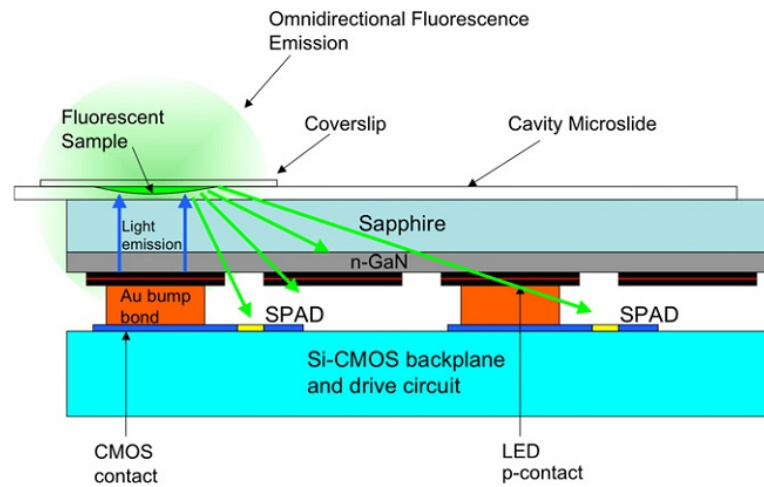


FIGURE 4.5: Cross-sectional schematic of the micro-LED/CMOS fluorescence excitation and detection chip.

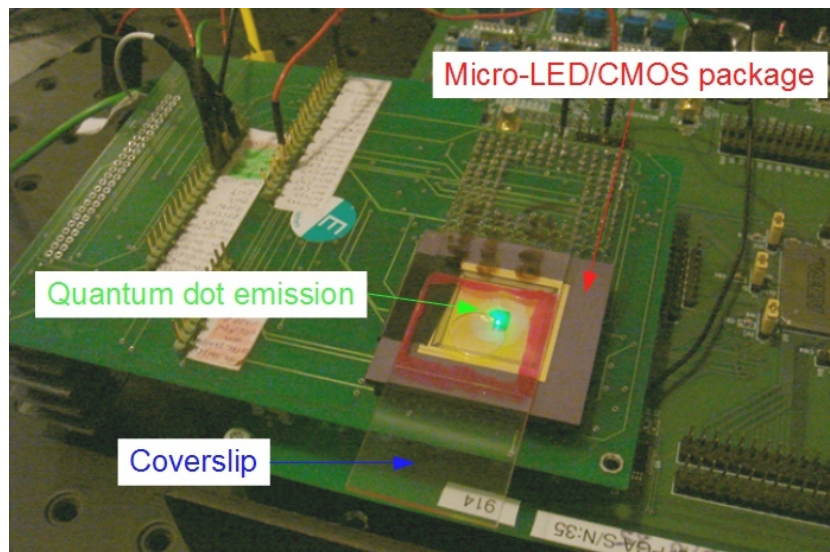


FIGURE 4.6: Photograph of the micro-LED/CMOS TCSPC system, showing the cavity microslide, the micro-LED/CMOS package, and the green emission from the quantum dot sample under micro-LED excitation.

dots (8 ns compared to 15-20 ns) then the emission from the quantum dots could still be clearly distinguished from the micro-LED excitation pulse.

4.3.2 Results - quantum dot fluorescence lifetimes

The instrument response function (IRF) is the response of the TCSPC system to a sample with $\tau = 0$. It is determined by the optical excitation pulse and the characteristic response of the detector and timing electronics. In the case of this micro-LED based TCSPC system, the optical excitation pulse from the micro-LED array dominates the IRF, so the IRF approximately represents the optical excitation pulse. The IRF was

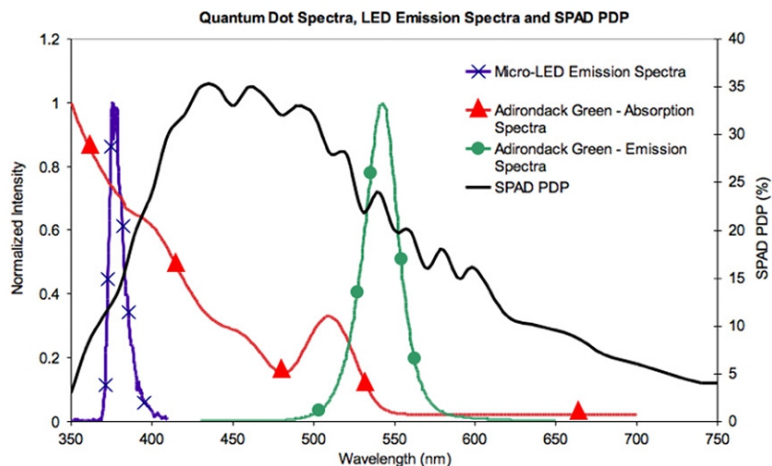


FIGURE 4.7: Quantum dot absorption and emission spectra, micro-LED emission spectra and SPAD PDP. Note that the emission of the micro-LED coincides with a range where the SPAD PDP is relatively low, helping to reduce photon counts caused by micro-LED emission.

measured using a Ludox dilute scattering solution, which is a non-fluorescent sample used here to provide a reference. The measured fluorescence decay curves are a convolution of the IRF and the fluorescence intensity decay of the sample. Fitting software was used to de-convolve the two responses and to fit to the samples decay characteristics.

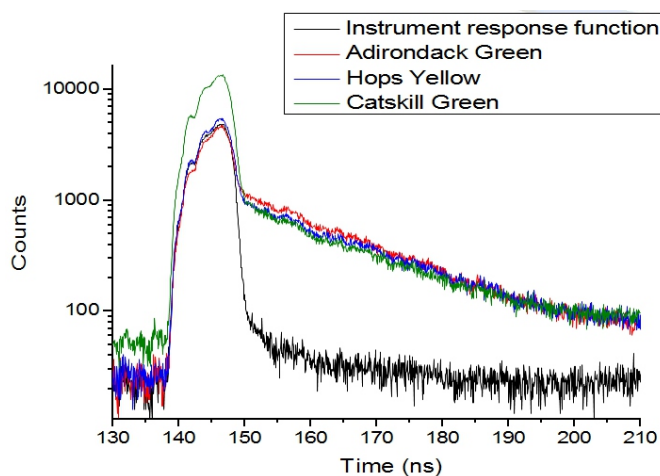


FIGURE 4.8: IRF and measured fluorescence decays of quantum dot samples.

The histograms recorded by measuring the three quantum dot samples in the micro-LED based TCSPC are shown in figure 4.8. As can be seen, the fluorescence decay curves from the quantum dots can be clearly distinguished from the micro-LED excitation pulse (represented here as the IRF). The curves were exported to the FASTTM fitting and lifetime extraction software from Edinburgh Instruments Ltd. The three samples were fitted as mono-exponential decays with lifetimes of 17.8, 17.2 and 19.1 ns for the Adirondack Green, Catskills Green and Hops Yellow quantum dots, respectively. The estimated measurement error was ± 100 ps, based on the timing jitter of the SPADs.

These extracted lifetimes are in good agreement with those quoted by the quantum dot manufacturer (15-20 ns), and measurements performed independently in a conventional TCSPC system, demonstrating that this system is suitable for measuring samples with relatively long lifetimes. These results were reported in [19]. In the following section a system capable of measuring samples with shorter lifetimes will be presented, which also allows for greatly improved filtering between the fluorescence excitation source and the detector.

4.4 TCSPC using a ‘third-generation’ CMOS-controlled micro-LED device

4.4.1 Lifetime measurement of organic semiconductors and colloidal quantum dots

Although a single-chip fluorescence excitation and detection chip was presented in the previous section and shown to be applicable to TCSPC measurements, the system had some drawbacks. First of all, the relatively long optical excitation pulses generated in the basic form made it difficult to accurately measure samples with short lifetimes. Many commonly used fluorophores have lifetimes of ≤ 5 ns, so the 8 ns optical pulses used in the device described in section 4.3 would largely obscure the decay curves from such samples. The second shortcoming of the device was that it was difficult to use spectral filters to prevent the detector counting photons from the micro-LED excitation source. Being able to use shorter optical pulses from the micro-LEDs and being able to place a filter between the micro-LED and the detector would allow for fluorescent samples with shorter lifetimes to be measured with greater accuracy. As such, an improved TCSPC system was developed based on the ‘third-generation’ of CMOS-controlled micro-LEDs. This section will discuss the application of the third-generation of CMOS-controlled micro-LEDs to a TCSPC system. The reader is referred back to chapter 3, section 3.4 for a detailed description of the fabrication, characterisation and operation of these devices.

Although the basic operating principle of the modified micro-LED based TCSPC system is broadly similar to that described by section 4.3 and figure 4.2, there are two key differences when compared to the previous system. First of all, sub-nanosecond optical pulses of ‘usable’ energy are possible using the third-generation CMOS-controlled micro-LEDs. Secondly, the SPAD array is no longer integrated on the CMOS control chip, but is now separate - effectively this is a two-chip system. This physical separation between the CMOS-controlled micro-LED array and the SPAD array allows for spectral filters to

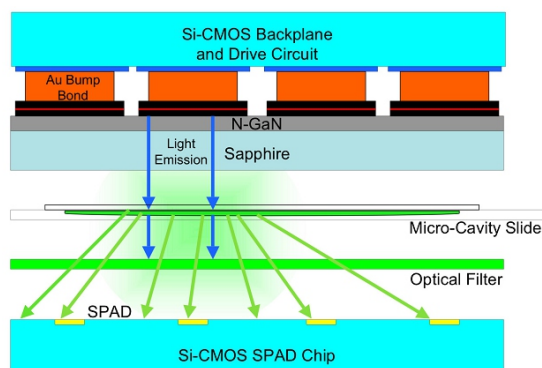


FIGURE 4.9: Cross-sectional schematic of a two chip, micro-LED/CMOS and SPAD array fluorescence excitation and detection chip.

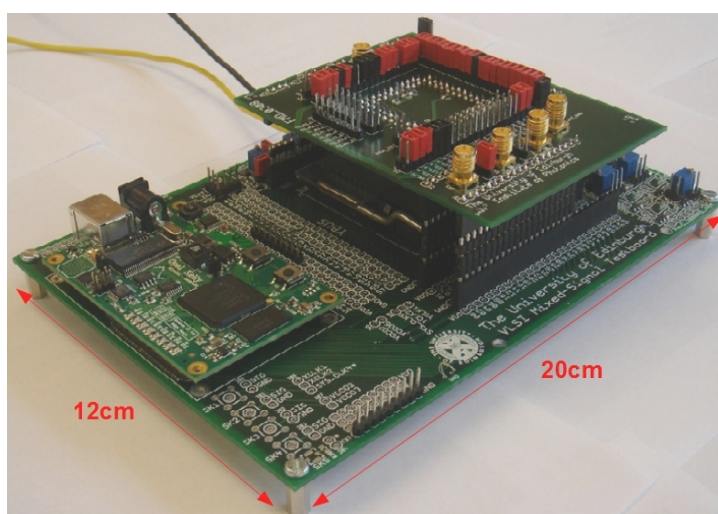


FIGURE 4.10: Photograph of the micro-LED/CMOS and SPAD TCSPC system, showing the motherboard, daughter cards and FPGA board.

be placed between the micro-LEDs and the SPADs. This is illustrated schematically in figure 4.9, which shows a cross-sectional schematic of the system. The fluorescent sample is now ‘sandwiched’ in between the two chips, with the SPAD array on the bottom and the CMOS-controlled micro-LED array on top. The SPAD and CMOS-controlled micro-LED arrays are on their own separate daughter cards, which are both connected to the same test motherboard as described in chapter 3, section 3.4.3. A high-pass spectral filter is placed between the sample and the SPAD array, allowing the longer-wavelength emission (represented by green arrows) from the sample to pass, but preventing the excitation light from the micro-LEDs (represented by blue arrows) from impinging on the SPADs. Although this system requires an additional chip and an optical filter it remains very compact, comfortably fitting onto a small motherboard as shown in figure 4.10. Indeed, this board could be shrunk considerably further by removing hardware that is not required for TCSPC measurements.

The light-emitting polymer BBEHP-PPV, an important organic laser gain medium, has

been reported to have a fluorescence lifetime of approximately 650 ps [20]. It was chosen for investigation using the two-chip TCSPC system in order to establish whether samples with sub-nanosecond fluorescence lifetimes could be accurately measured. BBEHP-PPV can be excited by micro-LEDs emitting at wavelengths in the UV to blue wavelengths (figure 4.11). A BBEHP-PPV sample was spin-coated onto a coverslip and placed in the measurement system between the SPAD and CMOS-controlled micro-LED arrays. A micro-LED array with peak emission of 450 nm was chosen. A 514 nm high-pass filter (Semrock, LP02-514RU-25) was used to prevent unabsorbed micro-LED light from being detected by the SPAD array. A single micro-LED pixel was chosen as the fluorescence excitation source, and the micro-LED was forward biased with a voltage of 4.88 V, with LED_GND = 0 V. This forward bias corresponds to a current of ≈ 80 mA and an average optical output power of ≈ 2.2 mW under CW operation. The optical pulse duration from was set to ≈ 0.9 ns, with a pulse repetition rate of 3 MHz.

A spin-coated sample of the light-emitting ‘T3’ truxene oligofluorene material, as introduced in chapter 1, section 1.4.1, was also measured using this system. The T3 was mixed into a blend with a polymeric host material prior to spin-coating. Further details on this composite blend material may be found elsewhere [21]. A third sample consisting of 609 nm peak-emission CdSe/ZnS colloidal quantum dots (CQDs) in toluene solution was also measured. The basic characteristics of these CQDs were introduced in chapter 1. For these measurements, the system was configured in an identical manner as for the BBEHP-PPV measurements as described above.

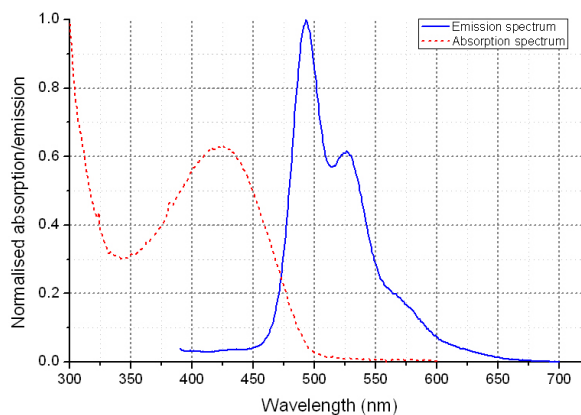


FIGURE 4.11: Absorption and emission spectra of a spin-coated film of BBEHP-PPV light-emitting polymer.

The results from the BBEHP-PPV TCSPC measurement are shown in figure 4.12. A fit was performed using Gray Labs TRI2 Time-resolved analysis software, version 2.1, kindly supplied by Dr. Paul Barber of the Gray Institute for Radiation and Oncology, University of Oxford. The measured data is shown in blue, the fit is shown in red, and the standard deviation residuals, are also shown in figure 4.12. The fit function was a

mono-exponential of the form:

$$I(t) = Z + A * e^{(-t/\tau)} \quad (4.2)$$

where $I(t)$ represents the fluorescence intensity from the sample as a function of time. The fit parameters found were $Z = 49.15 \pm 1.0$, $A = 7820 \pm 60.59$ and $\tau = 1.06 \pm 0.01$ ns, with $\chi^2 = 1.13$. The errors given in this case are the fitting errors as provided by the software. It can be seen in figure 4.12 that this fit fairly accurately describes the fluorescence decay of the BBEHP-PPV light-emitting polymer. Taking the error of the extracted value of τ to be the 100 ps of timing jitter of the SPADs, plus the fitting error from the software, then the fluorescence lifetime of the BBEHP-PPV sample is found to be 1.06 ± 0.11 ns, compared with the reported value of $\tau = 650$ ps given in the literature [20]. There is a discrepancy of around 300 ps in the measured and extracted values for τ , although the values agree within a factor of 2. Recalling that the 370 nm-emitting CMOS-controlled micro-LED arrays are able to produce shorter optical pulses than the 450 nm-emitting device used here (300 ps, compared to 820 ps), then repeating this demonstration using a shorter optical excitation pulse from a 370 nm device may allow for a more accurate value of τ to be extracted. It is also worth pointing out that whilst CMOS-controlled micro-LED based TCSPC will not be able to match the accuracy of more conventional laser-based TCSPC, this may not necessarily be a problem. For example, for a particular application the measurement system may only need to be capable of distinguishing between two fluorescent samples with fluorescence lifetimes that differ by an order of magnitude (e.g. 800 ps and 8 ns), a task that would be well within the capability of this CMOS-controlled micro-LED based TCSPC system.

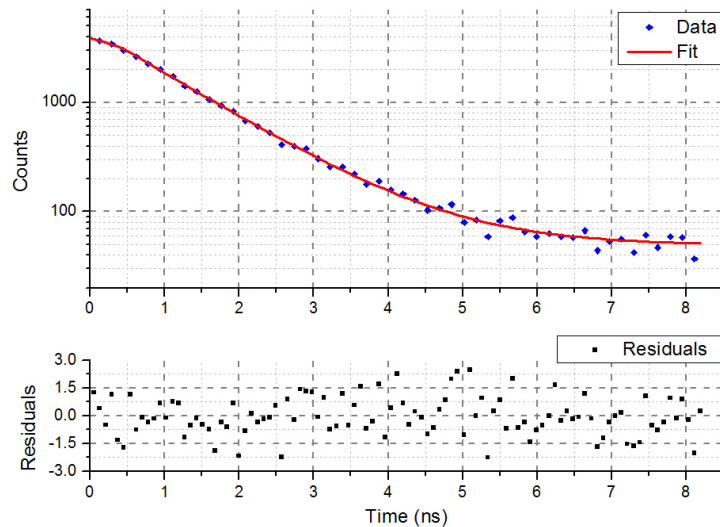


FIGURE 4.12: Measured fluorescence decay of BBEHP-PPV LEP. The measured data, fit and residuals are shown as blue, red and black, respectively. $\chi^2 = 1.13$.

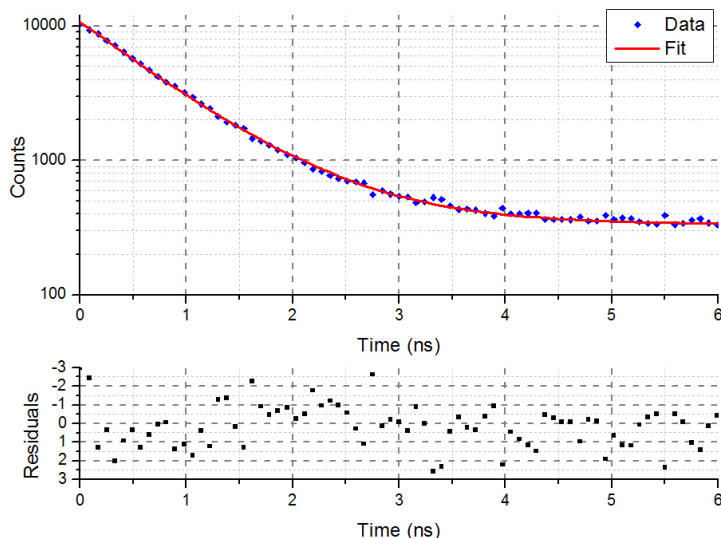


FIGURE 4.13: Measured fluorescence decay of T3 blend. The measured data, fit and residuals are shown as blue, red and black, respectively. $\chi^2 = 1.09$.

The results from the T3 blend measurement are shown in figure 4.13. A fit was performed using Gray Labs TRI2 Time-resolved analysis software, as described above. The measured data is shown in blue, the fit is shown in red, and the standard deviation residuals, are also shown in figure 4.13. The fit function was a bi-exponential of the form:

$$I(t) = Z + A1 * e^{(-t/\tau_1)} + A2 * e^{(-t/\tau_2)} \quad (4.3)$$

The fit parameters found were $Z = 334.22 \pm 1.72$, $A1 = 30350.8$, $\tau_1 = 0.67$ ns, $A2 = 12957 \pm 266.42$ and $\tau_2 = 0.89 \pm 0.01$ ns, with $\chi^2 = 1.09$. As above, the errors given are the fitting errors provided by the software. It can be seen in figure 4.13 that this fit fairly accurately describes the fluorescence decay of the T3 blend light-emitting polymer. Taking into account the 100 ps of timing jitter from the SPADs, the fluorescence lifetimes for the T3 blend were found to be $\tau_1 = 0.67 \pm 0.1$ ns and $\tau_2 = 0.89 \pm 0.1$ ns. This compares favourably with the previously reported measurements on similar spin-coated T3 blend samples, performed using a conventional TCSPC system, which found lifetime values of $\tau_1 = 0.68 \pm 0.01$ ns and $\tau_2 = 1.23 \pm 0.12$ ns [21]. Wu *et al.* attributed the dominant 0.68 ns component to the intrinsic lifetime component of the T3 molecules, and the longer 1.23 ns component to aggregation of T3 molecules within the blend [21].

For the CQD measurement a fit to the data was performed as described above. The measured data (blue), the fit (red) and the standard deviation residuals (black) are shown in figure 4.14. The fit function was a bi-exponential of the same form as described in equation 4.3. The fit parameters found were $Z = 48.01$, $A1 = 1152.96 \pm 34.25$, $\tau_1 = 32.74 \pm 0.37$ ns, $A2 = 1117.91 \pm 26.98$ and $\tau_2 = 11.94 \pm 0.39$ ns, with $\chi^2 = 1.03$. From figure 4.14 it can be observed that the fit fairly accurately describes the fluorescence

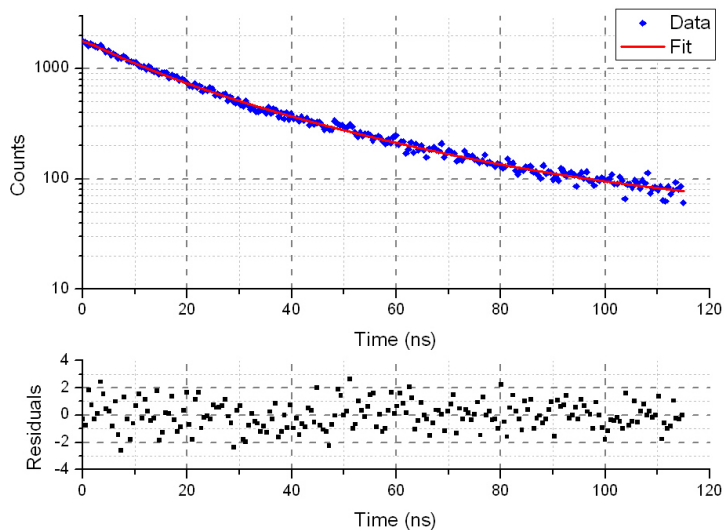


FIGURE 4.14: Measured fluorescence decay of CdSe/ZnS CQDs in toluene solution. The measured data, fit and residuals are shown as blue, red and black, respectively. $\chi^2 = 1.03$.

decay of the CQDs. Once again taking into account the 100 ps of timing jitter from the SPADs, the fluorescence lifetimes for the CQDs were found to be $\tau_1 = 32.74 \pm 0.47$ ns and $\tau_2 = 11.94 \pm 0.49$ ns. This is in reasonable agreement with previous reports which suggest that the lifetimes of CdSe/ZnS CQDs tend to be dominated by a 20-30 ns component, with a shorter component of the order of 5 ns [22].

4.4.2 Lifetime measurements of Rhodamine dyes using on-chip lifetime processing circuitry

Although the fluorescence lifetime systems presented in sections 4.3 and 4.4.1 demonstrate that micro-LEDs and SPADs can be used to produce potentially cheap and compact fluorescence excitation and detection micro-systems, they still rely on specialised electronic time-correlated photon counting modules which typically cost in excess of £10,000. This high price point provides a hurdle to the production of a widely-available TCSPC system. Performing fluorescence lifetime computation directly on a CMOS chip is an alternative approach. A two-chip system is presented in this section which computes a lifetime using circuitry integrated onto a SPAD array chip. This work was carried out by Dr. Bruce Rae from the University of Edinburgh. Aside from computing the fluorescence lifetime using this method rather than using a dedicated external TCSPC module, this system can be considered to be otherwise identical to that described in section 4.4. Some commonly-used fluorescent dyes were examined using this system, to investigate its accuracy. The energy level scheme for such dyes is as described in section 1.4.1.

The basic principle of the on-chip lifetime extraction method is as follows. As the decay histogram is being measured, it is split into two contiguous areas, termed D_0 and D_1 . From the two areas, the pre-exponential factor A and lifetime τ can be calculated as follows [23]:

$$\tau = \frac{-\Delta t}{\ln\left(\frac{D_1}{D_0}\right)} \quad \text{and} \quad A = \frac{D_0}{\tau\left(1 - \frac{D_1}{D_0}\right)} \quad (4.4)$$

This technique has the advantage that it does not need to fit to a large number of data points, allowing values of A and τ to be calculated much more quickly and easily than the NLLS method. This calculation is performed directly on-chip, removing the need for an external timing module. A more detailed description of the hardware implementation of this lifetime extraction method is reported elsewhere [16, 24].

The fluorescent dyes Rhodamine 6G (R6G) and Rhodamine B (RB) are commonly used short-lifetime dyes within the biomedical sciences. Samples of R6G, RB and a sample of ‘Hops Yellow’ quantum dots were measured using this two-chip TCSPC micro-system to test its accuracy. The R6G and RB samples were diluted in water and the quantum dots in toluene, with the concentrations being 250, 100 and 57 μM , respectively. The samples were sealed in a cavity micro-slide, each with a sample volume of 45 μL , with each slide being placed into the system in the same manner as described previously. A micro-LED with peak emission of 450 nm and a pulse FWHM of 910 ps was used to excite the samples. The recorded histograms are shown in figure 4.15. The lifetimes extracted from this data were 4.36, 1.34 and 13.81 ± 122 ns for the R6G, RB and quantum dot samples, respectively. As with the previous measurements, the estimated error is dominated by the SPAD timing jitter. The extracted lifetimes of the two Rhodamine samples are consistent with those reported elsewhere in the literature [25].

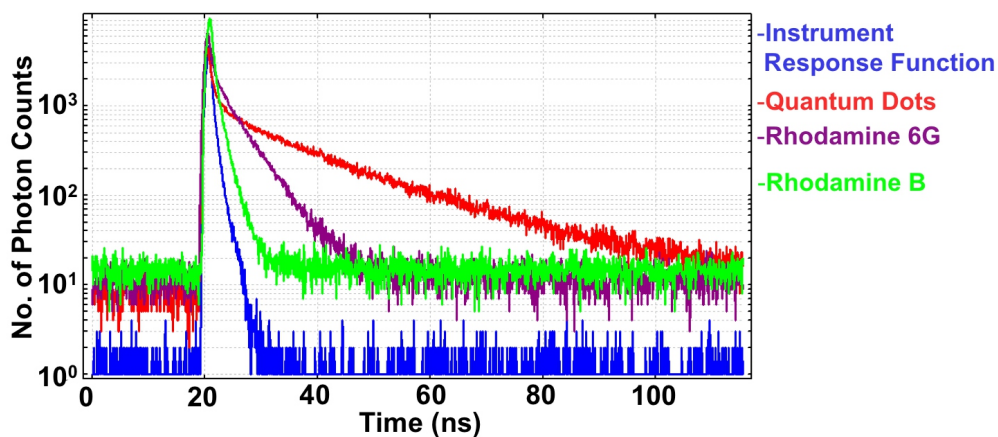


FIGURE 4.15: Measured fluorescence decays of R6G, RB and quantum dot samples. Also presented is the IRF, with 910 ps FWHM.

4.5 Summary

In this chapter, steady-state and time-resolved fluorescence measurements have been introduced, with a particular focus on time-resolved measurements. The instrumentation that is commonly used for time-resolved measurements has been presented and the motivation for using micro-LEDs as novel fluorescence excitation sources has been discussed.

A single-chip TCSPC system, based on the ‘first-generation’ of CMOS-controlled micro-LEDs, was described. This chip used a pulsed CMOS-controlled micro-LED, with a peak emission of 370 nm, as a fluorescence excitation source and an array of SPADs integrated onto the same CMOS chip as a fluorescence detector. This system was shown to be capable of allowing the fluorescence lifetimes of colloidal quantum dot samples to be accurately extracted.

A two-chip TCSPC system was also presented, based on the ‘third-generation’ of CMOS-controlled micro-LEDs. This system utilised the shorter optical pulses from the third-generation of CMOS-controlled micro-LEDs, and a different measurement configuration, to improve the accuracy of the measurements and allow samples with shorter radiative lifetimes to be determined more easily.

Both systems are ‘proof of principle’ demonstrations, which could be considerably improved but show that micro-LED arrays are promising light sources for time-resolved fluorescence measurements. Micro-LED arrays are potentially cheaper to fabricate, more robust, more user-friendly and more compact than the light sources typically used for time-resolved fluorescence measurements and could help move these powerful techniques out from specialised research laboratories and into more general point-of-care devices.

References

- [1] Marcel Bruchez, Mario Moronne, Peter Gin, Shimon Weiss, and A. Paul Alivisatos. Semiconductor Nanocrystals as Fluorescent Biological Labels. *Science*, 281(5385): 2013–2016, 1998.
- [2] Jeffrey Sipior, Gary M. Carter, Joseph R. Lakowicz, and Govind Rao. Blue light-emitting diode demonstrated as an ultraviolet excitation source for nanosecond phase-modulation fluorescence lifetime measurements. *Review of Scientific Instruments*, 68(7):2666–2670, 1997.
- [3] Chun En Kung and Jutta K. Reed. Microviscosity measurements of phospholipid bilayers using fluorescent dyes that undergo torsional relaxation. *Biochemistry*, 25(20):6114–6121, 1986.
- [4] Mingda She, Jun Xing, Wen-Ji Dong, Patrick K. Umeda, and Herbert C. Cheung. Calcium binding to the regulatory domain of skeletal muscle troponin c induces a highly constrained open conformation. *Journal of Molecular Biology*, 281(3):445 – 452, 1998. ISSN 0022-2836.
- [5] William R. Ware, Laurence J. Doemeny, and Thomas L. Nemzek. Deconvolution of fluorescence and phosphorescence decay curves. least-squares method. *The Journal of Physical Chemistry*, 77(17):2038–2048, 1973.
- [6] Joseph R. Lakowicz. *Principles of Fluorescence Spectroscopy*. Springer, 3rd edition, 2006.
- [7] D. E. Spence, P. N. Kean, and W. Sibbett. 60-fsec pulse generation from a self-mode-locked Ti:sapphire laser. *Optics Letters*, 16(1):42–44, 1991.
- [8] Rintaro Koda, Tomoyuki Oki, Takao Miyajima, Hideki Watanabe, Masaru Kuramoto, Masao Ikeda, and Hiroyuki Yokoyama. 100 W peak-power 1 GHz repetition picoseconds optical pulse generation using blue-violet GaInN diode laser mode-locked oscillator and optical amplifier. *Applied Physics Letters*, 97(2):021101, 2010.
- [9] C.D. McGuinness, K Sagoo, D McLoskey, and D.J.S. Birch. A new sub-nanosecond LED at 280 nm: application to protein fluorescence. *Measurement Science and Technology*, 15:L1–L4, 2004.
- [10] Tsutomu Araki and Hiroaki Misawa. Light emitting diode-based nanosecond ultraviolet light source for fluorescence lifetime measurements. *Review of Scientific Instruments*, 66(12):5469–5472, 1995. doi: 10.1063/1.1146519.

-
- [11] Kristina Davitt, Yoon-Kyu Song, William Patterson III, Arto Nurmikko, Maria Gherasimova, Jung Han, Yong-Le Pan, and Richard Chang. 290 and 340 nm UV LED arrays for fluorescence detection from single airborne particles. *Optics Express*, 13(23):9548–9555, 2005.
- [12] I. Rech, A. Restelli, S. Cova, M. Ghioni, M. Chiari, and M. Cretich. Microelectronic photosensors for genetic diagnostic microsystems. *Sensors and Actuators B: Chemical*, 100(1-2):158 – 162, 2004. ISSN 0925-4005.
- [13] A. Cleary, A. Glidle, P. J. R. Laybourn, S. García-Blanco, S. Pellegrini, C. Helfter, G. S. Buller, J. S. Aitchison, and J. M. Cooper. Integrating optics and microfluidics for time-correlated single-photon counting in lab-on-a-chip devices. *Applied Physics Letters*, 91(7):071123, 2007.
- [14] S. X. Jin, J. Shakya, J. Y. Lin, and H. X. Jiang. Size dependence of III-nitride microdisk light-emitting diode characteristics. *Applied Physics Letters*, 78(22):3532, 2001.
- [15] Day-Uei Li, Eleanor Bonnist, David Renshaw, and Robert Henderson. On-chip, time-correlated, fluorescence lifetime extraction algorithms and error analysis. *J. Opt. Soc. Am. A*, 25(5):1190–1198, 2008.
- [16] Day-Uei Li, Richard Walker, Justin Richardson, Bruce Rae, Alex Buts, David Renshaw, and Robert Henderson. Hardware implementation and calibration of background noise for an integration-based fluorescence lifetime sensing algorithm. *J. Opt. Soc. Am. A*, 26(4):804–814, 2009.
- [17] Dr. Wolfgang Becker. *The bh handbook*. Becker & Hickl GMBH, 2nd edition, 2006.
- [18] Wolfgang J Parak, Teresa Pellegrino, and Christian Plank. Labelling of cells with quantum dots. *Nanotechnology*, 16:R9–R25, 2005.
- [19] B R Rae, C Griffin, J McKendry, J M Girkin, H X Zhang, E Gu, D Renshaw, E Charbon, M D Dawson, and R K Henderson. CMOS driven micro-pixel LEDs integrated with single photon avalanche diodes for time resolved fluorescence measurements. *Journal of Physics D: Applied Physics*, 41(9):094011, 2008.
- [20] A Rose, ZG Zhu, CF Madigan, TM Swager, and V Bulovic. Sensitivity gains in chemosensing by lasing action in organic polymers. *Nature*, 434(7035):876–879, 2005.
- [21] M. Wu, E. Gu, A. Zarowna, A. L. Kanibolotsky, A. J. C. Kuehne, A. R. Mackintosh, P. R. Edwards, O. J. Rolinski, I. F. Perepichka, P. J. Skabara, R. W. Martin, R. A. Pethrick, D. J. S. Birch, and M. D. Dawson. Star-shaped oligofluorene

- nanostructured blend materials: controlled micro-patterning and physical characteristics. *Applied Physics A - Materials Science & Processing*, 97(1):119–123, OCT 2009. ISSN 0947-8396. doi: {10.1007/s00339-009-5308-x}.
- [22] Warren C. W. Chan, Dustin J. Maxwell, Xiaohu Gao, Robert E. Bailey, Mingyong Han, and Shuming Nie. Luminescent quantum dots for multiplexed biological detection and imaging. *Current Opinion in Biotechnology*, 13(1):40 – 46, 2002. ISSN 0958-1669.
- [23] Richard M. Ballew and J. N. Demas. An error analysis of the rapid lifetime determination method for the evaluation of single exponential decays. *Analytical Chemistry*, 61(1):30–33, 1989.
- [24] Bruce R. Rae, Keith R. Muir, Zheng Gong, Jonathan McKendry, John M. Girkin, Erdan Gu, David Renshaw, Martin D. Dawson, and Robert K. Henderson. A CMOS Time-Resolved Fluorescence Lifetime Analysis Micro-System. *Sensors*, 9(11):9255–9274, 2009. ISSN 1424-8220.
- [25] Inc. ISS. Lifetime data of selected fluorophores, Accessed October 2010 . URL http://www.iss.com/resources/reference/data_tables/LifetimeDataFluorophores.html.

Chapter 5

Micro-LEDs for visible light communications

In this chapter, the application of micro-LEDs to optical communications is investigated. The first section gives an overview of the use of LEDs for optical communications, identifying some key areas where micro-LEDs may be applied. The following section gives the results of frequency response measurements performed on individual micro-LED pixels in order to ascertain the bandwidth available from such devices, and gives some explanation for the different behaviour seen from devices with different designs. Data transmission measurements from a proof-of-principle system are also given, demonstrating error-free optical transmission of data using a single micro-LED pixel at rates in excess of 1 Gbit/s. Finally, the use of novel colour-converter materials based on quantum dots and light-emitting polymers is shown, which demonstrates that these materials offer superior optical modulation bandwidths to the phosphor materials commonly used in white LEDs.

5.1 Visible light communication using LEDs

LEDs have been widely used for decades in optical communications, for short distance free-space and fibre-based systems. Remote controls for consumer electronics are an everyday example of LEDs used for free-space optical communications, where IR-emitting GaAs or GaInAs LEDs are used to optically transmit data from the control to the equipment. An IR-emitting GaAs-based LED suitable for coupling to a silica fibre for optical communications was first demonstrated in 1971 by Burrus and Miller [1]. Since then, due to their low cost, IR-emitting LEDs have become the light source of choice for low to medium bit rate communications (up to ≈ 1 Gbit/s) over relatively short distances

(up to a few km) [2]. Arrays of IR-emitting GaAs resonant-cavity LEDs (RCLEDs) have also been demonstrated for indoor free-space communications at bit rates of up to 155 Mbit/s [3]. A RCLED is a micro-cavity LED structure which emits light normal to the epitaxial wafer surface.

LEDs that emit visible light are also used for so-called Visible Light Communications (VLC). Red-emitting GaInP LEDs are commonly used with polymer optical fibre (POF) for short distance (typically around 10m), low bandwidth (around 100 Mbit/s) communications. POF is cheaper, more robust and is easier to couple light into compared to silica fibre, due to its larger core diameter (up to 1 mm for POF, compared to 100 μm or less for silica fibres). Red light-emitting devices are of interest as there is relatively low loss and low dispersion at these wavelengths [2]. POF is increasingly used to provide optical fibre data links in specific operating environments - for example, POF is integrated into so-called 'infotainment' data links in over 90 models of car sold worldwide [4]. POF is also used for data links in home networks. POF can be fairly easily coupled to the optical data source and receiver, with the eye-safe visible light used to transmit data aiding the alignment, allowing POF networks to easily be connected by untrained persons. At present, most POF links are coupled with either Vertical Cavity Surface-Emitting Lasers (VCSELs) or RCLEDs. Red-emitting (650 nm peak emission) RCLEDs suitable for use with POF have been demonstrated to have modulation bandwidths in excess of 350 MHz [5].

For fibre-based communications, AlInGaN-based LEDs may be of particular interest as there exists an optical attenuation minimum in POF at around 510 nm in the green region of the spectrum [6], as shown in figure 5.1. This could allow for improved performance over systems using red-emitting light sources. Furthermore, the transmission window at 650 nm is fairly 'sharp', meaning that red-emitting light sources to be used for POF applications require a fairly well-defined and narrow emission linewidth, whereas the transmission window at green wavelengths is more forgiving. Green GaN-based LEDs with specially n-doped active layers have been reported with modulation bandwidths of up to 330 MHz [7], and green-emitting RCLEDs have been shown to be capable of transmitting data at 200 Mbit/s over 100 m of POF [6], although fabricating AlInGaN-based RCLEDs remains challenging due to the difficulties associated in producing microcavities in this alloy system [8].

Micro-LED devices are potentially interesting candidates for VLC applications, for a number of reasons. As mentioned in section 2.1.2, micro-LED devices have been demonstrated to have shorter optical turn-off times compared to conventional broad area LEDs,

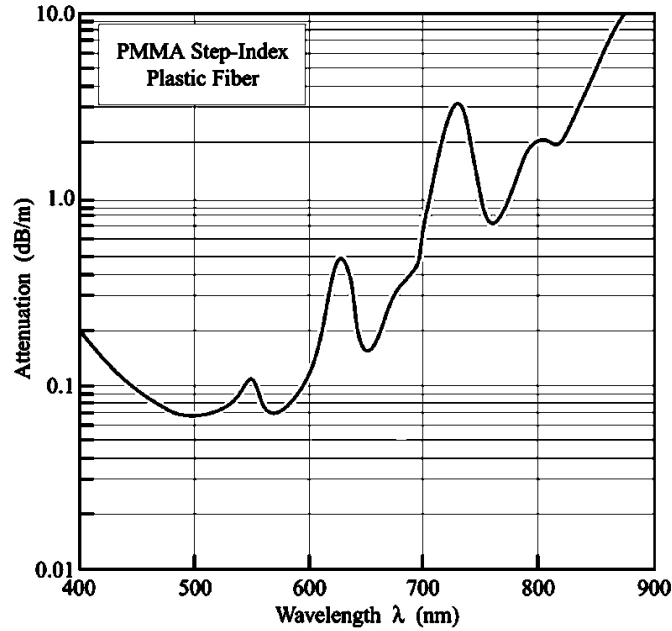


FIGURE 5.1: Attenuation versus wavelength for a step-index PMMA plastic optical fibre. From [2].

indicating that they have higher modulation bandwidths [9]. Furthermore, the micro-pixelated array nature of the devices potentially allows for an array of individually-modulated pixels to be coupled into an array of fibres, allowing parallel data transmission using a single LED chip. Arrays of refractive microlenses positioned with one microlens aligned to each emitter element can in principle be used to collimate the emission from a micro-LED array to aid the coupling of light into POF. Microlens arrays suitable for such an application have been fabricated from several compatible materials, including polymers [10], sapphire [11], GaN [12] and diamond [13]. Finally, micro-LED arrays are considerably easier to fabricate than RCLEDs or VCSELs and are therefore, in principle, cheaper and more manufacturable alternatives for VLC optical sources.

Another area of VLC involves using modulated white-emitting LEDs to transmit data optically whilst simultaneously providing general purpose white-light illumination. At present, early demonstrations of this have been implemented using LEDs with phosphor colour-converting materials with relatively long carrier lifetimes. As will be discussed in section 5.4, novel colour-converters provide an alternative approach which may allow high-bandwidth white light to be generated.

5.2 Micro-LED frequency response measurements

The amplitude of the output power of an AC-modulated LED is a function of the frequency of the AC (alternating current) signal. This defines the frequency response of

the LED. The bandwidth is taken to be the frequency at which the response (amplitude) is reduced to 50% (-3 dB) of its low frequency value. We may define the frequency response, $P(\omega)$, and the bandwidth, f_{3dB} , of an LED as follows [2]:

$$P(\omega) = \frac{1}{\sqrt{1 + (\omega\tau)^2}} \quad (5.1)$$

$$f_{3dB} = \frac{\sqrt{3}}{2\pi\tau} \quad (5.2)$$

where $\tau = RC$, is the RC time constant of the LED, with R and C representing the LED series resistance and capacitance, respectively. Alternatively, if we assume that the bandwidth of the LED is not limited by the RC time constant but instead by the carrier recombination process within the LED active region, we may define τ as average carrier lifetime. It is important to note that equations 5.1 and 5.2 provide an *approximation* of the frequency response of an LED, since the rise and fall times of a practical LED are often not exponential.

In order to assess the frequency responses of micro-LED devices, individual pixels from unpackaged, non-heatsinked micro-LED arrays were examined. A schematic of the frequency response measurement setup is shown in figure 5.2. A three pin ground-signal-ground (GSG) probe with a bandwidth of 40 GHz (Cascade Microtech, ACP40-A-GSG-125) was used to electrically address individual micro-LED pixels. The centre-to-centre pitch of the pins on the probe was 125 μm . The signal pin from the probe was placed on top of the micro-LED p-contact area, and the ground pins were placed onto the n-contact area. The micro-LEDs were then electrically driven by a signal consisting of both a DC and a small-signal AC component. The DC component was provided from a DC power supply, and the AC component was provided by a network analyser (Agilent Technologies 8753ES Option 011). The AC component consisted of a chirped sine wave, of fixed amplitude, and was combined with the DC signal by a three terminal bias-tee. The magnitude of the AC bias was approximately 7% of the DC bias. The optical output of the micro-LED was imaged onto the active area of an amplified fast photodiode (Newport 818-BB21A) having a bandwidth of 1.2 GHz. The AC-coupled output from this photodiode was returned to the input port of the network analyser. The network analyser recorded the amplitude of the electrical input from the photodiode as a function of frequency, allowing the frequency response of the micro-LED under test to be measured. A 1.2 GHz low-pass electrical filter was used between the photodiode and network analyser to reject high-frequency noise.

The photocurrent output (measured in amperes) from the photodiode is directly proportional to the optical power output from the micro-LED under test (measured in Watts). The network analyser measures the electrical power (also measured in Watts) from the

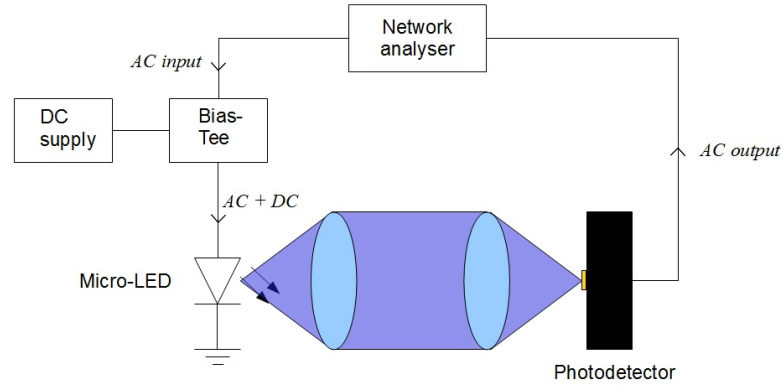


FIGURE 5.2: Schematic of the micro-LED frequency response measurement setup.

photodiode. Since electrical power is proportional to electrical current squared, the measured electrical power output from the photodiode is also proportional to the square of the micro-LED output power. It then follows that the optical -3 dB point is equivalent to the electrical -6 dB point [14]. The network analyser provides data in electrical dB, but for clarity all measured frequency response data presented in this thesis has been converted to optical dB. When -3 dB bandwidths are mentioned during the rest of this thesis, these will refer to the *optical* -3 dB bandwidth of the micro-LED.

5.2.1 16×16 individually-addressable micro-LED frequency responses

The frequency response of 16×16 element individually-addressable micro-LED arrays with respective peak emissions at 370, 405 and 450 nm were measured using the setup discussed previously. The -3 dB frequency as a function of applied DC current, from representative individual $72 \mu\text{m}$ diameter micro-LED pixels from each array, are shown in figure 5.3. It is observed that the -3 dB frequency of the pixels initially increases as the DC current increases, before appearing to reach a saturation point. It is also clear that the current versus bandwidth behaviour, and the maximum bandwidth, is different for devices emitting at the different emission wavelengths. Typical maximum bandwidths observed for the $72 \mu\text{m}$ diameter pixels were approximately 100 MHz at 370 nm, 150 MHz at 405 nm and 245 MHz at 450 nm. A random sample was taken of 8 pixels across the diagonal of the 450 nm array, and a variation of ± 10 MHz in the bandwidth of each pixel was found [15], suggesting that the frequency response of individual pixels across a micro-LED array is quite uniform. To the best of our knowledge, this work represents the highest bandwidth reported for a blue-emitting LED fabricated in the AlInGaIn alloy system.

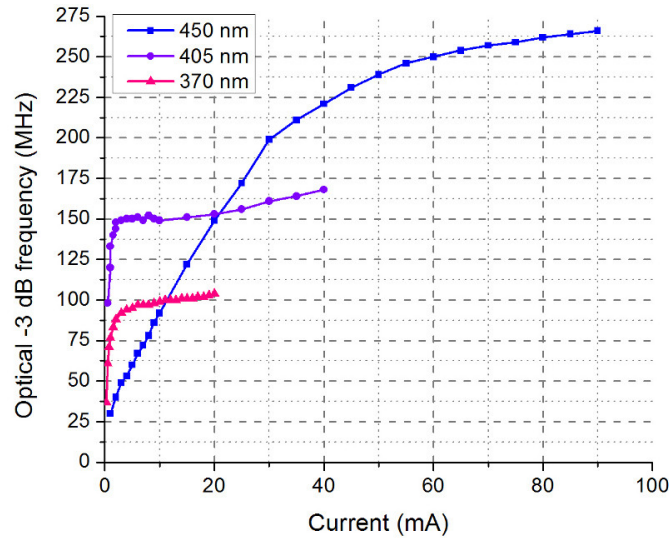


FIGURE 5.3: Frequency response of $72 \mu\text{m}$ diameter micro-LED pixels at several wavelengths, as a function of applied DC current [15].

5.2.2 8×8 individually-addressable micro-LED array frequency responses

As the 8×8 element micro-LED devices have pixel diameters ranging from 14 to $84 \mu\text{m}$, the frequency responses of the pixels in these arrays were investigated in order to determine if there is any variation in frequency response with pixel size. Individual pixels in the arrays were addressed using the GSG probe, either by placing the probe directly on top of the micro-LED array, or onto the pixel p-contact pad. No difference in frequency response was observed between the two different probing configurations, indicating that the contact pads did not affect the frequency response by e.g. adding significant parasitic capacitance.

Different sized pixels from devices with peak wavelengths ranging from 370 to 520 nm were tested. Their frequency response as a function of DC current was measured and, as with the measurements done on the 16×16 device, it was observed that the modulation bandwidth of each pixel was strongly dependent on the applied DC current. Figure 5.4 shows the maximum bandwidth observed, as a function of pixel size and emission wavelength, before device failure at high currents. A modulation bandwidth of almost 450 MHz was observed for the $44 \mu\text{m}$ diameter 450 nm-emitting micro-LED. As was the case with the measurements obtained in section 5.2.1, different performance was obtained from devices with different peak emission wavelengths, with the blue and green devices having considerably larger bandwidths than their UV and violet-emitting counterparts. Examining the modulation bandwidth of each peak wavelength device as a function of current density (the current normalised to the pixel area) indicates that for the same current density, the same modulation bandwidth is observed, regardless of the overall

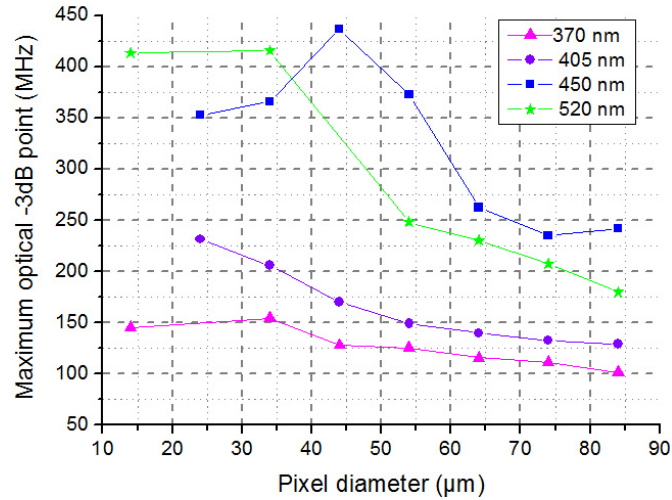


FIGURE 5.4: Maximum modulation bandwidth of micro-LED pixels, of different diameters, for 8×8 micro-LED arrays with peak emissions ranging from 370 to 520 nm.

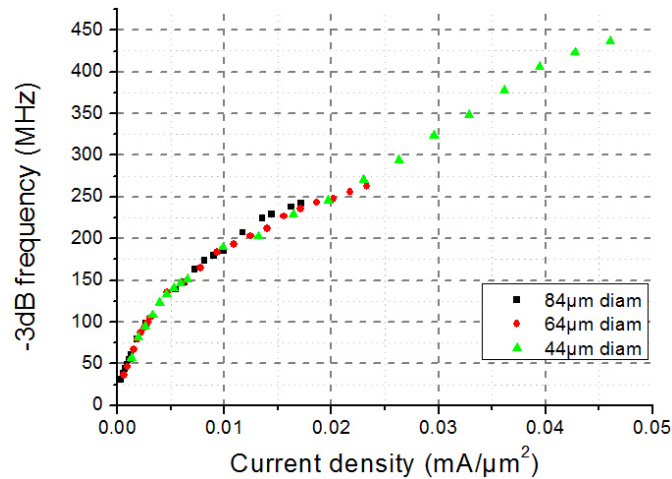


FIGURE 5.5: Bandwidth versus current density for different pixel sizes from the same 450 nm-emitting 8×8 micro-LED array.

pixel size. This is illustrated in figure 5.5, which shows that for the same current density, different sized pixels from the same 450 nm-emitting micro-LED array show the same modulation bandwidth. Another general trend that is observed for all wavelengths is that as the size of the micro-LED pixels are decreased, the maximum modulation bandwidth that can be achieved increases. These results suggest that the smaller pixels have higher modulation bandwidths because they are able to withstand higher operating current densities.

5.2.3 Current dependent micro-LED frequency response

Based on the data presented in sections 5.2.1 and 5.2.2, it can be seen that the frequency response of the micro-LED device seems to be determined by two factors - the epitaxial structure (which varies for different peak emission wavelengths) and the current density. As a consequence, since the smaller devices are able to withstand higher operating current densities, their maximum modulation bandwidth is higher than for otherwise identical larger pixels. Also, the relationship between current density and bandwidth will vary depending on the properties of the LED epitaxy used for each different peak emission wavelength. This section will aim to explain these differences in terms of the current dependent carrier recombination dynamics within the devices. Acknowledgement goes to Dr. Richard P. Green of University College Cork (formerly of the University of Glasgow) for derivation of the model.

The carrier lifetime, τ , within the LED active region may be described by the following equation [16]:

$$\tau(N) = \frac{1}{A + BN + CN^2} \quad (5.3)$$

where, A, B and C are the Shockley-Read-Hall non-radiative recombination, radiative recombination and Auger recombination coefficients, respectively. Having a complete set of lifetimes up to a given current I allows the carrier density $N(I)$ to be found through the following integral [17]:

$$N(I) = \frac{\eta_{int}}{ead} \int_0^I \tau dI \quad (5.4)$$

where η_{int} is the internal quantum efficiency (IQE) of the LED, e is the elementary charge, a is the active area of the LED and d is the active region thickness. For the data presented in this section, an estimated value of $\eta_{int} = 70\%$ was used, based on literature reports [18].

The current through the device can be split into two parts, the radiative current that results in the emission of photons, I_r , and that which is lost to non-radiative recombination paths, I_{nr} . The total current through the device, I , is thus given by:

$$I = I_r + I_{nr} \quad (5.5)$$

The total current, I , the radiative current, I_r , and the non-radiative current, I_{nr} are given by:

$$I = ead(A + BN^2 + CN^3) \quad (5.6)$$

$$I_r = ead(BN^2) \quad (5.7)$$

$$I_{nr} = ead(A + CN^3) \quad (5.8)$$

Equation 5.7 implies that a graph of I_r versus the carrier density squared, N^2 , would yield a straight line with gradient equal to $eadB$. Using L-I data for a given pixel, we may estimate the radiative current as follows:

$$I_r = e * \left(\frac{P}{\hbar\omega * nc} \right) \quad (5.9)$$

where P is the LED output power in Watts, $\hbar\omega$ is the energy of the emitted photons in Joules and nc is the collection efficiency, i.e. the ratio of the number of photons measured in the L-I data compared to the total number emitted by the LED active region. Assuming that every photon emitted into free space by the LED is collected by the photodiode during the L-I measurement, then nc is largely determined by the extraction efficiency, which is the ratio of photons that escape the LED die to the total number emitted by the LED active region. Due to total internal reflection, the majority of photons are trapped within the die. An estimated extraction efficiency of 6.5% was determined, so the value of nc was 0.065. The estimated extraction efficiency is consistent with literature reports [19].

A representative plot of I_r versus N^2 , from a 450 nm emission 44 μm diameter micro-LED, is shown in figure 5.6. It is clear that this plot is not a straight line, counter to that predicted by equation 5.7. In this case, we assume that B is a function of N , and we may define the function $B(N)$ as follows:

$$B(N) = \frac{1}{ead} \frac{dI}{d(N^2)} \quad (5.10)$$

$B(N)$ was calculated using equation 5.10 and the data from figure 5.6. Eliseev *et al.* [20] described the carrier density-dependence of B using a model as described by equation 5.11. In this model, B_0 represents the low-carrier-density limit of B and N^* is a fitting parameter, describing a saturation-type behaviour of the recombination coefficient. To fit this model to the $B(N)$ versus N data, B_0 was found by interpolating the $B(N)$ versus N data to find the value of B when $N = 0$. N^* was subsequently found by fitting the model to the $B(N)$ versus N data. The $B(N)$ versus N data points and the fitted curve are shown in figure 5.7. The parameter values found for this particular data set were $B_0 = 1.9 \times 10^{-16} \text{m}^3 \text{s}^{-1}$ and $N^* = 8.8 \times 10^{23} \text{m}^{-3}$.

$$B(N) = \frac{B_0}{1 + \frac{N}{N^*}} \quad (5.11)$$

Now we consider the non-radiative current. According to equation 5.3, since $A = 1/\tau_0$ we

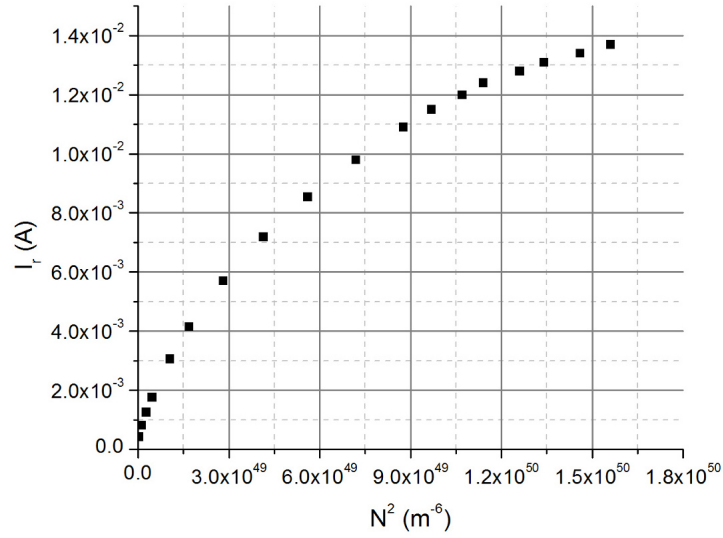


FIGURE 5.6: Radiative current versus carrier density squared for a 450 nm emitting, 44 μm diameter micro-LED pixel.

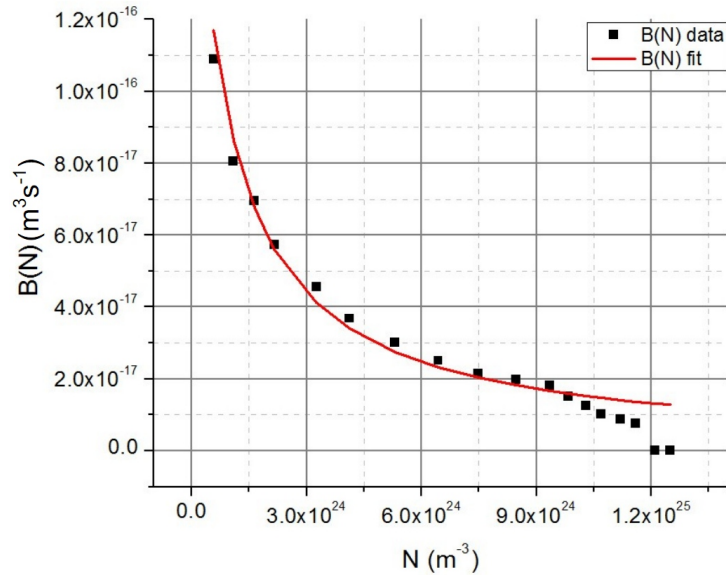


FIGURE 5.7: $B(N)$ versus N for a 450 nm emitting, 44 μm diameter micro-LED pixel. Data points calculated using the pixel L-I curve are shown in black, with the fit shown in red.

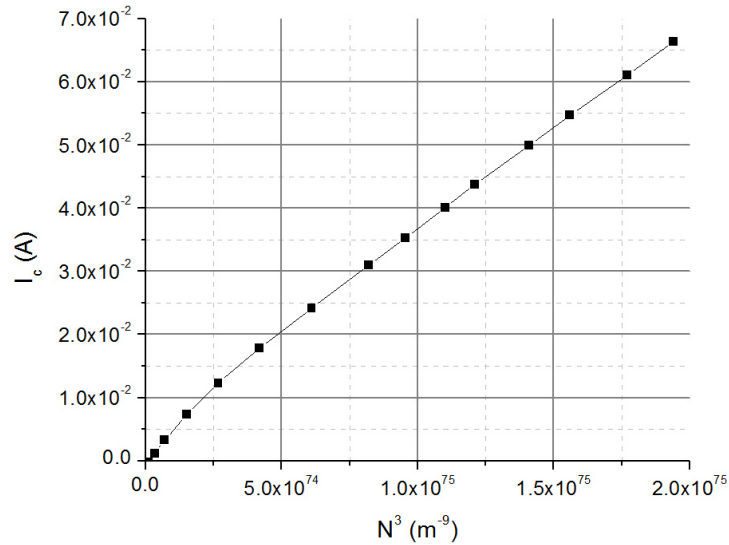
can determine the value of the A coefficient by interpolating the plot of carrier lifetime, τ , versus current density N to find τ_0 , i.e. τ when $N = 0$. For the data taken from the 450 nm emitting 44 μm pixel under consideration, a value of $A = 1.5 \times 10^8 \text{ s}^{-1}$ was found.

As equation 5.5 states, the non-radiative current I_{nr} can be found by subtracting the radiative current, I_r from the total current, I . Using the value of A given above, we can then determine the ‘Auger current’, I_c by subtracting $eadA$ from I_{nr} . Since $I_c = ead(CN^3)$, then a plot of I_c versus the carrier density cubed, N^3 , should be a straight

TABLE 5.1: Fitted coefficient values for data from 450 nm emission micro-LED of various pixel diameter.

	34 μm	44 μm	64 μm	74 μm	84 μm	Average
A (s^{-1})	3.2×10^8	1.5×10^8	1.28×10^8	1.2×10^8	1.2×10^8	1.7×10^8
B_0 ($m^3 s^{-1}$)	1.5×10^{-16}	1.9×10^{-16}	2.7×10^{-16}	2.2×10^{-16}	3.8×10^{-16}	3.0×10^{-16}
N^* (m^{-3})	1.1×10^{24}	8.8×10^{24}	5.9×10^{24}	5.6×10^{24}	3.2×10^{24}	8.7×10^{24}
C_0 ($m^6 s^{-1}$)	6.9×10^{-41}	1.0×10^{-41}	9.4×10^{-41}	4.2×10^{-41}	1.3×10^{-41}	1.1×10^{-41}

line with gradient equal to $eadC$. Figure 5.8 shows the plot of I_c versus N^3 for the pixel under consideration. This data can be reasonably approximated by a straight line, so we determine a value for C by dividing the gradient of this straight line by ead . For this data, a value of $C = 1 \times 10^{-41} m^6 s^{-1}$ was found. The coefficient values found by analysing data from 5 different sized pixels from a single 450 nm emitting 8×8 micro-LED array are summarised in table 5.1.

FIGURE 5.8: I_c versus N^3 for a 450 nm emitting, 44 μm diameter micro-LED pixel.

Now that we have values for each of the parameters, we may use these values with a slightly modified version of the model of $\tau(N)$ given in equation 5.3, in order to model the relationship between τ and N . This modified model is given by equation 5.12:

$$\tau(N) = \frac{1}{A + \frac{B_0}{1 + \frac{N}{N^*}} + CN^2} \quad (5.12)$$

A comparison of the measured data points taken directly from the bandwidth measurements as described in section 5.2, with the fitted model as described by equation 5.12, is shown in figure 5.9. From this graph, it can be seen that our model and the parameters found provide a fairly good fit to the observed data. Table 5.2 provides a comparison between the average coefficient values found here with some values reported in the literature. There is a fairly wide spread of reported values, the fitted values found here

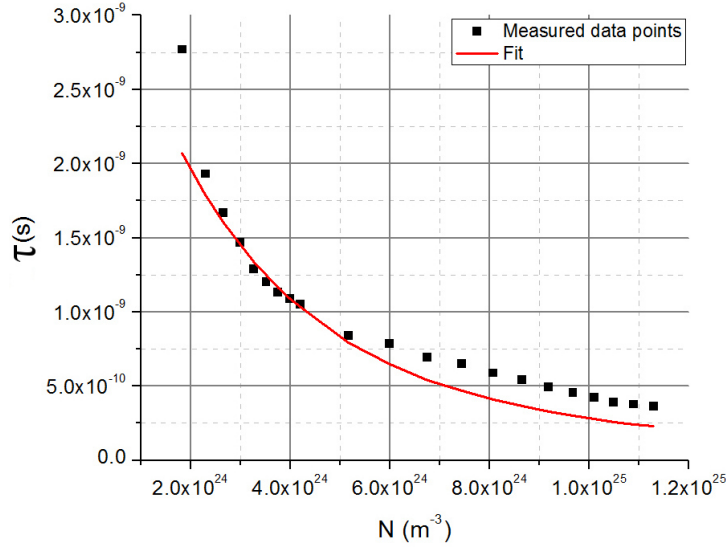


FIGURE 5.9: $\tau(N)$ versus N for a 450 nm emitting, 44 μm diameter micro-LED pixel. Data points calculated using modulation bandwidth data are shown in black, with the fit shown in red.

lie within these ranges. From this we may conclude that the method presented is valid for analysis of the 450 nm emitting micro-LED pixels and provides estimated coefficient values that are in reasonable agreement with other studies.

This model provides a possible explanation for the variation of micro-LED bandwidth with device geometry and epitaxial structure. As shown in section 2.3.2, smaller micro-LED pixels are able to withstand higher current densities (and thus carrier densities) due to their reduced operating temperatures [21]. According to equation 5.12, increased carrier densities result in shorter carrier lifetimes and hence higher modulation bandwidths. Thus, it is postulated that smaller micro-LEDs exhibit higher modulation bandwidths because they are able to operate with higher carrier densities than their larger counterparts. Furthermore, the parameter values used in equation 5.12 will vary depending on the properties of the epitaxial structure of the micro-LED, and hence will vary with micro-LED emission wavelength. Thus, this approach may also explain why micro-LED devices, which are otherwise identical apart from their epitaxial structure and emission spectra, show quite different bandwidth versus carrier density behaviours.

This approach did not yield a particularly good fit for the data measured from the 370 and 405 nm-emitting 8×8 devices, indicating that this model may not be appropriate for shorter-wavelength devices. Analysis of the 520 nm 8×8 array was not undertaken due to an incomplete set of data. It is important to note that the physical meaning of the C coefficient term here is normally taken to be Auger recombination. However, as previously described in detail in section 1.3.3, the magnitude of Auger recombination in AlInGaN materials remains a topic of intense debate. As such, the model presented here

TABLE 5.2: Average coefficient values from table 5.1 compared with literature reports

Emission wavelength (nm)	A (s^{-1})	B (m^3s^{-1})	C ₀ (m^6s^{-1})	Reference
450	1.7×10^8	5.0×10^{-17}	1.1×10^{-41}	This work
430	2×10^7	7×10^{-17}	$\frac{10^{-41}}{1+N/5 \times 10^{18}}$	David <i>et al.</i> [22]
440	2.11×10^7	1.3×10^{-17}	$1.4.2 \times 10^{-42}$	Shen <i>et al.</i> [23]
460	10^7	2×10^{-16}	7.2×10^{-41}	Ryu <i>et al.</i> [24]
407	10^7	2×10^{-17}	1.5×10^{-42}	Zhang <i>et al.</i> [25]
525	7×10^6	$\frac{3.6 \times 10^{-17}}{1+N/7 \times 10^{24}}$	2.7×10^{-42}	Eliseev <i>et al.</i> [20]
325	1.25×10^8	9.84×10^{-17}	5.37×10^{-40}	Shatalov <i>et al.</i> [26]
Not given	1.1×10^9	0.3×10^{-16}	-	Witzigmann <i>et al.</i> [27]
410	$0.2-2.7 \times 10^8$	2.25×10^{-17}	N/A	Hader <i>et al.</i> [28]

does not claim to explain the physical origin of the C coefficient term. Furthermore, it would be worthwhile repeating these measurements under short-pulsed operation, in order to remove any heating effects that may influence the behaviour of the micro-LED.

5.3 Data transmission using micro-LEDs

After measuring the modulation bandwidths of various formats of micro-LED devices, proof-of-principle experiments were carried out to demonstrate the optical transmission of data using micro-LED pixels.

For these experiments, representative micro-LED pixels were probed using a GSG probe, and their optical emission was imaged onto a photodiode in a similar fashion to that discussed in section 5.2. A DC current was combined with a modulated AC signal using a bias-tee, as with the frequency response measurements. In this case, the modulated AC signal was a pseudo-random bit sequence (PRBS) provided from a bit error rate test (BERT) system (Advantest, D3186 Pulse Pattern Generator and D3286 Error Detector). As the BERT did not have its own internal synthesiser, it was clocked using the output from a network analyser. The output of the photodetector was amplified using an external amplifier (HP8447D - dual stage 50dB electrical amplifier, 100kHz to 1.3 GHz), and returned to the BERT. A comparison between the transmitted and received bit patterns was performed by the BERT in order to ascertain the bit-error rate (BER). The BER is the ratio of incorrectly transmitted data bits to the total number of transmitted bits, so for example a BER of 1×10^{-3} would indicate there is 1 incorrectly transmitted bit out of every 1000 that were transmitted. The optical output from the micro-LED under test was attenuated using a neutral density filter wheel (ND wheel, Thor Labs NDM4/M) allowing the BER as a function of received optical power at the photodiode to be measured, with the DC bias to the micro-LED kept constant.

The modulated PRBS from the BERT was a non-return to zero (NRZ) data signal, with a variable peak-to-peak amplitude of 0.5 to 2 V. The BERT was not capable of directly modulating an LED, as the maximum forward bias it can supply is 1 V, well below the typical turn-on voltages for AlInGaN (micro-)LEDs. Therefore, the NRZ output of the BERT was level-shifted by combining the signal with a DC offset voltage, using a bias-tee. An illustration of the NRZ voltage signal used to drive the micro-LED pixel is shown in figure 5.10. The label a in figure 5.10 represents the modulation depth, which was set by the peak-to-peak amplitude of the BERT output. The 0 and 1 logic levels are shown, along with the DC offset level which is determined by the DC voltage supplied by a DC power supply. The optical power output from the micro-LED will be determined by this voltage signal, and the particular I-V, L-I and frequency response characteristics of each individual micro-LED.

For a truly random NRZ data stream, each bit in the sequence has a 50% probability of being either 1 or 0, regardless of the state of the preceding or subsequent bits. Therefore it is possible to have long sequences of consecutive identical digits (CIDs). These long sequences have a very low frequency content, and designing high-speed systems which can handle such content is not trivial. Therefore, data is usually encoded in order to ‘package’ the data in a more easily handled format. The encoding used typically aims to limit the length of CID sequences, and map the data to patterns that can be more easily distinguished from each other, all of which help improve the BER. Different PRBS lengths can be used to mimic data encoded using different schemes. For example, a short pattern length of $2^7 - 1$ bits is often used to test Ethernet communications systems as this provides a good approximation to actual Ethernet which encodes data into 10 bit long ‘packages’ using 8b10b encoding [29]. For this reason, to test the capability of micro-LEDs short PRBS lengths of $2^7 - 1$ and $2^9 - 1$ were used. A long PRBS length of $2^{31} - 1$ bits was also used, as long PRBS lengths are commonly used in Synchronous Optical network (SONET) telecommunications systems. Data transmission rates from 100 Mbit/s to 1.2 Gbit/s were investigated, including data transmission rates of 155 and 622 Mbit/s, which are examples of standard transmission rates used in SONET.

A $34 \mu\text{m}$ diameter micro-LED pixel from an 8×8 array with a peak emission of 520 nm was chosen for an optical data transmission demonstration. This was because (micro-)LEDs emitting at this wavelength are in the low-loss transmission window for polymer optical fibres (POF). The BER versus received optical power data was measured for each bit rate and PRBS length. The DC bias current provided to the micro-LED was 35 mA. Lower currents would inhibit the transmission of data at high data rates, because the response of the micro-LED at low currents is slow as discussed in the previous section, whereas very high currents would cause device failure due to heating effects. Thus 35 mA provided a compromise between device bandwidth and device reliability, though

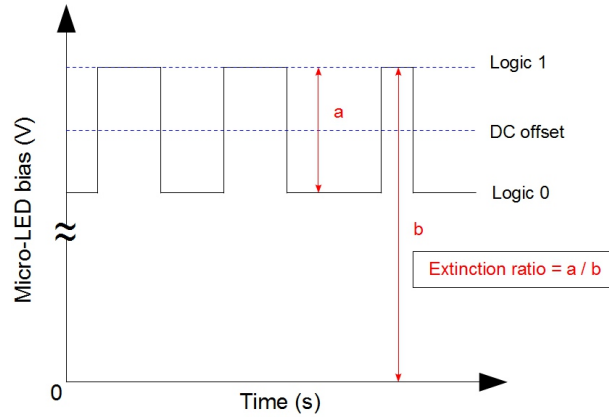


FIGURE 5.10: Illustration of the NRZ voltage input data signal to the micro-LED.

with suitable heat-sinking reliable operation at higher drive currents should be readily achievable. The maximum modulation depth directly available from the BERT, 2 V peak-to-peak, was used.

Figure 5.11 shows BERs versus received power, for various pattern lengths and bit rates from this pixel. Error-free transmission in this case is defined as an BER of $\leq 1 \times 10^{-10}$, or in other words the successful transmission of $\geq 1 \times 10^{10}$ bits without any errors. Figure 5.11 shows that error-free data transmission was achieved for bits rates of up to 1.1 Gbit/s for pattern lengths of 2^7-1 and 2^9-1 . Because the $2^{31}-1$ PRBS contains more frequent and longer CID sequences, it will contain more low frequency content which stresses the capabilities of the system, thus error-free data could only be achieved up to 800 Mbit/s for a PRBS of $2^{31}-1$.

An eye diagram is constructed by repeatedly sampling the received signal over a period of two clock cycles and at intervals of one clock cycle, and overlaying the observed data. Eye diagrams provide visual information regarding the received signal, such as noise and jitter, and an ‘open eye’ indicates that the data can be received error-free. Eye diagrams measured from the same micro-LED pixel used for the BER measurements performed above are given in figure 5.12. For each eye diagram, the micro-LED current = 35 mA and the PRBS length = $2^{31}-1$ bits. Bit rates from 155 Mbit/s to 1.2 Gbit/s are shown. At 155 Mbit/s, an open eye is clearly shown, indicating that error-free data transmission should be easily achievable at this data rate. However, patterning effects are beginning to become noticeable at 622 Mbit/s and the eye is beginning to close, which would indicate that more received power is required to achieve a given BER for this bit rate than for lower bit rates. At 1.2 Gbit/s, the eye is almost closed, indicating that error-free data transmission is not possible at this high bit rate. These conclusions are consistent with the measured BER versus received power data provided in figure 5.11.

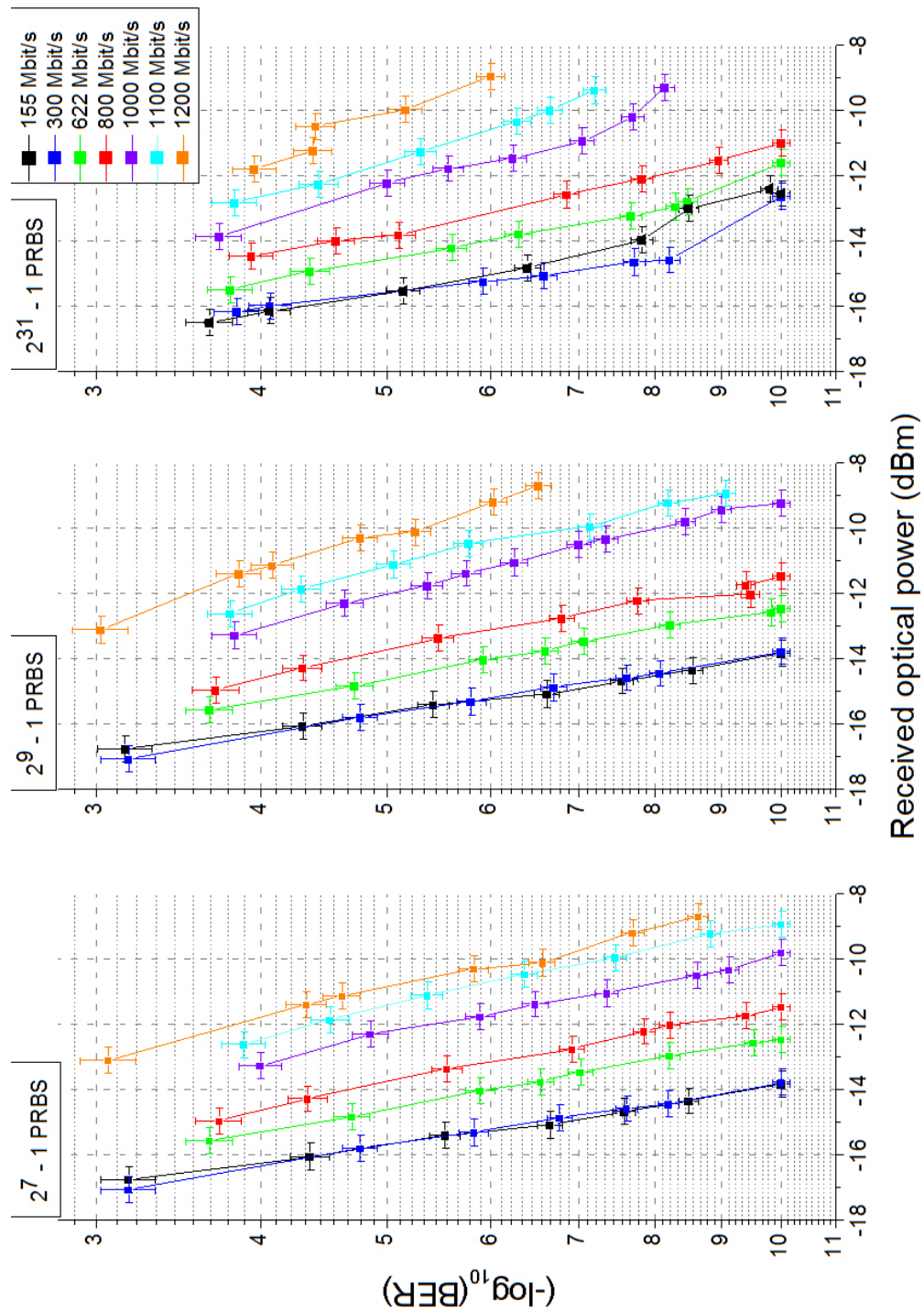


FIGURE 5.11: BERs measured from a 520 nm-emitting micro-LED at various bit rates, micro-LED current = 35 mA. PRBS lengths of 2^7-1 , 2^9-1 and $2^{31}-1$ bits, are shown.

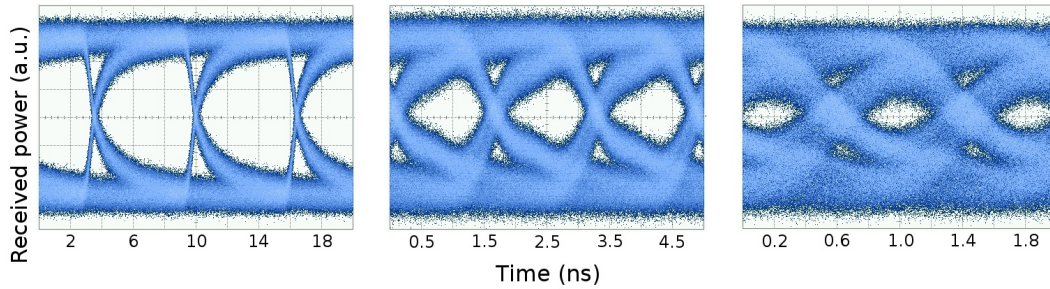


FIGURE 5.12: Eye diagrams measured from a 520 nm-emitting micro-LED at various bit rates, micro-LED current = 35 mA, PRBS = length $2^{31}-1$ bits. Bit rates of (l-r) 155 Mbit/s, 622 Mbit/s and 1.2 Gbit/s are shown.

As figure 5.11 suggests, the sensitivity of the overall system is fairly low. In other words, the required received optical power at the photodetector to achieve error-free data transmission is fairly high. Although the sensitivity of the present setup is low, it should be recognised that this is a first demonstration and sufficient to demonstrate the high-frequency modulation performance of the micro-LEDs. The sensitivity could be improved in future by optimising the components of the measurement system, for example by amplifying the output of the BERT to increase the modulation depth and thus improve the BER. Indeed, the BER versus received power performance of this system was examined with an increased modulation depth, the results of which will be discussed in the subsequent section.

5.3.1 Micro-LED optical data transmission with increased modulation depth

Intuitively, it would seem obvious that increasing the modulation depth of an optical data signal from an LED would be beneficial, since increasing the contrast between logic 0 and logic 1 levels (i.e. increasing the extinction ratio) makes distinguishing the two logic levels easier, which should result in a reduction in the BER. However, this is not necessarily the case, as will be shown in this section.

When using the output from the BERT, the maximum voltage modulation depth that can be applied to a micro-LED pixel is 2 V peak-to-peak. In order to increase the modulation depth, an electrical amplifier (JDS Uniphase, Optical Modulator driver H301-1110) was used to amplify the modulation depth to 5 V peak-to-peak. Figure 5.13 shows a comparison of the BER versus power for 3 different bit rates (155, 300 and 800 Mbit/s), for a PRBS length of $2^{31}-1$, for two different modulation depths, 2 and 5 V. It can be seen that for 155 and 300 Mbit/s, when the modulation depth is increased to 5 V, less received optical power is needed to achieve a given BER. This can be explained as the increased contrast between logic 0 and logic 1 increases the sensitivity of the overall

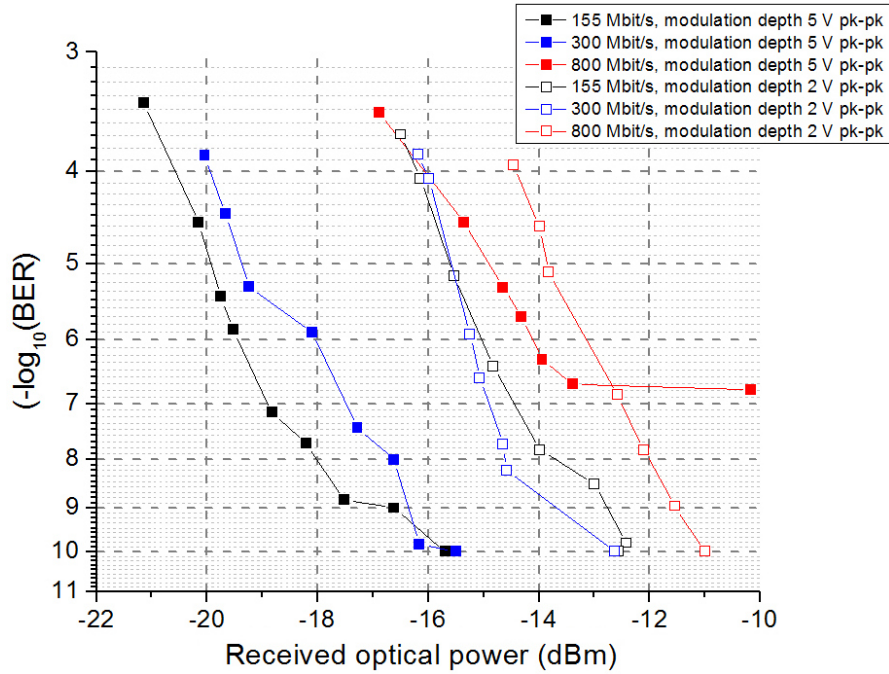


FIGURE 5.13: BERs measured from a 520 nm-emitting micro-LED at various bit rates and modulation depths. Micro-LED current = 35 mA, PRBS length of $2^{31}-1$. Modulation depths are 2 V (solid shapes) and 5 V (hollow shapes).

system. However, at 800 Mbit/s it is clear that error-free data transmission has been achieved with a modulation depth of 2 V, but not 5 V, suggesting that for higher bit rates, an increased modulation depth can actually be detrimental. This observation can be explained by considering the effect that the increased modulation depth has on the logic level transition speeds of the micro-LED. During a data sequence, there will be some points in the sequence where there are several logic 0 bits in succession. During this time, the bias voltage and bias current to the micro-LED will fall to its lowest level, determined by the modulation depth. As was discussed in section 5.2, the modulation bandwidth, and hence transition speed, of the micro-LEDs is dependent on the bias current - at low currents, the micro-LED bandwidth is lower, thus transitions between logic levels will be slower. Because a modulation depth of 5 V will place the micro-LED in a lower bias current regime during logic 0 bits than a modulation depth of 2 V, the micro-LED will respond more slowly to a transition from logic 0 to logic 1 for a modulation depth of 5 V, compared to 2 V. In effect, changing the modulation depth results in a trade-off between increased extinction ratio, and decreased modulation bandwidth. Less modulation bandwidth is required for lower bit rates, so sacrificing some bandwidth for an improved extinction ratio is beneficial. However, at higher bit rates, this loss of bandwidth results in an increase in the BER, which is not compensated for by the improved extinction ratio.

This effect can also be observed in the eye diagrams measured for the two different

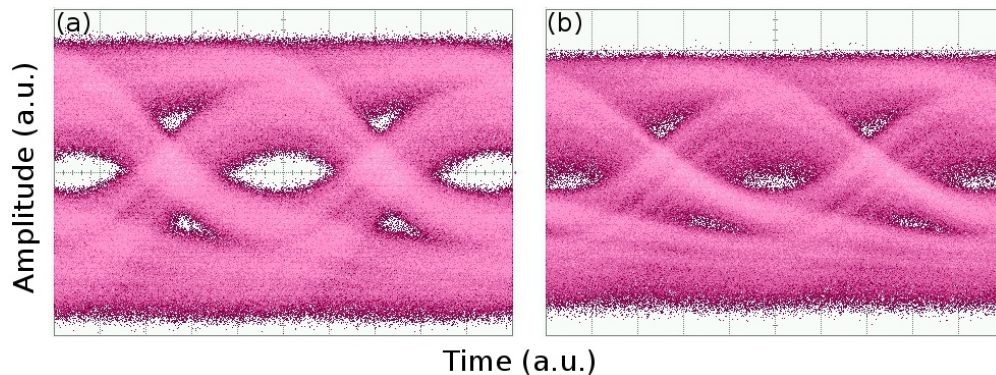


FIGURE 5.14: Eye diagrams from a 520 nm-emitting micro-LED at 1.1 Gbit/s, bias current = 35 mA, PRBS length of $2^{31}-1$. Modulation depth = (a) 2 V (b) 5 V.

modulation depths. Figure 5.14 shows eye diagrams measured from the same 520 nm-emitting micro-LED pixel, at the same bit rate, PRBS length and bias current (1.1 Gbit/s, $2^{31}-1$ and 35 mA, respectively), for modulation depths of 2 V and 5 V. Due to the effect described above, it can be clearly seen that the eye taken for a modulation depth of 5 V is more closed compared to that taken at 2 V. This is because the 0 to 1 logic transitions are slower for a modulation depth of 5 V, so the micro-LED output is often not able to reach the logic 1 level in time. In other words, the micro-LED output is often too slow to successfully transition from logic 0 to logic 1, resulting in an incorrect logic level being recorded by the receiver for these bits. This results in the increased BER for increased modulation depths at high bit rates as observed in figure 5.13.

5.4 Colour-conversion of micro-LED emission for white light communications

It is anticipated that in the near future LEDs will become the dominant form of light source for general illumination [30] as their cost continues to decrease and their efficiency continues to increase. White light communications (WLC) is a form of optical communication which aims to ‘piggy back’ on the roll-out of general white light illumination sources by utilising modulated white light for both general illumination and communications. Figure 5.15 shows an illustration of a possible white LED based communications link. In this system, the white LEDs are intensity modulated, allowing the optical transmission of data. Because the LED would be modulated at MHz data rates the human eye would not be able to distinguish any intensity flicker, allowing the same LEDs to provide general illumination. One potential advantage of such a technology is that it would allow wireless data transmission to be possible in areas where conventional radio-based Wi-Fi is not possible or desirable, such as within the cabin of a passenger aircraft or in a

hospital. In addition, WLC could also augment existing Wi-Fi by providing additional wireless bandwidth using the visible spectrum, which unlike radio-based transmissions does not require licensing. WLC has recently attracted attention from several research groups [31–34], and data transfer rates of up to 500 Mbit/s have been reported using systems based on commercial illumination white LEDs [34]. However, one issue is that these systems are currently based on conventional white LEDs which use a blue LED and a yellow-emitting phosphor to produce white light, as discussed previously in chapter 1. These materials have long phosphorescence lifetimes which limit the modulation bandwidth of the white light to the order of 5 MHz [32]. Using optical filters at the receivers to remove the slow yellow light component from the phosphor such that only the relatively fast blue LED emission is observed, increases the modulation bandwidth by at least an order of magnitude [32], although this comes at the expense of reducing the strength of the received signal. An interesting alternative to the phosphor materials would be to replace them with other colour-converting materials having shorter carrier lifetimes. Colloidal quantum dots (CQDs) and light-emitting polymers (LEPs), as discussed in chapter 1 section 1.4, are colour-converting materials with fluorescence lifetimes of the order of a few tens of nanoseconds for CQDs, and a few nanoseconds, or less, for the LEPs. As such, these materials have the potential to generate white light having a higher modulation bandwidth than conventional phosphor-based white LEDs.



FIGURE 5.15: Illustration of an envisaged visible light communications network, from [31].

5.4.1 Hybrid LED/colour-converter frequency response model

Before considering the overall response of a hybrid micro-LED/colour-converter device, we shall first consider the frequency response of a colour-converting material when excited by a light source with constant intensity. Conveniently, frequency-domain lifetime

measurements are a very well established technique which allows the fluorescence lifetime of a light-emitting sample to be inferred from its response to a modulated excitation source (see chapter 4). The basic principle of frequency-domain lifetimes measurements will first be discussed, before these techniques will be applied to explain how a colour-conversion material responds to excitation from a micro-LED at high frequencies.

Frequency-domain lifetime measurements use a sinusoidally-modulated excitation source, commonly an LED or laser diode, to excite a fluorescent sample. The sample will emit sinusoidally-modulated light having the same frequency as the source. However, the intensity modulation and phase shift of the sample light (relative to the excitation light) will vary depending on the frequency of the excitation source and the fluorescence lifetime of the sample, τ . The derivation of a mathematical model of this phenomenon, from [35], will now be discussed.

The sinusoidally-modulated excitation light source with frequency ω is described by the equation:

$$L(t) = a + b\sin\omega t \quad (5.13)$$

such that $m_L = b/a$ describes the modulation of the excitation source. The fluorophore excited state population at time t , $N(t)$, will be described a sinusoid with the same frequency but with a different modulation, and a phase shift, ϕ , relative to $L(t)$, as shown in figure 5.16:

$$N(t) = A + B\sin(\omega t - \phi) \quad (5.14)$$

We assume that the emission intensity of the fluorophore, $I(t)$, is proportional to $N(t)$.

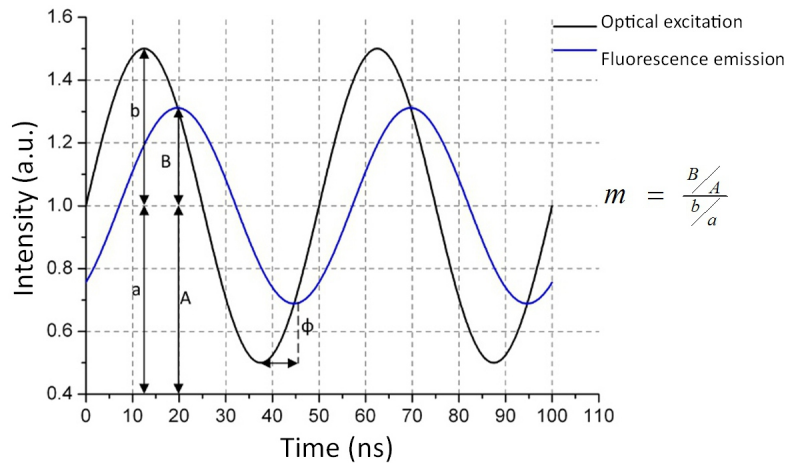


FIGURE 5.16: Illustration of the modulation and phase shift of a fluorescence emission, $N(t)$, relative to the excitation source, $L(t)$.

For a single-exponential decay, $I(t)$ is described by:

$$I(t) = I_0 \exp(-t/\tau) \quad (5.15)$$

A differential equation can then be defined which describes the time-dependent excited state population. The term $L(t)$ is a ‘forcing function’ which is the excitation source, whilst the remaining terms describe the transient response of the fluorophore:

$$dI(t)/dt = -\frac{1}{\tau}I(t) + L(t) \quad (5.16)$$

If equation 5.14 is substituted into 5.16, then the resulting equation describes the excited state population at any time, t . By expanding the resulting equation, and equating the terms in $\sin\omega t$, $\cos\omega t$ and the constant terms, we can obtain the relationship between ω , the amplitude-demodulation m , τ and ϕ :

$$\tan\phi = \omega\tau \quad (5.17)$$

$$m(\omega) = \frac{B/A}{b/a} = \frac{1}{\sqrt{1 + \omega^2\tau^2}} \quad (5.18)$$

From equations 5.17 and 5.18 we are able to describe the intensity de-modulation and phase shift of a fluorophore’s emission relative to the excitation source as a function of frequency, assuming that the fluorophore has a mono-exponential decay. In a frequency domain lifetime measurement, the parameters m and ϕ would be measured as a function of frequency and a fit would be performed with the resulting data in order to determine a value for the lifetime, τ . Many light-emitting materials however do not have a radiative decay that can be accurately described by a single exponential. These materials have decays which are best described by a multi-exponential decay function:

$$I(t) = \sum_{i=1} \alpha_i \exp\left(\frac{-t}{\tau_i}\right) \quad (5.19)$$

where α_i are the pre-exponential factors that describe the fractional contribution of each exponential to the overall decay. To describe the frequency response of fluorophores with multi-exponential decays, a more complex model must be used. For multi-exponential decays, the phase shift and de-modulation are described, respectively, by the equations 5.20 and 5.21 [36]:

$$\tan\phi = \frac{N_\omega}{D_\omega} \quad (5.20)$$

$$m = \frac{1}{\sqrt{N_\omega^2 + D_\omega^2}} \quad (5.21)$$

Where N_ω and D_ω are given by:

$$N_\omega = \sum_{i=1} \frac{\alpha_i \omega \tau_i^2}{(1 + \omega^2 \tau_i^2)} / \sum_{i=1} \alpha_i \tau_i \quad (5.22)$$

$$D_\omega = \sum_{i=1} \frac{\alpha_i \tau_i}{(1 + \omega^2 \tau_i^2)} / \sum_{i=1} \alpha_i \tau_i \quad (5.23)$$

As mentioned above, these models describe the frequency response of a fluorophore *when the excitation source is of a fixed intensity*. However it is fairly straightforward to consider the response when the excitation source is *not* of fixed intensity, as will be the case when a micro-LED modulated at high frequencies is the excitation source. For example, if at a given frequency the excitation source intensity is reduced by a factor of 0.8, and this excitation intensity is further reduced by a factor of 0.65 by the frequency response of fluorophore, then the overall intensity will be diminished by a factor of $0.8 \times 0.65 = 0.52$. This calculation is more conveniently performed when the de-modulation factors are expressed in decibels (dB). If the intensity de-modulation versus frequency of the micro-LED, m_{LED} , and that of the fluorophore, m_f , are both expressed in dB then the *overall* intensity de-modulation, m_{tot} , is given by the sum of m_{LED} and m_f :

$$m_{tot} = m_{LED} + m_f \quad (5.24)$$

A model to describe the response of a colour-converting material excited by a micro-LED, to be used for VLC, is now complete. A *Mathcad* program based on this model is presented in Appendix A, which analyses measured data for m_{tot} and m_{LED} , calculates m_f and fits to this to find the lifetime τ of the fluorescent sample under test. This program is used for analysing the data obtained in the experiments in the following sections.

5.4.2 Bandwidth of a hybrid micro-LED and quantum dot-based nanocomposite device

In this section, a micro-LED device that utilises CdSe/ZnS colloidal quantum dots (CQDs) for colour-conversion is presented. Different CQD samples are investigated, including a CQD blend which is suitable for white light generation when combined with a 450 nm-emitting micro-LED. The CQDs are incorporated into a polymeric host matrix to facilitate integration to the micro-LEDs. The short fluorescence lifetimes of the CQDs, when compared to that of phosphors, is shown to allow high modulation bandwidths of ≈ 32 MHz to be achieved when the samples are excited by a modulated micro-LED with a peak emission of 450 nm.

5.4.2.1 Experimental

Four CQD samples, prepared by Dr. Benoit Guilhabert and Dr. Nicolas Laurand, were examined with peak emission wavelengths of 535, 573, 600 and 624 nm and mean dot diameters of 7, 8, 8.2 and 8.7 nm, respectively. The CQDs were initially in a toluene solution, as supplied by the manufacturer (Evident Technologies, Inc.). The

polymeric matrix material chosen was Corin-XLS from Mantech. This material offers high durability, high transparency to visible light and is compatible with organic solvents which would allow it to be processed by techniques such as spray-coating and ink-jet printing. After a solvent exchange, the CQDs were incorporated into a polyimide-Tetrahydrofuran (THF) solution at a ratio of 50 mg of CQDs per mL of THF/polyimide (30 mg of polyimide per mL of THF). A fifth sample, termed ‘broad spectrum’, was created by blending the 535, 573, 600 and 624 nm CQDs at respective volume percentages of 83.3%, 14%, 1.7% and 1%. The resulting broad spectrum emission from this sample was intended to allow white light to be generated in combination with the 450 nm peak emission from a micro-LED. The samples were subsequently drop-cast onto 150 μm thick glass coverslips, and heated to approximately 60°C for 1 minute to allow the THF to evaporate and to cure the nanocomposite. The resulting sample thickness was approximately 100 to 200 μm . The CQD-to-polyimide ratio and the external conversion efficiency of each sample is given in table 5.3. Normalised photoluminescence emission spectra from each of the samples is given in figure 5.17.

TABLE 5.3: Nanocomposite sample composition and external conversion efficiency.

Nanocomposite sample name	CQD volume ratio	External conversion efficiency
535 nm	1.3%	7%
573 nm	1.3%	11%
600 nm	1.1%	25%
624 nm	0.8%	13%
Broad spectrum	1.3%	6.5%

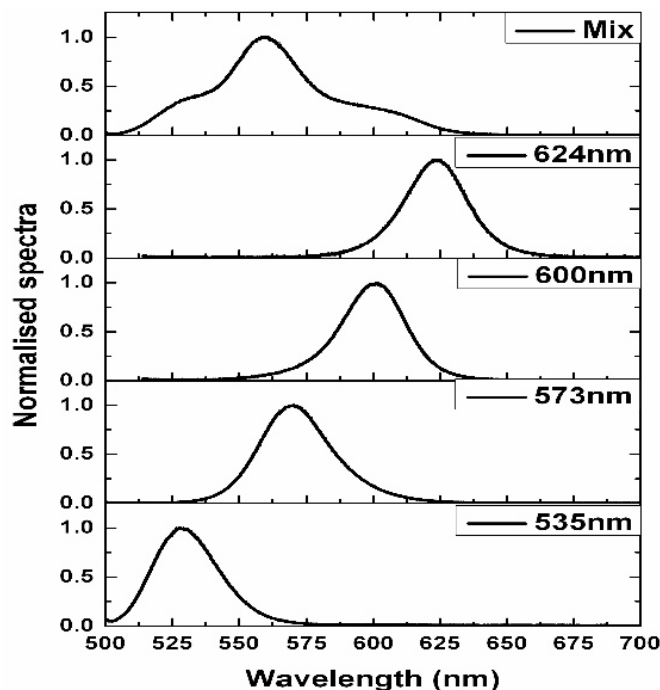


FIGURE 5.17: Normalised photoluminescence emission spectra of nanocomposite samples.

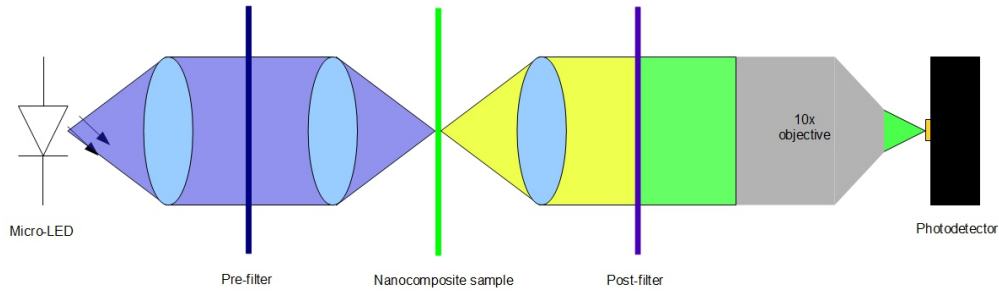


FIGURE 5.18: Schematic of the imaging and collection optics used to measure the response of a modulated polymer sample.

An $84\ \mu\text{m}$ diameter pixel from an 8×8 micro-LED array with peak emission of $450\ \text{nm}$ was chosen as the modulated excitation source for the frequency response measurements of the nanocomposite samples. A DC current of $75\ \text{mA}$ was combined with the AC signal from a network analyser (Agilent Technologies 8753ES Option 011) using a bias-tee. The micro-LED emission was imaged onto the nanocomposite sample, and the emission from the nanocomposite was imaged onto the photodetector (figure 5.18). The photodetector was the same as was used in section 5.2, having a cut-off frequency of $1.2\ \text{GHz}$. A $500\ \text{nm}$ low-pass ‘pre-filter’ (Thor Labs FES0500) was used to remove long wavelength emission from the micro-LED, and a $515\ \text{nm}$ high-pass ‘post-filter’ (Thor Labs FGL515) was used to prevent unabsorbed micro-LED emission from reaching the photodetector, whilst allowing the nanocomposite emission to pass. The purpose of using these filters was to ensure that the photodetector only measured modulated the emission from the nanocomposite, and not a mixture of nanocomposite emission and unabsorbed micro-LED emission. The photodetector output was then amplified using an external 50dB electrical amplifier (HP8447D - dual stage), and the output of this amplifier was filtered using a 0 to $1.2\ \text{GHz}$ electrical filter in order to reduce noise. This signal was delivered to the network analyser so that the overall bandwidth of the system could be measured. After the frequency response measurements were completed, the spectrum of the light that was imaged onto the detector was measured in order to check that the LED emission was not leaking through the sample and the filters and reaching the detector. A photograph of the imaging system used for these measurements is shown in figure 5.19.

5.4.2.2 Results and discussion

The frequency response of the micro-LED, m_{LED} , used to excite the LEP samples was measured in the absence of the sample and the filters, and the response of the hybrid micro-LED/CQD nanocomposite emission, m_{tot} , was subsequently measured with the filters in place. The modulation bandwidth of the micro-LED was $\approx 230\ \text{MHz}$ for all the

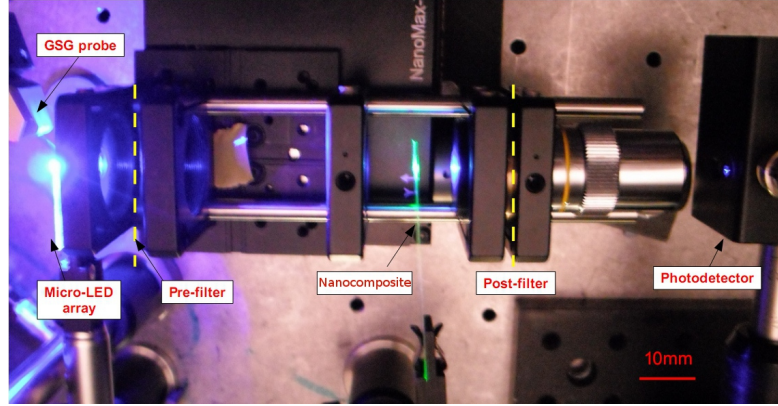


FIGURE 5.19: Plan view photograph of the imaging and collection optics used to measure the response of a modulated nanocomposite sample.

nanocomposite sample frequency response measurements. The overall response of the micro-LED and nanocomposite, m_{tot} , was measured, and by subtracting m_{LED} from m_{tot} the intrinsic frequency response of the nanocomposites, m_f , were derived as per equation 5.24. The resulting m_f plots were fitted to the expression given by equation 5.18, to find the effective carrier lifetimes, τ , and the modulation bandwidth of the nanocomposite sample, assuming a mono-exponential fluorescence decay. The measured and fitted plots of m_f , and the fitted values for τ and the modulation bandwidths are shown in figure 5.20. The coefficient of determination R^2 , is given for each fit which indicates the ‘goodness of fit’ to each set of data. A value of $R^2 = 1$ indicates a perfect fit to the data, with R^2 being defined according to the following equation:

$$R^2 = 1 - \frac{RSS}{TSS} \quad (5.25)$$

where RSS is the residual sum of squares, and TSS is the total sum of squares, defined as follows where f_i is the fitted value, y_i is the measured value and \bar{y} is the mean of the measure data:

$$RSS = \sum_i (y_i - f_i)^2 \quad \text{and} \quad TSS = \sum_i (y_i - \bar{y})^2 \quad (5.26)$$

It can be seen that for the nanocomposite samples, the overall modulation bandwidths range from 11.25 to 31.9 MHz. It may be noted that since the modulation bandwidth of the nanocomposite samples are of an order of magnitude lower than that of the micro-LED, that $m_{tot} \approx m_f$. The broad spectrum sample intended for white light generation was found to have a modulation bandwidth of 29.4 MHz. This represents an order of magnitude increase in the modulation bandwidth when compared the phosphorescent colour converters typically used in white LEDs, indicating that these quantum dot nanocomposites are promising alternatives to phosphors, allowing white light with higher modulation bandwidths to be generated. Data transmission was demonstrated using the broad spectrum sample to colour-convert the emission from a 450 nm 84 μm

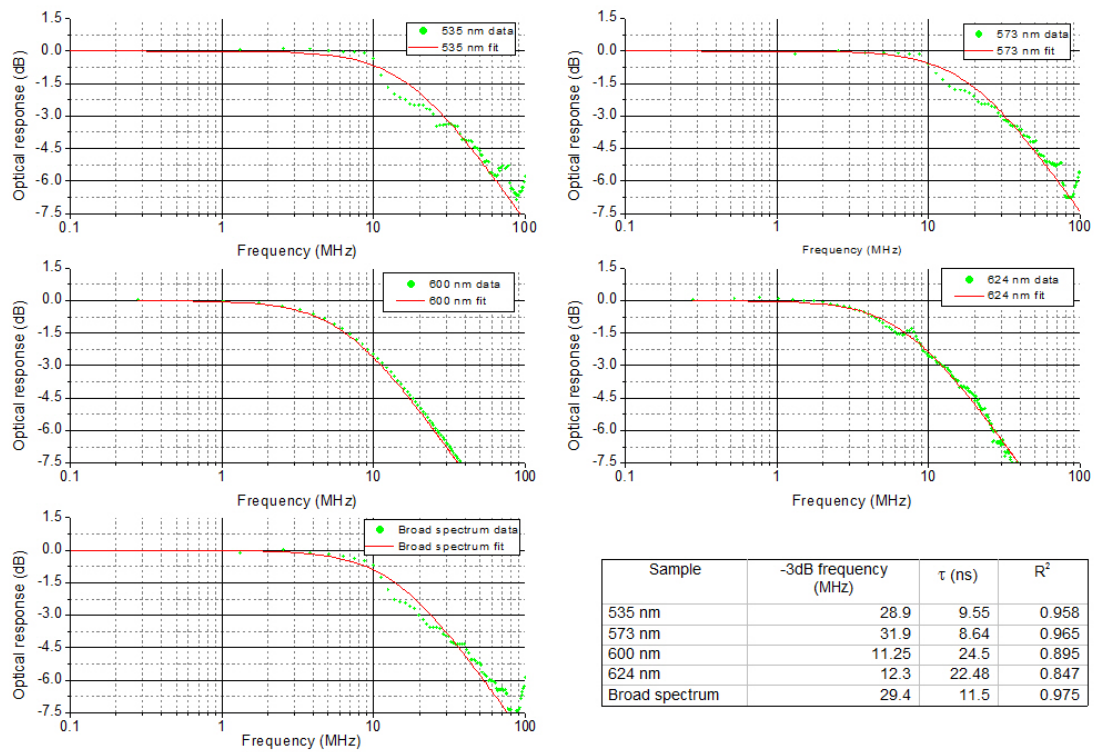


FIGURE 5.20: Measured and fitted frequency responses of the CQD nanocomposite samples.

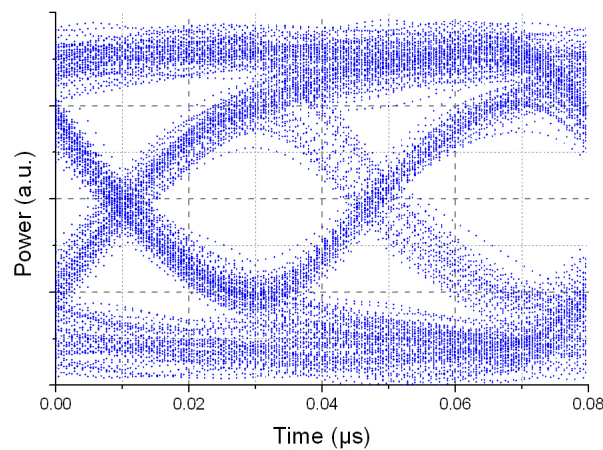


FIGURE 5.21: Eye diagram at 25 Mbit/s measured by optically modulating the broad spectrum nanocomposite blend. All LED light was filtered out so the modulation comes only from the emission of nanocomposite.

diameter pixel. The data transmission setup was identical to that described in section 5.3. As shown in figure 5.21, an open eye was observed for a bit rate of 25 Mbit/s. Although an integrated nanocomposite/micro-LED device has not been presented here, it would be fairly straightforward to integrate the nanocomposites with a micro-LED or LED device by spin-coating or ink-jet printing.

5.4.3 Bandwidth of hybrid micro-LED and LEP colour-converters

Although the previous section demonstrated that CQDs can allow an order of magnitude increase in the modulation bandwidth of colour-converted light, when compared to conventional phosphor materials, the bandwidths of the CQDs remain an order of magnitude of lower than that of the micro-LEDs themselves. The fluorescence lifetime of CQDs is typically of the 10-20 ns regime, however, light-emitting polymers (LEPs) have fluorescence lifetimes which are typically of the order of a few nanoseconds or less. Like the CQD nanocomposites, these materials have the advantage of being solution-processable, highly luminescent and suitable for white light generation using (micro-)LEDs [37]. In this section, colour-conversion of micro-LED emission using LEPs will be shown to allow colour-converted light with bandwidths greatly in excess of those possible using CQDs to be achieved.

5.4.3.1 Experimental

As the name suggests, Red F, a polyfluorene, is a light-emitting polymer which emits red light. Red F has been demonstrated as a component of a white-emitting blend which can be directly integrated with a UV-emitting micro-LED to produce a white light emitter [37]. Because this polymer was readily available and has a simple mono-exponential decay, it was chosen for an initial proof of principle demonstration of a high-bandwidth colour-conversion of micro-LED emission. The Red F sample was kindly provided by Dr. Colin Belton of Imperial College, London. A sample of the green-emitting LEP BBEHP-PPV (cf. chapter 4) was also investigated for modulated colour-converted light, and was kindly prepared by Dr. Nicolas Laurand of the Institute of Photonics. Both samples were in toluene solution and were drop-cast onto glass coverslips, with estimated polymer thicknesses of $\approx 0.5 \mu\text{m}$.

The absorption and emission spectra of the LEP samples are given in figure 5.22, along with the emission spectrum of the 450 nm micro-LED pixel used to excite them. As with the nanocomposite measurements in section 5.4.2.1, light from the excitation micro-LED was imaged onto the sample, and the LEP emission was imaged onto the detector. The same pre- and post-filters that were used in section 5.4.2.1 were also used here to prevent unabsorbed micro-LED from reaching the photodiode.

An $84 \mu\text{m}$ diameter micro-LED from an 8×8 array, with a peak emission of 450 nm, was used as the modulated pump source for the LEP samples. For both measurements, a DC bias of 50 mA was combined with the AC output of the network analyser. At this current, the DC output power of the micro-LED is reduced. Un-encapsulated LEP

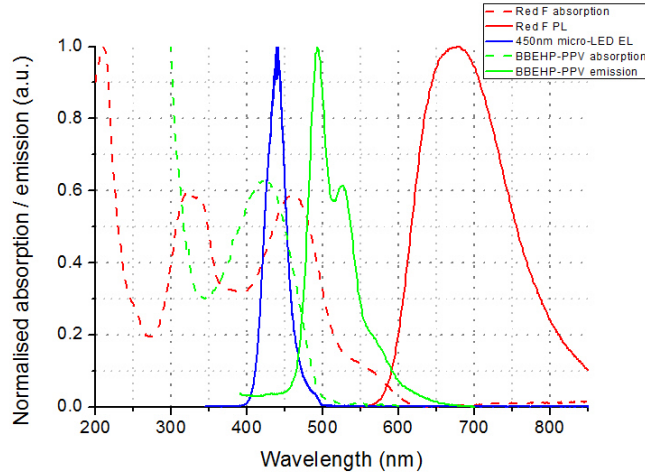


FIGURE 5.22: Absorption and emission spectra of Red F and BBEHP-PPV LEPs. Also shown is the electroluminescence spectra of the 450 nm micro-LED used to excite the LEP samples.

samples, such as used here, are susceptible to photo-degradation in the presence of oxygen and water [38], so reducing the light intensity delivered to the LEP samples allowed the operational lifetime of the samples to be extended. It should be noted that despite this issue of photo-degradation, LEP operational lifetimes can be extended by as much as a factor of 2500 by encapsulation [38], and that polymer-based LEDs exhibit operational lifetimes of around 20,000 hours [39]. The remainder of the measurement setup and procedure was identical to that described in section 5.4.2.1 for the CQD nanocomposite measurements.

5.4.3.2 Results and discussion

The frequency response of the micro-LED, m_{LED} , used to excite the LEP samples was measured in the absence of the sample and the filters, and the response of the hybrid micro-LED/LEP emission, m_{tot} , was subsequently measured with the filters in place. This is represented by the blue plot in figure 5.23, a modulation bandwidth of ≈ 165 MHz was found for the micro-LED. As before, the frequency response of the sample, m_f , was obtained by subtracting m_{LED} from the measured m_{tot} data. The radiative lifetime of the samples, τ , was found by fitting to the extracted m_f data, assuming a mono-exponential decay. The fitted m_f and the measured and fitted m_{tot} responses for both LEP samples are shown in figure 5.23.

For the Red F sample, a fluorescence lifetime of $\tau = 2.18$ ns was found by the fitting. This value is in excellent agreement with that determined by independent streak camera measurements performed by Dr. Colin Belton at Imperial College London, which indicated that Red F has a mono-exponential decay with $\tau = 2.31$ ns [40]. With a value of

$\tau = 2.18$ ns, the Red F sample was estimated to have a modulation bandwidth of 118.8 MHz, and the overall modulation bandwidth of the hybrid system was found to be 71.3 MHz. For the BBEHP-PPV sample, a value of $\tau = 0.42$ ns was found, giving a corresponding BBEHP-PPV bandwidth of 667.8 MHz. This value of τ agrees fairly well with that reported in the literature which suggests that the material has a mono-exponential decay with $\tau = 0.65$ ns [41], though it is in much better agreement with time-resolved measurements performed by colleagues from the Institute of Photonics which suggests that the material has a double-exponential decay with $\tau_1 = 0.16$ ns and $\tau_2 = 0.43$ ns. Given the relatively low frequency sweep these measurements were performed at, and bearing in mind the cut-off frequencies of the photodetector and the electrical filters used are around 1.2 GHz, the influence of the fast τ_1 component on the frequency response measurement will not be very apparent. Therefore, it is argued for these frequency response measurements that the BBEHP-PPV LEP can be fairly accurately modelled as having a mono-exponential decay with $\tau = 0.42$ ns. For the BBEHP-PPV measurement, the overall bandwidth was found to be ≈ 140 MHz.

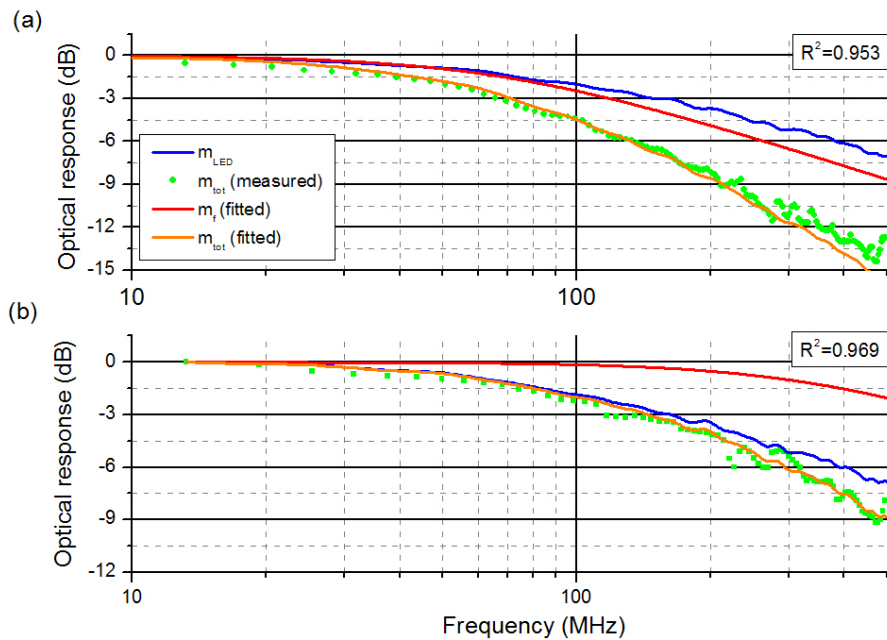


FIGURE 5.23: (Blue) measured frequency response of the 450 nm micro-LED excitation source, (red) the predicted frequency response of Red F polymer, (green) the measured and predicted (orange) overall frequency responses, for (a) Red F and (b) BBEHP-PPV LEPs.

For both LEP samples, the overall modulation bandwidths were greatly in excess of the bandwidths possible using phosphor or quantum dot-based colour converters. For the BBEHP-PPV sample in particular, the process of colour-converting the micro-LED emission did not greatly reduce the available bandwidth, a reduction from 165 MHz for the bare micro-LED to ≈ 140 MHz for the colour-converted light was observed for the

BBEHP-PPV sample. This demonstrates that LEPs with very short fluorescence lifetimes can be used to colour-convert the emission from (micro-)LEDs without sacrificing very much bandwidth. White-emitting LEP blends, integrated with micro-LEDs, have been reported with fluorescence lifetimes of the order of 1-2 ns [37], so a high-bandwidth white-emitting hybrid micro-LED/LEP device demonstration should be achievable in the near future. It should be noted that the use of CQDs and LEPs for colour conversion is also applicable to conventional broad-area LEDs, and is not limited to use with micro-pixelated LED arrays.

5.5 Summary

In this chapter the suitability of micro-LED arrays for optical communications has been investigated by analysing the fundamental frequency response of individual micro-LED pixels. The optical modulation bandwidths of the micro-LEDs were found to be as high as 450 MHz, which to the best of the author's knowledge is amongst the highest modulation bandwidths ever reported for AlInGaN-based LEDs. The modulated performance of the micro-LEDs was found to be dependent on several factors, namely the injected current density, the micro-LED pixel active area and the micro-LED peak emission wavelength (i.e. the micro-LED epitaxial structure). These trends have been attributed to the modulation bandwidth being dependent on the carrier density-dependent carrier recombination dynamics within the micro-LEDs, and a carrier density-dependent carrier lifetime model was presented to attempt to explain the frequency response behaviour of pixels in a 450 nm emitting micro-LED array.

Using a 34 μm diameter 520 nm-peak emission micro-LED pixel, a proof-of-concept data transmission measurement was undertaken which demonstrated error-free data transmission at bit rates of up to 1.1 Gbit/s. Although this does not yet represent a practical communications device, it illustrates the potential of the micro-LED arrays for optical communications, especially when the multi-emitter nature of the micro-LED arrays has yet to be exploited. Furthermore, substantial work in optimising the electrical drive, optical transmission and detection of the system could be done in order to improve the sensitivity and/or increase the error-free bit rate.

Finally, light-emitting polymers and quantum dot colour-converting materials have been shown to have the potential to be used together with micro-LEDs, or indeed standard broad-area LEDs, for the generation of white light with high modulation bandwidth. Conventional white LEDs which utilise phosphors emit white light with a bandwidth which is limited to around 5 MHz due to the long radiative lifetime of the phosphors. However, here it has been shown that quantum dots and light-emitting polymers can

be used to generate colour-converted light with modulation bandwidths that are up to two order of magnitude higher. Future work to integrate these materials with (micro-)LEDs would allow high-bandwidth white-emitting LEDs to be used for visible light communications.

References

- [1] C.A. Burrus and B.I. Miller. Small-area, double-heterostructure aluminum-gallium arsenide electroluminescent diode sources for optical-fiber transmission lines. *Optical Communications*, 4(4):307–309, 1971.
- [2] E.F. Schubert. *Light Emitting Diodes*. Cambridge University Press, 2nd edition, 2006.
- [3] D.C. O'Brien, G.E. Faulkner, E.B. Zyambo, K. Jim, D.J. Edwards, P. Stavrinou, G. Parry, J. Bellon, M.J. Sibley, V.A. Lalithambika, V.M. Joyner, R.J. Samsudin, D.M. Holburn, and R.J. Mears. Integrated transceivers for optical wireless communications. *Selected Topics in Quantum Electronics, IEEE Journal of*, 11(1):173 – 183, 2005.
- [4] MOST Cooperation. Annual Achievement Report 2010, Accessed September 2010 . URL http://www.mostcooperation.com/publications/brochures_newsletters/latest/index.html.
- [5] M.M. Dumitrescu, M.J. Saarinen, M.D. Guina, and M.V. Pessa. High-speed resonant cavity light-emitting diodes at 650 nm. *Selected Topics in Quantum Electronics, IEEE Journal of*, 8(2):219–230, 2002.
- [6] M. Akhter, P. Maaskant, B. Roycroft, B. Corbett, P. de Mierry, B. Beaumont, and K. Panzer. 200 Mbit/s data transmission through 100m of plastic optical fibre with nitride LEDs. *Electronics Letters*, 38(23):1457, 2002.
- [7] J.-W. Shi, J.-K. Sheu, C.-H. Chen, G.-R. Lin, and W.-C. Lai. High-speed GaN-based green light-emitting diodes with partially n-doped active layers and current-confined apertures. *IEEE Electron Device Letters*, 29(2):158–160, 2008.
- [8] A.J. Shaw, A.L. Bradley, J.F. Donegan, and J.G. Lunney. GaN resonant cavity light-emitting diodes for plastic optical fiber applications. *Photonics Technology Letters, IEEE*, 16(9):2006–2008, 2004.
- [9] S. X. Jin, J. Shakya, J. Y. Lin, and H. X. Jiang. Size dependence of III-nitride microdisk light-emitting diode characteristics. *Applied Physics Letters*, 78(22):3532, 2001.
- [10] C.W. Jeon, E. Gu, C. Liu J.M. Girkin, and M.D. Dawson. Polymer Microlens Arrays Applicable to AlInGaN Ultraviolet Micro-Light-Emitting Diodes. *IEEE Photonics Technology Letters*, 17(9):1887–1889, 2005.

- [11] Si-Hyun Park, Heonsu Jeon, Youn-Joon Sung, and Geun-Young Yeom. Refractive sapphire microlenses fabricated by chlorine-based inductively coupled plasma etching. *Applied Optics*, 40(22):3698–3702, 2001.
- [12] T. N. Oder, J. Shakya, J. Y. Lin, and H. X. Jiang. Nitride microlens arrays for blue and ultraviolet wavelength applications. *Applied Physics Letters*, 82(21):3692–3694, 2003.
- [13] H. W. Choi, E. Gu, C. Liu, C. Griffin, J. M. Girkin, I. M. Watson, and M. D. Dawson. Fabrication of natural diamond microlenses by plasma etching. *Journal of Vacuum Science Technology*, 23(1):130–132, 2005.
- [14] Inc. Advanced Photonix. Bandwidth terminology, Accessed August 2010. URL http://www.picometrix.com/pico_products/an_band_terms.asp.
- [15] Jonathan J. D. McKendry, Richard P. Green, A. E. Kelly, Zheng Gong, Benoit Guilhabert, David Massoubre, Erdan Gu, and Martin D. Dawson. High-Speed Visible Light Communications Using Individual Pixels in a Micro Light-Emitting Diode Array. *IEEE Photonics Technology Letters*, 22(18):1346 – 1348, 2010.
- [16] G.P. Agrawal and N.K. Dutta. *Semiconductor Lasers*. Kluwer Academic Publishers, 2nd edition, 1993.
- [17] G. E. Shtengel, D. A. Ackerman, P. A. Morton, E. J. Flynn, and M. S. Hybertsen. Impedance-corrected carrier lifetime measurements in semiconductor lasers. *Applied Physics Letters*, 67(11):1506–1508, 1995.
- [18] Ya-Ju Lee, Ching-Hua Chiu, Chih Chun Ke, Po Chun Lin, Tien-Chang Lu, Hao-Chung Kuo, and Shing-Chung Wang. Study of the excitation power dependent internal quantum efficiency in InGaN/GaN LEDs grown on patterned sapphire substrate. *Journal of Selected Topics in Quantum Electronics*, 15(4):1137 – 1143, 2009.
- [19] T. Fujii, Y. Gao, R. Sharma, E. L. Hu, S. P. DenBaars, and S. Nakamura. Increase in the extraction efficiency of GaN-based light-emitting diodes via surface roughening. *Applied Physics Letters*, 84(6):855–857, 2004.
- [20] Petr G. Eliseev, Marek Osin'ski, Hua Li, and Irina V. Akimova. Recombination balance in green-light-emitting GaN/InGaN/AlGaN quantum wells. *Applied Physics Letters*, 75(24):3838–3840, 1999.
- [21] Zheng Gong, Shirong Jin, Yujie Chen, Jonathan McKendry, David Massoubre, Ian. M. Watson, Erdan Gu, and Martin D. Dawson. Size-dependent light output,

- spectral shift, and self-heating of 400 nm InGaN light-emitting diodes. *Journal of Applied Physics*, 107(1):013103, 2010.
- [22] Aurélien David and Michael J. Grundmann. Droop in InGaN light-emitting diodes: A differential carrier lifetime analysis. *Applied Physics Letters*, 96(10):103504, 2010.
- [23] Y. C. Shen, G. O. Mueller, S. Watanabe, N. F. Gardner, A. Munkholm, and M. R. Krames. Auger recombination in InGaN measured by photoluminescence. *Applied Physics Letters*, 91(14):141101, 2007.
- [24] Han-Youl Ryu, Hyun-Sung Kim, and Jong-In Shim. Rate equation analysis of efficiency droop in InGaN light-emitting diodes. *Applied Physics Letters*, 95(8):081114, 2009.
- [25] M. Zhang, P. Bhattacharya, J. Singh, and J. Hinckley. Direct measurement of Auger recombination in $\text{In}_{0.1}\text{Ga}_{0.9}\text{N}/\text{GaN}$ quantum wells and its impact on the efficiency of $\text{In}_{0.1}\text{Ga}_{0.9}\text{N}/\text{GaN}$ multiple quantum well light emitting diodes. *Applied Physics Letters*, 95(20):201108, 2009.
- [26] Maxim Shatalov, Ashay Chitnis, Alexey Koudymov, Jianping Zhang, Vinod Adivarahan, Grigory Simin, and Muhammad Asif Khan. Differential carrier lifetime in AlGaIn based multiple quantum well deep UV light emitting diodes at 325 nm. *Japanese Journal of Applied Physics*, 41(Part 2, No. 10B):L1146–L1148, 2002.
- [27] B. Witzigmann, V. Laino, M. Luisier, U. T. Schwarz, G. Feicht, W. Wegscheider, K. Engl, M. Furlitsch, A. Leber, A. Lell, and V. Härle. Microscopic analysis of optical gain in InGaIn/GaN quantum wells. *Applied Physics Letters*, 88(2):021104, 2006.
- [28] J. Hader, J. V. Moloney, and S. W. Koch. Density-activated defect recombination as a possible explanation for the efficiency droop in GaN-based diodes. *Applied Physics Letters*, 96(22):221106, 2010.
- [29] Anritsu Corporation. Effect of PRBS pattern length on data-dependent jitter. Technical notes, white paper, April 2007. <http://www.anritsu.com/en-GB/Downloads/TechnicalNotes/WhitePaper/DWL2880.aspx>.
- [30] J. K. Kim and E. F. Schubert. Transcending the replacement paradigm of solid-state lighting. *Optics Express*, 16:21835–21842, 2008.
- [31] H. Elgala, R. Mesleh, and H. Haas. Indoor broadcasting via white LEDs and OFDM. *IEEE Transactions on Consumer Electronics*, 55(3):1127–1134, 2009.

- [32] Hoa Le Minh, D. O'Brien, G. Faulkner, Lubin Zeng, Kyungwoo Lee, Daekwang Jung, YunJe Oh, and Eun Tae Won. 100-Mb/s NRZ visible light communications using a postequalized white LED. *Photonics Technology Letters, IEEE*, 21(15):1063–1065, 2009.
- [33] J. Vucic, C. Kottke, S. Nerreter, A. Buttner, K.-D. Langer, and J. W. Walewski. White light wireless transmission at 200+ Mb/s net data rate by use of discrete-multitone modulation. *Photonics Technology Letters, IEEE*, 21(20):1511–1513, 2009. ISSN 1041-1135.
- [34] J. Vucic, C. Kottke, S. Nerreter, K. Langer, and J. Walewski. 513 Mbit/s Visible Light Communications Link Based on DMT-Modulation of a White LED. *Journal of Lightwave Technology*, 28(24):35123518, 2010.
- [35] Joseph R. Lakowicz. *Principles of Fluorescence Spectroscopy*. Springer, 3rd edition, 2006.
- [36] J.R. Lakowicz, G. Laczko, H. Cherek, E. Gratton, and M. Limkeman. Analysis of fluorescence decay kinetics from variable-frequency phase shift and modulation data. *Biophysical Journal*, 46:463 – 477, 1984.
- [37] C R Belton, G Itskos, G Heliotis, P N Stavrinou, P G Lagoudakis, J Lupton, S Pereira, E Gu, C Griffin, B Guilhabert, I M Watson, A R Mackintosh, R A Pethrick, J Feldmann, R Murray, M D Dawson, and D D C Bradley. New light from hybrid inorganic-organic emitters. *Journal of Physics D: Applied Physics*, 41(9):094006 (12pp), 2008.
- [38] S. Richardson, O. P. M. Gaudin, G. A. Turnbull, and I. D. W. Samuel. Improved operational lifetime of semiconducting polymer lasers by encapsulation. *Applied Physics Letters*, 91(26):261104, 2007.
- [39] I. D. Parker, Y. Cao, and C. Y. Yang. Lifetime and degradation effects in polymer light-emitting diodes. *Journal of Applied Physics*, 85(4):2441–2447, 1999.
- [40] C. Belton. personal communication.
- [41] A Rose, ZG Zhu, CF Madigan, TM Swager, and V Bulovic. Sensitivity gains in chemosensing by lasing action in organic polymers. *Nature*, 434(7035):876–879, 2005.

Chapter 6

Conclusions

This thesis presented work showing the application of micro-light-emitting diode arrays, based on the AlInGaN alloy system, to time-resolved fluorescent lifetime measurements and visible-light communications. Micro-LEDs were shown to be novel light sources for these applications, offering advantages of simplicity, robustness, reduced cost and reduced complexity when compared to more conventionally used light sources, such as Ti:sapphire lasers and resonant-cavity LEDs.

Chapter 1 provided a general introduction to LEDs, and more specifically to LEDs based on the AlInGaN alloy system. Over the last 25 years, advances in the growth of AlInGaN materials has allowed efficient LEDs to be fabricated across the visible spectrum, and also at increasingly shorter wavelengths into the UV. Although much work remains to tackle problems such as the ‘efficiency droop’, the ‘green-yellow gap’ and increase the light extraction efficiency, it is anticipated that white-emitting LEDs will replace incandescent and fluorescent bulbs over the coming decade to provide highly efficient general illumination sources. Typical epitaxial and die structures were presented, along with a summary of how these materials are grown and processed into LEDs. A brief introduction to colloidal quantum dots (CQDs) and light-emitting polymers (LEPs), used experimentally as fluorescent lifetime test samples and as colour-converters, was given.

The development of AlInGaN micro-LED arrays by various research groups was presented in chapter 2. Micro-LED arrays are a novel format of LED consisting of arrays of individually-controllable sub-100 μm diameter LED micro-emitters. These devices provide a micro-scale spatial and temporally-controllable output pattern which can be utilised for a wide range of applications. The design of micro-LED arrays fabricated by the Institute of Photonics was described, with a particular focus on the individually-addressable micro-LED arrays that were to be discussed later in the thesis. The typical performance

of these arrays, in terms of their I-V, L-I, nanosecond pulsed output and emission spectra was presented in order to provide the reader with an understanding of the capabilities of the devices. Key performance highlights include up to 5 mW from a single 72 μm diameter pixel, and high output pulse intensities which suggest that micro-LED arrays may be capable of photo-pumping organic semiconductor lasers (OSLs). The possibility of photo-pumping OSLs with micro-LEDs is particularly exciting, as this would remove the necessity to use large benchtop laser pump sources and allow these highly versatile format of laser devices to be used outside of research laboratories.

Chapter 3 discussed the integration of micro-LEDs with CMOS driver array chips, which were designed by colleagues at the University of Edinburgh. These CMOS chips allow arrays of individually-addressed micro-LED pixels to each be driven by separate elements in an array of CMOS drivers via a simple computer interface and test board. This approach allows the potential of the individually-addressable arrays to be realised. A summary of CMOS technology was presented before a more detailed description of the electronic circuitry implemented in the various iterations of CMOS driver chips. The performance of integrated micro-LED/CMOS devices was shown. Some key highlights include the generation of sub-nanosecond optical pulses, modulation of individual pixels at >110 MHz, and simple computer control of the micro-LED array output. The sub-nanosecond pulsed output capability of the CMOS-controlled micro-LEDs means that they are suitable candidates for optical excitation sources for time-resolved fluorescence measurements. These are powerful measurement techniques commonly used in the life sciences for analysing samples, which conventionally rely on bulky, expensive and complex optical excitation sources and detectors. Proof-of-principle demonstrations of compact systems utilising CMOS-controlled micro-LED array and array of single-photon avalanche diodes were presented in chapter 4. These system were shown to be capable of reasonably accurate fluorescent lifetime measurements of samples of colloidal quantum dots, light-emitting polymers and organic dyes.

Chapter 5 described the characterisation of the frequency-modulated performance of micro-LED pixels. Arrays of micro-LED pixels have potential applications in both free-space and fibre-coupled optical communications. Modulation bandwidths of micro-LEDs with various sizes and emission wavelengths was characterised, with bandwidths of up to nearly 450 MHz demonstrated. A demonstration of error-free optical data transmission using a single 34 μm diameter 520 nm-emitting micro-LED was shown at bit rates of up to 1.1 Gbit/s. To the best of the author's knowledge, these micro-LED devices have some of the highest modulation bandwidths of LED fabricated in the AlInGaN alloy system. Furthermore, these micro-LEDs are fabricated used fairly standard photolithography and commercial LED wafers, and do not require any complex fabrication steps, such as the deposition of dielectric mirrors or specially doped active regions, unlike some

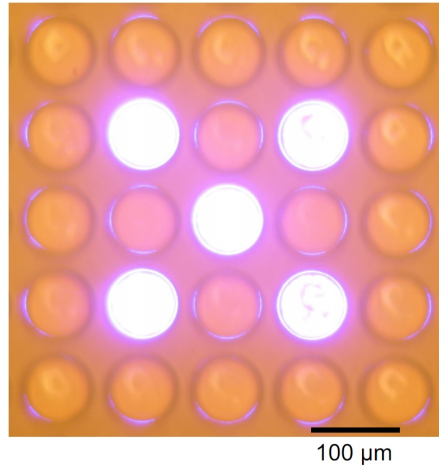


FIGURE 6.1: Optical micrograph image showing 5 pixels from a 405 nm emitting micro-LED array driven by a ‘fourth generation’ CMOS chip.

other reports of high-bandwidth LED devices. Coupled with the potential for multi-channel parallel communication using a single array, micro-LEDs have great potential as novel optical communication devices. Novel approaches to the generation of high-bandwidth white light using CQDs and LEPs was also presented, showing that it is possible, using CQDs and LEPs, to produce wavelength-converted (micro-)LED emission with a significantly higher bandwidth compared to conventional white-LEDs which use phosphor colour converters.

6.1 Future work

As discussed in chapter 2, section 2.3.3, the pulsed output powers that can be attained from micro-LED pixels are of the order that using them to optically-pump an organic semiconductor laser may be feasible. New micro-LED device designs made specifically for the purpose of optical pumping may be required to maximise the performance of the micro-LED pump source. Laser-lift off of the sapphire substrate [1] could conceivably allow the OSL to be directly integrated onto the micro-LEDs, maximising the energy density delivered to the OSL. A CMOS-driver array, such as the designs described in chapter 3, may be used to drive the micro-LEDs under pulsed operation for optical pumping of OSLs, such a hybrid CMOS/AlInGaN/OSL device would allow an array of OSLs to be computer controlled by a simple user interface and portable control board, representing a significant improvement on almost all existing OSL devices which are typically pumped with bulky, complex and expensive pump lasers.

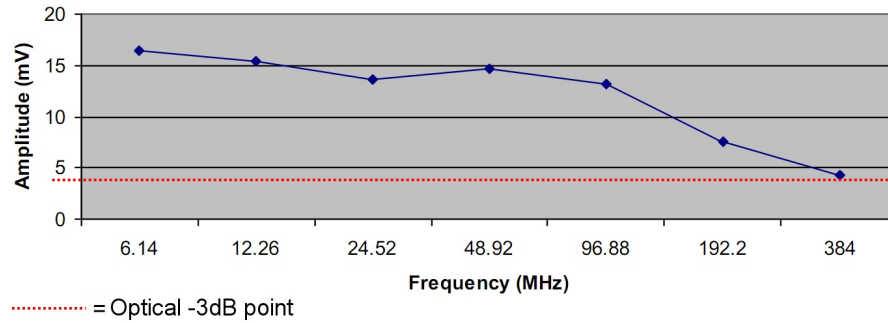


FIGURE 6.2: Frequency response of a 450 nm peak emission micro-LED pixel driven by the new ‘fourth generation’ CMOS chip. Approximate modulation bandwidth is 200 MHz. Micro-LED diameter is 14 μm , 40 mA current.

As was mentioned in chapter 3, a new ‘fourth-generation’ CMOS driver chip has been fabricated. Improvements implemented in this new design, compared to the prior ‘third-generation’ design, include a larger array (16×16 , compared to 8×8), a smaller driver-to-driver pitch (100 μm , compared to 200 μm), higher driver bandwidth, and a solution to the electrical crosstalk problem as described in section 3.4.4. Figure 6.1 shows an optical micrograph of a device in operation. Future work using this device includes the basic characterisation of the performance of CMOS-controlled micro-LED arrays made using this new design. This new CMOS chip has also been fabricated with visible light communications in mind, and as such allows micro-LED pixels to be modulated at higher frequencies than the previous incarnations of CMOS driver. Early characterisation of the new devices indicates that these CMOS micro-LED pixels have modulation bandwidths which are roughly comparable to that of the bare un-bonded micro-LEDs, as shown in figure 6.2, which is significantly higher than the 70 MHz bandwidth of the previous generation of CMOS-controlled micro-LEDs. The simple control over all elements within a CMOS-controlled micro-LED array also makes multi-path optical data transmission feasible using a single device. Figure 6.3 shows early results from optical data transmission experiments using a 450 nm peak emission micro-LED array controlled by a fourth-generation CMOS chip. 16 micro-LED pixels were simultaneously modulated with 16 different data input signals, with the optical output of one pixel imaged onto a photodiode. The pseudo-random input data (green) and received optical waveforms (yellow) for data transmission at 50 Mbit/s and 133 Mbit/s are shown in figure 6.3, respectively.

Further work using the time-resolved fluorescence measurement capabilities of the CMOS-controlled micro-LED arrays, as discussed in chapter 4, is ongoing. Trapping cells using CMOS-controlled micro-LED arrays using opto-electronic tweezers has already been demonstrated [2], and the possibility that the same CMOS/micro-LED device could also be used to perform a fluorescent lifetime measurement on trapped cells is currently under consideration.

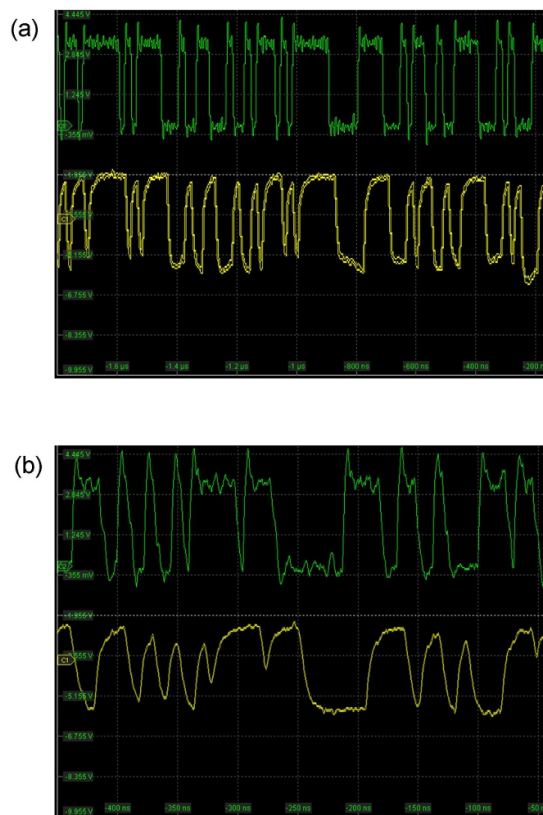


FIGURE 6.3: Optical data transmission using a CMOS-controlled micro-LED array. Courtesy of Dr. Bruce Rae and Mr. Shuialong Zhang.

Promising work towards a high-bandwidth white-emitting (micro-)LED was presented in chapter 5.4 using CQDs and LEPs in place of the conventional phosphors used in most commercial white LEDs. However, the modulation bandwidth of a fully-integrated hybrid device has not yet been demonstrated. Work is ongoing to progress towards this target, and in the longer term a demonstration of a fully integrated high-bandwidth white-emitting hybrid device should be feasible.

References

- [1] M. K. Kelly, O. Ambacher, R. Dimitrov, R. Handschuh, and M. Stutzmann. Optical process for lift-off of Group III-nitride films. *Physica Status Solidi (a)*, 159:R3, 1997.
- [2] A. Zarowna-Dabrowska, S.L. Neale, D. Massoubre, J. McKendry, B.R. Rae, H. Yin, R.K. Henderson, M.J. Rose, M.D. Dawson, J.M. Cooper, and E. Gu. Miniaturised optoelectronic tweezers controlled by GaN micro light emitting diode arrays, Paper MN4. In *23rd Annual Meeting of the IEEE Photonics Society, Denver, Colorado, USA*, 2010.

Appendix A

Mathcad code for extracting radiative lifetime from frequency response measurements

The following *Mathcad* code was used to extract a value for the fluorescence lifetime, τ , from the measured frequency response of a light emitting material, which was modulated by an LED with a frequency response given by M_{LED} . The frequency response of the light emitting material is defined as M_{tot} and the response of the polymer defined as M_f . This particular code is only valid when the light emitting material has a mono-exponential decay. In the example below, the light emitting material is the LEP Red F, and the LED is a 450nm-emitting 72 μ m diameter micro-LED.

First we import the network analyser data for the LED response and the measured LED + polymer response.

Data :=

	0	1
0	-38.064	-46.617
1	-38	-47.266
2	-38.029	...

We import the measured frequency responses of the micro-LED and the overall system, Mtot.

Note: this data is electrical dB

LEDdata := Data⁽⁰⁾

Mtot_data := Data⁽¹⁾

f := for i ∈ 0..800

$$f_i \leftarrow \left(75 \cdot 10^{-3} \right) + \left[\frac{i \left(500 - 75 \cdot 10^{-3} \right)}{800} \right]$$

 f

Define the corresponding frequency range for the Mtot data, i.e. 75kHz to 500MHz, 801 data points

f2 := for i ∈ 0..800

$$f_i \leftarrow \left(75 \cdot 10^{-3} \right) + \left[\frac{i \left(1000 - 75 \cdot 10^{-3} \right)}{800} \right]$$

 f

Define the corresponding frequency range for LED data, 75kHz to 1000MHz, 801 data points

inter := cspline(f2, LEDdata)

LED := interp(inter, f2, LEDdata, f)

Interpolate LED data over the 75kHz to 500MHz range, for use in our fitting below

Now we convert the measured response data from electrical dB (taken from detector) to optical dB and then normalise this data.

$$\text{LEDlinear} := 10 \left(\frac{\text{LED}}{20} \right) \cdot 1 \cdot 10^{-3} \quad \text{Mtot_linear} := 10 \left(\frac{\text{Mtot_data}}{20} \right) \cdot 1 \cdot 10^{-3}$$

$$\text{LEDnorm} := \frac{\text{LEDlinear}}{\max(\text{LEDlinear})}$$

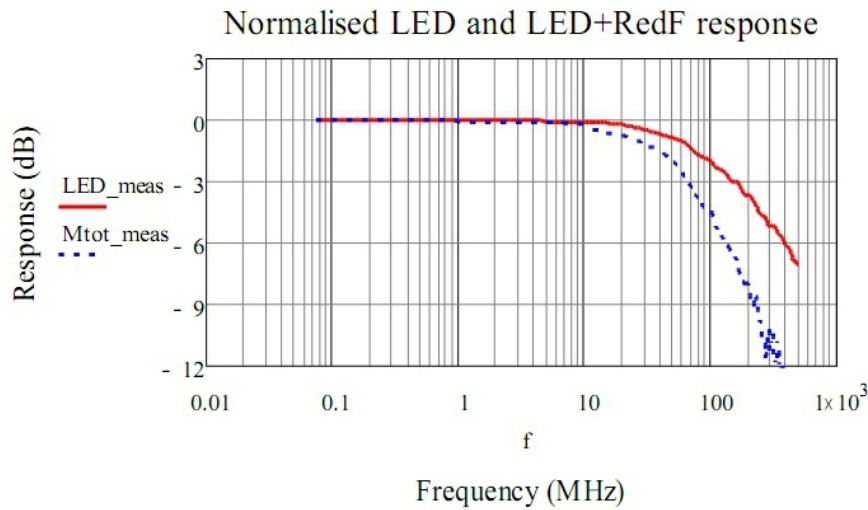
$$\text{Mtot_smoothed} := \text{medsmooth}(\text{Mtot_linear}, 15)$$

The Mtot data is smoothed

$$\text{LED_meas} := 10 \cdot \log(\text{LEDnorm})$$

$$\text{Mtot_norm} := \frac{\text{Mtot_smoothed}}{\text{Mtot_smoothed}_0}$$

$$\text{Mtot_meas} := 10 \cdot \log(\text{Mtot_norm})$$



Fitting

We will find the best fit to the Red F lifetime, τ , based on the measured frequency response of the LED, M_{LED} and of the overall system, M_{tot} . Firstly, we shall find the frequency response of the Red F sample, M_f , by subtracting M_{LED} from M_{tot} .

$$M_f_meas := M_{tot_meas} - LED_meas$$

We linearise the data, for fitting.

$$M_f_lin := 10^{\left(\frac{M_f_meas}{10}\right)}$$

We define the fit function to be used by Mathcad to find τ :

$$fit(f, \tau) := \frac{\left[1 + \left(2 \cdot \pi \cdot \frac{f}{1 \cdot 10^{-6}} \right)^2 \cdot \tau^2 \right]^{\frac{-1}{2}}}{\frac{4000000000000 \cdot \pi^2 \cdot \tau^2 \cdot f^2}{\left(4000000000000 \cdot \pi^2 \cdot \tau^2 \cdot f^2 + 1 \right)^{\frac{3}{2}}}}$$

$$guess := 2.31 \cdot 10^{-9}$$

We provide Mathcad with a guess of the 'true' value of τ . This guess is based on streak camera measurement performed on Red F by Dr. Colin Belton from Imperial College London.

$$\tau_{fit} := \text{genfit}(f, M_f_lin, guess, fit)$$

$$\tau_{fit} = 2.179 \times 10^{-9}$$

This is our fitted value for Tau

$$\text{fitresp}(f) := \left[1 + \left(2 \cdot \pi \cdot \frac{f}{1 \cdot 10^{-6}} \right)^2 \cdot \tau_{\text{fit}}^2 \right]^{\frac{-1}{2}}$$

$Mf_{\text{fit}} := 10 \cdot \log(\text{fitresp}(f))$ **This is our fitted Red F frequency response, M_f**

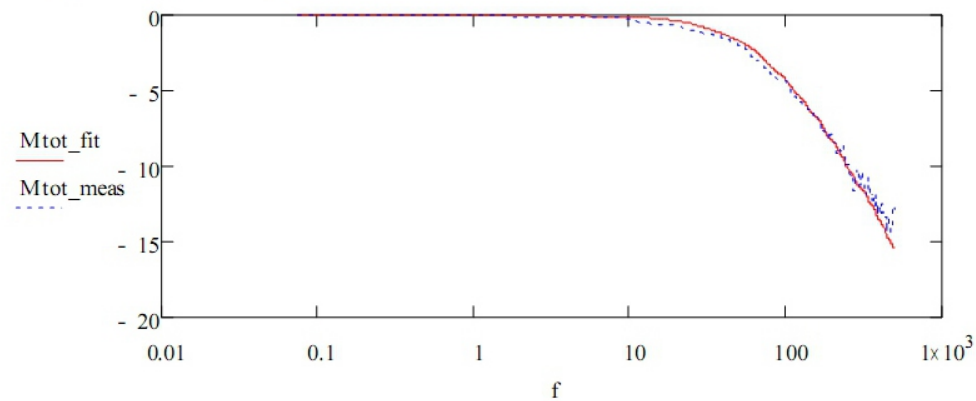
$$P_{3\text{dB}} := \frac{\sqrt{3}}{2 \cdot \pi \cdot \tau_{\text{fit}} \cdot 1 \cdot 10^6}$$

$P_{3\text{dB}} = 126.518$

This is the -3dB bandwidth of the Red F material, in MHz.

Now we may use this fitted data to provide an estimation of the overall frequency response, M_{tot} to see how closely this compares with our actual measured data.

$M_{\text{tot_fit}} := Mf_{\text{fit}} + \text{LED_meas}$



Appendix B

Publications

Journal publications

1. B.R. Rae, C. Griffin, J. McKendry, J.M. Girkin, H.X. Zhang, E. Gu, D. Renshaw, E. Charbon, M.D. Dawson, and R.K. Henderson, ‘CMOS driven micro-pixel LEDs integrated with single-photon avalanche diodes for time-resolved fluorescence measurements’, *Journal of Physics D: Applied Physics*, 41, 094011 (2008).
2. H.X. Zhang, D. Massoubre, Z. Gong, B. Guilhabert, J. McKendry, C. Griffin, E. Gu, and M.D. Dawson, ‘Individually-addressable flip-chip AlInGaN micro-pixelated light emitting diode arrays with high CW and nanosecond output power’, *Optics Express*, 16, 9918 (2008).
3. J. McKendry, D. Massoubre, Z. Gong, B. Guilhabert, E. Gu, M.D. Dawson, B. Rae, K. Muir, D. Renshaw, and R.K. Henderson, ‘Individually-addressable flip-chip AlInGaN micro-LED arrays with CMOS control and nanosecond output pulses’, *IEEE Photonics Technology Letters*, 21, 811 (2009).
4. B.R. Rae, K.R. Muir, Z. Gong, J. McKendry, J.M. Girkin, E. Gu, D. Renshaw, M.D. Dawson, and R.K. Henderson, ‘A CMOS time-resolved fluorescence lifetime analysis micro-system’, *Sensors*, 9, 9255 (2009).
5. D. Elfström, B. Guilhabert, J. McKendry, S. Poland, Z. Gong, D. Massoubre, G. Valentine, E. Gu, and M.D. Dawson, ‘Maskless ultraviolet photolithography based on CMOS-driven micro-pixel light emitting diodes’, *Optics Express*, 17, 23522 (2009).
6. Z. Gong, S.R. Jin, Y.J. Chen, J. McKendry, E. Gu and M.D. Dawson, ‘Size-dependent light output, spectral shift and self-heating of 400nm near-ultraviolet InGaN light emitting diodes’, *Journal of Applied Physics*, 107, 013103 (2010).

7. J. McKendry, Z. Gong, R.P. Green, B. Guilhabert, D. Massoubre, E. Gu, A.E. Kelly, and M.D. Dawson, ‘High Speed Visible Light Communications Using Individual Pixels in a Micro Light-Emitting Diode Array’, *IEEE Photonics Technology Letters*, 22, 1346 - 1348 (2010).
8. Bruce R. Rae, Jingbin Yang, J. McKendry, Zheng Gong, David Renshaw, John M. Girkin, Erdan Gu, Martin D. Dawson and Robert K. Henderson, ‘A Vertically Integrated CMOS Microsystem for Time-Resolved Fluorescence Analysis’, *IEEE Transactions on Biomedical Circuits and Systems*, 4, 437-444 (2010).
9. A. Zarowna-Dabrowska, S.L. Neale, D. Massoubre, J. McKendry, B.R. Rae, R.K. Henderson, M.J. Rose, H. Yin, J.M. Cooper, E. Gu and M.D. Dawson, ‘Miniaturized optoelectronic tweezers controlled by GaN micro-pixel light emitting diode arrays’, *Optics Express*, 19, 2720-2728 (2011).

Conference submissions

1. J. McKendry, C. Griffin, H.X. Zhang, Z. Gong, B. Guilhabert, D. Massoubre, E. Gu, M.D. Dawson, B.R. Rae, D. Renshaw, and R. Henderson, ‘Micro-pixelated flip-chip InGaN light-emitting diodes integrated with CMOS’, *2nd EOS Topical Meeting on Optical Microsystems*, (Capri, Italy, September 2007).
2. D. Massoubre, H.X. Zhang, J. McKendry, C. Griffin, B. Guilhabert, Z. Gong, E. Gu, and M.D. Dawson, ‘Flip-chip micro-pixel AlInGaN-based LED arrays with high CW and nanosecond output power’, Paper WU1, *20th Annual Meeting of the IEEE Lasers and Electro-Optics Society* (Lake Buena Vista, Florida, October 2007).
3. C. Griffin, J. McKendry, H.X. Zhang, E. Gu, B.R. Rae, R. Henderson, D. Renshaw, J.M. Girkin, and M.D. Dawson, ‘CMOS-integrated flip-chip micro-pixel InGaN LED arrays for on-chip microfluorimetry’, Paper WU4, *20th Annual Meeting of the IEEE Lasers and Electro-Optics Society* (Lake Buena Vista, Florida, October 2007).
4. J. McKendry, C. Griffin, H.X. Zhang, Z. Gong, B. Guilhabert, D. Massoubre, E. Gu, J.M. Girkin, M.D. Dawson, B.R. Rae, and R. Henderson, ‘Micro-pixelated flip-chip InGaN light emitting diodes integrated with CMOS control backplane’, *Europtrode IX* (Dublin, March 2008).
5. Z. Gong, H.X. Zhang, D. Massoubre, C. Griffin, J. McKendry, E. Gu, and M.D. Dawson, ‘Flip-chip, micro-pixelated InGaN LED arrays: attractive sources for

- micro-displays, colour conversion, fluorescence detection, and hybrid integration of organic/inorganic semiconductors', *2008 International Workshop on Nitride Semiconductors*, (IWN 2008, Montreux, October 2008).
6. D. Elfström, B. Guilhabert, C. Griffin, D. Massoubre, H.X. Zhang, J. McKendry, Z. Gong, E. Gu, and M.D. Dawson, 'Quantum dot nanocomposites as color converters for micro-pixelated gallium nitride light-emitting diodes', Paper WK2, *21st Annual Meeting of the IEEE Lasers and Electro-Optics Society*, (LEOS 2008, Newport Beach, CA, November 2008).
 7. J. McKendry, B.R. Rae, Z. Gong, B. Guilhabert, D. Massoubre, E. Gu, D. Renshaw, R.K. Henderson, and M.D. Dawson, 'Individually-addressable III-nitride micro-LED arrays for integrated CMOS control', Paper TuN2, *22nd Annual Meeting of the IEEE Photonics Society*, (Belek-Antalya, Turkey, October 2009).
 8. D. Massoubre, J. McKendry, B. Guilhabert, Z. Gong, I.M. Watson, E. Gu, and M.D. Dawson, 'Fabrication of planar GaN-based micro-pixel light emitting diode arrays', Paper MK2, *22nd Annual Meeting of the IEEE Photonics Society*, (Belek-Antalya, Turkey, October 2009).
 9. B.R. Rae, K.R. Muir, D. Renshaw, R.K. Henderson, J. Girkin, Zheng Gong, J. McKendry, E. Gu, M.D. Dawson, 'A vertically integrated CMOS micro-system for time-resolved fluorescence analysis', *IEEE Biomedical Circuits and Systems Conference*, BioCAS 2009.
 10. B.R. Rae, J. McKendry, Z. Gong, E. Gu, D. Renshaw, M.D. Dawson, and R.K. Henderson, 'A 200MHz, 300ps, 0.5pJ/ns optical pulse generator array in 0.35m CMOS', *IEEE International Solid-State Circuits Conference 2010*, (San Francisco CA, Feb. 2010).
 11. N. Laurand, J. McKendry, B. Guilhabert, A.E. Kelly, E. Gu, and M.D. Dawson, 'Modulation bandwidth and effective carrier lifetime of colloidal quantum dot nanocomposites', *6th International Conference on Quantum Dots*, (Quantum Dots 2010, Nottingham, April 2010).
 12. A. Zarowna-Dabrowska, S.L. Neale, D. Massoubre, J. McKendry, B.R. Rae, H. Yin, R.K. Henderson, M.J. Rose, M.D. Dawson, J.M. Cooper and E. Gu, 'Miniaturised Optoelectronic Tweezers Controlled by GaN Micro Light Emitting Diode Arrays', Paper MN4, *23rd Annual Meeting of the IEEE Photonics Society*, (Denver, Colorado, November 2010).
 13. N. Laurand, J. McKendry, B. Guilhabert, A.E. Kelly, B.R. Rae, R.K. Henderson, D. Massoubre, Z. Gong, E. Gu and M.D. Dawson, 'Hybrid Organic/Inorganic

Nanocrystal-Based Composite for Color-Conversion and Visible Light Communications', Paper TuE5, *23rd Annual Meeting of the IEEE Photonics Society*, (Denver, Colorado, November 2010).